

Mechanisms of Aggregation and Separation of Water and Solids from  
Bitumen Froth using Cluster Size Distribution

by

Nitin Arora

A thesis submitted in partial fulfillment of the requirements for the degree of

Master of Science

in

CHEMICAL ENGINEERING

Department of CHEMICAL AND MATERIALS ENGINEERING  
University of Alberta

© Nitin Arora, 2016

## **Abstract**

The large-scale corrosion and equipment damage caused by water and solids respectively in bitumen froth necessitate their removal using various methods. This study is aimed at understanding how water and solids aggregate (water-water, water-solid and solid-solid) in bitumen froth and what the dominant aggregation/ settling mechanism is during gravity separation (coalescence, flocculation and sweep flocculation).

Initially, we compared two mixing/ settling tank designs: one with side sampling ports and another with top sampling ports, to ensure that our sampling method is robust and gives a representative sample. The side sampling design gave more meaningful results for the two test emulsions. Bitumen froth contains a large amount of water and solids. Hence, a robust image analysis algorithm was developed to quantify the type of clusters (water-water or water-solid), the cluster size and the number of drops and/or particles in the cluster. Using this clustering algorithm, it was found that water drops flocculate with each other and also sweep flocculate the nearby solids. A low water concentration in the product layer also ensured low solids concentration. Solid-solid aggregates were rarely observed. The change in water drop size distribution over 60 min of settling indicated some evidence of coalescence. Coalescence was also visually observed for free water which could happen over hours or even days. Hence, flocculation and sweep flocculation are both important settling mechanisms for the demulsifier used in this study. Changing the mixing conditions (demulsifier injection concentration and mixing energy) did not change the dominant settling mechanism. Good mixing promotes aggregate growth, resulting in faster settling and lower final water and solids concentrations, both of which are crucial for industrial operations.

## **Acknowledgements**

I would like to thank Dr. Suzanne Kresta for believing in me and guiding me throughout the program. I want to thank Colin Saraka for providing support with experiments, meaningful discussions and great team work. Many thanks to Akorede Awosemo, Michaela Chemello for help in conducting experiments and Márcio Machado for providing guidance from time to time. I want to thank Alena Kukukova for allowing me to use her PNN Matlab code. Herb Green, from machine shop, deserves special appreciation as he provided quick solutions and always find time for me.

I want to thank our project sponsors, Samson Ng and Sujit Bhattacharya, from Syncrude Research who always found time to meet us in person, review my research findings and provided great feedback. They also shared their research findings with us.

Finally, I would like to thank my family who has strengthened me throughout my life. My father, Sushil Kumar Arora and my mother, Neeru Arora always encouraged me to achieve great heights. My wife, Swapnali Shende, has been a strong guiding partner and is indeed my better half.

# Table of Contents

<b>Chapter 1: Mixing, Settling and Oil Sands Extraction .....</b>	<b>1</b>
1.1.1 Froth Treatment .....	2
1.1.2 Emulsion and Emulsion Stability.....	3
1.1.3 Demulsifier .....	5
1.2 Mixing and Settling.....	6
1.2.1 Mixing Characterization .....	6
1.2.2 Meso-Mixing.....	10
1.2.3 Settling Mechanism .....	10
1.2.4 Sedimentation .....	15
1.2.5 Froth Mixing Studies .....	16
1.3 Research Objective .....	16
References.....	18
<b>Chapter 2: Comparison of Sampling Orientation for Water/ Solids Settling</b>	
<b>Experiments in a Diluted Bitumen System.....</b>	<b>24</b>
2.1 Abstract.....	24
2.2 Introduction.....	24
2.3 Experimental.....	25
2.4 Results.....	28
2.4.1 Standard Deviation.....	29
2.4.2 Full Profile Analysis of Water Concentration .....	30
2.4.3 Microscope Results.....	33
2.5 Conclusion .....	37
Nomenclature.....	37
Acronyms .....	38
References.....	38
<b>Chapter 3: Clustering Analysis for Characterization of Flocs/ Agglomerates in</b>	
<b>Bitumen Froth Images.....</b>	<b>40</b>
3.1 Introduction.....	40

3.2 Image Analysis Methods.....	45
3.2.1 Point Nearest Neighbor ( <i>PNN</i> ) .....	50
3.2.1.1 Introduction.....	50
3.2.2.2 <i>PNN</i> Analysis Set Up.....	52
3.2.2.3 <i>PNN</i> Results .....	55
3.3 Clustering Algorithm Steps.....	61
3.3.1 Pre-Processing of Images.....	61
3.3.2 Removing Fines and Separating Touching Objects.....	64
3.3.3 Separating Water and Solids from Pre-Processed Image .....	69
3.3.4 Marking Centroids .....	71
3.3.5 Detecting Clusters.....	72
3.3.6 Finding Cluster Information .....	74
3.3.7 Results.....	75
3.3.8 Strengths and Limitations .....	80
3.4 Conclusions.....	80
References.....	81
<b>Chapter 4: Settling Mechanisms in Bitumen Froth.....</b>	<b>85</b>
4.1 Experimental.....	85
4.1.1 Premixing.....	87
4.1.2 Naphtha Blending (Froth + Naphtha) .....	88
4.1.3 Demulsifier Dispersion [(Froth + Naphtha) + Demulsifier] .....	89
4.1.4 Sedimentation .....	91
4.1.5 Sampling Schedule.....	91
4.1.6 Experimental Design and Hypothesis.....	92
4.2 Results.....	94
4.2.1 No Demulsifier Run Results .....	95
4.2.2 Factorial Design Run Results.....	96
4.2.2.1 Qualitative Image Analysis.....	100
4.2.2.2 Clustering Image Analysis.....	106
4.2.2.3 Drop Size Distribution and Coalescence .....	117
4.2.3 Circulation Pattern Run Results.....	122

4.2.4 <i>OWS</i> and <i>CPA</i> Analysis .....	128
4.3 Conclusion .....	133
4.4 Future Work .....	135
References .....	136
<b>References (All) .....</b>	<b>139</b>
<b>Appendix A: Experimental Data .....</b>	<b>149</b>
<b>Appendix B1: Repeatability Experiments (Side vs. Top Sampling) for Diluted Bitumen .....</b>	<b>155</b>
<b>Appendix B2: Repeatability Experiments (Side vs. Top sampling) for Water in Mineral Oil .....</b>	<b>159</b>
<b>Appendix B3: Bitumen Froth Experimental Procedure .....</b>	<b>162</b>
<b>Appendix C1: Standard Operating Procedure for Sending <i>OWS/CPA/EXM</i> Samples to Syncrude .....</b>	<b>167</b>
<b>Appendix C2: Standard Operating Procedure for Receiving Feed Material from Syncrude .....</b>	<b>172</b>
<b>Appendix C3: Lab floor Cleaning and General Housekeeping .....</b>	<b>174</b>
<b>Appendix D1: Karl Fischer Procedure .....</b>	<b>176</b>
<b>Appendix D2: Microscope Image Acquisition Procedure .....</b>	<b>182</b>

## List of Tables

<b>Table 1-1:</b> Power numbers ( $N_p$ ) for various impellers in the fully turbulent regime with 4 standard baffles in a standard geometry stirred tank [adapted from (Hemrajani and Tatterson, 2004)].....	8
<b>Table 2-1:</b> Repeatability test results of water content for top and side sampling methods at 3 sampling heights ( $z_2$ , $z_3$ and $z_4$ ) and two liquid-liquid systems.....	30
<b>Table 2-2:</b> Water content of samples (wt %) collected from 4 different heights during a 60 min settling period at poor mixing conditions in top sampling <i>CIST</i> for diluted bitumen .....	36
<b>Table 3-1:</b> Repeatability of index of dispersion ( $I$ ) for random data generated for object A and object B using <i>rand</i> ( ) function.....	56
<b>Table 3-2:</b> Normalized index of dispersion, as a measure of clustering for several clustering scenarios (Figure 3-8 and Figure 3-9) for object A and object B .	57
<b>Table 3-3:</b> Effect of cluster orientation on index of dispersion for object A (when B is randomly dispersed) for different grid sizes .....	59
<b>Table 3-4:</b> Effect of cluster spacing on normalized index of dispersion for object A (when B is randomly dispersed) .....	59
<b>Table 3-5:</b> Effect of percentage of clustered objects on index of dispersion .....	60
<b>Table 3-6:</b> Example of connectivity matrix: First row (1, 2) indicates object number 1 and 2 are connected and so on .....	73
<b>Table 4-1:</b> Composition of supplied bitumen froth.....	87
<b>Table 4-2:</b> Premixing can geometry and mixing parameters .....	88
<b>Table 4-3:</b> Mixing specifications for naphtha blending (Froth + Naphtha) step.....	89
<b>Table 4-4:</b> Mixing conditions for demulsifier dispersion step .....	90
<b>Table 4-5:</b> Operating conditions and run summary for bitumen froth experiments using Rushton ( <i>RT</i> ), A310 and Intermig ( <i>IM</i> ) impellers .....	91

**Table 4-6:** Variable range for demulsifier dispersion in bitumen froth experiments using Rushton (*RT*), *A310* and Intermig (*IM*) impellers ..... 93

**Table 4-7:** Comparison of Rushton and A310 runs at same mixing conditions ..... 127

**List of Figures**

**Figure 1-1:** Illustration of water-in-oil emulsion (left) and oil-in-water emulsion (right) with emulsifier molecules shown as jagged lines..... 4

**Figure 1-2:** Schematic of a stirred tank with impeller diameter (*D*), impeller off-bottom clearance (*C*), tank diameter (*D*), liquid height (*H*) and impeller rotational speed (*N*)..... 7

**Figure 1-3:** Three steps of coalescence: drop collision, film drainage and film breakage ..... 11

**Figure 1-4:** Sweep flocculation happens when a faster settling floc surpasses small drops which then become part of the floc..... 14

**Figure 2-1:** The geometry for side (left) and top (right) sampling orientations in the *CIST* ..... 26

**Figure 2-2:** Experimental set up showing side (Left) and top (Right) sampling *CIST* along with needles used for withdrawing samples ..... 28

**Figure 2-3:** Microscope slide preparation involves putting a drop of liquid on to silanized microscope slide using a Pasteur pipette and covering it with a cover slip (image source: creative commons)....28

**Figure 2-4:** Water content of samples collected from 4 different heights during a 60 min settling period at favorable mixing conditions for water in diluted bitumen with (a): Side sampling *CIST* (Refer data: run #*RB*, Table A-1) and (b): Top sampling *CIST* (Refer data: run #*RA*, Table A-1)..... 31

**Figure 2-5:** Water content of samples collected from 4 different heights during a 60 min settling period using side and top sampling needles from same *CIST* for water in mineral oil (Refer data: Table A-3) ..... 32

<b>Figure 2-6:</b> Diluted bitumen microscope image captured with 40x lens at favorable mixing conditions, (a): no aggregates in feed can sample after premixing, (b): solid-water aggregates 60s after demulsifier addition at $z_1$ in top sampling <i>CIST</i> , shown in rectangular box.....	33
<b>Figure 2-7:</b> Diluted bitumen microscope image captured with 10x lens at favorable mixing conditions in side sampling <i>CIST</i> , (a): showing solid-water aggregate for sample (5 min at $z_2$ ), (b): aggregates were absent for sample (7 min at $z_2$ ) .....	34
<b>Figure 2-8:</b> Diluted bitumen microscope image showing solid-water aggregates at favorable mixing conditions for sample (5 min at $z_2$ ) in side sampling <i>CIST</i> , (a): 10x lens with solid-water aggregate in rectangular box, (b): 40x lens at same location as image (a), with arrows indicating water drops trapped in the aggregate.....	35
<b>Figure 2-9:</b> Diluted bitumen microscope image captured with 40x lens, showing loosely packed solid-water aggregates at poor mixing conditions.....	36
<b>Figure 3-1:</b> Illustration of hollow object (left) such as water and filled object (right) such as solids on a microscope image. Their shapes are frequently non-spherical. ....	43
<b>Figure 3-2:</b> Representative diluted froth images captured with a 40x lens containing (a): water-water flocs and (b): solid-solid chains.....	43
<b>Figure 3-3:</b> Representative diluted froth images captured with a 40x lens containing (a): water-solid flocs with water drops indicated by an arrow and (b): water-water chains .....	43
<b>Figure 3-4:</b> Representative diluted froth images showing examples of (a): free water covered with solids and bitumen clay skins, (b): free water containing trapped bitumen drop (rectangle) and bitumen film (arrow) at interface, (c): free water aggregates .....	45
<b>Figure 3-5:</b> Diluted froth image showing (a): water-water floc and (b): water-water chains. Nearest neighbor distance of Figure (a) and Figure (b) are shown in	

Figure (c) and Figure (d).Nearest neighbor direction (radians) of Figure (a) and Figure (b) are shown in Figure (e) and Figure (f). .....	47
<b>Figure 3-6:</b> (a): Dendrogram for image shown in Figure 3-5a with object set number and their separation distance ( $\mu\text{m}$ ) on horizontal and vertical axis respectively, (b): Two group of clusters identified with dendrogram, one with yellow circles and other with green arrows .....	49
<b>Figure 3-7:</b> Point Nearest Neighbor method showing single hexagon in a grid. Each grid point (black circles) looks for nearest water drop (red circles) and solid (blue rectangles) in image space [Modified significantly from Kukukova et al. (2011)] .....	51
<b>Figure 3-8:</b> Test images containing two objects: object A (red) and object B (green) with hexagonal grid points (blue) shown for three scenarios, (a): A and B randomly distributed, (c): A aggregated but B randomly dispersed and (e): A aggregated and B aggregated separately. The point-nearest object distribution for Figures (a), (c) and (e) is shown in Figures (b), (d) and (f) respectively. 53	
<b>Figure 3-9:</b> Test images containing two objects: object A (red) and object B (green) with hexagonal grid points (blue) shown for three scenarios, (a): A and B aggregated together, (c): A aggregated in long vertical chains but B randomly dispersed and (e): A aggregated in long horizontal chains and B aggregated separately. The point-nearest object distribution for Figures (a), (c) and (e) is shown in Figures (b), (d) and (f) respectively. ....	54
<b>Figure 3-10:</b> Effect of AB clustering on normalized index of dispersion. case 1: A clustered B clustered separately, case 2: AB clustered , case 3: AB cluster rearranged. Object A are circles and object B are triangles. ....	58
<b>Figure 3-11:</b> Frequency distribution (bins = 40) for froth image shown in Figure 3-5a..	61
<b>Figure 3-12:</b> Pre-processing (Leo, 2013) of a froth image shot with 40x microscope lens, (a): color image [produced with permission from Awosemo (2016)], (b): greyscale image, (c): image (b) after contrast enhancement, (d): image (c) after homomorphic compression, (e): image (d) after bi-level thresholding, (f): image (e) with objects touching left and top edge removed, objects smaller than $2.3\mu\text{m}$ (20 pixels) removed.....	63

<b>Figure 3-13:</b> Separation of touching objects, (a): binary image processed without watershed segmentation, (b) binary image processed with watershed segmentation. Single centroid is detected for touching objects (connected black pixels shown in yellow box).....	66
<b>Figure 3-14:</b> Euclidean distance map of the left image, shown in the right, where maximum brightness is assigned to the foreground pixel (black) farthest from background pixel (white). The right image is colored for illustration. ....	67
<b>Figure 3-15:</b> Microscope image showing edges of over-segmented free water being detected as solids (blue centroids). (a): Original color image, (b): Same image after clustering algorithm .....	68
<b>Figure 3-16:</b> Separation of a watershed segmented image (a) into two images, (b): water only image containing objects with form factor between 0 and 0.5, (c): solids only image containing objects with form factor between 0.5 and 1. ....	70
<b>Figure 3-17:</b> Breadth First Search algorithm to find all the connected nodes in a cluster. Nodes are detected in alphabetic order. ....	74
<b>Figure 3-18:</b> Algorithm output for image with water-water cluster obtained after processing of color image shown in Figure 3-5a. Red and blue centroids represent water and solids. Red, green and blue lines represent water-water, water-solid and solid-solid clusters respectively.....	76
<b>Figure 3-19:</b> Frequency distribution (bins = 20) of number of objects per cluster and size of cluster for image shown in Figure 3-18. Water-water, water-solid and solid-solids cluster information is shown.....	77
<b>Figure 3-20:</b> Algorithm output for image with water-solid cluster obtained after processing of color image shown in Figure 3-4a. Red and blue centroids represent water and solids. Red, green and blue lines represent water-water, water-solid and solid-solid clusters respectively.....	78
<b>Figure 3-21:</b> Frequency distribution (bins = 20) of number of objects per cluster and size of cluster for image shown in Figure 3-20. Water-water, water-solid and solid-solids cluster information is shown.....	79

<b>Figure 4-1:</b> Bitumen froth experimental set up.....	86
<b>Figure 4-2:</b> Effect of favorable vs. poor mixing conditions at 50 ppm and 150 ppm bulk concentration of demulsifier. Data produced with permission, Chong (2013) .....	93
<b>Figure 4-3:</b> Water content (wt%) as a function of settling time at two sampling heights ( $z_1$ and $z_4$ ) for runs: <i>ND1</i> and <i>ND2</i> , with no demulsifier addition .....	95
<b>Figure 4-4:</b> Water content (wt%) as a function of settling time at two sampling heights ( $z_1$ and $z_2$ ) for factorial design runs ( <i>FD1 - FD4</i> ). Runs are coded from the best ( <i>FD1</i> : high J, low IC) to the worst ( <i>FD4</i> : low J, high IC) mixing conditions.....	97
<b>Figure 4-5:</b> The difference in water content between first ( $z_1$ ) and second sampling ( $z_2$ ) height as a function of settling time for factorial design runs ( <i>FD1- FD4</i> )...	98
<b>Figure 4-6:</b> Regression coefficients ( $\beta$ ) for multi variable regression of water content at height $z_1$ for factorial design runs .....	99
<b>Figure 4-7:</b> Qualitative image analysis from beginning (0 min) till the end of settling (60 min) for best mixing conditions ( <i>FD1</i> : J+, IC-), indicating the types of species and aggregates, along with Karl-Fischer pie chart for comparison	102
<b>Figure 4-8:</b> Qualitative image analysis from beginning (0 min) till the end of settling (60 min) for worst mixing conditions ( <i>FD4</i> : J-, IC+), indicating the types of species and aggregates, along with Karl-Fischer pie chart for comparison	103
<b>Figure 4-9:</b> Representative microscope image at 60 min and height $z_1$ ( $z/H = 0.23$ ) for (a): good (run <i>FD1</i> ) and (b): bad (run <i>FD4</i> ) mixing conditions .....	105
<b>Figure 4-10:</b> Representative microscope image at 60 min at height $z_4$ ( $z/H = 0.82$ ), for (a): good (run <i>FD1</i> ) and (b): bad (run <i>FD4</i> ) mixing conditions .....	105
<b>Figure 4-11:</b> An illustration of cluster size depending on spatial orientation. Red and blue dots correspond to centroids of water and solid respectively.....	107
<b>Figure 4-12:</b> Comparison between <i>W-W</i> and <i>W-S</i> Sauter mean ( $D_{32}$ ) cluster size for all images in a single sample (e.g.: 3 min at height $z_1$ ). Each data point corresponds to the mean cluster size for that image.....	108
<b>Figure 4-13:</b> Mean cluster size as a function of settling time at a single sampling height .....	110

- Figure 4-14:** Correlation coefficient ( $R^2$ ) between  $W-W$  and  $W-S$  Sauter mean ( $D_{32}$ ) cluster size at multiple sampling heights and mixing conditions. Runs:  $FDI$  and  $FD4$  are at the best and worst mixing conditions respectively..... 111
- Figure 4-15:** Comparison between  $W-W$  and  $S-S$  Sauter mean ( $D_{32}$ ) cluster size for all images in a single sample (e.g.: 3 min at height  $z_l$ ). Each data point corresponds to mean cluster size for that image. .... 112
- Figure 4-16:** Correlation coefficient ( $R^2$ ) between  $W-W$  and  $S-S$  Sauter mean ( $D_{32}$ ) cluster size at multiple sampling heights and mixing conditions. Runs:  $FDI$  and  $FD4$  are best and worst mixing conditions respectively. .... 112
- Figure 4-17:** Microscope image showing small water drops ( $\sim 2 \mu\text{m}$ ) being detected as solids (blue centroids). (a): Original color image, (b): Same image after clustering algorithm..... 114
- Figure 4-18:** Correlation coefficient ( $R^2$ ) between  $KF$  water content (wt%) and  $W-W$  cluster size ( $D_{32}$ ) at multiple sampling heights and mixing conditions .. 116
- Figure 4-19:** Correlation coefficient ( $R^2$ ) between  $KF$  water content (wt%) and [ $W-W$  cluster size ( $D_{32}$ ) times total number of  $W-W$  clusters per images in a sample] at multiple sampling heights and mixing conditions. .... 116
- Figure 4-20:** Water drop size distribution of all samples at height  $z_l$  for naphtha blending ( $A-ZI$ ), demulsifier dispersion ( $B-ZI$ ) and settling samples (3 min to 60 min) at favorable mixing conditions ( $FDI$ : high  $J$ , low  $IC$ ) ..... 118
- Figure 4-21:** Comparison of water drop size distribution between  $FDI$  (high  $J$ , low  $IC$ ) and  $FD4$  (low  $J$ , high  $IC$ ) at height  $z_l$  for naphtha blending ( $A-ZI$ ) and end of settling (30 and 60 min) samples ..... 118
- Figure 4-22:** Coalescence of free water in bitumen froth is a slow process, (a): image taken at time = 0 hr, (b): image taken at same location at time = 16 hr. ... 120
- Figure 4-23:** Coalescence of free water in bitumen froth is a slow process, image taken at same location at (a): time = 0 hr, (b): time = 1 hr, (c): time = 17 hr. Some interfaces did not break for coalescence to happen. .... 121
- Figure 4-24:** Water content (wt%) as a function of settling time at two sampling heights ( $z_l$  and  $z_d$ ) for circulation pattern runs:  $CA1$  and  $CA2$  with A310 impellers

and runs: <i>CR1</i> and <i>CR2</i> with Rushton impellers ( <i>RT</i> ). For both impellers, same mid-level <i>J</i> and <i>IC</i> were used.....	123
<b>Figure 4-25:</b> Representative microscope image at 10 min and height $z_l$ for (a): <i>CR1</i> run, (b): <i>CR2</i> run, (c): <i>CA1</i> run and (d): <i>CA2</i> run. All runs were conducted at same mixing conditions.....	124
<b>Figure 4-26:</b> Mean cluster size as a function of settling time at height $z_l$ for circulation pattern runs conducted at same mixing conditions ( <i>J</i> and <i>IC</i> ) .....	125
<b>Figure 4-27:</b> Comparison of drop size distribution between Rushton runs ( <i>CR1</i> and <i>CR2</i> ) at height $z_l$ for naphtha blending (A-Z1), 10 min and 60 min of settling .	126
<b>Figure 4-28:</b> Comparison of drop size distribution between A310 runs ( <i>CA1</i> and <i>CA2</i> ) at height $z_l$ for 3, 10 and 60 min of settling .....	126
<b>Figure 4-29:</b> Relation between solids ( <i>OWS</i> ) and water ( <i>KF</i> ) content present in top layer ( $z/H = 0.1$ ) after 60 min of settling for 10 experiments.....	129
<b>Figure 4-30:</b> Relation between solids in top ( $z/H = 0.1$ ) and middle ( $z/H = 0.5$ ) layers after 60 min of settling for 10 experiments .....	130
<b>Figure 4-31:</b> Relation between water ( <i>OWS</i> ) in top ( $z/H = 0.1$ ) and middle ( $z/H = 0.5$ ) layers after 60 min of settling for 10 experiments .....	130
<b>Figure 4-32:</b> Relation between solids and water ( <i>KF</i> ) in bottom layer ( $z/H = 0.9$ ) after 60 min of settling for 10 experiments .....	131
<b>Figure 4-33:</b> <i>OWS</i> oil content (bitumen + naphtha) comparison between top and bottom layers for all 10 experiments .....	132
<b>Figure 4-34:</b> Computerized Particle Analysis ( <i>CPA</i> ) of solids collected after <i>OWS</i> analysis, in supplied undiluted froth and end of settling diluted froth for no demulsifier run .....	133

## Nomenclature

$C$	impeller off-bottom clearance (m)
$C_d$	drag coefficient of a settling particle
$C.G.y$	y-coordinate of centroid ( $\mu\text{m}$ )
$C.G.z$	z-coordinate of centroid ( $\mu\text{m}$ )

$C(t)$	water concentration (wt%) determined from Karl-Fischer instrument
$d_d$	drop/ particle diameter (m)
$d_i, d_j$	drop/ particle diameter of bin class i and j ( $\mu\text{m}$ )
$d_i$	cluster size (or max centroid-centroid distance) for $i^{\text{th}}$ bin
$d_{inj}$	demulsifier injection pipe diameter (m)
$d_p$	diameter of the sphere having same projected area as the particle (m)
$D10$	number mean
$D32$	Sauter mean
$d_s$	diameter of the sphere having same surface area as the particle (m)
$d_v$	diameter of the sphere having same volume as the particle (m)
$d_{v0.1}$	diameter below which 10 % volume of the distribution lies ( $\mu\text{m}$ )
$dy$	horizontal spacing between points in hexagonal grid (pixels)
$d_{yz}$	diagonal spacing between points in hexagonal grid (pixels or $\mu\text{m}$ )
$dz$	vertical spacing between points in hexagonal grid (pixels or $\mu\text{m}$ )
$D$	impeller diameter (m)
$F$	compressive force holding the drops together (N)
$g$	gravitational acceleration ( $= 9.8 \text{ m/s}^2$ )
$h_c$	critical film thickness (m) leading to rupture and successful coalescence
$h_o$	initial continuous phase film thickness (m)
$H$	mixing tank liquid height (m)
$H_{imp}$	impeller blade height (m)
$I$	index of dispersion
$J$	mixing energy (J/kg)
$k_b$	Boltzmann constant
$k_i$	constants used in equations
$K$	hydrodynamic volume factor for settling equation
$m$	number of hexagonal grid points
$n$	number of objects
$n_i$	number of clusters of certain size in $i^{\text{th}}$ bin
$n_r$	Richardson-Zaki number for hindered settling equation
$N_{px}$	number of pixels in an object

$N$	impeller rotational speed ( $s^{-1}$ )
$N_p$	power number of impeller
$P$	impeller shaft power consumption, not including gear loss (W)
$P(x; \bar{X})$	Poisson probability
$Q$	demulsifier injection rate ( $m^3/s$ )
$r_i$	circumscribed radius of object $i$ ( $\mu m$ )
$r/R$	radius of sampling point/ inner radius of <i>CIST</i>
$Re$	Reynolds number
$R^2$	regression coefficient
$s$	sample standard deviation (wt %)
$S$	upper impeller submergence below liquid surface (m)
$t$	bi-level thresholding value for image segmentation (0 - 255)
$t_c$	drop-drop contact time (s)
$t_{mix}$	mixing time (min)
$T$	mixing tank diameter (m)
$T_b$	temperature (K)
$F$	threshold distance value for determining if objects are connected ( $\mu m$ )
$U_z$	local mean fluid velocity along z-axis (m/s)
$u_z$	rms fluid velocity along z-axis (m/s)
$V_{imp}$	volume of fluid swept by impeller ( $m^3$ )
$V_t$	terminal settling velocity of drop/ particle (m/s)
$V_{tank}$	mixing tank liquid volume ( $m^3$ )
$x$	grid point-nearest object distance
$X_i$	factorial design level for variable $i$ ( $BC, IC, J$ )
$\bar{X}$	sample mean (wt %)
$y_i$	y-coordinate ( $\mu m$ )
$z_i$	z-coordinate ( $\mu m$ )
$z$	sampling depth below liquid surface (mm)
$z/H$	sampling height below liquid surface/ liquid height
$\alpha_{ij}$	flocculation collision frequency
$\beta$	regression coefficient

$\varepsilon$	rate of dissipation of turbulent kinetic energy by mass (W/kg)
$\varepsilon_{avg}$	rate of energy dissipation distributed over tank volume (W/kg)
$\varepsilon_{imp}$	maximum energy dissipation, in impeller zone (W/kg)
$\eta$	length of Kolmogorov scale eddy (m)
$\mu$	population mean (wt %)
$\mu_c$	continuous phase viscosity (Pa.s)
$\nu$	fluid kinematic viscosity ( $\mu_c/\rho_c$ ) [ $m^2/s$ ]
$\rho_d$	drop/particle (dispersed phase) density ( $kg/m^3$ )
$\rho_c$	continuous phase density ( $kg/m^3$ )
$\sigma'$	surface tension (N/m or $J/m^2$ )
$\sigma$	population standard deviation (wt %)
$\tau$	continuous film drainage time (s) for coalescence
$\varphi_d$	particle volume fraction (0 - 1)

## Acronyms

<i>BC</i>	bulk concentration of demulsifier (ppm by wt)
<i>CA</i>	circulation pattern runs with A310 impellers (2 in number)
<i>C/H</i>	carbon-to-hydrogen ratio (mol/mol)
<i>CIST</i>	confined impeller stirred tank
<i>CPA</i>	computerized particle analyzer for solid size distribution
<i>CR</i>	circulation pattern runs with Rushton impellers (2 in number)
<i>CSR</i>	complete spatial randomness of objects in a given space
<i>DS</i>	Dean Stark method for oil, solid and water analysis
<i>EDM</i>	Euclidean distance map
<i>EXM</i>	extraneous matter for solid analysis
<i>EO</i>	ethylene oxide monomer in demulsifier
<i>FD</i>	factorial design runs varying <i>J</i> and <i>IC</i> (4 in number)
<i>HLB</i>	hydrophile-lyophile balance
<i>IC</i>	injection concentration of demulsifier (wt %)

<i>IM</i>	Intermig impellers
<i>KF</i>	Karl Fischer moisture analyzer
<i>KNN</i>	k-nearest neighbor method for identifying clusters
<i>N/A</i>	not applicable
<i>ND</i>	no demulsifier runs (2 in number)
<i>O/H</i>	oxygen-to-hydrogen ratio (mol/mol)
<i>OWS</i>	oil-water-solid analysis
<i>PBTD</i>	pitched blade turbine down-pumping impeller
<i>PNN</i>	point-to-nearest neighbor method for identifying clusters
<i>PO</i>	propylene oxide monomer in demulsifier
<i>PSV</i>	primary separation vessel, for separating sands and heavy solids from oil
<i>RGB</i>	24-bit color image (red, green and blue channels)
<i>RT</i>	Rushton impellers
<i>SCO</i>	synthetic crude oil, produced from bitumen recovered from oil sands
<i>S-S</i>	solid-solid connected in a cluster based on a distance function
<i>UEP</i>	ultimate eroded point
<i>W-S</i>	water and solids connected in a cluster based on a distance function
<i>W-W</i>	water-water drops connected in a cluster based on a distance function

## Chapter 1: Mixing, Settling and Oil Sands Extraction

Canadian crude oil reserves are the third largest reserves in the world, most of which are in the form of oil sands (“Oil Sands,” 2016). In 2014, Alberta produced 2.3 million barrels per day of crude oil derived from oil sands, with total remaining reserves estimated to be 163.5 billion barrels (Alberta Energy Regulator, 2015).

Oil sands is a naturally occurring complex mixture of bitumen, sand, fine clays and as-mined water. Bitumen is a hydrocarbon mixture just like crude oil, but with higher density, viscosity, metals and acidity (Masliyah et al., 2011a). Bitumen does not flow at room temperature and has high molecular mass, hence it requires upgrading to form synthetic crude oil (*SCO*) that can be processed in conventional refineries to yield gasoline, diesel and petrochemicals (Masliyah et al., 2011a)<sup>1</sup>.

Oil sands are extracted using surface mining for shallow depths after removing overburden. Deeper oil sand deposits require high pressure steam injection for extraction. Surface mined oil sand ores are crushed and mixed with hot water and caustic to recover the oil (Clark, 1929). The ore-water slurry is pipelined to the primary separation vessel (*PSV*) where air bubbles attach to bitumen drops and aid in recovery. Bitumen froth collected from the top of the *PSV* is deaerated before being fed to the froth treatment plant where water and solids are removed. Bitumen recovery from oil sands is dependent on several factors such as ore grade (bitumen content), fines content, divalent cations and solids hydrophobicity (Liu et al., 2005).

Mixing is often an ignored unit operation. Try putting a spoon of sugar into water and you will note that without mixing, sugar dissolves slowly even if the amount is below the solubility limit. A harder mixing problem is mixing oil and water. In this case, water and oil would not mix at all if not for an external mixer such as a fork or whisk at home or an impeller at the industrial scale. The range of industrial mixing operations includes mixing of miscible or immiscible liquids, solid-liquid mixing, gas-liquid mixing, mixing sensitive reactions, and complex combinations of these. Mixing is essential to oil sands operations in several processes such as bitumen liberation from oil sand lumps, bitumen

---

<sup>1</sup> Pages 1, 5

solvent dilution (for removing water and solids) and removal of fines clays from tailings through coagulating agents. Mixing also finds application in industries such as wastewater treatment, pharmaceuticals, food, pulp and paper, with equipment selection depending upon the process objective and scale (industrial or bench) of the process. For further discussion of specific mixing problem, refer to Paul et al., 2004, and Kresta et al., 2015.

### 1.1.1 Froth Treatment

Deaerated bitumen froth typically contains 60 % bitumen, 30 % water and 10 % solids by mass (Gray et al., 2009). The water contains salts that contribute to corrosion in downstream equipment and solids are responsible for accelerated equipment wear and catalyst poisoning (Rao and Liu, 2013). Industrially, water and solids removal is facilitated by addition of either partially aromatic (naphtha) or aliphatic (paraffin) solvent (diluent). Diluent addition reduces the continuous phase viscosity and increases the density difference between water and bitumen, resulting in faster settling as per Stokes equation ( $Re < 0.1$ ),

$$V_t = \frac{g d_d^2 (\rho_d - \rho_c)}{18 \mu_c}$$

(Equation 1-1)

where  $V_t$  is the drop or particle terminal settling velocity,  $d_d$  and  $\rho_d$  are drop/particle size and density,  $\rho_c$  and  $\mu_c$  are the continuous phase density and viscosity, and  $g$  is gravitational acceleration.

Both naphtha and paraffinic solvents are used in commercial operations. Naphtha diluent yields ~1.5 - 2.5 wt% water and ~ 0.4 - 0.8 wt% solids in the final bitumen product (Masliyah et al., 2011a)<sup>2</sup>. Paraffinic diluent operation must be above the critical dilution ratio resulting in asphaltene precipitation that causes zone settling and nearly complete water/solids removal (Yang and Czarnecki, 2002; Long et al., 2002). However, paraffin method yields lower bitumen recovery, requires more solvent and higher capital

---

<sup>2</sup> Page 25-26

cost in comparison to the naphthenic method (Masliyah et al., 2011b)<sup>3</sup>. The paraffinic method employs gravity settling whereas the naphthenic method uses centrifuges and inclined plate settlers. Diluent selection is dependent on site-specific economics and on downstream upgrading capabilities. The focus of this thesis is the naphthenic method which operates commercially at a naphtha-to-bitumen dilution ratio of 0.7 by weight at 80°C (Shelfantook, 2004). The residual water and solids in this method form a very stable emulsion which requires demulsifier for further bitumen clarification and dewatering.

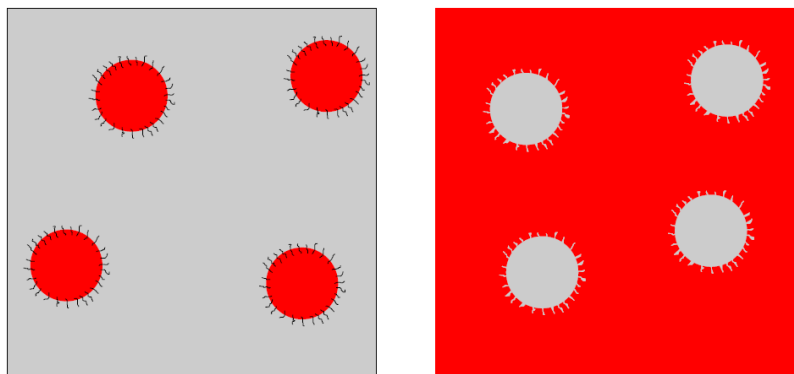
### **1.1.2 Emulsion and Emulsion Stability**

Figure 1-1 shows water-in-oil and oil-in-water emulsions that form when two immiscible liquids are mixed. Emulsions can form naturally (e.g.: oil in water emulsion in case of raw and homogenized milk) or be synthesized [e.g.: water in oil emulsion in case of moisturizing creams (Lefebvre, 1979)] and can be desirable or undesirable depending on the process (Schramm, 1992). Water-in-bitumen emulsions form naturally and are undesirable because of corrosion and other problems. Emulsions are thermodynamically unstable<sup>4</sup>, therefore stabilizing agents (or emulsifiers) need to be added to the emulsion (McClements, 2015). Emulsifiers (e.g.: surfactants, bi-wettable solids) have an affinity for both water and oil and hence sit at the interface. Figure 1-1 shows emulsifier (exaggerated in size) as jagged lines. They prevent aggregation of drops and hence retard oil-water separation. Emulsifiers are more soluble in one phase (oil or water) and they stabilize emulsions. The more soluble phase is on continuous side (Bancroft, 1913).

---

<sup>3</sup> Page 378-380

<sup>4</sup> Micro emulsions, whose drops are in nano scale range are considered thermodynamically stable



**Figure 1-1:** Illustration of water-in-oil emulsion (left) and oil-in-water emulsion (right) with emulsifier molecules shown as jagged lines

The water-in-bitumen emulsion is stabilized by natural surface active components such as clays, asphaltenes and naphthenic acids (Rao and Liu, 2013). These components can form rigid skins on the interface that require ~10 000 g force for phase separation (Czarnecki and Moran, 2005). Asphaltenes are the family of compounds in crude oil that are insoluble in aliphatic solvents (n-pentane and n-heptane) but soluble in toluene (Masliyah et al., 2011b). They have hydrophilic (polar heteroatoms) and hydrophobic (fused aromatic rings with aliphatic chains) parts making them surface active (Espinat et al., 2004). The water-insoluble component of asphaltene molecules is believed to be responsible for stabilizing this emulsion (Gu et al., 2002). Additionally, the authors noted that the asphaltenes at the interface had higher  $C/H$  (higher aromaticity) and higher  $O/H$  ratios (higher polarity) in comparison to the ones in bulk. Asphaltenes adsorb irreversibly at the interface and do not get removed even after repeated toluene washing (Solovyev et al., 2006). Asphaltenes are known to self-aggregate and their aggregates stabilize the emulsion (Sjöblom et al., 2007).

The evidences on the contribution of resins to emulsion stability are conflicting. Resins, structurally similar to asphaltenes, are soluble in aliphatic solvents (Masliyah et al., 2011b). Khristov et al. (2000) claimed that a combination of resins and asphaltenes forms more stable films than either individual component. McLean and Kilpatrick (1997) asserted that at high resin-to-asphaltene ratio, resin reduces emulsion stability by attaching itself to asphaltene and reducing its ability to attach to the interface. At low ratios, asphaltene remains surface active.

Solids and naphthenic acids also stabilize the emulsion. Kotlyar et al. (1999) identified solids associated with bitumen as ultrafine clays and a few sulfur and titanium containing minerals. Solids get coated with asphaltenes, become hydrophobic and stabilize the emulsion (Sullivan and Kilpatrick, 2002). Hydrophilic solids stabilize oil-in-water emulsions whereas hydrophobic solids stabilize water-in-oil emulsions (Bancroft, 1913). Naphthenic acids are carboxylic acids with aliphatic and cyclo-aliphatic chains. They are surface active and form nano-aggregates: crystalline structures that stabilize the emulsion (Ese and Kilpatrick, 2004). There is a complex interaction of adsorbing species at the oil-water interface rendering the separation of water and solids from bitumen a daunting task.

### **1.1.3 Demulsifier**

These rigid films can be broken by demulsifier addition (Zhang et al. 2003). Demulsifiers are surface active species that can change interfacial properties such as interfacial tension, interface thickness, strength, elasticity and promote coalescence or flocculation of dispersed phase drops (Feng et al., 2009). They may do so by displacing the natural stabilizers and changing the solids wettability (Kokal, 2005). Using an Atomic Force Microscope, Zhang et al. (2003) showed that demulsifiers disrupt asphaltenes film uniformity and hence its ability to stabilize the emulsion. There are two main types of demulsifiers: flocculation enhancing and coalescence enhancing. Flocculation refers to bridging of water drops to form big aggregates whereas coalescence refers to fusion of two drops into one big drop with a corresponding reduction in surface area. These settling mechanisms are discussed in more detail in Section 1.2.3. Flocculation based demulsifiers lead to more bitumen losses (to settled tailings), rag layer formation and are susceptible to overdosing (Czarnecki et al., 2007). Rag layer is a layer that forms at the oil-water interface and prevents settling of water and solids. This layer can have a complex water-in-oil-in-water emulsion along with asphaltenes and solids (Czarnecki et al., 2007). Peña et al. (2005) found that the combination of both types of demulsifier resulted in better performance than the either one. Flocculation followed by coalescence has also been suggested for ethyl cellulose based demulsifiers (Feng et al., 2010).

Demulsifier selection is process and site specific. Demulsifier needs to be injected at the optimum dosage: low dosage results in insufficient dewatering and high dosage hinders dewatering (Chong et al., 2016). Surfactant blends such as amines, copolymers of propylene oxide and ethylene oxide are generally used for water-in-bitumen emulsion (Rao and Liu, 2013). Three demulsifier properties are considered important: *HLB*, molecular weight, and structure. The hydrophile-lipophile balance (*HLB*) is a measure of demulsifier affinity for oil and water, with higher values indicating a water-loving tendency. *HLB* values of 15 - 20 were recommended after testing various demulsifiers on bitumen froth (Stasiuk and Schramm, 2001). Polyethylene oxide (*EO*) and polypropylene oxide (*PO*) content in the polymer are adjusted to achieve the desired *HLB* level. Larger molecular weights were shown to be more effective (Berger et al., 1987). Demulsifiers with branched and dendrimer structures gave better dewatering (Zhang et al., 2005). Flocculation enhancing demulsifiers have higher molecular weight, lower surface activity and are slow acting relative to coalescence based demulsifiers (Madjlessikupai, 2012).

## **1.2 Mixing and Settling**

### **1.2.1 Mixing Characterization**

Mixing definition has come a long way from saying “it is well mixed” to three quantifiable dimensions : intensity of segregation (mass), scale of segregation (length) and rate of reduction of segregation (time) [Kukukova et al., 2009]. For instance, intensity of segregation would refer to the uniformity of demulsifier concentration in a bulk solution. Scale of segregation would refer to the size distribution of dispersed water, solids and their flocs. Rate of segregation would mean the time it takes for demulsifier to be mixed into the solution so that the concentration becomes uniform.

Depending on geometry and scale, mixing is achieved through a variety of flow devices such as stirred tanks, static mixers, T-mixers, and even pumps. The mixing regime or turbulence level in a stirred tank as shown in Figure 1-2, can be determined by the Reynolds number ( $Re$ , Equation 1-2), which is the ratio of inertial to viscous forces (Rushton et al., 1950).

$$Re = \frac{\rho_c ND^2}{\mu_c}$$

(Equation 1-2)

where  $\rho_c$  and  $\mu_c$  are the continuous phase or fluid density and viscosity,  $N$  is the impeller rotational speed and  $D$  is the impeller diameter. For an impeller,  $Re < 10$  corresponds to the laminar regime and  $Re > 10\,000$  corresponds to turbulent regime (Hemrajani and Tatterson, 2004). The energy added at the impeller dissipates in the tank. Note that  $Re > 10\,000$  would ensure turbulent regime in impeller zone but  $Re > 300\,000$  is required for completely turbulent flow throughout the tank (Machado et al., 2013).

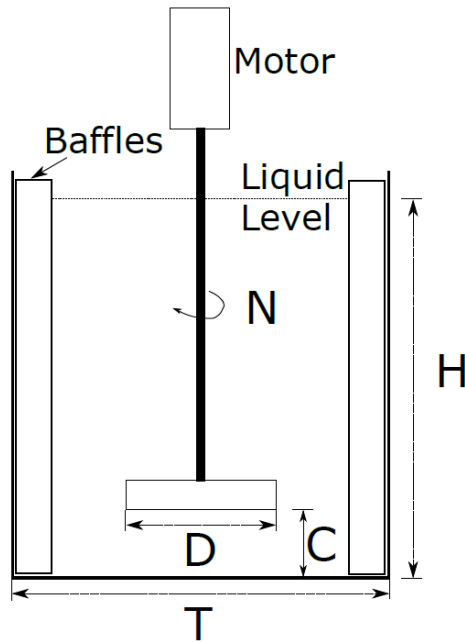


**Figure 1-2:** Schematic of a stirred tank with impeller diameter ( $D$ ), impeller off-bottom clearance ( $C$ ), tank diameter ( $D$ ), liquid height ( $H$ ) and impeller rotational speed ( $N$ )

The power number ( $N_p$ ), a measure of energy consumption in a stirred tank and is also used to characterize different impellers (Rushton et al., 1950).

$$N_p = \frac{P}{\rho N^3 D^5}$$

(Equation 1-3)

P is the shaft power delivered to the impeller,  $\rho$  is fluid density, N is impeller rotational speed and D is impeller diameter. Table 1-1 gives  $N_p$  values for different impellers used in this thesis when they are installed in a standard geometry stirred tank configuration.  $N_p$  depends on  $Re$ , impeller type, impeller geometry (number of blades, blade width), tank geometry ( $D/T$ ,  $C/T$ ) and number of baffles (Hemrajani and Tatterson, 2004). In the fully turbulent regime,  $N_p$  stays constant because viscous forces become negligible in comparison to inertial forces.

**Table 1-1:** Power numbers ( $N_p$ ) for various impellers in the fully turbulent regime with 4 standard baffles in a standard geometry stirred tank [adapted from (Hemrajani and Tatterson, 2004)]

<b>Impeller Type</b>	<b>Power Number (<math>N_p</math>)</b>
Lightnin A310	0.3
Ekato Intermig 2-Blade $D/T=0.7$	0.6
45° Pitched Blade Turbine 4-Blade	1.3
Rushton 6-Blade	5

Terms such as flocculation, coagulation and aggregation are used interchangeably to mean that drops are clustered together. These flocs can grow or break depending on the turbulence imparted by impeller. Turbulence helps to promote drop-drop collision and hence promote floc formation. The length scale of smallest turbulent eddies is given by the Kolmogorov scale ( $\eta$ )

$$\eta = \left( \frac{\nu^3}{\varepsilon} \right)^{\frac{1}{4}}$$

(Equation 1-4)

where  $\nu$  is fluid kinematic viscosity ( $m^2/s$ ) and  $\varepsilon$  is the local rate of dissipation of turbulent kinetic energy dissipation per unit mass ( $W/kg$ ). At this scale, the eddy viscous forces are nearly equal to inertial forces due to the mass of the eddy. Drops break up when the external forces by turbulent eddies overcomes internal and interfacial tension forces that resist deformation (Hinze, 1955). Similarly, flocs break up when the external force due to turbulent eddies overcomes the cohesive force that binds flocs together. The

maximum drop size is limited to some multiple of Kolmogorov scale whereas the minimum drop size is restricted to Kolmogorov scale and other drops formed during fragmentation (Zhou and Kresta, 1998).

The energy dissipation ( $\varepsilon$ ) varies by a factor of 100 in a stirred tank (Zhou and Kresta, 1996). The confined impeller stirred tank (*CIST*) is a novel bench scale mixing and settling tank that provides much more uniform turbulence than a standard stirred tank (Machado and Kresta, 2013).  $\varepsilon$  varies by a factor of 6-18 in the *CIST* (Machado and Kresta, 2013) which was used in this study. The maximum energy dissipation ( $\varepsilon_{imp}$ ) in the impeller discharge stream involves measuring local fluid velocity, but it can be approximated by the following equation (Kresta and Brodkey, 2004)

$$\varepsilon_{imp} \sim \frac{P}{\rho V_{imp}} = \frac{4N_p N^3 D^3}{\pi H_{imp}}$$

(Equation 1-5)

In this equation, P is the impeller shaft power,  $V_{imp}$  is volume of liquid in the impeller swept zone and  $H_{imp}$  is the impeller blade height. Numerous correlations between maximum stable drop size ( $d_{max}$ ) and maximum energy dissipation ( $\varepsilon_{imp}$ ) are available in the literature. Davies (1987) provided the following correlation that holds for range of mixing devices when the dispersion is fully stabilized.

$$d_{max} \sim \varepsilon_{imp}^{-\frac{2}{5}}$$

(Equation 1-6)

The variables used in this study: mixing energy dissipation ( $\varepsilon_{imp}$ ) and mixing time ( $t_{mix}$ ) can be combined into single variable, mixing energy ( $J = \varepsilon_{imp} \times t_{mix}$ ). Mixing energy (J) has been used recently as a scale up variable for flocculation of clay in mature fine tailings (Demoz, 2015) and is discussed further in Machado and Kresta (2015).

## 1.2.2 Meso-Mixing

The dispersion of additive such as demulsifier in diluted bitumen is prone to meso-mixing. Meso-mixing happens if the additive flow rate is higher than the local mixing rate at the feed point, leading to plume formation (Bourne, 2003). This high concentration plume can lead to secondary undesirable mechanisms such as side reactions (Bourne, 2003) and reduced demulsifier performance (Laplante et al., 2015). Meso-mixing effects can be mitigated by increasing the turbulence at feed point (Bhattacharya and Kresta, 2004), or lowering the feed rate and injection concentration (Torbacke and Rasmuson, 2001). The demulsifier feed rates were calculated using Equation 1-7 to prevent meso-mixing. For derivation of equation, refer to Chong (2013)<sup>5</sup>. Because of the observation of meso-mixing effects driven by high local concentrations, the injection concentration (*IC*) was classified as a mixing variable. When the injection concentration is reduced, the amount of mixing required is reduced.

$$Q = 0.54 \frac{v^{0.5} \times U_z \times d_{inj}^{1.5}}{u_z^{0.5}}$$

(Equation 1-7)

where *Q* is the injection rate, *v* is the kinematic viscosity, *U<sub>z</sub>* and *u<sub>z</sub>* are the local mean and rms velocity along the *z*-axis respectively and *d<sub>inj</sub>* is the inside diameter of the injection pipe.

## 1.2.3 Settling Mechanism

Water and oil phases may separate through several mechanisms: flocculation, coalescence and Ostwald ripening. Ostwald ripening refers to the growth of big drops at the expense of small drops through solubility of the latter in continuous phase (“Emulsion Stability and Testing,” 2011). This process was not observed for bitumen froth and hence is not discussed here. Micron sized water drops and solids settle at slow rate. This settling rate can be enhanced by increasing their effective size (Equation 1-1) through flocculation and coalescence.

---

<sup>5</sup> Appendix A

Coalescence is a three-step process (Leng and Calabrese, 2004), as shown in Figure 1-3:

1. Collision of two dispersed phase drops
2. Continuous phase film drainage
3. Film breakage and coalescence of drops

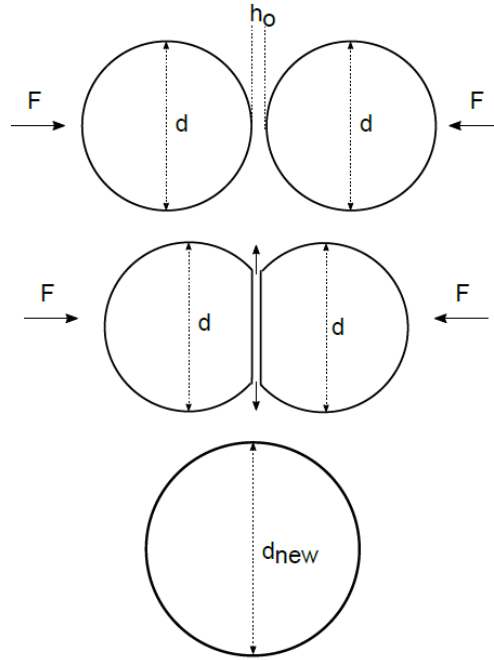


**Figure 1-3:** Three steps of coalescence: drop collision, film drainage and film breakage

The first step is carried out by Brownian motion of drops in the sub-micron range and fluid mixing (Kolmogorov and other turbulence scales) for bigger drops. The second step involves squeezing out the thin film of continuous phase (oil in case of colliding water drops) to a critical thickness ( $h_c$ ). At this thickness, the film breaks and two drops coalesce to form a big single drop. Coalescence is governed by following equation (Das et al., 1987)

$$\text{Coalescence frequency} = \text{Collision frequency} \times \text{Coalescence efficiency}$$

(Equation 1- 8)

Several coalescence models are available in the literature. Coualoglou and Tavlarides (1977) model is discussed here (Equation 1-9, Equation 1-10) to give the reader an idea of the variables that effect coalescence. Assuming both colliding drops

have the same diameter, the collision frequency (Equation 1-9) depends on drop diameter ( $d$ ) and the local energy dissipation ( $\varepsilon$ ). The coalescence efficiency (Equation 1-10) depends on several variables such as continuous phase properties ( $\mu_c$ ,  $\rho_c$ ,  $\sigma'$ ), contact force ( $F$ ), initial film thickness ( $h_0$ ) and critical film thickness ( $h_c$ ). The time for which drops are in contact ( $t_c$ ) needs to be greater than film drainage time ( $\tau$ ) for successful coalescence (Leng and Calabrese, 2004).

$$\text{Collision frequency} = k_1 \times d^{\frac{7}{3}} \times \varepsilon^{\frac{1}{3}}$$

(Equation 1-9)

$$\text{Coalescence efficiency} = k_2 \times \exp\left(-\frac{\tau}{t_c}\right)$$

$$\tau = \frac{3\mu_c F d^2}{64\pi\sigma'^2} \left( \frac{1}{h_c^2} - \frac{1}{h_0^2} \right)$$

$$t_c \approx \frac{(2d)^{\frac{2}{3}}}{\varepsilon^{\frac{1}{3}}}$$

(Equation 1-10)

Increasing energy dissipation ( $\varepsilon$ ) increases collision rate but decreases coalescence efficiency. Gentle shear (low  $\varepsilon$ ) is recommended so that the collision rate increases while the contact times ( $t_c$ ) are long enough to lead to successful coalescence (Leng and Calabrese, 2004). Hence, energy dissipation is a suitable variable for this mechanistic study. The coalescence model assumes isotropic turbulence and a rigid interface. The rigid asphaltene films and solids trapped at the water-bitumen interface could increase drainage time tremendously and may even prevent coalescence.

Flocculation is a process that involves drop collisions leading to formation of an aggregate called floc. Flocculation is a two-step process:

1. Collision of two or more dispersed phase drops or particles
2. Inter-drop attractive or repulsive forces determine if drops and/or particles stick together or separate

This process is used for solid-liquid separation in waste water treatment and oil-water separation in emulsions through additives that suppress repulsive (steric, double layer) inter-droplet forces. Hence, droplet and particle terms will be used interchangeably in the discussion. Flocs generally have a loose-fractal structure which means that they are self-similar irrespective of the scale (Serra and Casamitjana, 1998). Floc size and floc density determine their settling rate and floc strength (measure of adhesion force between drops) determines if the floc grows or breaks while passing through impeller zone. Most flocs are formed by the collision of existing flocs with individual drops (Everett, 1988) and flocs with smaller constituting drops are stronger than those with bigger drops (Selomulya et al., 2002). It is well known that for a given energy dissipation rate,  $\epsilon$  (often mistakenly called mean shear in the water treatment literature), the maximum floc size reaches a steady state that is a balance between floc growth and fragmentation. Similar to coalescence, flocculation is governed by collision frequency ( $\alpha_{ij}$ ) and flocculation efficiency. While the latter depends on the net attraction or repulsion force, the former is governed by the type of flocculation mechanisms (Rahmani et al., 2004):

1. Perikinetic flocculation (or flocculation due to Brownian motion, Equation 1-11)
2. Orthokinetic flocculation (or flocculation due to fluid mixing, Equation 1-12)
3. Sweep flocculation (or differential particle settling, Equation 1-13)

$$\alpha_{ij} = \frac{2k_b T_b}{3\mu} \frac{(d_i + d_j)^2}{d_i d_j}$$

(Equation 1-11)

$$\alpha_{ij} = \frac{(d_i + d_j)^3}{6} \sqrt{\frac{\epsilon}{\nu}}$$

(Equation 1-12)

$$\alpha_{ij} = \frac{\pi g}{72\mu} (d_i + d_j)^2 |\Delta\rho_i d_i^2 - \Delta\rho_j d_j^2|$$

(Equation 1-13)

Brownian flocculation is significant only for micron and sub-micron sized drops (Levich, 1962). Sweep flocculation happens when a faster settling big drop forms an aggregate with a slow moving small drop as shown in Figure 1-4. This type of flocculation is significant only if there is large difference in drop sizes and is a strong function of differential settling rate (Rahmani et al., 2004). Fluid mixing (both bulk flow and various scales of turbulence) brings drops together and promotes orthokinetic flocculation. Assuming there is no floc break up, Gregory (2009) proved that the floc growth rate is exponential in orthokinetic flocculation vs. linear in perikinetic flocculation. Big flocs generally have low strength and density and they may break if they experience high energy dissipation. A power-law relationship has been observed between the floc breakage rate and the energy dissipation rate (Rahmani et al., 2004). Similar to coalescence, observations suggest that flocculation is enhanced by gentle mixing (low  $\epsilon$ ) [Dyer and Manning, 1999].

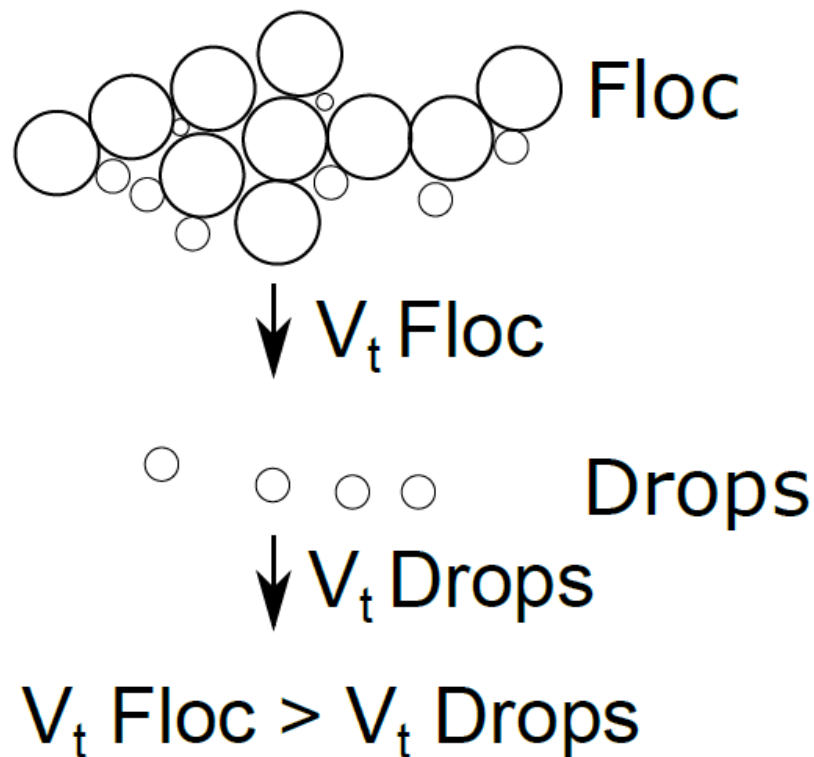


**Figure 1-4:** Sweep flocculation happens when a faster settling floc surpasses small drops which then become part of the floc

## 1.2.4 Sedimentation

Equation 1-1 is the simplest settling equation built on several assumptions: Stokes regime, rigid particle, spherical particle shape, no aggregation or repulsion between particles, no hindrance due to particle crowding and no settling vessel wall effects (Masliyah et al., 2011c). There are numerous equations available in the literature which allows some of these assumptions to be released. The settling of large quantities of water and solids in stationary bitumen froth would be likely determined by the hindered settling equation (Masliyah et al., 2011c)

$$V_t = \frac{g d_d^2 (\rho_d - \rho_c)}{18 \mu_c} \frac{(1 - K\phi_d)^{n_r}}{1 + 0.15 \text{Re}^{0.687}}$$

(Equation 1-14)

Note the difference between Equation 1-1 and Equation 1-14. The Reynolds number ( $\text{Re} = \frac{d_d V_t \rho_c}{\mu_c}$ ) accounts for the particle settling regime (laminar, transitional or turbulent).  $\phi_d$  is particle volume fraction and  $n_r$  is the Richardson-Zaki number whose value is 4.7 for the Stokes regime ( $\text{Re} < 0.1$ ).  $K$  is the hydrodynamic volume factor that accounts for particle-particle aggregation or repulsion and its value can vary from 1 (no interaction) to 3. The solution to this equation is iterative. Particle settling can thus be divided into 4 types based on particle concentration and morphology (Crittenden and Montgomery, 2012):

1. Individual particle settling (no hindrance from other particles)
2. Flocculated particle settling
3. Hindered particle settling
4. Compression settling

The first two settling types are observed for low particle concentration whereas the third and fourth types are observed for concentrated suspensions. In compression settling, a group of settled particles behaves as a porous bed whose packing results in additional release of continuous phase fluid.

### 1.2.5 Froth Mixing Studies

Bhardwaj and Hartland (1994) reported that for water in diluted bitumen emulsions after demulsifier addition, coalescence happened very fast in the first few minutes followed by slow coalescence over a long period of time. Mason et al. (1995) found that higher demulsifier bulk concentration and longer mixing times promoted drop growth of water in diluted bitumen emulsions. Rahmani et al. (2004) applied population balance modeling to study the effect of energy dissipation and solvent type on asphaltene aggregation kinetics in diluted bitumen. Ng et al., (2015) invented a process flow scheme for enhancing demulsifier effectiveness using mixing energy. Kailey and Behles (2015) compared two demulsifier compositions for water and solid removal efficiency in bitumen froth. From these collected studies, it is clear that demulsifier dosage and mixing energy are both important variables.

### 1.3 Research Objective

The highlights of previous froth studies are summarized here. Laplante (2011) defined an experimental protocol for testing demulsifier at standard mixing conditions in a *CIST*. He demonstrated that the demulsifier performance can be enhanced by as much as 100 % through increasing energy dissipation, increasing mixing time and pre-dilution of demulsifier (low *IC*) [Laplante, 2011; Laplante et al., 2015]. Chong (2013) and Leo (2013) conducted experiments for a different demulsifier composition using same experimental set up and found similar results. Overdosing of demulsifier (excess *BC*) can be detrimental to the process performance. This effect can be mitigated by using high mixing energy (*J*) and pre-dilution of demulsifier (Chong et al., 2016). Chong (2013) also set the experimental foundation for the froth experiments discussed in Chapter 4. Leo (2013) developed an algorithm to determine the water drop size distribution in diluted bitumen images. He found that peak of the distribution remained at 4  $\mu\text{m}$  and deduced similar effect of mixing variables as Chong (2013) using number of drops per sample slide.

The research objectives are summarized below:

1. Determine the dominant aggregation and settling mechanism of water and solids (coalescence, flocculation and sweep flocculation) in bitumen froth for a given demulsifier. Only one demulsifier was evaluated in this study. We wanted to know if which of these three mechanisms is dominant.
2. Determine if the mixing variables (demulsifier injection concentration and mixing energy) used in this study affect the dominant settling mechanism
3. Determine if the dominant settling mechanism is affected by sampling height
4. Determine if solids prefer to settle with other solids or water drops
5. In the previous studies, the dewatering rate (from water concentration profiles) during a 60 min settling period was reported to be high in first 10 min followed by a slow settling period till 60 min. The significance of 10 min mark was not known (Leo, 2013).

Before getting into settling mechanisms, we wanted to ensure that our sampling method is robust and we are getting representative sample. We tested two *CIST* sampling orientations (top and side), as discussed in Chapter 2. In order to determine the dominant settling mechanism, we needed an image analysis method to distinguish the type of aggregates (water-water or water-solid) seen on bitumen froth images. Leo (2013)'s drop size distribution algorithm was designed for spherical water drops in diluted bitumen which contained few solids. His method could not be applied to bitumen froth, which is an upstream product of diluted bitumen that contains a significantly higher quantity of water and solids. Leo's method could not be used here because in bitumen froth, some water species were non-spherical, effect of solids could not be ignored and the method is not designed to distinguish aggregates (water-water or water-solid). A new image analysis method called the clustering algorithm was developed and then used to analyze bitumen froth images as shown in Chapter 3. The objective of this new algorithm was not to determine just the water or solid size distribution but the type and size of the

aggregates that form (water-water or water-solid or solid-solid). The bitumen froth experimental results are discussed in Chapter 4. This study also presents sampling at 4 heights in comparison to one height in previous studies.

## References

- Alberta Energy Regulator, 2015. Alberta's Energy Reserves 2014 and Supply/Demand Outlook, 2015-2024.
- Bancroft, W.D., 1913. The Theory of Emulsification, *V. J. Phys. Chem.*, **17**, 501–519, doi:10.1021/j150141a002.
- Berger, P.D. et al., 1987. Designing and Selecting Demulsifiers for Optimum Field Performance Based on Production Fluid Characteristics, in: SPE International Symposium on Oilfield Chemistry.
- Bhardwaj, A., Hartland, S., 1994. Kinetics of Coalescence of Water Droplets in Water-in-Crude Oil Emulsions, *J. Dispers. Sci. Technol.*, **15**, 133–146, doi:10.1080/01932699408943549.
- Bhattacharya, S., Kresta, S.M., 2004. Surface Feed with Minimum by-Product Formation for Competitive Reactions, *Chem. Eng. Res. Des.*, **82**, 1153–1160, doi:http://dx.doi.org/10.1205/cerd.82.9.1153.44173.
- Bourne, J.R., 2003. Mixing and the Selectivity of Chemical Reactions, *Org. Process Res. Dev.*, **7**, 471–508, doi:10.1021/op020074q.
- Chong, J.Y., 2013. Mixing Effects on Chemical Demulsifier Performance in Diluted Bitumen and Froth, MSc Thesis, University of Alberta, Canada.
- Chong, J.Y. et al., 2016. Reduce Overdosing Effects in Chemical Demulsifier Applications by Increasing Mixing Energy and Decreasing Injection Concentration, *Energy and Fuels*, **30**, 5183–5189, doi:10.1021/acs.energyfuels.6b00621.
- Clark, K.A., 1929. The Separation of the Bitumen from Alberta Bituminous Sands, *Can. Inst. Min. Met. Bull.*, **22**, 1385–1395.
- Coulaloglou, C.A., Tavlarides, L.L., 1977. Description of Interaction Processes in Agitated Liquid-Liquid Dispersions, *Chem. Eng. Sci.*, **32**, 1289–1297.
- Crittenden, J.C., Montgomery, W.H. (Firm), 2012. Chapter 10: Gravity Separation, in: *MWH's Water Treatment: Principles and Design*, John Wiley & Sons, 641–726.
- Czarnecki, J., Moran, K., 2005. On the Stabilization Mechanism of Water-in-Oil Emulsions in Petroleum Systems, *Energy and Fuels*, **19**, 2074–2079,

doi:10.1021/ef0501400.

- Czarnecki, J. et al., 2007. On the “Rag Layer” and Diluted Bitumen Froth Dewatering. *Can. J. Chem. Eng.*, **85**, 748–755, doi:10.1002/cjce.5450850520.
- Das, P.K. et al., 1987. Coalescence of Drops in Stirred Dispersion. A White Noise Model for Coalescence, *Chem. Eng. Sci.*, **42**, 213–220.
- Davies, J.T., 1987. A Physical Interpretation of Drop Sizes in Homogenizers and Agitated Tanks, Including the Dispersion of Viscous Oils, *Chem. Eng. Sci.*, **42**, 1671–1676, doi:10.1016/0009-2509(87)80172-0.
- Demoz, A., 2015. Scaling Inline Static Mixers for Flocculation of Oil Sand Mature Fine Tailings, *AIChE J.*, **61**, 4402–4411.
- Dyer, K.R., Manning, A.J., 1999. Observation of the Size, Settling Velocity and Effective Density of Floccs, and their Fractal Dimensions, *J. Sea Res.*, **41**, 87–95.
- Emulsion Stability and Testing, 2011, Part. Sci., *Drug Dev. Serv. Br.* 2.
- Ese, M.H., Kilpatrick, P.K., 2004. Stabilization of Water in Oil Emulsions by Naphthenic Acids and their Salts: Model Compounds, Role of pH, and Soap: Acid Ratio, *J. Dispers. Sci. Technol.*, **25**, 253–261, doi:10.1081/DIS-120038634.
- Espinat, D. et al., 2004. Effects of Temperature and Pressure on Asphaltenes Agglomeration in Toluene. A Light, X-ray, and Neutron Scattering Investigation, *Energy and Fuels*, **18**, 1243–1249, doi:10.1021/ef030190.
- Everett, D.H., 1988. *Basic Principles of Colloid Science*, Royal Society of Chemistry: London.
- Feng, X. et al., 2010. Mechanistic Study on Demulsification of Water-in-Diluted Bitumen Emulsions by Ethylcellulose, *Langmuir*, **26**, 3050–3057, doi:10.1021/la9029563.
- Feng, X. et al., 2009. Biodegradable Polymer for Demulsification of Water-in-Bitumen Emulsions, *Energy and Fuels*, **23**, 451–456, doi:10.1021/ef800825n.
- Gray, M. et al., 2009. Physics in the Oil sands of Alberta, *Phys. Today*, **62**, 31–35.
- Gregory, J., 2009. Monitoring Particle Aggregation Processes, *Adv. Colloid Interface Sci.*, **147**, 109–123.
- Gu, G. et al., 2002. Influence of Water-Soluble and Water-Insoluble Natural Surface Active Components on the Stability of Water-in-Toluene-Diluted Bitumen Emulsion, *Fuel*, **81**, 1859–1869, doi:10.1016/S0016-2361(02)00113-8.
- Hemrajani, R., Tatterson, G., 2004. Chapter 6: Mechanically Stirred Vessels, in: Paul,

- E.L. et al. (Eds.), Handbook of Industrial Mixing: Science and Practice. John Wiley and Sons, Inc., Hoboken, New Jersey, 345–390, doi:10.1002/0471451452.ch6.
- Hinze, J.O., 1955. Fundamentals of the Hydrodynamic Mechanism of Splitting in Dispersion Processes, *AIChE J.*, **1**, 289–295, doi:10.1002/aic.690010303.
- Kailey, I., Behles, J., 2015. Evaluation of the Performance of Newly developed Demulsifiers on Dilbit Dehydration, Demineralization, and Hydrocarbon Losses to Tailings, *Ind. Eng. Chem. Res.*, **54**, 4839–4850, doi:10.1021/acs.iecr.5b00435.
- Khristov, K. et al., 2000. Thin Liquid Film Technique - Application to Water-Oil-Water Bitumen Emulsion Films, *Colloids Surfaces A Physicochem. Eng. Asp.*, **174**, 183–196, doi:10.1016/S0927-7757(00)00510-0.
- Kokal, S.L., 2005. Crude Oil Emulsions: A State-of-the-Art Review, *SPE Prod. Facil.*, **20**, 5–13.
- Kotlyar, L.S. et al., 1999. Solids Associated With the Asphaltene Fraction of Oil Sands Bitumen, *Energy and Fuels*, **13**, 346–350, doi:10.1021/ef980204p.
- Kresta, S.M., Brodkey, R.S., 2004. Chapter 2: Turbulence in Mixing Applications, in: Paul, E.L. et al. (Eds.), Handbook of Industrial Mixing: Science and Practice. John Wiley and Sons, Inc., Hoboken, New Jersey, 19–87, doi:10.1002/0471451452.ch2.
- Kresta, S.M. et al. (Eds.), 2015. Advances in Industrial Mixing: A Companion to the Handbook of Industrial Mixing. John Wiley & Sons Inc., Hoboken, New Jersey.
- Kukukova, A. et al., 2009. A New Definition of Mixing and Segregation: Three Dimensions of a Key Process Variable, *Chem. Eng. Res. Des.*, **87**, 633–647, doi:10.1016/j.cherd.2009.01.001.
- Laplante, G.P., 2011. On Mixing and Demulsifier Performance in Oil Sands Froth Treatment, MSc Thesis, University of Alberta, Canada.
- Laplante, P. et al., 2015. Demulsifier Performance in Froth Treatment: Untangling the Effects of Mixing, Bulk Concentration and Injection Concentration Using a Standardized Mixing Test Cell (CIST), *Fuel Process. Technol.*, **138**, 361–367, doi:http://dx.doi.org/10.1016/j.fuproc.2015.05.028.
- Lefebvre, E.G., 1979. US Patent 4 165 385: Water-in-Oil Emulsion for Skin Moisturizing.
- Leng, D.E., Calabrese, R. V., 2004. Chapter 12: Immiscible Liquid – Liquid Systems, in: Paul, E.L. et al. (Eds.), Handbook of Industrial Mixing: Science and Practice. John Wiley and Sons, Inc., Hoboken, New Jersey, 639–753.

- Leo, S.S., 2013. Measurement and Analysis of Changes in Drop Size Distribution during Bitumen Clarification using Image Analysis, MSc Thesis, University of Alberta, Canada.
- Levich, V.G., 1962. Physicochemical Hydrodynamics, Prentice Hall, Englewood Cliffs, New Jersey.
- Liu, J. et al., 2005. Processability of Oil Sand Ores in Alberta, *Energy and Fuels*, **19**, 2056–2063, doi:10.1021/ef050091r.
- Long, Y. et al., 2002. Stability and Settling Characteristics of Solvent-Diluted Bitumen Emulsions, *Fuel*, **81**, 1945–1952, doi:10.1016/S0016-2361(02)00132-1.
- Machado, M.B. et al., 2013. Transition from Turbulent to Transitional Flow in the Top Half of a Stirred Tank, *Chem. Eng. Sci.*, **98**, 218–230.
- Machado, M.B., Kresta, S.M., 2013. The Confined Impeller Stirred Tank (CIST): a Bench Scale Testing Device for Specification of Local Mixing Conditions Required in Large Scale Vessels, *Chem. Eng. Res. Des.*, **91**, 2209–2224, doi:10.1016/j.cherd.2013.06.025.
- Madjlessikupai, M., 2012. Study of the Rag Layer: Characterization of Solids, MSc Thesis, University of Alberta, Canada.
- Masliyah, J.H. et al., 2011a. Chapter 1: Introduction to the Athabasca Oil Sands, in: *Handbook on Theory and Practice of Bitumen Recovery from Athabasca Oil Sands, Volume 1: Theoretical Basis*, Kingsley Knowledge Publishing, 1–39.
- Masliyah, J.H. et al., 2011b. Chapter 7: Froth Treatment Fundamentals, in: *Handbook on Theory and Practice of Bitumen Recovery from Athabasca Oil Sands, Volume 1: Theoretical Basis*, Kingsley Knowledge Publishing, 349–386.
- Masliyah, J.H. et al., 2011c. Chapter 3: Fluid Particle Dynamics as Applied to Oil Sands Operations, in: *Handbook on Theory and Practice of Bitumen Recovery from Athabasca Oil Sands, Volume 1: Theoretical Basis*, Kingsley Knowledge Publishing, 129–172.
- Mason, S.L. et al., 1995. Drop Size and Concentration Profile Determination in Petroleum Emulsion Separation, *Colloids Surfaces A Physicochem. Eng. Asp.*, **96**, 85–92, doi:10.1016/0927-7757(94)03030-4.
- McClements, D.J., 2015. Chapter 7: Emulsion Stability, in: *Food Emulsions (Principles, Practices, and Techniques)*, CRC Press, Boca Raton, Florida, 289–382, doi:10.1201/b18868-8.
- McLean, J.D., Kilpatrick, P.K., 1997. Effects of Asphaltene Solvency on Stability of

- Water-in-Crude-Oil Emulsions, *J. Colloid Interface Sci.*, **189**, 242–253, doi:10.1006/jcis.1997.4807.
- Ng, Y.M.S. et al., 2015. CA Patent 2851192: Demulsifier Injection System for Froth Treatment Product Quality Enhancement.
- Oil Sands [WWW Document], 2016, Can. Assoc. Pet. Prod., URL <http://www.capp.ca/canadian-oil-and-natural-gas/oil-sands> (accessed 2.2.16).
- Paul, E.L. et al. (Eds.), 2004. Handbook of Industrial Mixing: Science and Practice. John Wiley and Sons, Inc., Hoboken, New Jersey.
- Peña, A. a. et al., 2005. Chemically Induced Destabilization of Water-in-Crude Oil Emulsions, *Ind. Eng. Chem. Res.*, **44**, 1139–1149, doi:10.1021/ie049666i.
- Rahmani, N.H.G. et al., 2004. Evolution of Asphaltene Floc Size Distribution in Organic Solvents under Shear, *Chem. Eng. Sci.*, **59**, 685–697.
- Rao, F., Liu, Q., 2013. Froth Treatment in Athabasca Oil Sands Bitumen Recovery Process : A Review. *Energy and Fuels*, **27**, 7199–7207, doi:10.1021/ef4016697.
- Rushton, J.H. et al., 1950. Power Characteristics of Mixing Impellers, *Chem. Eng. Prog.*, **46**, 395–404.
- Schramm, L.L., 1992. Chapter 1: Petroleum Emulsions: Basic Principles, in: Schramm, L.L. (Ed.), *Emulsions: Fundamentals and Applications in the Petroleum Industry*, American Chemical Society, Washington, DC, 1–49.
- Selomulya, C. et al., 2002. Aggregation Mechanisms of Latex of Different Particle Sizes in a Controlled Shear Environment, *Langmuir*, **18**, 1974–1984.
- Serra, T., Casamitjana, X., 1998. Effect of the Shear and Volume Fraction on the Aggregation and Breakup of Particles, *AIChE J.*, **44**, 1724–1730.
- Shelfantook, W.E., 2004. A Perspective on the Selection of Froth Treatment Processes, *Can. J. Chem. Eng.*, **82**, 704–709.
- Sjöblom, J. et al., 2007. Chapter 21: The Role of Asphaltenes in Stabilizing Water-in-Crude Oil Emulsions, in: Mullins, O.C. et al. (Eds.), *Asphaltenes, Heavy Oils, and Petroleomics*, Springer Science and Business Media, 580.
- Solovyev, A. et al., 2006. Langmuir Films of Bitumen at Oil / Water Interfaces, *Energy and Fuels*, **20**, 1572–1578, doi:10.1021/ef050409f.
- Stasiuk, E.N., Schramm, L.L., 2001. The Influence of Solvent and Demulsifier Additions on Nascent Froth Formation during Flotation Recovery of Bitumen from Athabasca Oil Sands, *Fuel Process. Technol.*, **73**, 95–110, doi:http://dx.doi.org/10.1016/S0378-

3820(01)00197-7.

Sullivan, A.P., Kilpatrick, P.K., 2002. The Effects of Inorganic Solid Particles on Water and Crude Oil Emulsion Stability, *Ind. Eng. Chem. Res.*, **41**, 3389–3404, doi:10.1021/ie010927n.

Torbacke, M., Rasmuson, Å.C., 2001. Influence of Different Scales of Mixing in Reaction Crystallization, *Chem. Eng. Sci.*, **56**, 2459–2473, doi:http://dx.doi.org/10.1016/S0009-2509(00)00452-8.

Yang, X., Czarnecki, J., 2002. The Effect of Naphtha to Bitumen Ratio on Properties of Water in Diluted Bitumen Emulsions, *Colloids Surfaces A Physicochem. Eng. Asp.*, **211**, 213–222, doi:10.1016/S0927-7757(02)00279-0.

Zhang, L.Y. et al., 2003. Langmuir and Langmuir-Blodgett Films of Mixed Asphaltene and a Demulsifier, *Langmuir*, **19**, 9730–9741, doi:10.1021/la034894n.

Zhang, Z. et al., 2005. Demulsification by Amphiphilic Dendrimer Copolymers, *J. Colloid Interface Sci.*, **282**, 1–4, doi:http://dx.doi.org/10.1016/j.jcis.2004.08.144.

Zhou, G., Kresta, S.M., 1996. Distribution of Energy between Convective and Turbulent-Flow for 3 Frequently used Impellers, *Chem. Eng. Res. Des.*, **74**, 379–389.

Zhou, G., Kresta, S.M., 1998. Correlation of Mean Drop Size and Minimum Drop Size with the Turbulence Energy Dissipation and the Flow in an Agitated Tank, *Chem. Eng. Sci.*, doi:10.1016/S0009-2509(97)00438-7.

## **Chapter 2: Comparison of Sampling Orientation for Water/Solids Settling Experiments in a Diluted Bitumen System<sup>6</sup>**

### **2.1 Abstract**

The objective of this study was to determine if the sampling orientation (horizontal or vertical) affects the measured water concentration during settling of diluted bitumen after addition of demulsifier. Two confined impeller stirred tanks (*CIST*'s): one with side sampling ports and another with top sampling ports; were used for comparison. The two sampling methods were compared using repeatability analysis at a single location and comparison of full water profiles over time. Both diluted bitumen and water in mineral oil systems were tested. While the two methods were statistically equivalent, side sampling was easier to perform and was selected for further use.

### **2.2 Introduction**

The effect of mixing on demulsifier performance in froth treatment was recently reported by two authors (Laplante, 2011; Chong, 2013). They showed that the mixing energy plays as important a role as the demulsifier bulk concentration and that pre-dilution of the demulsifier enhances the process outcome. Both studies were carried out in a confined impeller stirred tank (*CIST*), which provides more uniform flow and turbulence distribution than a conventional stirred tank (Machado and Kresta, 2013).

The diluted bitumen system contains dispersed water drops and solids [heavy minerals such as Titanium, Zirconium and clays (Tipman, 2013)<sup>7</sup>] and the aim was to get representative local solid and water concentrations. MacTaggart (1993) found that measuring solid concentration in a slurry mixing tank is really difficult due to its dependence on several parameters such as sampling velocity, sampling tube face (tapered or flat), sampling tube size, particle size and bulk solid concentration. The authors

---

<sup>6</sup> A version of this chapter has been published: Nitin Arora, Akorede Awosemo, Márcio B. Machado\*, and Suzanne M. Kresta, 2015, *Comparison of Sampling Orientation for Water/Solids Settling Experiments in a Diluted Bitumen System*, 15th European Conference on Mixing, Saint Petersburg, June 28-July 3, 6 pgs.

<sup>7</sup> Page 215

indicated that the complex flow patterns in a stirred tank interfere with obtaining a representative sample but the flow pattern in the impeller plane is well defined for radial impellers. In the literature, particle inertia and density differences are cited as the root cause of sampling errors in multi-phase systems. In diluted bitumen, the density difference is relatively small [dispersed water phase ( $1200 \text{ kg/m}^3$ ,  $<40 \text{ }\mu\text{m}$ ); continuous bitumen phase ( $900 \text{ kg/m}^3$ )] and the fine clays ( $< 2\mu\text{m}$ ) have very low inertia (Czarnecki and Moran, 2007). Kuzmanic and Rušić (1999) studied side sampling for floating solid concentration in a stirred tank. The authors found that the solid concentration was dependent on sampling port design and sampling velocity and the differences between the port designs are diminished by sampling at higher velocity.

The effect of sampling orientation for the complex multi-phase diluted bitumen system was investigated in this work. Two tank designs (side sampling and top sampling) were compared. The objective is to take samples at different heights in the *CIST* to observe the details of settling, coalescence, and flocculation after addition of demulsifier. The primary objective in this paper is to determine if the sampling orientation affects the sampling accuracy. The focus of this study was concentration of water rather than solids.

## 2.3 Experimental

The experiments were carried out using the protocol reported by Laplante (2011). Diluted bitumen was heated to  $76.5^\circ\text{C}$  in the original sampling can and re-suspended using a  $45^\circ$  *PBTD* impeller with baffles attached to the lid. The re-suspended diluted bitumen was transferred to the *CIST* where demulsifier was injected, mixed and allowed to settle for 60 min at  $76.5^\circ\text{C}$ . The top sampling and side sampling *CIST* geometries are compared in Figure 2-1. All samples were taken close to impeller at the mid-baffle plane. It is assumed that the water content is axisymmetric, particularly close to the impeller. The height ( $z$ ) was measured from the liquid surface ( $z = 0$ ) to the *CIST* bottom ( $z = 225$  mm), and the sampling locations were the same for both orientations [ $(r/R, z)$ : ( $0.5, z_1 = 52$  mm), ( $0.9, z_2 = 96$  mm), ( $0.9, z_3 = 140$  mm), ( $0.9, z_4 = 184$  mm)].

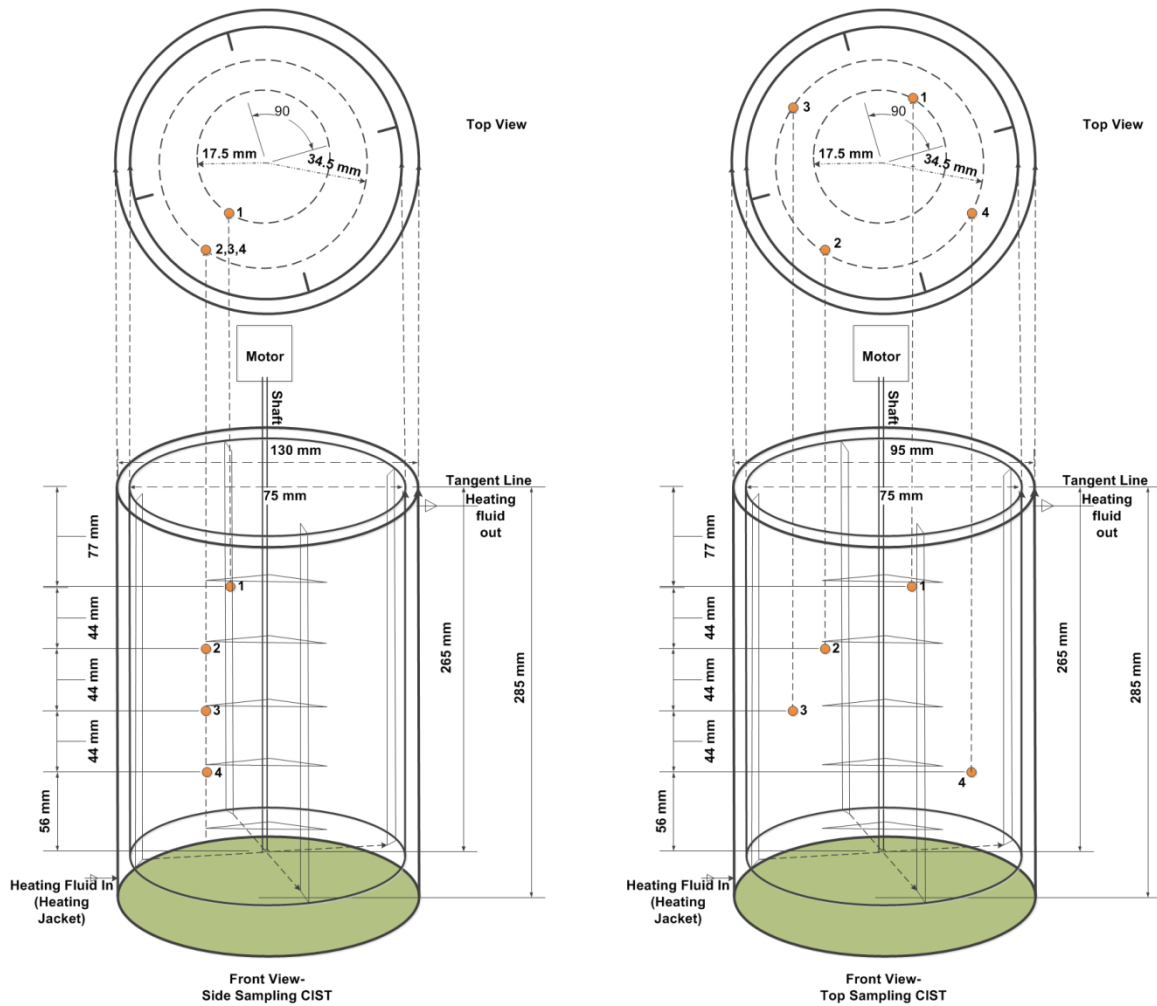


**Figure 2-1:** The geometry for side (left) and top (right) sampling orientations in the *CIST*

Three variables were varied during this study: bulk demulsifier concentration ( $BC$ ), injection concentration ( $IC$ ) and mixing energy ( $J$ ). The mixing energy ( $J$ ) is the product of power/mass in the impeller swept volume ( $P/\rho V_{imp}$ ) and mixing time ( $t_{mix}$ ). Injection concentration is identified as a mixing variable because a high injection concentration sets up the conditions for a high concentration feed plume and meso-mixing effects that may interfere with demulsifier dispersion and hence its effectiveness. The experiments were conducted at the following operating conditions: four runs with favorable mixing conditions ( $IC = 3$  wt %,  $J = 24\,000$  J/kg) and high bulk concentration ( $BC = 50$  ppm by wt), and four runs with poor mixing conditions ( $IC = 12$  wt %,  $J = 120$  J/kg) and low bulk concentration ( $BC = 27$  ppm by wt). These conditions were chosen based on previous results reported by Chong (2013). During settling, samples were taken at all four

sampling heights at 1, 3, 5, 7, 10, 30 and 60 min using 45° tapered 14 gauge Hamilton needles attached to an auto-pipette as shown in Figure 2-2. The top and side sampling orientation were also compared using a repeatability test. Six samples each of side and top orientation were taken at heights  $z_2$ ,  $z_3$  and  $z_4$  at 10, (15 or 20) and 30 min respectively. All 12 samples for each height were collected from the same tank in a time span of 3 to 4 min. Two repeatability runs were performed.

To confirm if one sampling technique is better than the other, the effect of sampling orientation was also evaluated using a water in mineral oil emulsion. 950 ml of Crystal Plus 70FG Mineral Oil ( $\rho_c = 860 \text{ kg/m}^3$  at 25°C and  $\nu_c = 12.6 \times 10^{-6} \text{ m}^2/\text{s}$  at 40°C) was added to the side sampling *CIST* and Rushton impellers were run at 600 rpm. The density and viscosity of mineral oil at room temperature was chosen to be similar to that of diluted bitumen at 80°C ( $\rho_c = 860 \text{ kg/m}^3$  and  $\nu_c = 6.1 \times 10^{-6} \text{ m}^2/\text{s}$ ). Oil soluble Tergitol NP-4 ( $HLB = 8.9$ ) surfactant at a concentration of  $5 \times 10^{-4} \text{ M}$  was added to the oil to stabilize the emulsion. 50ml (5.8 wt %) of ultrapure deionized water was injected slowly (to prevent plume formation) using a syringe pump. The water and surfactant were injected above the upper impeller blade tip to promote fast dispersion into the mineral oil. The experiment was conducted at room temperature. The impellers were run for 15 min which includes the 5 min of slow water injection by syringe pump. The  $J$  value for this experiment was 38 000 J/kg. Once the impellers were stopped, samples were taken at heights  $z_2$  and  $z_4$  at 1, 3, 5, 7, 10, 30 and 60 mins using both top and side sampling from the same *CIST*. The repeatability test was also performed for this emulsion.

A Karl Fischer moisture analyzer was used to determine the water content of the diluted bitumen and water-mineral oil samples. A drop of sample was retained for microscope slide preparation after its silanization using the procedure set by Leo (2013). Figure 2-3 shows how the microscope slide was prepared. The detailed experimental procedure and sampling routine for diluted bitumen and water-oil systems are described in Appendix B1 and B2 respectively.

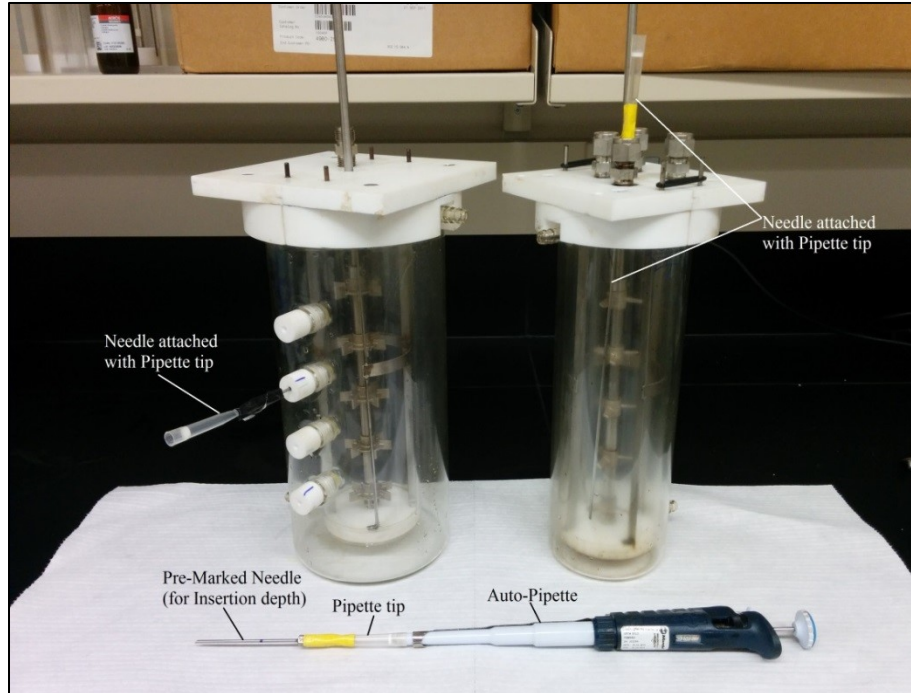


**Figure 2-2:** Experimental set up showing side (Left) and top (Right) sampling CIST along with needles used for withdrawing samples



**Figure 2-3:** Microscope slide preparation involves putting a drop of liquid on to silanized microscope slide using a Pasteur pipette and covering it with a cover slip (image source: creative commons)

## 2.4 Results

The first test of the two sampling orientations was a comparison of the standard deviations at three sampling heights for two liquid-liquid dispersions: water in diluted bitumen and water in mineral oil. Statistical analysis including hypothesis testing and outlier removal were applied to the data. As a second test, water profiles with respect to

time and height were compared as a check on whether the one sampling method gave more physically realistic results and fewer outliers.

### 2.4.1 Standard Deviation

The average values of water concentration and the associated standard deviations are shown in Table 2-1. The set data from which these means ( $\bar{X}$ ) and standard deviations ( $s$ ) are calculated, is shown in Table A-2 (Appendix A). Of the nine comparisons (without removing outliers), the top sampling has a higher standard deviation than side sampling for 5 cases, the two methods have nearly same standard deviation for 3 cases and top sampling has lower deviation than side sampling for 1 case. This leads one to believe that side sampling gives more consistent results than top sampling. Considering the mean values, the top result deviates significantly from the side result in three cases (highlighted in bold, Table 2-1), two of which are at the furthest distance from the liquid surface.

Statistical analysis was conducted to verify the comparison. One outlier can offset the standard deviation of the technique significantly especially for this small sample size of 6. Using the Grubbs test (Grubbs, 1950) at a 5 % level of significance, 3 outliers were removed: 2 from top sampling and 1 from side sampling. The Grubbs test relies on the assumption that there is only one outlier in the data set and the sample data is normally distributed. This was verified using Kolmogorov-Smirnov one sample test (Tobias and Croarkin, 2003)<sup>8</sup>. The revised mean and standard deviation after removing outliers are also reported in Table 2-1. After removing outliers, the standard deviation of top sampling was higher for 3 cases, the two methods had same standard deviation for 4 cases and top sampling has lower standard deviation for 2 cases. This leads us to a different conclusion that both sampling techniques have a similar standard deviation and similar numbers of outlying points. Hypothesis testing (without removing outliers) using the Two Sample F-Test (Tobias and Croarkin, 2003)<sup>9</sup> at a 5% level of significance was also conducted to compare standard deviations ( $\sigma$ ). The null Hypothesis ( $\sigma_{top} = \sigma_{side}$ ) was accepted for all cases. A Hypothesis t-test was used for comparison of means ( $\mu$ ) of the two methods. The null hypothesis ( $\mu_{top} = \mu_{side}$ ) was accepted for all cases except 30 min at

---

<sup>8</sup> Section: 1.3.5.16. Kolmogorov-Smirnov Goodness-of-Fit test

<sup>9</sup> Section: 1.3.5.9. F-Test for Equality of Two Variances

$z_4$  (poor mixing-diluted bitumen) and 10 min at  $z_2$  (water in mineral oil). Full water concentration profiles are considered next to determine if one of these methods is more physically robust.

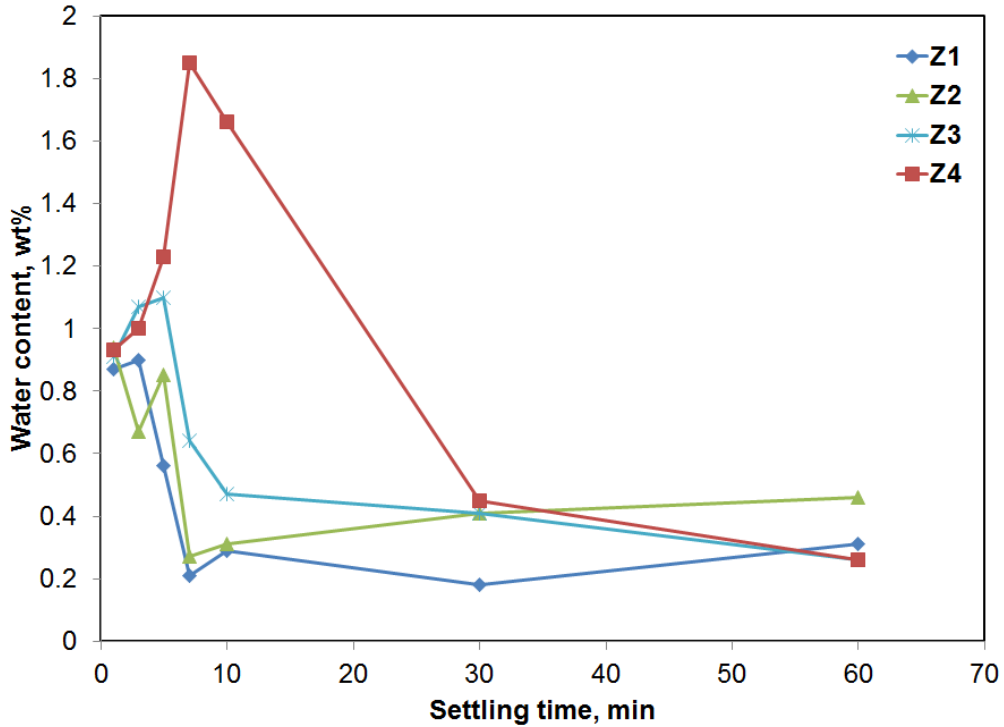
**Table 2-1:** Repeatability test results of water content for top and side sampling methods at 3 sampling heights ( $z_2$ ,  $z_3$  and  $z_4$ ) and two liquid-liquid systems

		Top	Side	Top	Side	Top	Side
		10 min at $z_2$		20 min at $z_3$		30 min at $z_4$	
		Water Content, wt %					
Poor Mixing-Diluted Bitumen	$\bar{X}$	0.76	0.78	0.87**	0.85**	<b>2.18</b>	0.65
	$s$	0.13	0.07	0.05**	0.04**	0.19	0.20
Favorable Mixing-Diluted Bitumen	$\bar{X}$	0.47 0.40*	0.46 0.49*	0.40	0.38	<b>0.36</b>	0.45
	$s$	0.17 0.04*	0.08 0.03*	0.04	0.06	0.10	0.05
Water in Mineral Oil emulsion	$\bar{X}$	<b>0.87</b>	1.19	1.49	1.48	0.75 0.65*	0.63
	$s$	0.18	0.26	0.39	0.22	0.25 0.06*	0.17

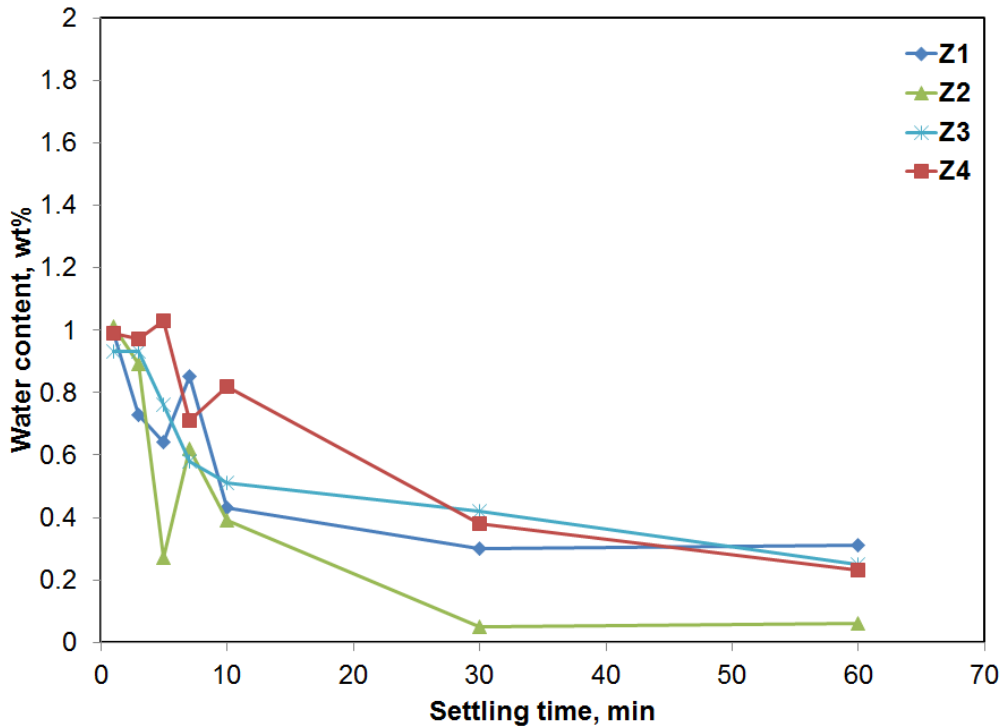
\* values recalculated after removal of one clear outlier, \*\*15 min at  $z_3$

## 2.4.2 Full Profile Analysis of Water Concentration

The water content results for favorable mixing with diluted bitumen in side sampling *CIST* are shown in Figure 2-4a. The water content at heights  $z_1$ ,  $z_2$  and  $z_3$  decreased during the first 7 min of settling and simultaneously the water content at height  $z_4$  reached a peak value of 1.85 wt % which is even higher than the initial water content of 1.19 wt %. This implies that the water from heights  $z_1$ ,  $z_2$  and  $z_3$  had settled to height  $z_4$  and the rate of water settling below height  $z_4$  is slow. Figure 2-4b shows that the expected increase in water concentration at  $z_4$  was not observed at same operating conditions in the top sampling *CIST*. This supports a hypothesis that the long sampling probe reduces the accuracy of sampling.



(a)



(b)

**Figure 2-4:** Water content of samples collected from 4 different heights during a 60 min settling period at favorable mixing conditions for water in diluted bitumen with (a): Side sampling *CIST* (Refer data: run #*RB*, Table A-1) and (b): Top sampling *CIST* (Refer data: run #*RA*, Table A-1)

Figure 2-5 for water in mineral oil shows that top and side sampling give widely different water concentrations, particularly during the initial stages of settling. The profiles converge at 30 and 60 min. This appears to be due to the settling of free water below  $z_4$ . Top sampling flattens out the water profile for both diluted bitumen and water-mineral oil systems, and does not appear to accurately sample the water content.

This anomaly in the top sampling data could be due to disturbance of the settling system due to the long length (247 mm for height  $z_4$ ) of the sampling probe, or small changes in the angle of sampling of the needle. For the side sampling *CIST*, the sampling location is more precise as the sampling needle is guided by tight clearance slot and lower insertion length (45 mm for height  $z_4$ ).

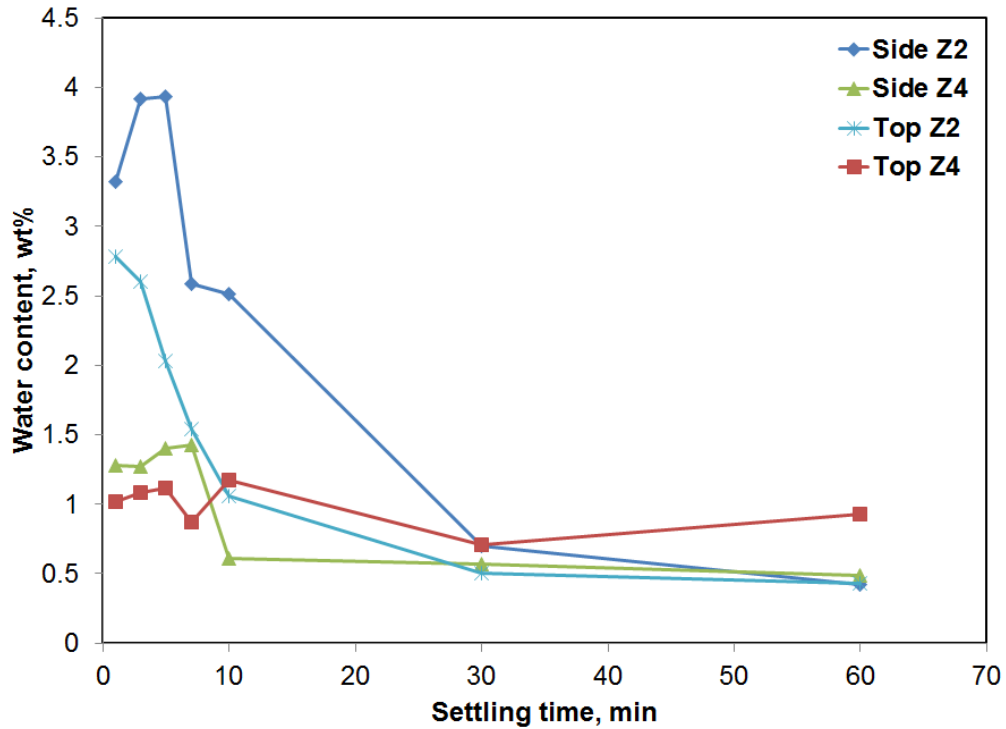


**Figure 2-5:** Water content of samples collected from 4 different heights during a 60 min settling period using side and top sampling needles from same *CIST* for water in mineral oil (Refer data: Table A-3)

### 2.4.3 Microscope Results

For all the samples that were analyzed by Karl-Fischer titration, a drop of diluted bitumen was retained for preparing microscope slides and subsequent image acquisition. Solid-water aggregates such as the ones shown in Figure 2-6b were seen at favorable mixing conditions ( $BC = 50$  ppm,  $IC = 3$  wt %,  $J = 24\ 000$  J/kg) at 1, 3 and 5 min of settling at top three sampling heights ( $z_1$ ,  $z_2$  and  $z_3$ ) in side sampling *CIST*. These fractal aggregates were not present in premix sample (feed can, Figure 2-6a) but were present in samples collected during mixing (1 min after demulsifier addition). We believe that the demulsifier aids in formation of these aggregates and that they sweep flocculate (Melik and Fogler, 1984) small drops and solids while settling, resulting in even bigger aggregates and faster settling.

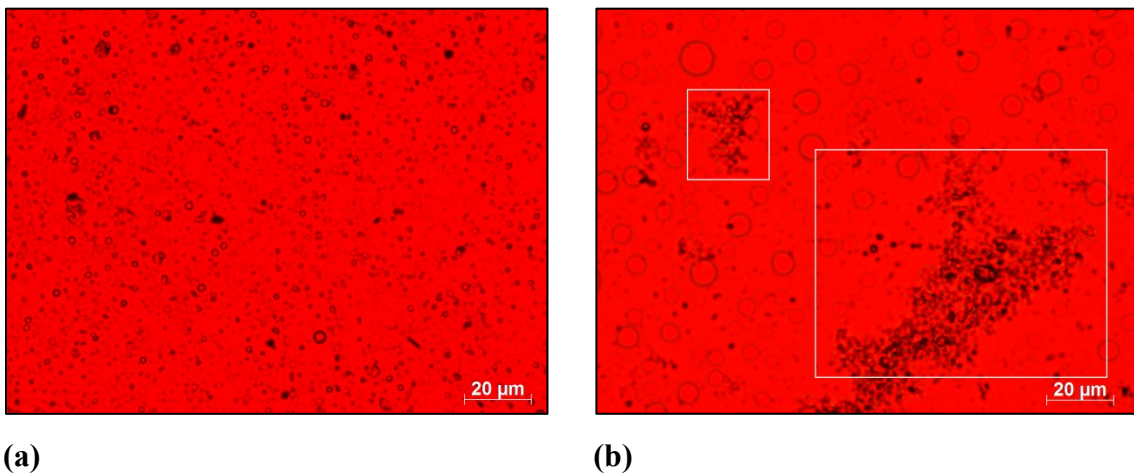


**Figure 2-6:** Diluted bitumen microscope image captured with 40x lens at favorable mixing conditions, (a): no aggregates in feed can sample after premixing, (b): solid-water aggregates 60s after demulsifier addition at  $z_1$  in top sampling *CIST*, shown in rectangular box.

These aggregates were present at 5 min at top three sampling heights ( $z_1$ ,  $z_2$  and  $z_3$ ) but went missing at 7 min as illustrated in Figure 2-7. The Karl Fischer data for this run (#RB) is shown in Figure 2-4a. Close inspection of *KF* data indicates that maximum dewatering rate (maximum slope) lies between 5 and 7 min for the top three sampling heights. This leads to two conclusions, one that the presence of solid-water aggregates was responsible for fast dewatering in the first 7-10 min of settling and, second that *KF*

and microscope data can be related. The reduced rate of dewatering after 10 min is owed to the absence of aggregates. At sampling height  $z_4$ , the transition from aggregates to no aggregates happened between 10 and 30 min. This agrees with maximum slope as per  $KF$  data in Figure 2-4a. Although solid-water aggregates were present in run#  $RA$  (top sampling  $CIST$  at favorable mixing conditions), a similar neat relation between  $KF$  and microscope data could not be established. For this run, the aggregates were present in first 10 min of settling at all heights but went missing at 30 and 60 mins. This confirms the earlier observation that top sampling method failed to capture the full kinetics of the system.

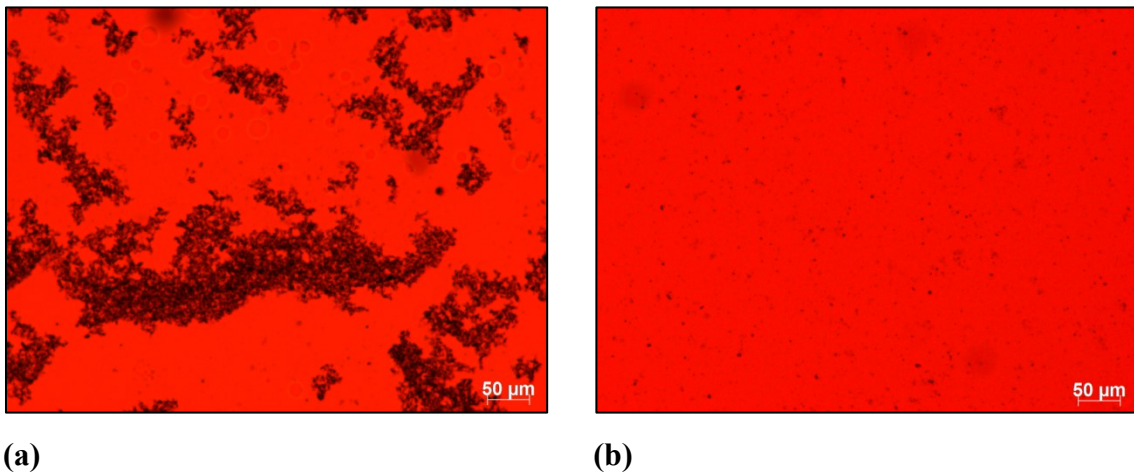


**Figure 2-7:** Diluted bitumen microscope image captured with 10x lens at favorable mixing conditions in side sampling  $CIST$ , (a): showing solid-water aggregate for sample (5 min at  $z_2$ ), (b): aggregates were absent for sample (7 min at  $z_2$ )

The size of these aggregates ranged from 20  $\mu\text{m}$  to greater than 600  $\mu\text{m}$  at various sampling heights and settling times. Note that these aggregates look hazy especially on images taken with 40x lens (compare Figure 2-8a and Figure 2-8b). Images taken with 10x lens provide sharp and high level view of these aggregates.

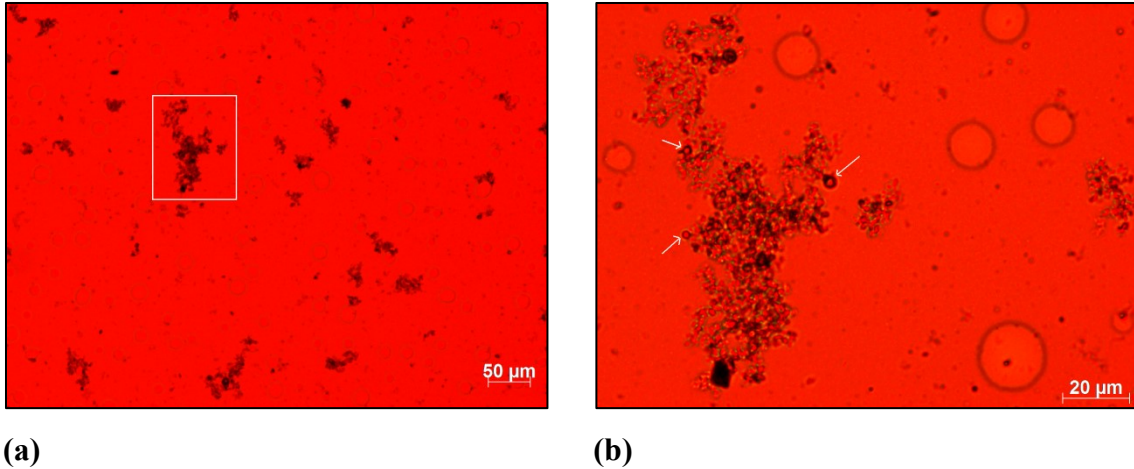


**Figure 2-8:** Diluted bitumen microscope image showing solid-water aggregates at favorable mixing conditions for sample (5 min at  $z_2$ ) in side sampling CIST, (a): 10x lens with solid-water aggregate in rectangular box, (b): 40x lens at same location as image (a), with arrows indicating water drops trapped in the aggregate

The solid-water aggregates were also present in diluted bitumen runs with poor mixing conditions ( $BC = 27$  ppm,  $IC = 12$  wt %,  $J = 120$  J/kg). However, these aggregates were much smaller and more loosely packed, Figure 2-9 in comparison to the favorable mixing conditions runs, Figure 2-7a. Smaller aggregates would sweep less water drops /solids with slow or no settling.  $KF$  data for poor mixing conditions showed negligible water settling as shown in Table 2-2. The poor mixing condition runs did not aid in the comparison of sampling methods. Both, demulsifier dosage ( $BC$ ) and mixing conditions ( $IC$  and  $J$ ) work synergistically to form bigger aggregates and cleaner product layer.

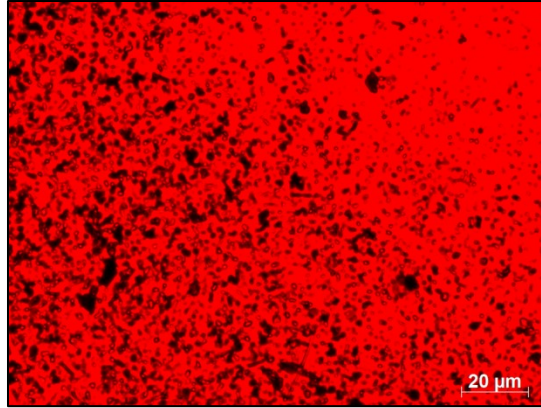


**Figure 2-9:** Diluted bitumen microscope image captured with 40x lens, showing loosely packed solid-water aggregates at poor mixing conditions

**Table 2-2:** Water content of samples (wt %) collected from 4 different heights during a 60 min settling period at poor mixing conditions in top sampling CIST for diluted bitumen

Sampling Height	Settling Time, min						
	1	3	5	7	10	30	60
$z_1$	0.68	0.66	0.69	0.73	0.71	0.71	0.62
$z_2$	0.63	0.61	0.65	0.62	0.63	0.61	0.62
$z_3$	0.69	0.68	0.66	0.70	0.67	0.59	0.66
$z_4$	0.71	0.64	0.72	0.69	0.73	0.68	0.65

Water-mineral oil images did not provide insight into which sampling method was better. The water drops quickly coalesced into large islands of free water in the water-mineral oil system before image acquisition, which could be due to insufficient surfactant injection or the inability of the surfactant to resist coalescence. Ideally, a different surfactant that resists coalescence and produces a drop size distribution similar to diluted bitumen should be used.

## 2.5 Conclusion

Using a repeatability test, extracting 6 top and 6 side samples from the same tank, side and top sampling techniques were compared for water in diluted bitumen and water in mineral oil systems. Side sampling had lower standard deviation than top sampling for 5 out of 9 cases before removing outliers considering both liquid-liquid systems. After removing outliers using Grubbs test, both methods had similar standard deviations. A hypothesis test confirmed this observation. Hence, both methods had similar statistical standard deviation which is a measure of method repeatability.

The water profile with respect to settling time and sampling height indicated that side and top sampling can give different water profiles during the initial stage of settling (<30 min) as shown in Figure 2-4a and Figure 2-4b respectively. Top sampling water profiles are flattened out in comparison to side sampling water profiles at same mixing conditions and do not appear to accurately capture settling dynamics in the vessel. Diluted bitumen microscope images (at favorable mixing conditions in side sampling *CIST*) suggested that solid-water aggregates were responsible for the sharp dewatering rate (Karl-Fischer water concentration) in the first 10 min of settling. This relationship between microscope and Karl-Fischer data could not be established for the same conditions in the top sampling *CIST*. Hence, the top sampling method was not able to capture flocs and aggregates. It is difficult to conclude which method is better but due to ease of sampling and physically more meaningful results, the side sampling technique was selected over top sampling.

## Nomenclature

$J$	mixing energy (J/kg)
$P$	impeller power consumption (W)
$r/R$	radius of sampling point/ inner radius of <i>CIST</i>
$s$	sample standard deviation (wt %)
$t_{mix}$	mixing time (min)
$V_{imp}$	impeller swept volume (m <sup>3</sup> )
$\bar{X}$	sample mean (wt %)

$z$	sampling depth below liquid surface (mm)
$\rho$	fluid density (kg/m <sup>3</sup> )
$\sigma$	population standard deviation (wt %)
$\mu$	population mean (wt %)

## Acronyms

<i>BC</i>	bulk concentration of demulsifier (ppm by wt)
<i>CIST</i>	confined impeller stirred tank
<i>IC</i>	injection concentration of demulsifier (wt %)
<i>KF</i>	Karl Fischer moisture analyzer
<i>PBTD</i>	pitched blade turbine down-pumping impeller

## References

- Chong, J.Y., 2013. Mixing Effects on Chemical Demulsifier Performance in Diluted Bitumen and Froth, MSc Thesis, University of Alberta, Canada.
- Czarnecki, J., Moran, K., 2007. On the “Rag Layer” and Diluted Bitumen Froth dewatering, *Can. J. Chem. Eng.*, **85**, 748–755.
- Grubbs, F.E., 1950. Sample Criteria for Testing Outlying Observations, *Ann. Math. Stat.*, **21**, 27–58.
- Kuzmanic, N., Rušic, D., 1999. Solids concentration measurements of floating particles suspended in a stirred vessel using sample withdrawal techniques, *Ind. Eng. Chem. Res.*, **38**, 2794–2802.
- Laplante, G.P., 2011. On Mixing and Demulsifier Performance in Oil Sands Froth Treatment, MSc Thesis, University of Alberta, Canada.
- Leo, S.S., 2013. Measurement and Analysis of Changes in Drop Size Distribution during Bitumen Clarification using Image Analysis, MSc Thesis, University of Alberta, Canada.
- Machado, M.B., Kresta, S.M., 2013. The Confined Impeller Stirred Tank (CIST): A bench scale testing device for specification of local mixing conditions required in large scale vessels, *Chem. Eng. Res. Des.*, **91**, 2209–2224, doi:10.1016/j.cherd.2013.06.025.
- MacTaggart, R.S., 1993. Sample Withdrawal from a Slurry Mixing Tank, *Chem. Eng.*

Sci., **48**, 921–931.

Melik, D.H., Fogler, H.S., 1984. Gravity-Induced Flocculation, *J. Colloid Interface Sci.*, **101**, 72–83, doi:10.1016/0021-9797(84)90009-2.

Tipman, R., 2013. Chapter 7: Froth Treatment, in: Masliyah, J.H. et al. (Eds.), *Handbook on Theory and Practice of Bitumen Recovery from Athabasca Oil Sands, Volume II: Industrial Practice*, Kingsley Knowledge Publishing, 211–253.

Tobias, P., Croarkin, C. (Eds.), 2003. *NIST/SEMATECH Ebook of Statistical Methods*. National Institute of Standards and Technology, U.S. department of commerce.

## Chapter 3: Clustering Analysis for Characterization of Flocs/ Agglomerates in Bitumen Froth Images

The removal of water and solids from bitumen froth is a critical step in bitumen extraction from Athabasca oil sands. Micro-scale water and solids aggregate to form big clusters that settle fast and facilitate the oil-water and oil-solids separation. Diluted bitumen contains primarily spherical water drops in the 1 - 10  $\mu\text{m}$  range with a number mean at 3 - 4  $\mu\text{m}$  (Masliyah et al., 2011b<sup>10</sup>; Leo, 2013). Upon demulsifier addition, these drops can be observed using images taken from microscope slides and monitoring drop coalescence and flocculation over time. Automated image analysis of drop size distributions in simple two phase oil-water emulsions is a continually developing research area (Pacek et al., 1994; Ribeiro, 2004; Alban et al., 2004; Rourke and MacLoughlin, 2005). Leo (2013) developed an image analysis protocol for determining drop size distribution of spherical water drops in diluted bitumen. Unfortunately, this protocol does not work for froth as the water drops (especially free water) are not spherical and there is higher quantity of solids in froth than in diluted bitumen. In this chapter, an image pre-processing protocol and cluster detection algorithm were developed to study water-water (*W-W*), solids-solids (*S-S*) and water-solids (*W-S*) clustering in diluted froth. The method provides both visual and quantitative information about clusters: the species (*W-W*, *W-S* and *S-S*), number of objects per cluster, and cluster size. The goal of the analysis is to determine the dominant interaction among the three possible combinations (*W-W*, *W-S* and *S-S*) and how this changes with mixing variables, settling time and sampling height (Chapter 4).

### 3.1 Introduction

Bitumen froth from a water based oil sands extraction plant consists of 20 - 35 % water and 5 - 15 % solids by mass (Tipman, 2013)<sup>11</sup>. The solids consist of silica sand,

---

<sup>10</sup> Page 349

<sup>11</sup> Page 214 - 217

fine clays  $< 2 \mu\text{m}$  (Masliyah et al., 2011d)<sup>12</sup> and heavy minerals such as Titanium and Zirconium. These minerals are hydrophobic and hence are dispersed in the continuous bitumen (oil) phase (Tipman, 2013)<sup>11</sup>. Bitumen froth is very viscous, does not flow at room temperature and could not be imaged without dilution with naphtha solvent. The product, diluted bitumen, typically contains  $< 2.5 \%$  emulsified water and  $\sim 0.35 \%$  solids by mass (Tipman, 2013)<sup>13</sup>. Demulsifiers are injected in commercial plants because they target the interfacially active species and enhance oil-water separation through mechanisms such as flocculation and coalescence (Masliyah et al., 2011b). For the discussion in this thesis, *diluted froth* refers to bitumen froth that has been diluted with naphtha but not given enough time to settle whereas, *diluted bitumen* would refer to the same mixture after it has been sent through centrifuges and settlers when the water is reduced to  $\sim 2.0 \text{ wt}\%$  and the solids content to  $\sim 0.5 \text{ wt}\%$ .

One millilitre diluted froth samples from a confined impeller stirred tank (*CIST*) were collected in a sample vial using a silanized sampling needle attached to auto-pipette (Figure 2-2). A pre-silanized Pasteur pipette was used to draw liquid from the vial and place a drop on a pre-silanized microscope slide. An unsilanized cover slip was placed on the liquid drop to secure the sample from ambient dust. The cover slip was unsilanized because silanization was difficult to do on super thin glass and the results were worse than for the unsilanized case. The same practice has been followed by Syncrude and Laplante (2011). Steel (needle) and glass surfaces (Pasteur pipette and slide) were silanized to make them hydrophobic so that water drops did not stick to the surface and undergo coalescence. Such coalescence would not be representative of the conditions in the *CIST*. The sample vial, *CIST* and impellers were not silanized because of a much lower wetted surface area per fluid volume ratio [*CIST* =  $0.01 \text{ m}^2/\text{m}^3$ , sample vial =  $0.66 \text{ m}^2/\text{m}^3$ , sampling needle =  $2500 \text{ m}^2/\text{m}^3$  and microscope slide/ cover slip =  $41700 \text{ m}^2/\text{m}^3$  (average liquid sample thickness =  $26 \mu\text{m}$ )]. The microscope slides were observed using Carl Zeiss Axio Scope A1 light transmission microscope equipped with Axio Cam ICC 1

---

<sup>11</sup> Page 214 - 217

<sup>12</sup> Page 179

<sup>13</sup> Page 218

(1.4 mega pixel CCD camera). Silanization is performed inside fume hood using the following steps (Leo, 2013). Skinner et al. (1989) used a similar silanization procedure.

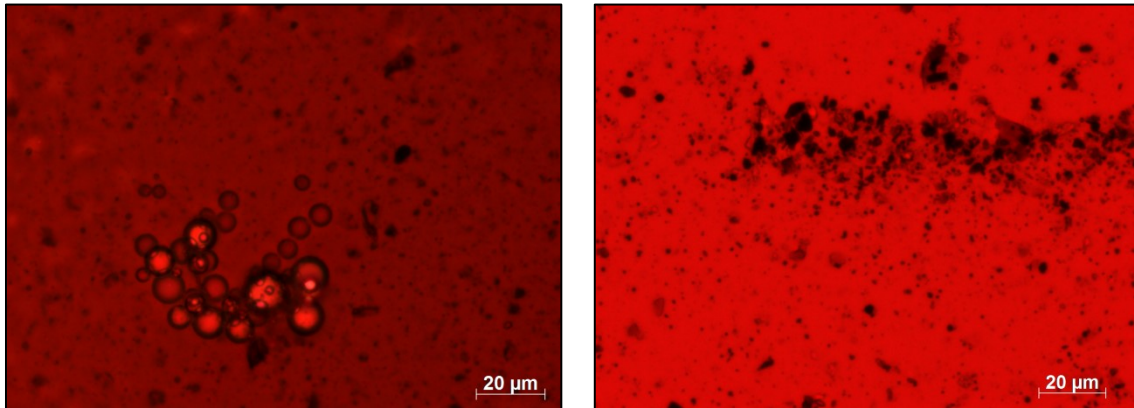
1. Immerse slides, needles and/or pipettes in the silanization solution (5% dimethyldichlorosilane in heptane) for 5 min. Remove them and allow them to air dry.
2. Dip the dried slides in toluene up and down five times. For needles and pipettes, draw the toluene in and out five times using an auto-pipette. Allow them to air dry.
3. Repeat step 2 with acetone.

Silane undergoes a hydrolysis-condensation reaction with glass surface. In the condensation reaction, water is released that needs to be removed to optimum quantity. Toluene has limited solubility for water and produces good quality monolayers of chemically adsorbed silane (Dey and Naughton, 2016). Acetone removes water (Li et al., 2012) and excess silane (Dey and Naughton, 2016; Li et al., 2012) that is loosely adsorbed on the glass surface.

It is important to understand the characteristics of diluted froth images for their subsequent image analysis. On the slides, water appears as a hollow object, as shown in Figure 3-1 while solids appear as irregular filled objects, also shown in Figure 3-1 for comparison. Figure 3-2 and Figure 3-3 illustrate representative diluted froth images captured with a microscope equipped with both 10x and 40x lens. Figure 3-2a and Figure 3-2b show the presence of three-dimensional water-water flocs and solid-solid chains respectively. Solid-solid chains were rarely encountered and mostly observed towards the slide/ cover slip edge. Figure 3-3a shows an example of solid-water association that occurred only in the runs with demulsifier addition. Similar solid-water aggregates were seen for diluted bitumen experiments (Chapter 2). Figure 3-3b shows water-water chains that are believed to be artifact caused by scratches on a slide (recession on the surface) or inadequate or uneven silanization (which can render some parts of the surface more hydrophilic than others).



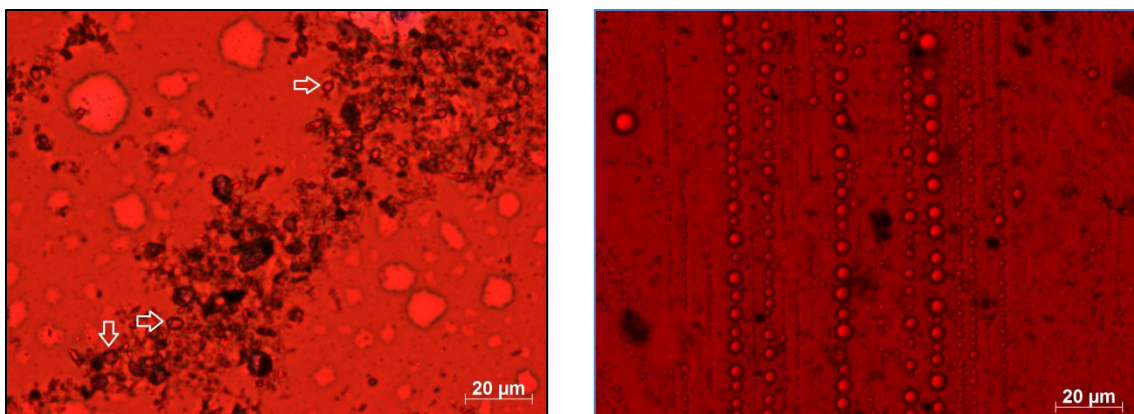
**Figure 3-1:** Illustration of hollow object (left) such as water and filled object (right) such as solids on a microscope image. Their shapes are frequently non-spherical.



**(a)**

**(b)**

**Figure 3-2:** Representative diluted froth images captured with a 40x lens containing (a): water-water flocs and (b): solid-solid chains



**(a)**

**(b)**

**Figure 3-3:** Representative diluted froth images captured with a 40x lens containing (a): water-solid flocs with water drops indicated by an arrow and (b): water-water chains

Figure 3-4a shows free water body that has non-spherical shape with rough surface and an approximate size of 50  $\mu\text{m}$ . Free water is a term commonly used to indicate water bodies that have large size and would settle out rapidly (Kokal, 2005). High surfactant loading is responsible for a water-oil interface that has varying texture (smooth, rough and pitted areas) and non-spherical shape (Eisenhower and Jantunen-Cross, 2013)<sup>14</sup>. The free water surface has been reported to be covered with mineral solids and bitumen-clay skins (Jiang et al., 2008). Figure 3-4b displays that free water can trap bitumen drops inside them or at the interface with other free water bodies leading to bitumen losses to tailings. A good demulsifier should maximize dewatering and demineralization while minimizing bitumen losses. Coalescence enhancing demulsifiers have lower bitumen losses to underflow than flocculation enhancing demulsifiers (Czarnecki et al., 2007). Figure 3-4c shows free water aggregates with size greater than 1000  $\mu\text{m}$ . Figure 3-4c was prepared by stitching 10 images (shot with 10x lens) in Photoshop using the procedure given in Appendix D2.

---

<sup>14</sup> Page 370

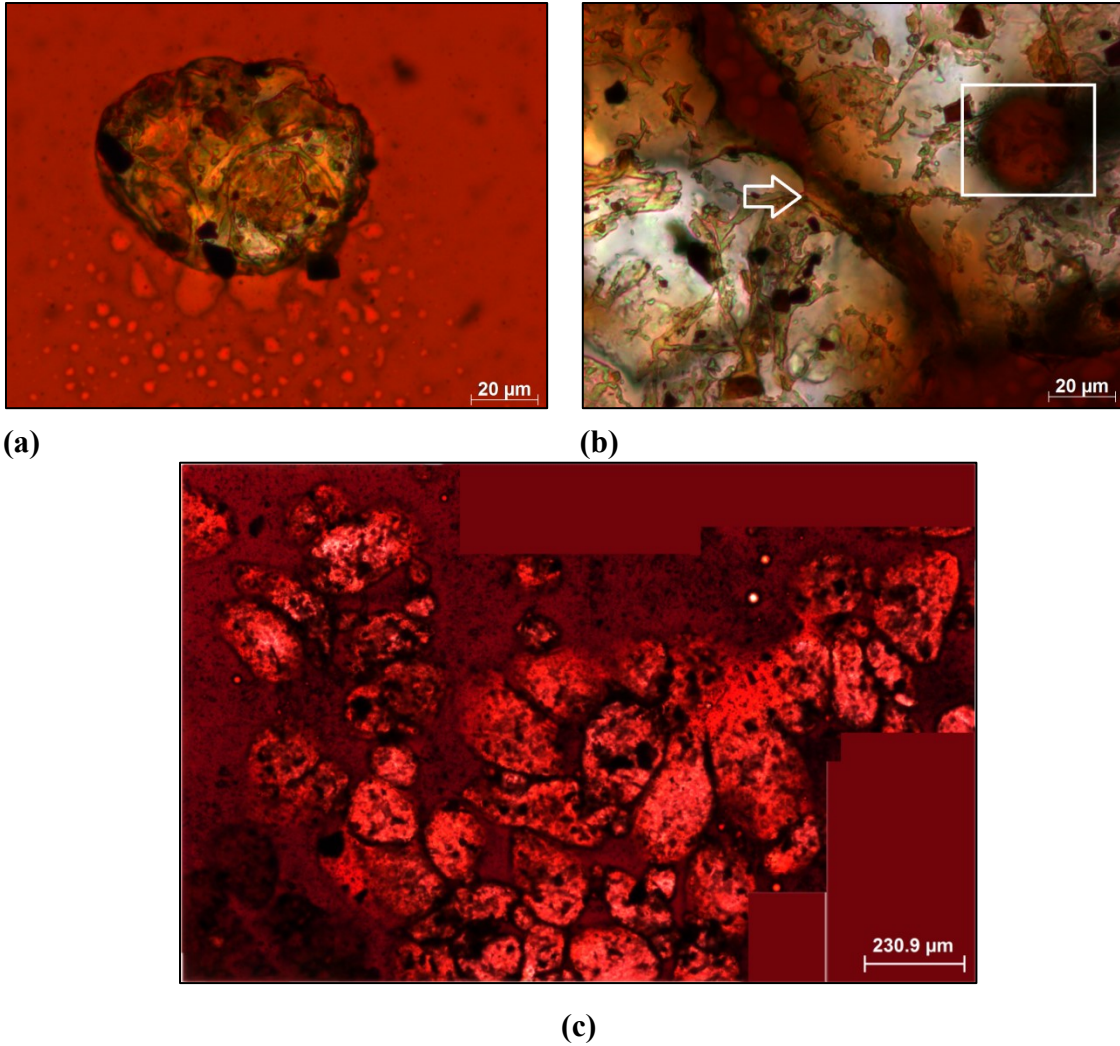
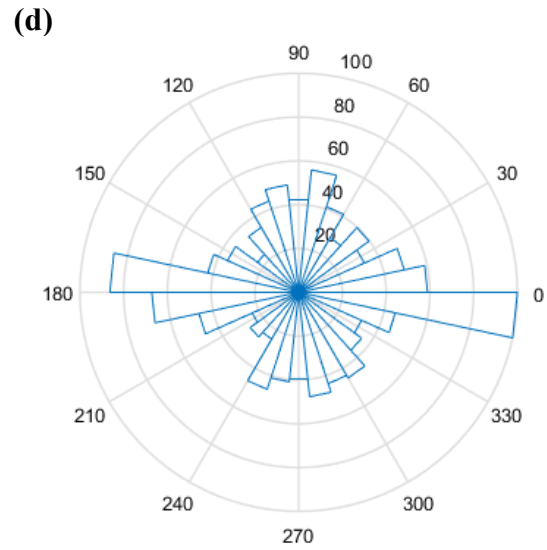
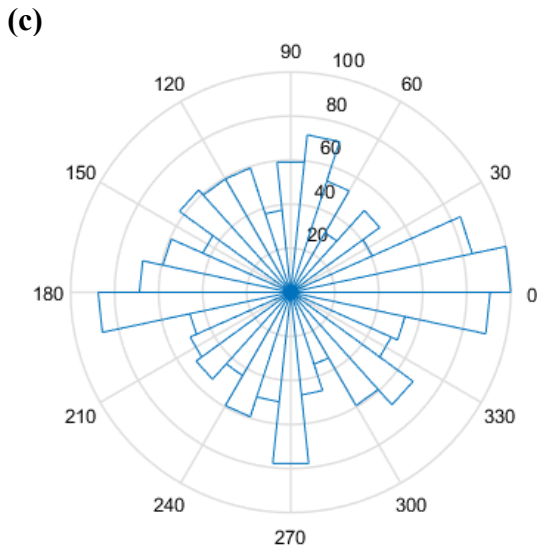
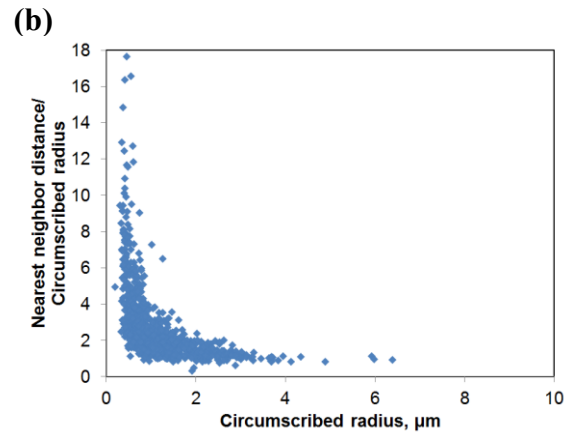
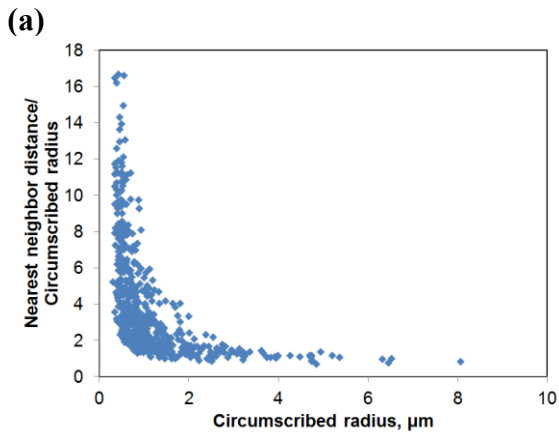
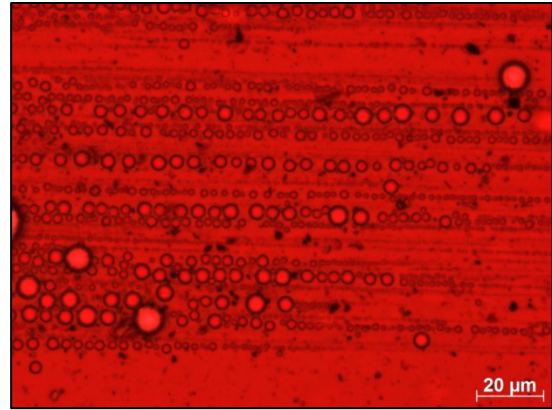
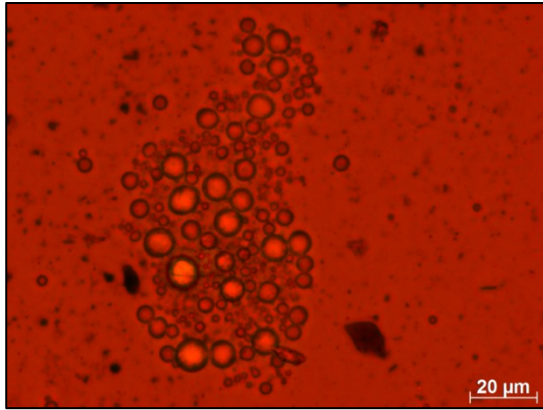


**Figure 3-4:** Representative diluted froth images showing examples of (a): free water covered with solids and bitumen clay skins, (b): free water containing trapped bitumen drop (rectangle) and bitumen film (arrow) at interface, (c): free water aggregates

### 3.2 Image Analysis Methods

An image space can be thought of as certain number of pixels in the  $y$  and  $z$  directions. The coordinates  $(y, z)$  of objects (e.g.: water or solid) indicate their position in the image space. Several nearest neighbor analysis methods are available to determine if objects are clustered or randomly distributed. Figure 3-5a and Figure 3-5b show representative images of water-water floc and water-water chain respectively. The nearest object distance and direction can be obtained using Photoshop with Fovea Pro 4 plugin. Figure 3-5c and Figure 3-5d show the object-object nearest neighbor distance for all

objects (water and solids) in Figure 3-5a and Figure 3-5b respectively. The number of objects in Figure 3-5a and Figure 3-5b was 561 and 971 respectively. The nearest neighbor distance trend did not change much between the two images. Figure 3-5e and Figure 3-5f show the rose plot for all objects shown in Figure 3-5a and Figure 3-5b respectively. This plot gives the polar direction (radians) of the nearest neighbor and is an indication of anisotropy (non-uniform object distribution). For a perfectly uniform object distribution (isotropic), the rose plot should be a circle. The number of pies in both plots is 30. The length of the pie represents the number of neighbors in that direction. The length of pie in both rose plots was normalized with the longest pie on the scale of 0 to 100. Therefore, the longest pie has a magnitude of 100 as shown in Figure 3-5e and Figure 3-5f. The normalization was done so that both plots could be compared. Both plots show that most objects have nearest neighbor either left or right which agrees with the respective images. Figure 3-5f is more stretched in the horizontal direction than Figure 3-5e, because Figure 3-5f has more neighbors in that direction. Both distance and direction methods are of limited use as they do not distinguish between the objects (water vs. solids).



(e)

(f)

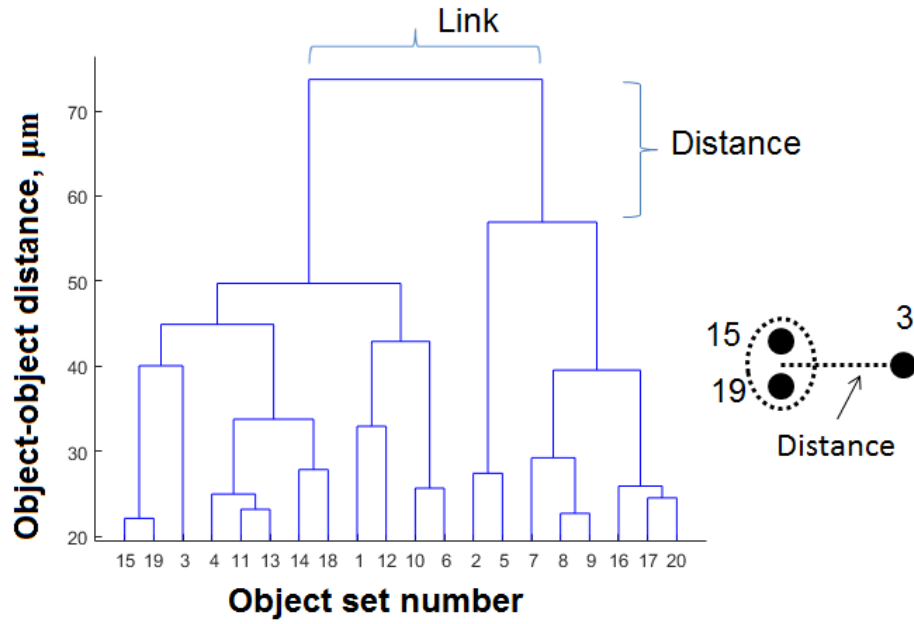
**Figure 3-5:** Diluted froth image showing (a): water-water floc and (b): water-water chains. Nearest neighbor distance of Figure (a) and Figure (b) are shown in Figure (c) and Figure (d). Nearest neighbor direction (radians) of Figure (a) and Figure (b) are shown in Figure (e) and Figure (f).

Several machine learning algorithms such as k-nearest neighbor (*KNN*), minimal spanning tree, and dendrogram determine the number of clusters (Russ, 2002a)<sup>15</sup> but the underlying assumption that all objects are clustered is flawed for the case of froth. For instance, the dendrogram for Figure 3-5a is shown in Figure 3-6a. Recall that the number of objects in Figure 3-5b was 561. Therefore, the object numbers shown on horizontal axis of Figure 3-6a should be 561, which is difficult to plot. Therefore, these objects were collapsed to show only 20 sets (or groups of objects). The dendrogram works on the principle that all objects can be considered to be connected to each other at some distance. The horizontal lines represent the links or connection between two connected object sets (for example: object set number 15 and 19 are connected as shown in horizontal axis of Figure 3-6a) and the height of vertical line indicates the distance between the object sets in  $\mu\text{m}$ . A horizontal cut of the dendrogram between 60 and 70  $\mu\text{m}$  would divide all the objects into two clusters. Figure 3-6b highlights the flaw of this clustering method as all objects are part of either a first or second cluster (shown in red and blue dots). Another method based on quadrants divides the image area into equal sized quadrants and the number of objects in each quadrant is then compared with average number of objects per unit area (Diggle, 2013a)<sup>16</sup>. This method for determining clustering is sensitive to the number of quadrants.

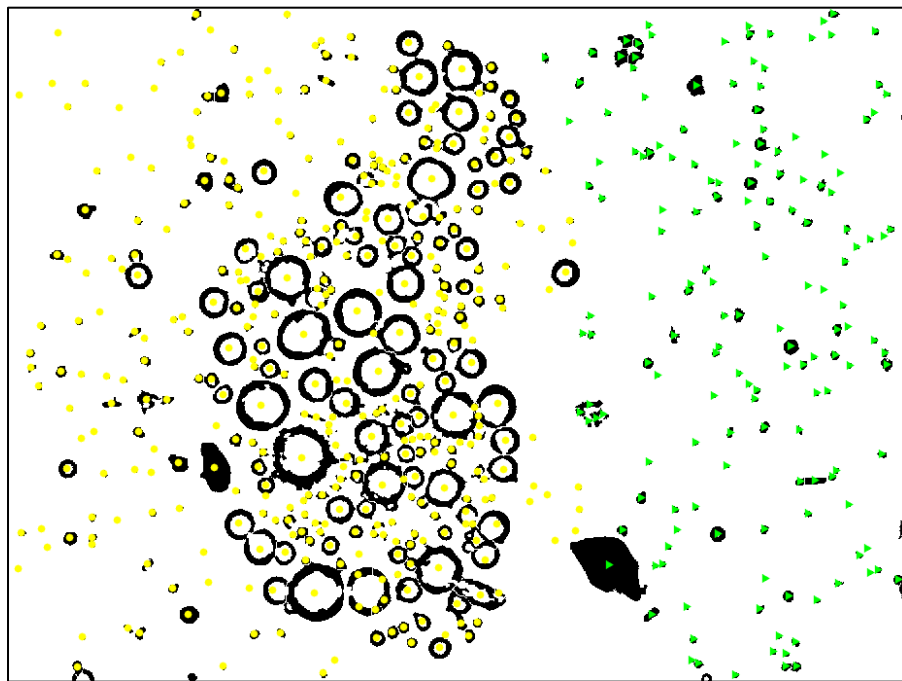
---

<sup>15</sup> Section: *KNN* and cluster analysis

<sup>16</sup> Page 29



(a)



(b)

**Figure 3-6:** (a): Dendrogram for image shown in Figure 3-5a with object set number and their separation distance ( $\mu\text{m}$ ) on horizontal and vertical axis respectively, (b): Two group of clusters identified with dendrogram, one with yellow circles and other with green arrows

### 3.2.1 Point Nearest Neighbor (*PNN*)

This method for cluster identification seemed promising. The method works on the principle that objects (e.g., water and solids on a microscope image) if randomly distributed, follow a Poisson distribution (Haight, 1967). The *PNN* method had several limitations and, in the end, could not be used to analyze the diluted froth images. The results are included here for completeness and context.

#### 3.2.1.1 Introduction

Kukukova et al. (2011) used point-to-nearest neighbor (*PNN*) analysis to determine the scale of segregation in a micromixer and a stirred tank. The scale of segregation is a measure of the macro-segregation of the dispersed phase such as suspended particles in a continuous stirred tank. As stated before, an image space can be thought of as certain number of pixels along the  $y$  and  $z$  axis and the object coordinates  $(y_i, z_i)$  represent their position in this space. The *PNN* method involves superimposing a hexagonal grid of points as shown in Figure 3-7, over an image space (Kukukova et al., 2011). Only one hexagon is shown here for illustration but in reality there are several hexagons distributed in a grid over the image space. For every grid point, the distance to nearest object is recorded and the frequency (or number)-distance distribution is compared with a Poisson distribution. If the frequency distribution follows a Poisson distribution, then the objects are randomly distributed; otherwise they are clustered or self-avoiding. The following equation describes the Poisson function (Kukukova et al., 2011).

$$P(x; \bar{X}) = \frac{\bar{X}^x e^{-\bar{X}}}{x!}$$

(Equation 3-1)

where  $P(x; \bar{X})$  is the probability of Poisson function,  $x$  is the point-nearest object distance, point refers to the hexagonal grid points superimposed on the image under study,  $\bar{X}$  is the mean distance, and  $x!$  is the factorial of  $x$ . Complete spatial randomness (*CSR*) is built on the hypothesis that all the objects follow a Poisson distribution which is an idealized

standard and may be hard to achieve (Diggle, 2013b)<sup>17</sup>. Clustering of objects results in a wider distribution (higher standard deviation) than the Poisson distribution whereas self-avoiding objects result in a narrower distribution (Kukukova et al., 2011). Hence, this method can be used to quantify differences between random, clustered and self-avoiding objects.

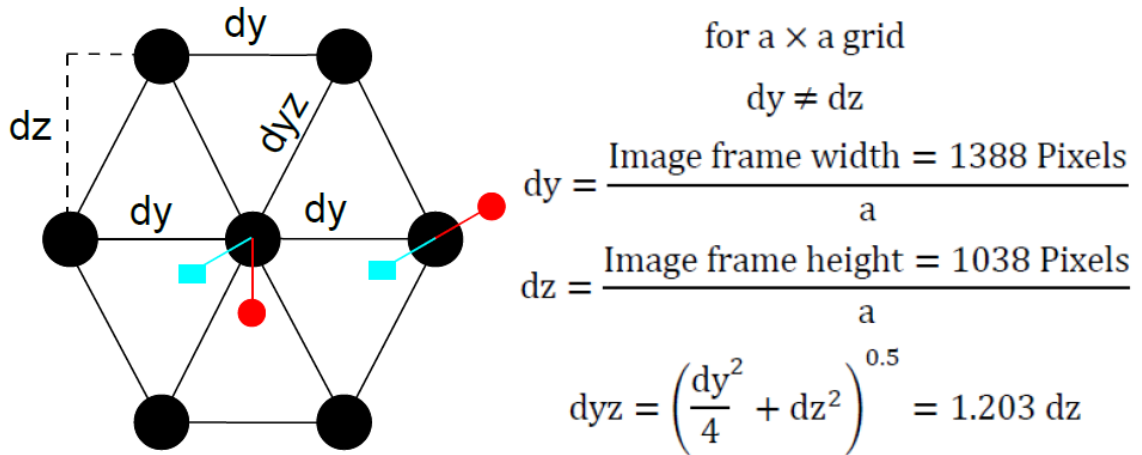


**Figure 3-7:** Point Nearest Neighbor method showing single hexagon in a grid. Each grid point (black circles) looks for nearest water drop (red circles) and solid (blue rectangles) in image space [Modified significantly from Kukukova et al. (2011)]

Let us say that there are  $m$  grid points and  $n$  objects. The  $m$  grid points are distributed in an  $(a \times a)$  grid such that  $a = \sqrt{n}$  where  $n$  is the number of objects. Increasing  $a$  improves the resolution of  $PNN$  distribution and  $a$  should be adjusted according to the number of object data (Kukukova et al., 2011). The mean grid point spacing is obtained by averaging the distance of all 6 outer hexagon points from the center point, shown in Figure 3-7.

$$\text{Mean grid spacing} = \frac{2 \times dy + 4 \times dyz}{6} = 1.248 dz$$

(Equation 3-2)

---

<sup>17</sup> Page 10

where  $dy$  is the horizontal spacing and  $d_{yz}$  is the diagonal spacing. The index of dispersion ( $I$ ) has been recommended to quantify clustering.

$$I = \frac{\sigma^2}{\bar{X}}$$

(Equation 3-3)

where  $\bar{X}$  is the average point-object nearest distance and  $\sigma$  is the sample standard deviation of these distances. For a Poisson distribution,  $\sigma^2 = \bar{X}$ , so  $I = 1$  for a random distribution.  $I > 1$  indicates clustering whereas  $I < 1$  indicates a self-avoiding distribution.

### 3.2.2.2 PNN Analysis Set Up

Before performing the *PNN* analysis on froth images, a series of test images containing two objects (object A and object B) analogous to water and solids were constructed to test different clustering scenarios and orientation effects. Figure 3-8 and Figure 3-9 show these test images and their distribution. These images helped to validate the code and identify the method limitations. A baseline test image, Figure 3-8a containing 54 objects A and 54 objects B randomly distributed in an image space ( $1388 \times 1038$  pixels, same as froth image size) was constructed using the *rand* ( ) function in Microsoft excel. The pre-assigned coordinates of A and B were then imported into Matlab where hexagonal grid of 121 points ( $11 \times 11$ ) was generated. Recall that the number of grid points need to be greater than or equal to number of objects which is 108 in this case. For each grid point, distance to nearest object A and nearest object B was determined after modifying Kukukova (2011)'s Matlab code. Her code had only one type of object.

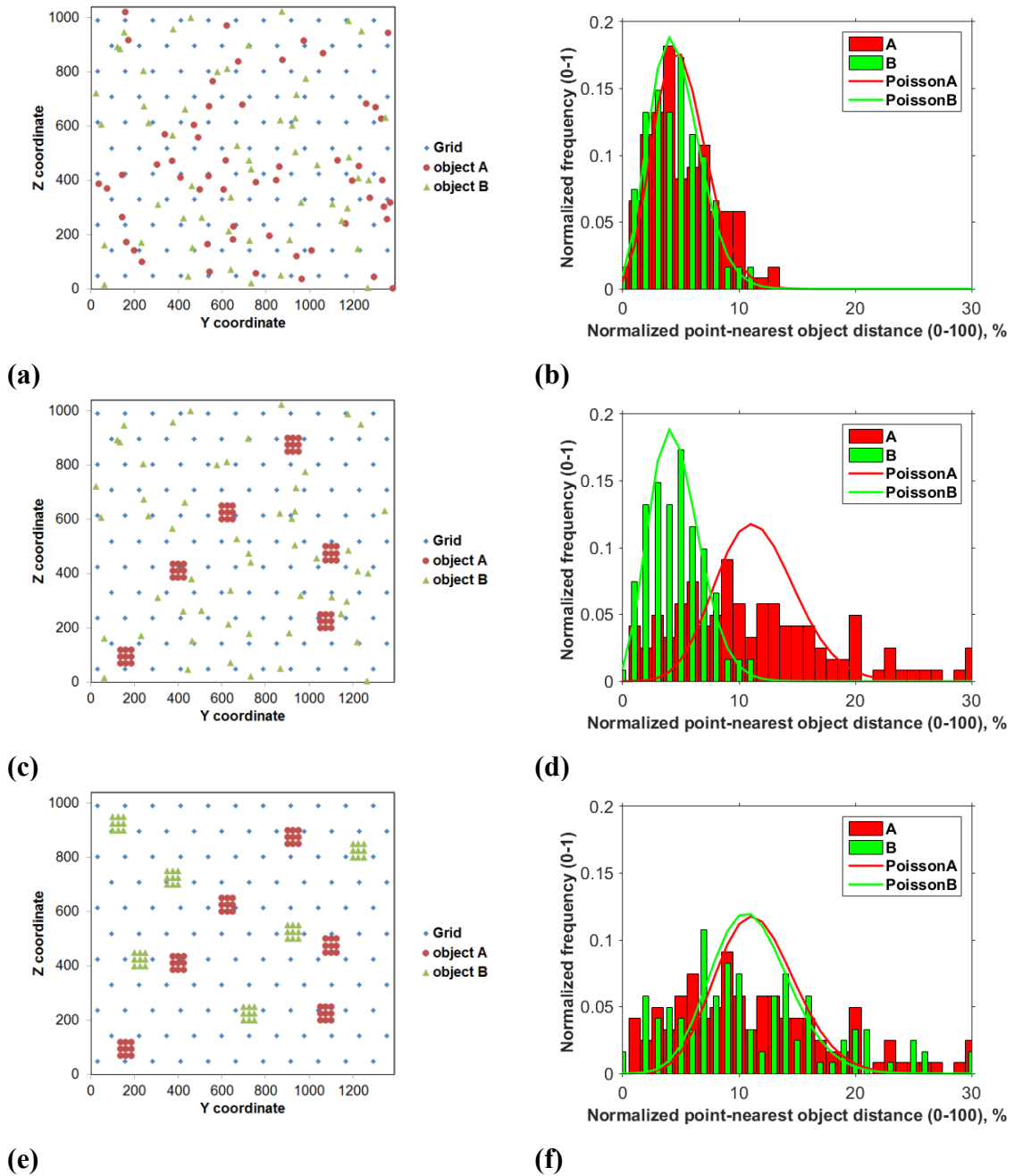


**Figure 3-8:** Test images containing two objects: object A (red) and object B (green) with hexagonal grid points (blue) shown for three scenarios, (a): A and B randomly distributed, (c): A aggregated but B randomly dispersed and (e): A aggregated and B aggregated separately. The point-nearest object distribution for Figures (a), (c) and (e) is shown in Figures (b), (d) and (f) respectively.

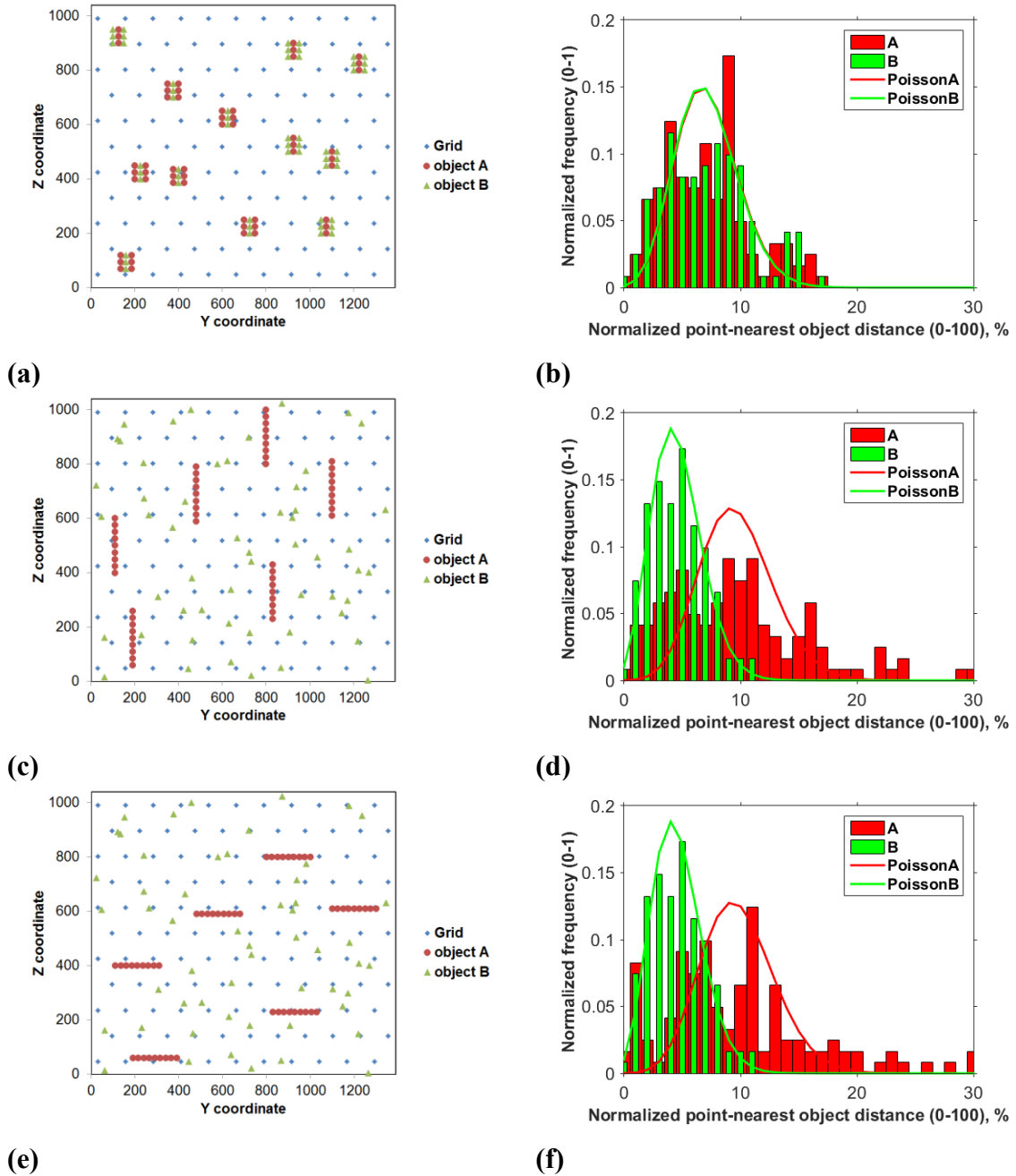


**Figure 3-9:** Test images containing two objects: object A (red) and object B (green) with hexagonal grid points (blue) shown for three scenarios, (a): A and B aggregated together, (c): A aggregated in long vertical chains but B randomly dispersed and (e): A aggregated in long horizontal chains and B aggregated separately. The point-nearest object distribution for Figures (a), (c) and (e) is shown in Figures (b), (d) and (f) respectively.

### 3.2.2.3 PNN Results

#### Effect of Clustering

Figure 3-8 and Figure 3-9 shows six clustering scenarios and their respective distribution. The frequency (or number) distribution of grid point-object A or B distance is compared with a Poisson distribution. The mean of Poisson distribution (Equation 3-1) was set equal to mean of the distance distribution it was compared against. Therefore, two Poisson distributions can be seen-one corresponding to object A and other corresponding to object B. The point-object distance is normalized on the scale of 0 to 100 with the diagonal of the image (= 1733.2 pixels). Figure 3-8a shows baseline image where both objects are randomly distributed and the hexagonal grid is shown in blue dots. Figure 3-8b shows the frequency distribution corresponding to Figure 3-8a and it is clear that it deviates slightly from Poisson distribution. This confirms that *CSR* is hard to achieve. Figure 3-8c shows that A is clustered but B is randomly distributed and Figure 3-8d shows that the frequency distribution of A widens and deviates from a Poisson distribution as expected. When B is clustered as shown in Figure 3-8e, its distribution also deviates from Poisson distribution as shown in Figure 3-8f. Unexpectedly, when A and B are clustered with each other as shown in Figure 3-9a, their distribution as shown in Figure 3-9b narrows in comparison to Figure 3-8f. We will return to this case later. The shape of cluster, square for object A in Figure 3-8c vs. longitudinal for object A in Figure 3-9c did not alter the distribution significantly. The number of bins in the distributions shown in Figure 3-8 and Figure 3-9 is 30.

#### Index of Dispersion

As discussed before, index of dispersion (Equation 3-3)  $> 1$  is an indication of clustering whereas  $I = 1$  corresponds to *CSR*. Table 3-1 shows the  $I$  values for 5 data sets of random points generated by *rand()* function. The  $I$  value varied from 1.16 to 1.83. Therefore, *CSR* could not be achieved by *rand()* function. Table 3-1 shows the baseline average  $I$  value (shown in bold) that was used for normalizing index of dispersion for clustering scenarios illustrated in Figure 3-8 and Figure 3-9.

Table 3-2 shows the index of dispersion value for six clustering scenarios discussed above. When A or B is randomly distributed (row 1), its  $I$  value is within  $1 \pm 0.2$  because it is normalized. When A is clustered but B randomly dispersed (row 2), the  $I$  value for object A increases to 3.33. Similarly,  $I$  value for B increases when B is clustered (row 3). However, the  $I$  value for B is 2.67 which is lower than 3.32 for object A. Figure 3-8e explains this anomaly as the clusters of B are more distributed in image space than those of A. Hence, the spatial distribution of clusters in image space can also affect the  $I$  value. The  $I$  value drops for both A and B drops when they are aggregated with each other (row 4). Square clustering (row 3) gave a higher  $I$  value than longitudinal clustering (row 5 and 6). Row 3, 5 and 6 correspond to Figure 3-8c, Figure 3-9c and Figure 3-9e respectively. Cluster orientation (horizontal or vertical) also affected the  $I$  value. Hence, the index of dispersion agrees with frequency distribution trends for determining clustering effects.

**Table 3-1:** Repeatability of index of dispersion ( $I$ ) for random data generated for object A and object B using *rand* ( ) function

Random Case number	Index A	Index B
1	1.60	1.28
2	1.04	1.46
3	1.29	1.83
4	1.58	1.76
5	1.33	1.16
<b>Average</b>	<b>1.37</b>	<b>1.50</b>

**Table 3-2:** Normalized index of dispersion, as a measure of clustering for several clustering scenarios (Figure 3-8 and Figure 3-9) for object A and object B

Object A	Object B	Index A	Index B
random	random	1.23	0.81
aggregated	random	3.33	0.81
aggregated	aggregated	3.32	2.67
A and B aggregated together		1.43	1.29
aggregated as vertical chain	random	2.81	0.81
aggregated as horizontal chain	random	3.20	0.81

### **AB Clustering and Rearrangement**

When A and B are aggregated with each other, the index value for both A and B drops in comparison to the case where A and B are aggregated separately as shown in row 3 and 4 of Table 3-2. Row 3 corresponds to clustering scenario shown in Figure 3-8e whose distribution is given in Figure 3-8f. Row 4 corresponds to clustering scenario shown in Figure 3-9a whose distribution is given in Figure 3-9b. This anomaly was investigated. The number of object A and object B was 54 each in both cases. Figure 3-8e shows the A clustered B clustered case that had 6 clusters with 9 objects per cluster for both A and B. However, for AB cluster case shown in Figure 3-9a, there were 6 clusters with (3 object A, 6 object B) and 6 clusters with (6 object A, 3 object B). This resulted in a lower number of objects (A or B) per cluster and hence a drop in index of dispersion.

If the number of object A or B per cluster is kept constant (9 in this case), then the normalized index of dispersion remains the same or increases slightly as shown in Figure 3-10. Case 1 shows the A clustered B clustered scenario as shown in Figure 3-8e and row 3 of Table 3-2. When comparing case 2 with case 1 in Figure 3-10, index A remains nearly same but index B increases significantly from 2.67 to 3.53. This happened because the clusters for B were more concentrated in one section of image space in case 2 than case 1 as explained in the section above. Comparing case 3 with case 2 as shown in Figure 3-10, rearrangement of A and B within the cluster did not alter the index significantly.

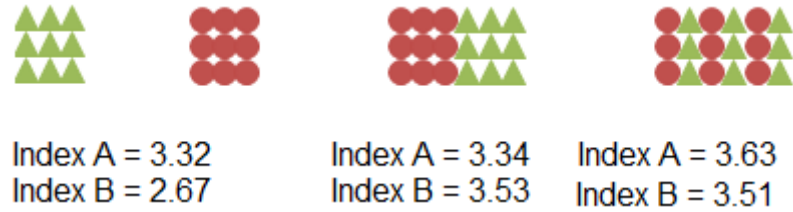


**Figure 3-10:** Effect of AB clustering on normalized index of dispersion. case 1: A clustered B clustered separately, case 2: AB clustered , case 3: AB cluster rearranged. Object A are circles and object B are triangles.

### Effect of Clustering Orientation

Table 3-3 highlights the impact of clustering orientation (vertical, angled or horizontal) of object A on its index of dispersion. The index value is not normalized here for easy comparison between different grid sizes. Object B was randomly distributed for this case and hence its  $I$  values are not shown. Cluster spacing (object-object distance within a cluster) and number of objects per cluster were kept constant during this analysis. The  $I$  value increased by 13% from 3.85 to 4.38 as the orientation of the cluster was changed from vertical to horizontal. On thorough investigation, it was found that this dramatic change is because each hexagonal unit in the grid is an irregular hexagon (unequal side length) with diagonal distance ( $dyz = 1.12 \times dz$ ). For a regular hexagon, diagonal dimension is equal to side dimension. We believe that this problem should subside with a regular hexagonal grid. Increasing the grid size beyond the number of objects (54 data points each for both A and B) did not alter the  $I$  value substantially as shown in Table 3-3. This means that this method can be misleading for froth images containing chains or flocs depending on their orientation.

**Table 3-3:** Effect of cluster orientation on index of dispersion for object A (when B is randomly dispersed) for different grid sizes

Orientation	Index A		
	Grid 121=11 × 11	Grid 225 = 15 × 15	Grid 1089 = 33 × 33
Vertical	3.85	3.86	3.87
Angled 45°	3.97	4.01	4.02
Horizontal	4.38	4.31	4.27

### Effect of Cluster Spacing

Cluster spacing refers to the distance between adjacent data points in a cluster. Table 3-4 emphasizes that increasing the data point-data point spacing by 500 % results in the 10 % increase in the index of dispersion. So, clustering spacing does not have a significant impact on *I* value.

**Table 3-4:** Effect of cluster spacing on normalized index of dispersion for object A (when B is randomly dispersed)

Cluster Spacing (Pixel)	Normalized Index A
5	3.04
15	3.20
25	3.34

### Extent of Clustering

The number of objects that are part of a cluster were increased and their effect on index of dispersion was evaluated. Table 3-5 shows that the index of dispersion increases significantly if at least 50 % of the objects are clustered. Non-clustered small objects such as fine solids can dilute the effect of clustering and hence this method cannot be used for diluted froth images.

**Table 3-5:** Effect of percentage of clustered objects on index of dispersion

No of Objects Clustered (%)	Normalized Index A
0	1.23
25	1.42
50	1.45
100	3.33

### **Froth Image Example**

Figure 3-11 shows *PNN* results for froth image shown in Figure 3-5a. The number of water drops and solids on the image were 161 and 400 respectively. The method for distinguishing water from solids is discussed in Section 3.3. The hexagonal grid of 625 points ( $25 \times 25$ ) was superimposed on the image. The frequency distribution indicates that water is clustered whereas solids are randomly distributed which agrees with Figure 3-5a. The non-normalized index of dispersion for water was 6.77 and for solids was 0.71. Hence, the *PNN* method was successful in identifying *W-W* cluster for this image. However, this method would not be able to detect *W-S* clustering.

This *PNN* method did not work for froth images because of the high clustering requirement ( $> 50\%$  of objects should be clustered), noisy coordinates due to dirt or solid (which dilutes the effect of clustering) and different results depending on cluster orientation (horizontal, vertical or angled). This method was not used to analyze the diluted froth images. The *PNN* method provides an overall clustering tendency of objects in an image. It does not provide information such as number of clusters, their size and location on the image. A new clustering algorithm based on object-object distance was developed for this project. This algorithm was followed for analyzing froth images and is discussed in the following section.

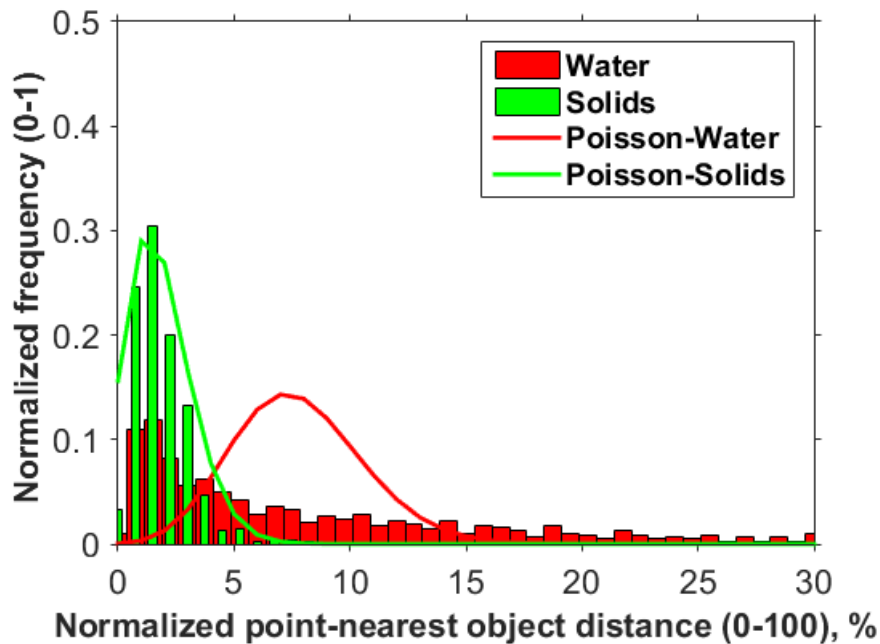


**Figure 3-11:** Frequency distribution (bins = 40) for froth image shown in Figure 3-5a

### 3.3 Clustering Algorithm Steps

As mentioned before, there was a need to identify and quantify the clusters in froth images. A method based on object-object distance is used here to quantify clusters and study the dominating interactions in an image. For instance, we want to find out if solids have more tendency to agglomerate with each other or with water. The image pre-processing was done in Adobe Photoshop CC (32-bit version with Fovea Pro 4 plugin) but the clustering algorithm was run in Matlab 2015a. Following are the algorithm steps.

#### 3.3.1 Pre-Processing of Images

Leo's (2013) protocol for drop sizing of spherical drops laid a strong foundation for pre-processing of diluted bitumen images. The steps from Figure 3-12a to Figure 3-12e were implemented based on Leo's (2013) protocol. The steps are outlined here but for detailed descriptions, refer to his thesis (Leo, 2013). These steps are performed in Adobe Photoshop with Fovea Pro 4 plugin on images captured using 40x microscope lens.

- A. Conversion from color RGB {red, green and blue} (Figure 3-12a) to greyscale image (Figure 3-12b): Set *Image > Mode to Lab color* and delete *channel a* and *alpha2*. Set *Image>Mode to greyscale*.
- B. Improve image contrast and fix exposure difference across the image (Figure 3-12b to Figure 3-12c): Set *Filter\*IPAdjust > AutoLevel* using both *bright and dark pixels*.
- C. Suppress the variation in illumination (incident light) and increase the variation in reflectance (reflected light) to remove periodic noise and enhance contrast (Figure 3-12c to Figure 3-12d). Set *Filter\*IP Adjust > Homomorphic range compression*.
- D. In this step, the greyscale image from step C (Figure 3-12d) is converted to binary image (Figure 3-12e) using *Filter\*IP Thresholding > Bi-Level Thresholding* using *Johannsen method* (Johannsen and Bille, 1982).

24-bit RGB image has 3 channels (red, green and blue) with each channel containing  $2^8$  possible ranges of color intensity values for each pixel in a channel (Photoshop Help/Color modes, 2015). The 8-bit grey scale image has a single channel with  $2^8$  (= 256) shades of grey ranging from black (0) to white (255) (Photoshop Help/Color modes, 2015). Bi-level thresholding sets a threshold value ( $t$ ) ranging from 0 to 255 such that all pixels with brightness  $< t$  are set to foreground color (black) and the rest are set to background color (white). The black pixels refer to objects (water or solids). The binary image is useful for analyzing objects with very less computational power in comparison to greyscale image.

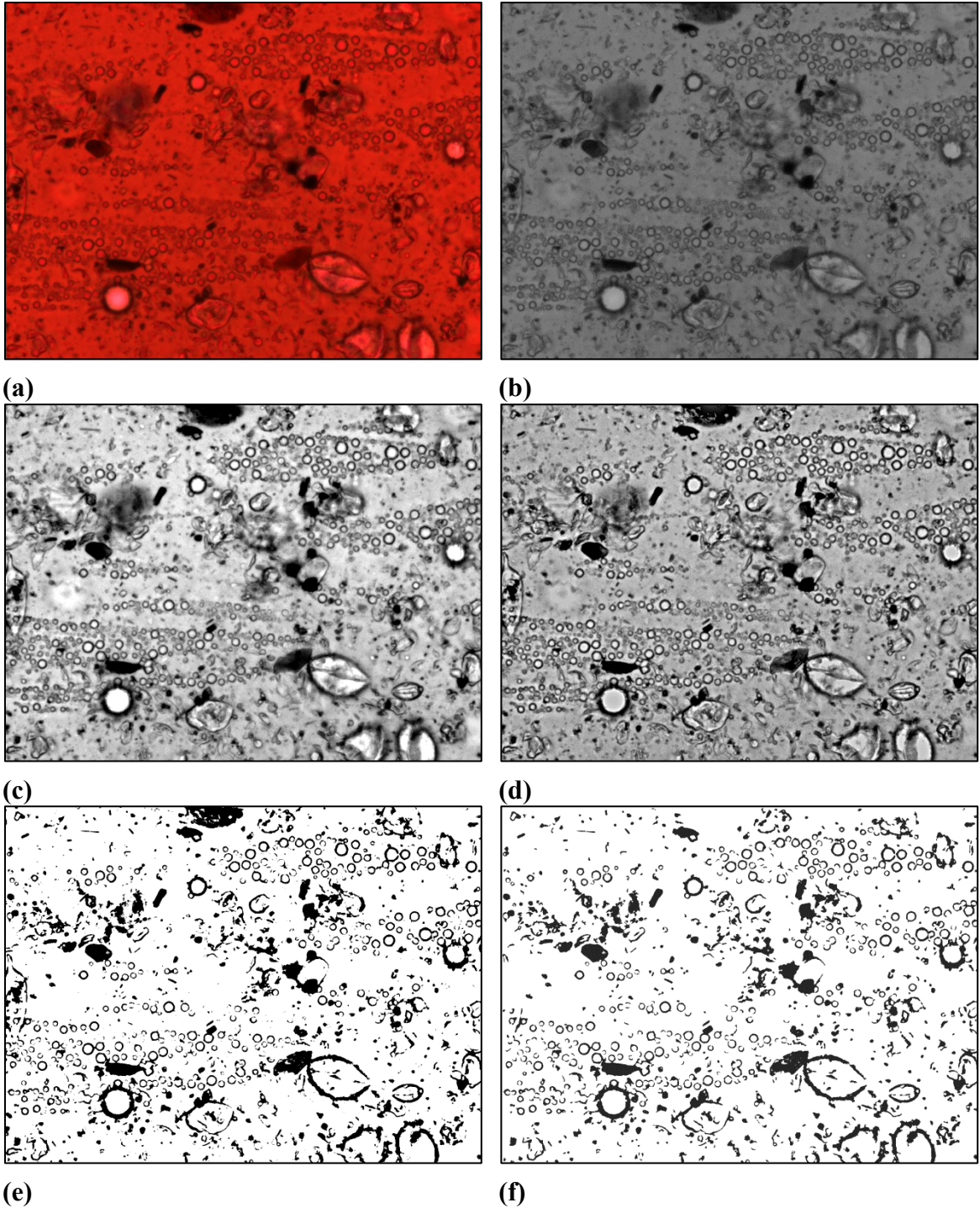


**Figure 3-12:** Pre-processing (Leo, 2013) of a froth image shot with 40x microscope lens, (a): color image [produced with permission from Awosemo (2016)], (b): greyscale image, (c): image (b) after contrast enhancement, (d): image (c) after homomorphic compression, (e): image (d) after bi-level thresholding, (f): image (e) with objects touching left and top edge removed, objects smaller than  $2.3\mu\text{m}$  (20 pixels) removed

### 3.3.2 Removing Fines and Separating Touching Objects

In Figure 3-12f, objects smaller than 20 pixels (2.3  $\mu\text{m}$ ) are removed to reduce data noise (Set *Filter*>*IP\*Measure Features* > *Reject Features*). 2.3  $\mu\text{m}$  was used as rejection criteria because it is close to the image resolution and helps to remove fine objects. The same command also removes the objects touching left and top side of the image. Large objects are more likely to touch the edges of field of view and get biased in the object counting (Russ, 2002b)<sup>18</sup>. For unbiased counting, objects touching left and top side of the image should be removed and those touching bottom and right edge should be unaffected (Russ, 2002b)<sup>18</sup>. After fines are removed from microscope images, there are touching objects (water-water or water-solid) that can cause problems in the centroid detection step (Section 3.3.4). If objects are not separated, one centroid is detected for two touching objects instead of two centroids. The separation is facilitated using watershed segmentation as shown in Figure 3-13.

A different image was used in Figure 3-13 to illustrate the effect of separation of touching objects. Following are the steps:

- A. Open the image in Photoshop (called display image) and save it in program memory: Set *Filter\*IP 2<sup>nd</sup> Image* > *Swap with 2<sup>nd</sup>*. This command swaps the *display* image with the *memory* image. We need to have same image in both display and memory for two image addition in step E.
- B. Step B ensures that we have same image in display and memory. It could have been accomplished using Set *Filter\*IP 2<sup>nd</sup> Image*> *Recall 2<sup>nd</sup>* that would overwrite the display image with the memory image. But *Recall 2<sup>nd</sup>* command has a bug which is being fixed by Reindeer Graphics (supplier of Fovea Pro4). As a way around, the same step is accomplished by selecting a previous *history* state using *Windows* > *Previous history*.
- C. In this step, holes within objects (e.g. water drop, Figure 3-1) are filled (with black pixels) using *Filter* > *IP\*Morphology* > *Fill holes*. The holes within water

---

<sup>18</sup> Section: Counting features

drops need to be filled otherwise watershed segmentation would not work and it would segment the drops into many small fragments (Russ, 2011).

- D. Watershed segmentation is accomplished by using *Filter > IP\*Morphology > Watershed segmentation*
- E. Image addition: The *display* and the *memory* images are added using *Filter > IP\*Math > General math > Add*. Set *Add constant* to 0. This step retains the watershed separation lines (that separate touching objects) but reverses step C.

The Steps A-E are not executed on Figure 3-13a but are performed on Figure 3-13b. Figure 3-13a shows that a single centroid is detected for touching objects (connected black pixels). Therefore, for proper quantification of cluster size and other properties, this segmentation step is essential.

How does watershed segmentation work? This method converts a binary image (black and white) to a grey scale image (255 brightness values) such that foreground pixel (black) which is farthest from the background pixel (white) is assigned maximum brightness as shown in Figure 3-14. This is called “Euclidean (or linear) distance map” (*EDM*) because the brightness values are proportional to the distance (Russ, 2011). The brightest pixels in this figure at the center of the circle, called “ultimate eroded points (*UEP*)” (Russ, 2011). The black pixels are added to *UEP* with distance map information on the constraint that no new black pixel would be added that connects two growing *UEPs*. This results in a watershed separation line (white pixels) between two previously touching objects.

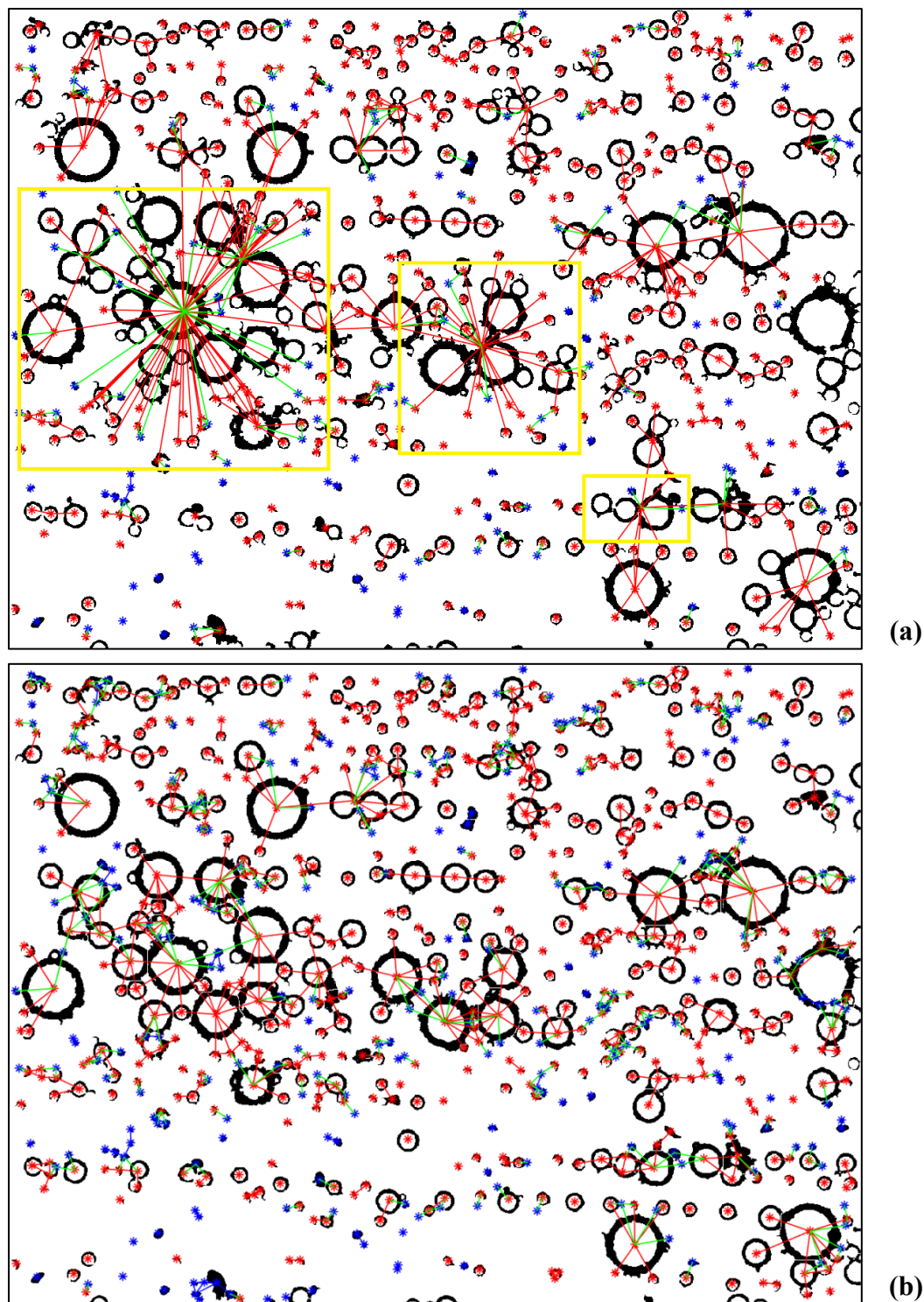


**Figure 3-13:** Separation of touching objects, (a): binary image processed without watershed segmentation, (b) binary image processed with watershed segmentation. Single centroid is detected for touching objects (connected black pixels shown in yellow box).

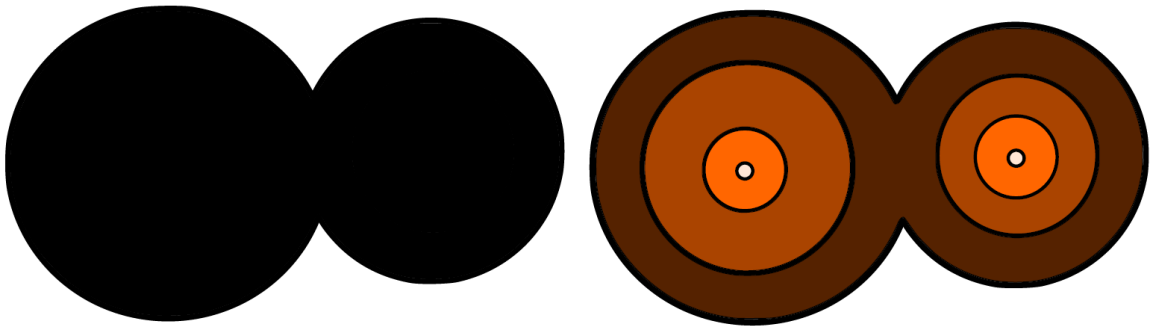


**Figure 3-14:** Euclidean distance map of the left image, shown in the right, where maximum brightness is assigned to the foreground pixel (black) farthest from background pixel (white). The right image is colored for illustration.

The method works only for smooth convex objects with limited overlap between touching objects (Ferreira and Rasband, 2012). Free water has a non-spherical and irregular outline. Therefore, free water gets over-segmented as shown in Figure 3-15. The images containing a lot of free water are not analyzable using this method. The method is also known for over-segmentation of touching objects resulting in creation of fake objects (Hamarneh and Li, 2009; Jung and Scharcanski, 2005). Although the method has several limitations, it is much faster and less biased than manual separation of touching objects (using a white brush to separate touching black objects in Photoshop). The watershed segmentation method reduced the processing time of a sample (containing 30 - 50 images) from 60 min (manual separation) to 30 min. 196 samples (~10 000 images) were analyzed for the experiments discussed in Chapter 4.

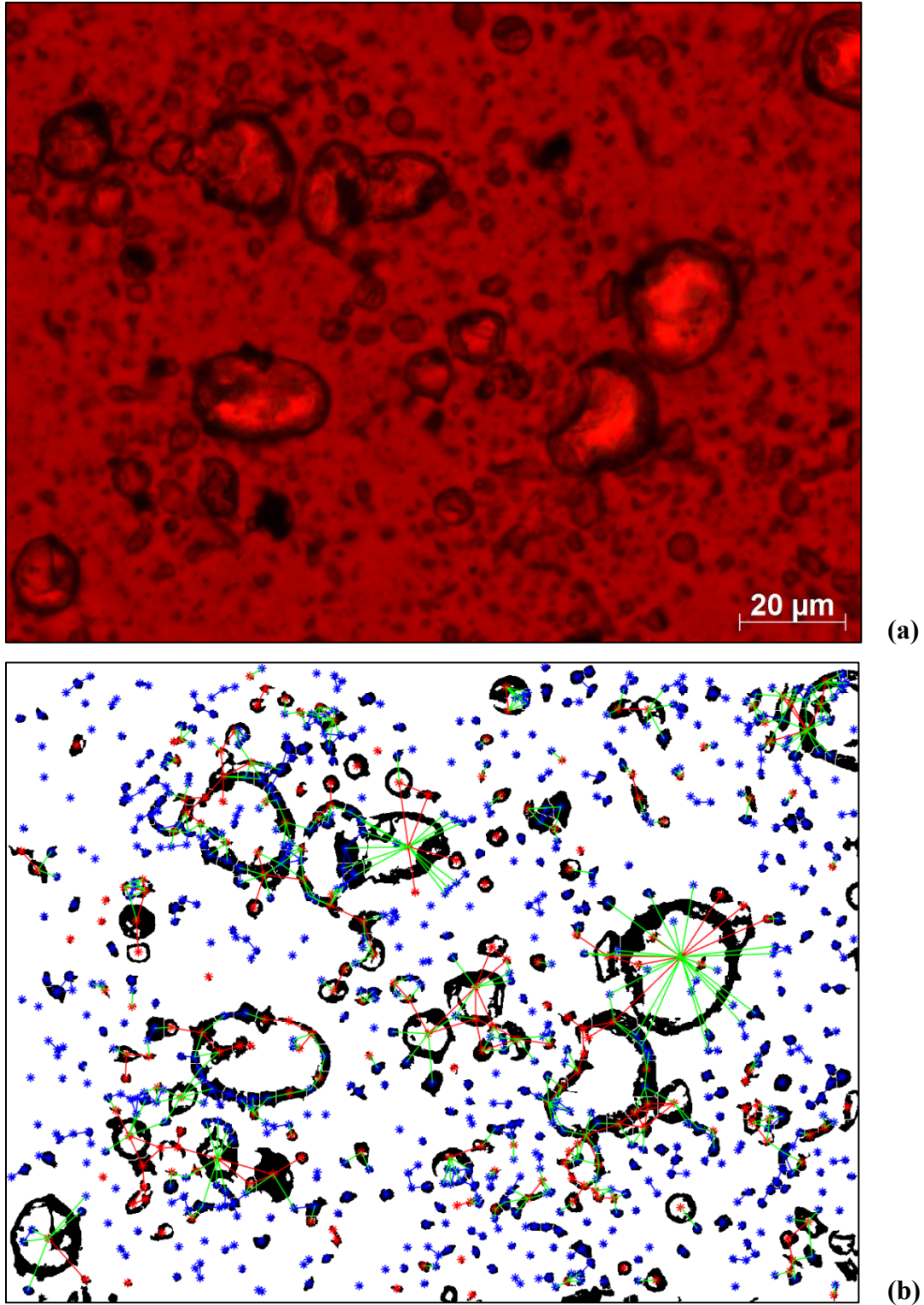


**Figure 3-15:** Microscope image showing edges of over-segmented free water being detected as solids (blue centroids). (a): Original color image, (b): Same image after clustering algorithm

### 3.3.3 Separating Water and Solids from Pre-Processed Image

Although diluted froth has several complex phases and components, we have simplified the problem by assuming that there are two types of objects on the microscope images: hollow water drops and filled solids as shown in Figure 3-1. Zawala et al., (2012) determined the mineral content of asphaltene aggregates in paraffinic froth treatment using the assumption that the solids are black filled objects. This difference between water and solids results in a different range of form factor (Equation 3-4) values which was then used in this work to separate the two objects.

$$\text{Form Factor} = \frac{4\pi \times \text{Area}}{\text{Perimeter}^2}$$

(Equation 3-4)

where the projected Area of an object is measured by the product of number of black pixels times the area of each pixel (Russ, 2002b)<sup>19</sup>. The perimeter of an object is the sum of the internal and external boundaries of an object found by forming a smooth contour along the boundary (Neal et al., 1998). The form factor is a measure of object's sphericity. It varies from 0 to 1 and for a filled circle (no internal boundaries), the form factor is 1. For a perfect hollow circle such as water drops, the form factor will drop to a very low value because only the boundary area is calculated and has two perimeters, internal and external. Figure 3-16 shows an example of separating water and solids from an image. A form factor less than 0.5 was used as a filter to extract water drops as shown in Figure 3-16b using *Filter > IP\*Measure Features > Select Features > Parameter > Form Factor*. Solids were put in the category of high form factor (0.5 to 1) as shown in Figure 3-16c. Note that there are some solids connected to water drops in Figure 3-16b and Figure 3-16c. Hence, touching water and solid objects (that were not separated by watershed segmentation) may end up in the water only or the solids only image depending on the form factor value. The cut off value of 0.5 was chosen after analyzing a range of different images encountered in diluted froth.

---

<sup>19</sup> Table 2: Representative Shape Descriptors

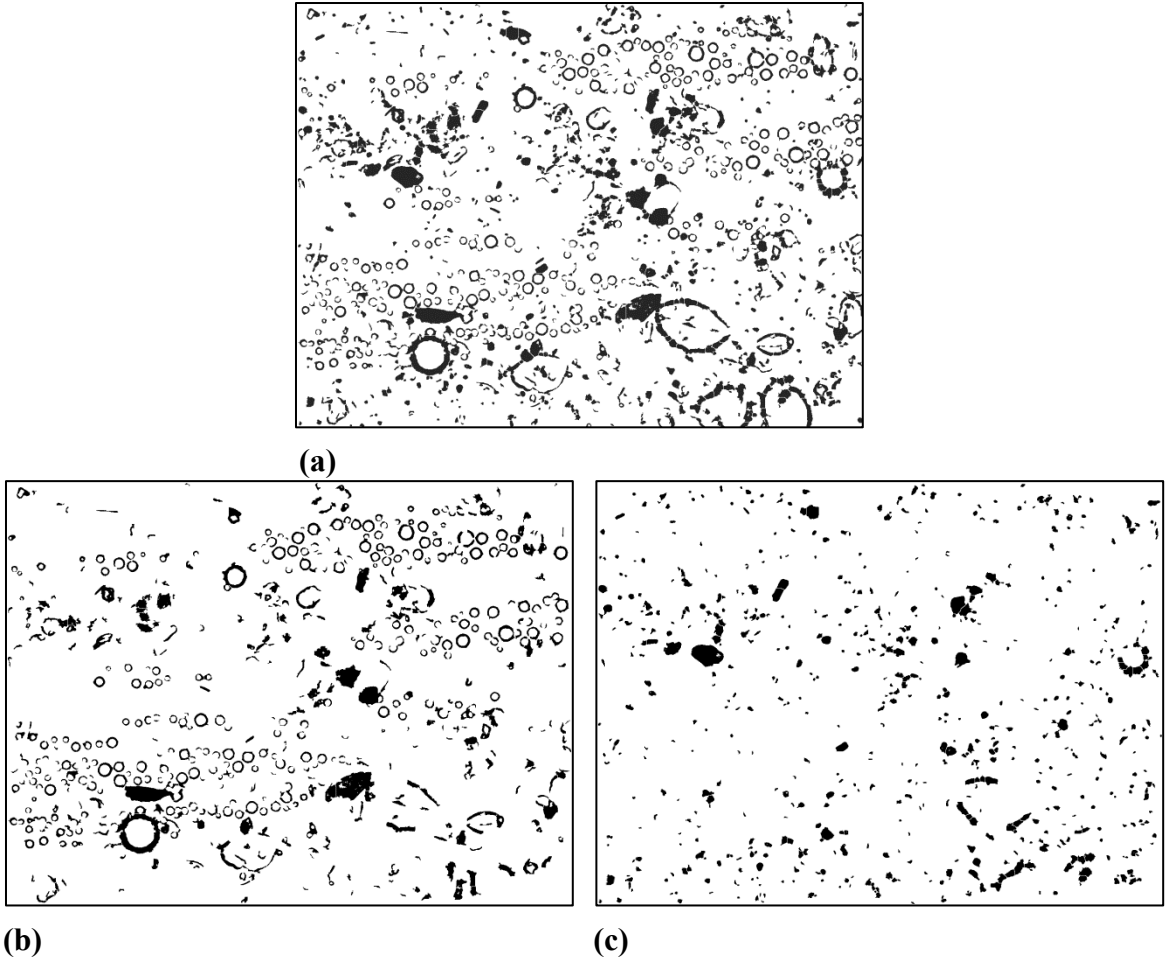


**Figure 3-16:** Separation of a watershed segmented image (a) into two images, (b): water only image containing objects with form factor between 0 and 0.5, (c): solids only image containing objects with form factor between 0.5 and 1.

The hole factor is another way to separate water and solids from the image but it is not discussed in detail because the form factor approach was more robust. The hole factor (Russ, 2002c)<sup>20</sup> is defined as

$$\text{Hole Factor} = \frac{(\text{Filled area} - \text{Area})}{\text{Filled Area}}$$

(Equation 3-5)

<sup>20</sup> Section: Global Measurements and Stereology

where Area refers to the area of black pixels in the image and Filled Area refers to the hollow section inside the circle, see left image of Figure 3-1. The edges of water drops may get partially removed after bi-level thresholding and hole factor approach works only if the objects are closed.

### 3.3.4 Marking Centroids

Matlab and Photoshop (Fovea Pro 4 plug in) were assessed in this study using a test image containing hollow and filled circles. Fovea was able to mark centroids for both types of objects. Matlab *regionprops* failed to detect centroids of filled circles and also detected an artefact centroid which was center of the image. Therefore, Fovea was selected for further use.

Two text files containing centroid and radius information are generated in Photoshop, one corresponding to the water only image, Figure 3-16b and another corresponding to solids only image, Figure 3-16c. The command: *Filter > IP\*Measure Features > Measure all features > create a new file* is used to generate the text file. These two text files and the parent image containing water and solids, Figure 3-16a are imported into Matlab for further analysis. The centroid or center of gravity is determined by averaging the coordinates of each pixel contained in the object (Russ, 2002b)<sup>21</sup>.

$$C. G._y = \frac{\sum y_i}{N_{px}}; C. G._z = \frac{\sum z_i}{N_{px}}$$

(Equation 3-6)

where C.G.<sub>y</sub> and C.G.<sub>z</sub> refer to the y and z coordinates of centroid, y<sub>i</sub> and z<sub>i</sub> refer to the pixel coordinates along the y and z axes respectively and N<sub>px</sub> is the number of pixels in the object (all connected black pixels). For non-convex objects such as a crescent moon, the centroid lies outside the object. This method for centroid determination gives equal weight to each pixel. Other methods involve pixel brightness, such as the weighted centroid. This would require a lot of computational time and hence is not implemented.

---

<sup>21</sup> Section: Determining Location

**Note:** The steps explained in Sections 3.3.1 to 3.3.4 were automated within Photoshop (*File > Automate > Create droplet*) so that same set of pre-processing steps are executed for all images. This automation speeds up the process.

### 3.3.5 Detecting Clusters

Water and solid centroids are marked in red and blue on the parent image (e.g: Figure 3-16a). For every water drop and every solid particle, the centroid-to-centroid distance for all other drops and solids is measured. If the distance is less than a threshold value, then the centroids of corresponding objects are connected by red (*W-W*), green (*W-S*) or blue (*S-S*) lines as shown in Figure 3-15b. The figure helps to visualize the dominating interaction (*W-W* or *W-S*). Initially, the threshold distance ( $\mathbb{T}$ ) was defined using Equation 3-7 but after some analysis it was found that Equation 3-8 is better.

$$\mathbb{T}, \mu\text{m} = \max(1.2 \times (r_1 + r_2), 3)$$

(Equation 3-7)

where  $r_1$  and  $r_2$  correspond to the circumscribed radii of object 1 and object 2 respectively. Recall that radius information was also contained in text files imported into Matlab. The minimum distance between two objects is equal to sum of their respective radii and a 20 % margin is added to this distance.  $3 \mu\text{m}$  is used as the lower limit because most water drops have a diameter of 3 - 4  $\mu\text{m}$ . This lower limit was added to give a chance to fine objects (that have negligible radius) to be connected to other objects. This function does not have any upper limit which leads to higher threshold for bigger objects leading to some bias. A modified threshold function [(Equation 3-8), suggested by Saraka, C., Pers. Corr., Dec 2015] was introduced. This function was adopted for all image analysis results shown in this chapter and Chapter 4. The new function has a lower as well as upper limit ( $r_1 + r_2 + 3$ ).

$$\mathbb{T}, \mu\text{m} = \max [\min \{1.2 \times (r_1 + r_2), r_1 + r_2 + 3 \}, 3]$$

(Equation 3-8)

The remainder of this section describes how Matlab code keeps track of the objects that belong to one cluster or another. Let *coordinateW* and *coordinateS* be matrix of size  $(m \times 2)$  and  $(n \times 2)$  where  $m$  represents the number of water objects and  $n$  represent the number of solid objects in the image being analyzed. The first and second column of these matrices represents  $y$  coordinates and  $z$  coordinates respectively. Matlab *pdist* function is used to find the  $W$ - $W$ ,  $W$ - $S$  and  $S$ - $S$  Euclidean distances. *pdist* of *coordinateW* results in a matrix of size  $[1 \times \{m(m-1)/2\}]$  and *squareform* of *pdist* matrix provides  $(m \times m)$  matrix. The *pdist* function performs faster distance calculation than conventional *for* loop because it knows that distance of object to itself is 0 and object 1 - object 2 and object 2 - object 1 distance are same. If *coordinateW* and *coordinateS* matrices are vertically concatenated (or stacked) and *pdist* function is performed on them, then the resulting matrix has sub matrices that contain  $W$ - $W$ ,  $W$ - $S$  and  $S$ - $S$  distances (Equation 3-9).

$$\text{squareform}(\text{pdist} \begin{bmatrix} \text{coordinate}W_{m \times 2} \\ \text{coordinate}S_{n \times 2} \end{bmatrix}) = \begin{bmatrix} W - W_{m \times m} & W - S_{m \times n} \\ S - W_{n \times m} & S - S_{n \times n} \end{bmatrix}_{(m+n, m+n)}$$

(Equation 3-9)

The sub-matrices from Equation 3-9 are extracted and the distance between objects is compared to the threshold function (Equation 3-8). If the distance between two objects is less than the threshold value, the corresponding objects are connected (red, green or blue lines) and their object numbers are recorded in a connectivity matrix. An example of a connectivity matrix is shown below in Table 3-6. Three connectivity matrices corresponding to  $W$ - $W$ ,  $W$ - $S$  and  $S$ - $S$  clusters are generated. This matrix is fed to Breadth First Search code that determines all the connected objects that belong to single cluster.

**Table 3-6:** Example of connectivity matrix: First row (1, 2) indicates object number 1 and 2 are connected and so on

1	2
2	4
4	5

### 3.3.6 Finding Cluster Information

Figure 3-15b shows a sample clustering algorithm output. While this figure helps to visualize the interaction, but there was a need to quantify the clustering information such as type of a cluster ( $W-W$  or  $W-S$  or  $S-S$ ), the cluster size and the number of objects per cluster. This information was obtained by Matlab code written using Breadth First Search (Lee, 1961) technique. A cluster is a set of connected nodes (centroid of each object) and the type of cluster is determined by the color of connected lines (red, green or blue). The breadth first search (Figure 3-17) finds all parent nodes (eg. node a) first and then move on to daughter nodes (eg. node b, c, d) and so on by sorting through the connectivity matrix (Table 3-6). The figure illustrates the alphabetical order in which nodes are detected using this algorithm. Once all the connected nodes of a cluster have been identified, the number of connected nodes (or objects) can be determined. The size of a cluster is determined by finding the maximum linear distance between any two nodes within a cluster. This gives us a distribution of cluster size and number of objects per cluster for three types of clusters ( $W-W$ ,  $W-S$  or  $S-S$ ). Three or more connected nodes are counted as a cluster.

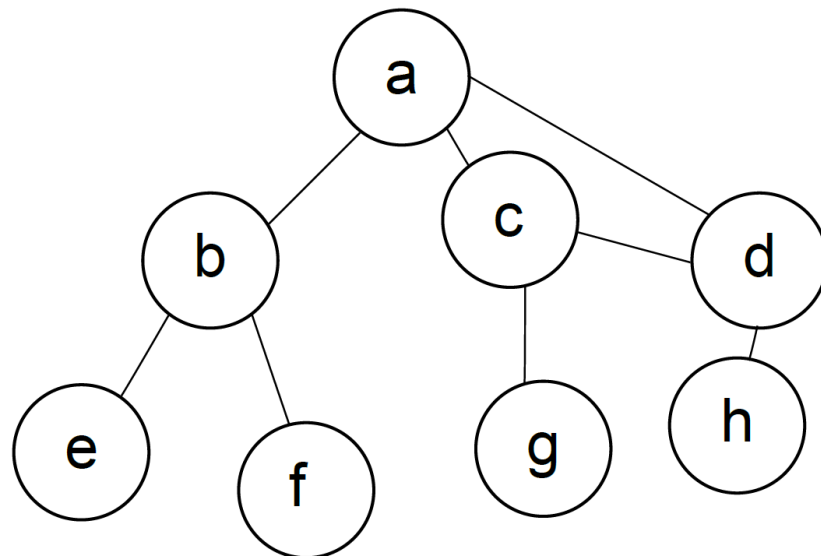


**Figure 3-17:** Breadth First Search algorithm to find all the connected nodes in a cluster. Nodes are detected in alphabetic order.

### 3.3.7 Results

Two image cases will be discussed here, one for a *W-W* aggregate and another for a *W-S* aggregate. Figure 3-18 shows an example of *W-W* aggregate for the colored image shown in Figure 3-5a. The color image is pre-processed according to the steps outlined in sections 3.3.1 to 3.3.6. It is clear that the form factor approach separates the water (red dots) and solids (blue dots) effectively. The detected clusters are shown with red, green and blue lines in Figure 3-18. Visually, more red lines and fewer green lines can be seen. This indicates that *W-W* interaction followed by *W-S* interaction is dominating on this image. Note that for a given microscope slide, one image is 160  $\mu\text{m}$  wide  $\times$  120  $\mu\text{m}$  high and ideally 23 000 images would be required to cover the slide completely. The decision of dominating interaction was made based on few images (30 – 50). The slide locations where aggregates were present were more frequently imaged. One slide is a drop of sample withdrawn from 1ml of diluted froth.

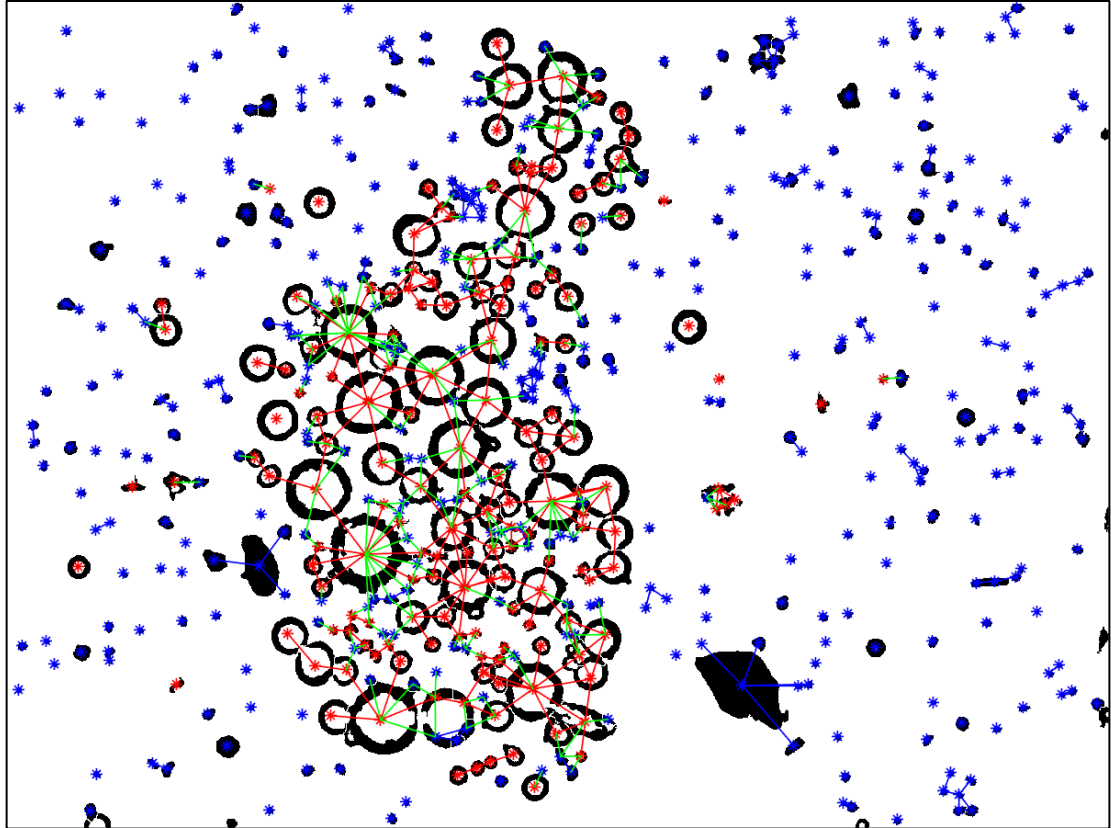


**Figure 3-18:** Algorithm output for image with water-water cluster obtained after processing of color image shown in Figure 3-5a. Red and blue centroids represent water and solids. Red, green and blue lines represent water-water, water-solid and solid-solid clusters respectively.

The quantitative cluster information for this image: number of objects per cluster and cluster size; are shown in Figure 3-19. The wider number and size distribution for  $W-W$  clusters agrees with visual observations. The size of the biggest  $W-W$  and  $W-S$  clusters are  $104 \mu\text{m}$  and  $53.4 \mu\text{m}$  respectively. Few  $S-S$  interactions were observed in Figure 3-18 and a similar observation is evident from the distribution in Figure 3-19. The biggest  $S-S$  cluster is  $19.9 \mu\text{m}$  which means this interaction is insignificant for this image in comparison to the other two cluster types. Fast settling rate requires big and dense aggregates. This image indicates that water prefers to settle with other water drops and solids.

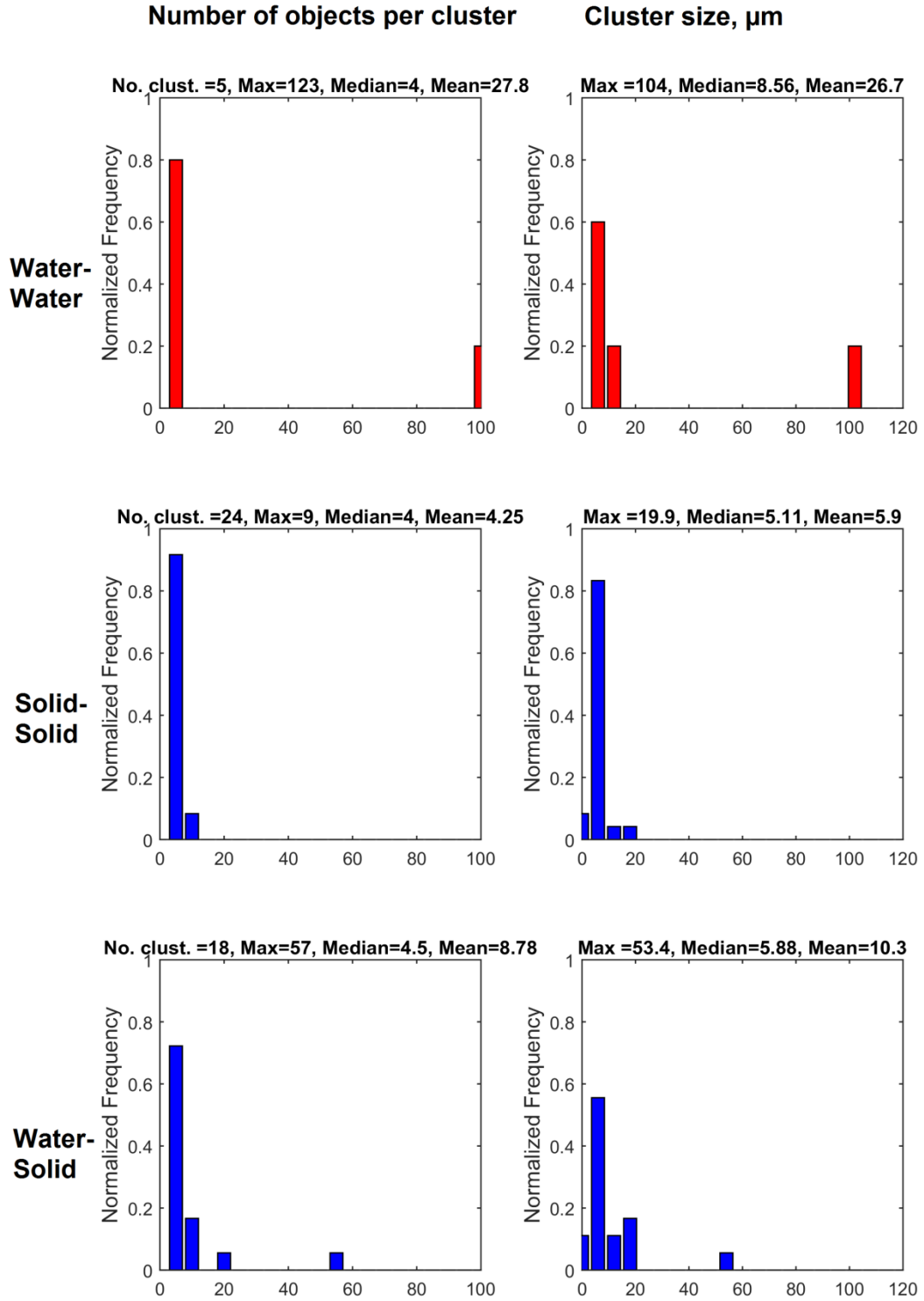


**Figure 3-19:** Frequency distribution (bins = 20) of number of objects per cluster and size of cluster for image shown in Figure 3-18. Water-water, water-solid and solid-solids cluster information is shown.

The second example discussed here is the *W-S* aggregate shown in Figure 3-20. Again, form factor works well to separate water and solids. Visually, *W-S* and *S-S* clusters can be seen. This observation agrees with the results of the frequency distribution shown in Figure 3-21. The biggest *W-S* and *S-S* clusters are 36.9  $\mu\text{m}$  and 18.6  $\mu\text{m}$  respectively. The number of objects per *W-W* cluster (12) and their cluster size is small indicating that this interaction is minimal for this image. The horizontal axis shown on Figure 3-21 for number and size distribution is different from Figure 3-19. This was done for illustrating the distribution better. For all the images analyzed in bitumen froth experiments, the bin size for number and size distribution was kept constant (=20).

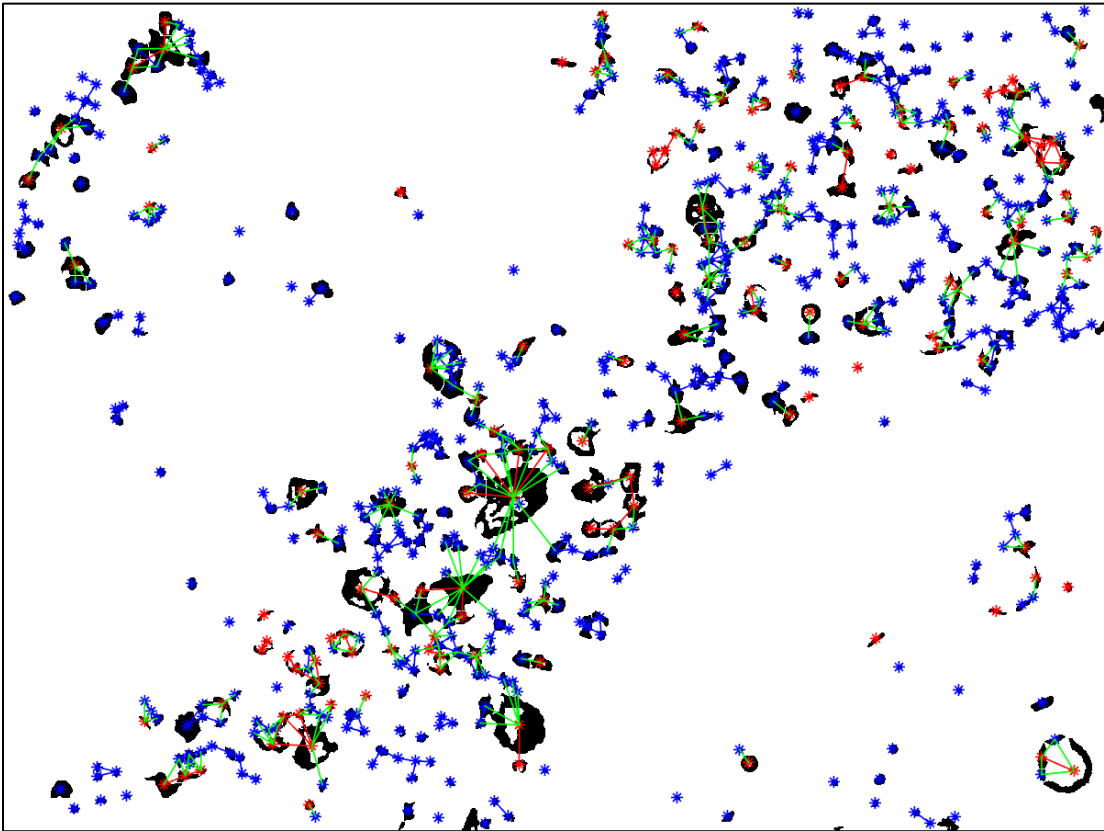


**Figure 3-20:** Algorithm output for image with water-solid cluster obtained after processing of color image shown in Figure 3-4a. Red and blue centroids represent water and solids. Red, green and blue lines represent water-water, water-solid and solid-solid clusters respectively.

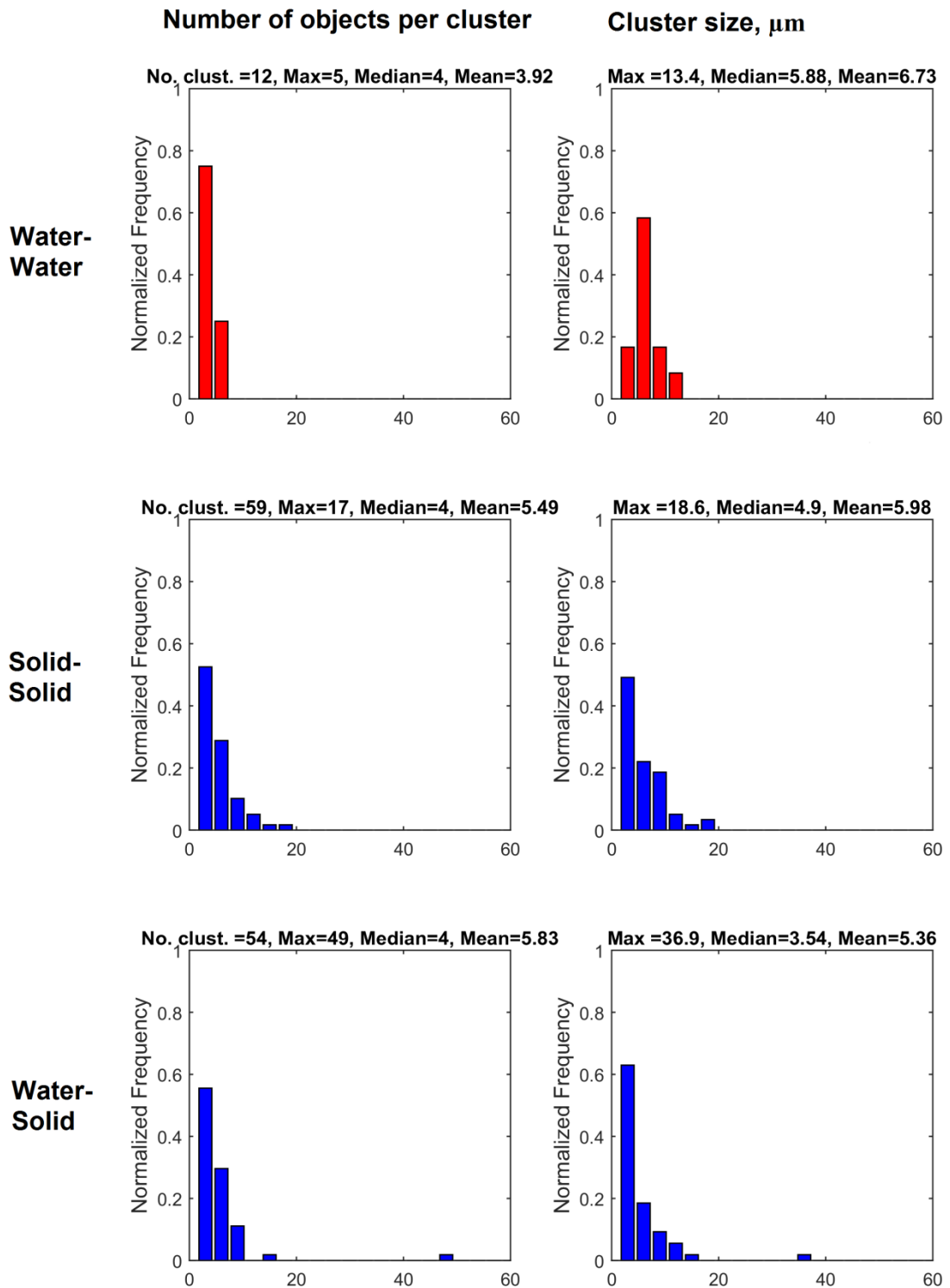


**Figure 3-21:** Frequency distribution (bins = 20) of number of objects per cluster and size of cluster for image shown in Figure 3-20. Water-water, water-solid and solid-solids cluster information is shown.

### 3.3.8 Strengths and Limitations

The strength of the algorithm lies in distinguishing between *W-W*, *W-S* and *S-S* clusters both qualitatively (clustered image) and quantitatively (distribution). The *PNN* method could not identify *W-S* clusters but was able to identify *W-W* and *S-S* clusters. The *PNN* method also could not identify the number and size of clusters in an image. All other methods which were considered failed to separate water from solids and so could not identify the different types of clusters. The clustering algorithm works well for images taken with a 40x lens and is able to determine the size of the aggregates if they fit within one image.

The clustering algorithm has some limitations. While conversion from greyscale to binary image using the Johannsen method (Johannsen and Bille, 1982), some objects on the froth images are lost to the background. The Johannsen method yields good results in comparison to other methods (such as Ostu method) especially when removing halo objects (unfocussed) that are artifacts. Sharply focused images are required for the best image analysis results. Images are carefully chosen to minimize objects being lost to background. For concave objects such as a crescent moon, the algorithm will detect a centroid that may lie outside the object. This does not pose a serious problem but the cluster size would be a bit off.

Watershed segmentation was used to eliminate the manual separation of touching objects but it over-segments irregular objects. For this reason, free water cannot be analyzed using this method. Also, most free water bodies are larger than the 40x frame (160  $\mu\text{m}$  wide and 120  $\mu\text{m}$  high) and sometimes even bigger than the 10x frame (641  $\mu\text{m}$  wide and 480  $\mu\text{m}$  high). 10x images have insufficient resolution to distinguish between water and solids and hence cannot be used with this algorithm.

### 3.4 Conclusions

Four clustering methods: nearest neighbor distance, nearest neighbor direction, dendrogram and Point Nearest Neighbor (*PNN*) method were evaluated. All methods except the *PNN* were not able to distinguish between water and solids present in the froth

images. The *PNN* method was able to identify if water or solid was aggregated with itself but it failed to identify water-solid aggregates. The *PNN* method required at least 50% of the objects to be clustered in order to be detectable as clusters and the method was sensitive to cluster orientation (vertical or horizontal). The *PNN* method provides a measure of the overall clustering tendency of objects in an image but does not provide quantitative cluster information such as number of clusters in an image, number of objects in a cluster, and cluster size.

The clustering algorithm developed with image pre-processing in Photoshop and cluster analysis in Matlab overcame the limitations of *PNN* method. The clustering algorithm based on object-object distance was able to identify the type of cluster (water-water or water-solid or solid-solid), the cluster size and the number of objects in a cluster. The method helped to identify the dominating interaction (water-water or water-solid) for images taken with 40x microscope lens. However, the clustering algorithm was not able to analyze free water because of its irregular shape and size larger than image frame. Free water is analyzed qualitatively using a 10x microscope lens that presents a bird eye view. The clustering algorithm combined with qualitative image observation and analysis was selected for analyzing bitumen froth images. These results are presented in Chapter 4.

## References

- Alban, F.B. et al., 2004. Dynamic Tracking of Fast Liquid–Liquid Dispersion Processes with a Real-Time in-Situ Optical Technique, *Chem. Eng. Res. Des.*, **82**, 1054–1060, doi:<http://dx.doi.org/10.1205/0263876041580631>.
- Czarnecki, J. et al., 2007. On the “Rag Layer” and Diluted Bitumen Froth Dewatering, *Can. J. Chem. Eng.*, **85**, 748–755, doi:10.1002/cjce.5450850520.
- Dey, T., Naughton, D., 2016. Cleaning and Anti-Reflective (AR) Hydrophobic Coating of Glass Surface: a Review from Materials Science Perspective, *J. Sol-Gel Sci. Technol.*, **77**, 1–27, doi:10.1007/s10971-015-3879-x.
- Diggle, P.J., 2013a. Chapter 2: Preliminary Testing, in: *Statistical Analysis of Spatial and Spatio-Temporal Point Patterns*, Third Edition, C and H/CRC Monographs on Statistics and Applied Probability, Chapman and Hall/CRC, 17–37, doi:10.1201/b15326-3.
- Diggle, P.J., 2013b. Chapter 1: Introduction, in: *Statistical Analysis of Spatial and Spatio-*

- Temporal Point Patterns, Third Edition, C and H/CRC Monographs on Statistics and Applied Probability, Chapman and Hall/CRC, 1–16, doi:10.1201/b15326-2.
- Ferreira, T., Rasband, W., 2012. Watershed [WWW Document], Image J User Guid., URL <http://imagej.nih.gov/ij/docs/guide/146-29.html#toc-Subsection-29.8>.
- Haight, F.A., 1967. Handbook of the Poisson Distribution, Publications in Operations Research: no. 11, Wiley, New York.
- Hamarneh, G., Li, X., 2009. Watershed Segmentation Using Prior Shape and Appearance Knowledge, *Image Vis. Comput.*, **27**, 59–68, doi:10.1016/j.imavis.2006.10.009.
- Jiang, T. et al., 2008. Using Silicate and pH Control for Removal of the Rag Layer Containing Clay Solids Formed During Demulsification, *Energy and Fuels*, **22**, 4158–4164, doi:10.1021/ef8001845.
- Johannsen, G., Bille, J., 1982. A Threshold Selection Method Using Information Measures, in: ICPR, 140–143.
- Jung, C.R., Scharcanski, J., 2005. Robust Watershed Segmentation Using Wavelets, *Image Vis. Comput.*, **23**, 661–669, doi:10.1016/j.imavis.2005.03.001.
- Kokal, S.L., 2005. Crude Oil Emulsions: A State-of-the-Art Review, *SPE Prod. Facil.*, **20**, 5–13.
- Kukukova, A. et al., 2011. Measuring the Scale of Segregation in Mixing Data, *Can. J. Chem. Eng.*, **89**, 1122–1138, doi:10.1002/cjce.20532.
- Kukukova, A., 2011. Spatial Statistics as a Means of Characterizing Mixing and Segregation, PhD Thesis, University of Alberta, Canada.
- Lee, C.Y., 1961. An Algorithm for Path Connections and its Applications, *Electron. Comput. IRE Trans.*, **EC-10**, 1389–1401, doi:10.1109/TEC.1961.5219222.
- Leo, S.S., 2013. Measurement and Analysis of Changes in Drop Size Distribution during Bitumen Clarification using Image Analysis, MSc Thesis, University of Alberta, Canada.
- Li, W. et al., 2012. Au/SiO<sub>2</sub> as a Highly Active Catalyst for the Selective Oxidation of Silanes to Silanols, *Chem. Commun.*, **48**, 9183, doi:10.1039/c2cc33949h.
- Eisenhawer, A., Jantunen-Cross, K., 2013. Chapter 11: Speciality Chemicals in Oil Sands Extraction, in: Masliyah, J.H. et al. (Eds.), *Handbook on Theory and Practice of Bitumen Recovery from Athabasca Oil Sands, Volume II: Industrial Practice*, Kingsley Knowledge Publishing, 363–387.
- Masliyah, J.H. et al., 2011b. Chapter 7: Froth Treatment Fundamentals, in: *Handbook on*

- Theory and Practice of Bitumen Recovery from Athabasca Oil Sands, Volume 1: Theoretical Basis, Kingsley Knowledge Publishing, 349–386.
- Masliyah, J.H. et al., 2011d. Chapter 4: Physical and Chemical Properties of Oil Sands, in: Handbook on Theory and Practice of Bitumen Recovery from Athabasca Oil Sands, Kingsley Knowledge Publishing, 173–256.
- Neal, B. et al., 1998. A Superresolution Approach to Perimeter Measurement, *J. Comput. Assist. Microsc.*, **10**, 11–21.
- Pacek, A.W. et al., 1994. On the Structure of Turbulent Liquid-Liquid Dispersed Flows in an Agitated Vessel, *Chem. Eng. Sci.*, **49**, 3485–3498.
- Photoshop Help/Color modes [WWW Document], 2015, Adobe URL, <https://helpx.adobe.com/photoshop/using/color-modes.html> (accessed 4.13.15).
- Ribeiro, M., 2004. Non-Invasive System and Procedures for the Characterization of Liquid–Liquid dispersions, *Chem. Eng. J.*, **97**, 173–182, doi:10.1016/S1385-8947(03)00179-7.
- Rourke, A.M.O., Macloughlin, P.F., 2005. A Comparison of Measurement Techniques Used in the Analysis of Evolving Liquid – Liquid Dispersions, **44**, 885–894, doi:10.1016/j.cep.2004.10.001.
- Russ, J.C., 2011. Chapter 7: Processing Binary Images, in: *The Image Processing Handbook*, Sixth Edition, CRC Press, doi:10.1201/b10720-9.
- Russ, J.C., 2002a. Chapter 10: Feature Recognition and Classification, in: *The Image Processing Handbook*, Fourth Edition, CRC Press, doi:10.1201/9781420040760.ch10.
- Russ, J.C., 2002b. Chapter 9: Feature-Specific Measurements, in: *The Image Processing Handbook*, Fourth Edition, CRC Press, doi:10.1201/9781420040760.ch9.
- Russ, J.C., 2002c. Chapter 8: Global Image Measurements, in: *The Image Processing Handbook*, Fourth Edition, CRC Press, doi:10.1201/9781420040760.ch8.
- Skinner, F.K. et al., 1989. Contact Angle Measurements from the Contact Diameter of Sessile Drops by Means of a Modified Axisymmetric Drop Shape Analysis, *J. Colloid Interface Sci.*, **130**, 25–34, doi:http://dx.doi.org/10.1016/0021-9797(89)90074-X.
- Tipman, R., 2013. Chapter 7: Froth Treatment, in: Masliyah, J.H. et al. (Eds.), *Handbook on Theory and Practice of Bitumen Recovery from Athabasca Oil Sands, Volume II: Industrial Practice*, Kingsley Knowledge Publishing, 211–253.

Zawala, J. et al., 2012. Settling Properties of Aggregates in Paraffinic Froth Treatment, *Energy and Fuels*, **26**, 5775–5781, doi:10.1021/ef300885t.

## Chapter 4: Settling Mechanisms in Bitumen Froth

In Chapter 2, it was concluded that side sampling is a more suitable sampling method than top sampling for diluted bitumen and water-mineral oil systems. In this campaign, experiments were performed with bitumen froth, an upstream product in froth treatment, using side sampling from a confined impeller stirred tank (*CIST*). Froth is a viscous multiphase fluid which typically contains 60 % bitumen, 30 % water and 10 % solids by mass (Masliyah et al., 2011b)<sup>22</sup>. The experimental procedure was modified from Chong (2013). The objective was to study settling, coalescence, and flocculation after addition of demulsifier. Clustering image analysis (as developed in Chapter 3) was used to determine the cluster type and size as a function of mixing conditions, sampling height and settling times. Quantitative water (Karl-Fischer) and solid (Dean-Stark) concentration results are compared with the trends observed in the corresponding microscope images.

### 4.1 Experimental

The experiments were performed in the *CIST* to provide standardized mixing conditions before sedimentation (Laplante, 2011). The experiment is performed in four stages: premixing, naphtha blending, demulsifier dispersion and sedimentation. Chong (2013) determined that the [(Froth + Demulsifier) + Naphtha] addition order performed better than the [(Froth + Naphtha) + Demulsifier] order. Laminar flow dominates the (Froth + Demulsifier) mixing step in the [(Froth + Demulsifier) + Naphtha] order whereas transitional to turbulent flow dominates both naphtha blending and demulsifier dispersion in the case of [(Froth + Naphtha) + Demulsifier] mixing. Four different impellers (Internig, A310, Rushton and *PBTD*) have been used in this and previous studies (Chong, 2013; Leo, 2013; Laplante, 2011). Rushton turbine impellers cause localized mixing or even cavern formation in the laminar regime and hence, are unsuitable for this application (Hemrajani and Tatterson, 2004)<sup>23</sup>. The [(Froth + Naphtha) + Demulsifier] order was adopted for this study to ensure that the mixing conditions in the lab could be scaled up to turbulent flow conditions in the plant setting.

---

<sup>22</sup> Page 349

<sup>23</sup> Page 383

The experimental layout is shown in Figure 4-1 and the detailed experimental procedure is given in Appendix B3. Feed preparation involves heating the bitumen froth and naphtha, followed by premixing the froth in the feed can. Naphtha is preheated separately and then added to the bitumen froth to give naphtha to bitumen ratio of 0.7 by mass. Both fluids are transferred to the side sampling *CIST* where the naphtha blending, demulsifier dispersion and sedimentation steps are executed.

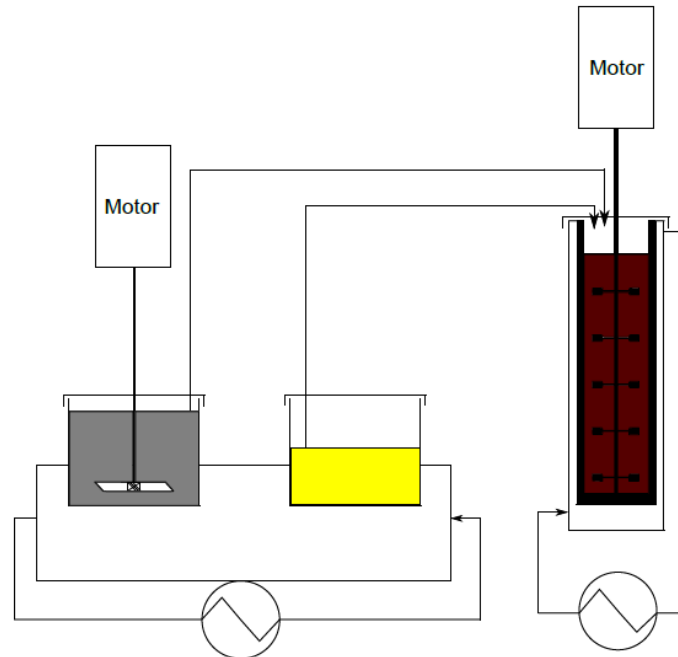


**Figure 4-1:** Bitumen froth experimental set up

The bitumen froth, naphtha and demulsifier (34 wt % active ingredient concentration) were supplied by Syncrude Research. Table 4-1 gives the average composition of water and solids over 11 samples of the as-supplied bitumen froth. This is a typical (average quality) industrial froth composition. The oil-water-solid (OWS) analysis was obtained using the Dean-Stark method (Bulmer and Starr, 1979), which has a confidence level of  $\pm 0.5\%$ . Computerized Particle Analysis (*CPA*) provides volumetric particle size distribution of dried solids (left after *OWS* analysis) using laser low angle forward scattering. The composition of bitumen froth may vary depending upon the source of the oil sands, the upstream extraction temperature and the chemical additives used (Romanova et al., 2004). Chong's (2013) froth experiments were conducted with a

froth containing 26 % water and 24.1 % solids by weight. Appendix C1, C2 and C3 describe the logistics, safety and housekeeping practices associated with the experiments.

**Table 4-1:** Composition of supplied bitumen froth

Average bitumen content (wt %)	60
Average water content (wt %)	28.3
Average solids content (wt %)	11.2
Solids size, $d_{v0.1}/ d_{v0.5}/ d_{v0.9}$ ( $\mu\text{m}$ )	1.6/ 22.8/ 169.8

#### 4.1.1 Premixing

The bitumen froth cans were stored upside down in the refrigerator at 5°C so that water and solids settled to the can bottom arrive at the lid surface where they can be recovered for re-dispersion. This helps in the uniform dispersion of solids and water during premixing. On the day of the experiment, the can was taken out of the refrigerator and heated to 70°C for 1.5 hours without mixing in the ethylene glycol heating bath. Then, the froth was premixed using two  $T/10$  baffles and a 45° pitched blade turbine (*PBTD*) impeller at 1000 rpm for 15 min while the froth was heated to 80°C. The premixing can dimensions and the operating conditions are shown in Table 4-2. The naphtha was heated to 80°C for half an hour without mixing. The froth and naphtha were transferred to the *CIST* for subsequent steps.

**Table 4-2:** Premixing can geometry and mixing parameters

Impeller Type	45° <i>PBTD</i>
Tank diameter, $T$ (m)	0.1
Impeller diameter, $D$ (m)	0.06
Liquid height, $H$ (m)	0.08
Off-bottom clearance, $C$ (m)	0.02
Impeller speed, $N$ (rpm)	1000
Reynolds number, $Re$ ***	84*-195**
Mixing time, $t_{mix}$ (min)	15

\*for a dynamic viscosity =  $811.4 \times 10^{-3}$  N.s/m<sup>2</sup> at 70°C (Seyer and Gyte, 1989)

\*\*for a dynamic viscosity =  $349.7 \times 10^{-3}$  N.s/ m<sup>2</sup> at 80°C (Seyer and Gyte, 1989)

\*\*\*for a density = 1138.1 kg/m<sup>3</sup> at 80°C (Chong, 2013)

#### 4.1.2 Naphtha Blending (Froth + Naphtha)

To ensure the same liquid height in the *CIST* for all the experiments, an additional froth can was premixed (Section 4.1.1) before the day of the experiment and transferred to other cans so that all samples weighed 780 g (includes empty can and lid weight). The jacketed *CIST* was held at a temperature of 80°C while premixing was in progress using ethylene glycol as the heating fluid. Naphtha was transferred to the *CIST*, followed by bitumen froth to prevent the froth from sticking to the glass surface. Mixing conditions are detailed in Table 4-3. Blending was done at equal high energy dissipation ( $\epsilon_{imp}$ ) and equal mixing time ( $t_{mix}$ ) for all impellers (Rushton, Intermig and A310) to ensure that naphtha and froth were well blended and this step did not affect the experiment outcome. The mixing time is the time for which impellers were run at a certain rotational speed ( $N$ ) shown in Table 4-3. The mixing time was kept longer than the blend time. The blend time correlations strictly apply to mixing of two completely miscible liquids with similar viscosity. The same impellers were used in both the naphtha blending and the demulsifier dispersion steps in each run. The impellers were equally spaced, with an upper impeller submergence of  $D$  and the lowest impeller clearance of  $D/3$ . The power numbers ( $Np$ ) were supplied by Machado and Kresta (2013). The Reynolds numbers of all impellers fall in the turbulent regime.

**Table 4-3:** Mixing specifications for naphtha blending (Froth + Naphtha) step

Impeller Type	Intermig	Rushton	A310
Tank diameter, $T$ (m)	0.075	0.075	0.075
Liquid height, $H$ (m)	0.225	0.225	0.225
Number of impellers	6	5	5
Impeller diameter, $D$ (m)	0.05	0.038	0.038
Off-bottom clearance, $C$ (m)	0.017	0.013	0.013
Submergence, $S$ (m)	0.05	0.038	0.038
Impeller speed, $N$ (rpm)	1060	600	1250
Tank volume, $V_{tank}$ (m <sup>3</sup> )	$9.94 \times 10^{-4}$	$9.94 \times 10^{-4}$	$9.94 \times 10^{-4}$
Total impeller volume, $V_{imp}$ (m <sup>3</sup> )	$1.68 \times 10^{-4}$	$4.31 \times 10^{-5}$	$5.23 \times 10^{-5}$
$N_p$ per impeller	0.62	4.13	0.56
$\varepsilon_{imp} \sim P/\rho V_{imp}$ (W/kg)*	<b>38.2</b>	<b>38.0</b>	<b>38.4</b>
Reynolds number, $Re^{**}$	7240	2367	4932
<b>Mixing time, <math>t_{mix}</math> (min)***</b>	<b>2</b>	<b>2</b>	<b>2</b>

\*total power input

\*\*for a kinematic viscosity =  $6.1 \times 10^{-6}$  m<sup>2</sup>/s at 80°C (Laplante, 2011)

\*\*\*Mixing time = naphtha mixing time  $\neq$  blend time

### 4.1.3 Demulsifier Dispersion [(Froth + Naphtha) + Demulsifier]

The demulsifier supplied at 34 wt % active ingredient concentration was diluted with xylene to the desired injection concentration ( $IC$ , 12 - 21 wt %). The bulk concentration ( $BC$ ) of 150 ppm by mass was the same for all runs with demulsifier in this campaign. Two runs were conducted without adding demulsifier. The demulsifier was injected using a syringe pump attached to 3 mm tubing. The tube was located directly above the top impeller blade tip in the  $CIST$  to promote rapid dispersion. A low  $IC$  (injection concentration) and injection at the blade tip minimize high local demulsifier concentrations, thus limiting meso-mixing effects and secondary undesirable mechanisms (Laplante et al., 2015). Intermig and Rushton impellers were used for low ( $X_J = -1$ ) and high ( $X_J = +1$ ) mixing energy respectively as shown in Table 4-4. The low and high energy dissipation levels ( $\varepsilon_{imp}$ ) correspond to flow in an empty pipe vs. flow in a static mixer in the plant setting. For mid-level energy ( $X_J = 0$ ), the Rushton and A310 at same mixing energy ( $J = \varepsilon_{imp} \times t_{mix}$ , Table 4-4) were used to test the hypothesis that the flow pattern due to different impellers does not matter and  $J$  could be used as a more general

scaling variable. The demulsifier injection rate must be low enough to minimize meso-mixing. It was determined using (Equation 4-1, from Chong, 2013), with the results shown in Table 4-5.

$$Q = 0.54 \frac{v^{0.5} \times U_z \times d_{inj}^{1.5}}{u_z^{0.5}}$$

(Equation 4-1)

where Q is the injection rate, v is the kinematic viscosity, U<sub>z</sub> and u<sub>z</sub> are the local mean and rms velocity along the z-axis respectively and d<sub>inj</sub> is the inside diameter of the injection pipe. The local values of U<sub>z</sub> and u<sub>z</sub> in the CIST were provided from Machado and Kresta (2013) using Laser Doppler Velocimetry. A repeatable injection location (r/R = 0.5, z = 30 mm below liquid level) was set using a port located at r/R = 0.5 on the tank lid and tubing marked for injection depth.

**Table 4-4:** Mixing conditions for demulsifier dispersion step

Impeller Type	Intermig	Rushton	A310	Rushton
Mixing energy level	$X_J = -1$	$X_J = 0$	$X_J = 0$	$X_J = +1$
$N_p$ per impeller	1.07	4.64	0.64	4.13
$\varepsilon_{imp} \sim P/\rho V_{imp}$ (W/kg)	3.54	22.53	22.44	37.96
Reynolds number, $Re^*$	2732	1913	3945	2367
Mixing time, $t_{mix}$ (min)	2	9	9	10
<b>Mixing energy, J (J/kg)</b>	<b>425</b>	<b>12164</b>	<b>12120</b>	<b>22778</b>

\*for a kinematic viscosity =  $6.1 \times 10^{-6}$  m<sup>2</sup>/s at 80°C (Laplante, 2011)

**Table 4-5:** Operating conditions and run summary for bitumen froth experiments using Rushton (*RT*), A310 and Intermig (*IM*) impellers

$X_J$ , $X_{IC}$	Run	Naphtha Blending	Demulsifier Dispersion	Demulsifier Injection	
				Rate (ml/hr)	Volume (ml)
+ <i>N/A</i>	<i>ND1</i>	<i>RT</i> (600 rpm, 2 min)	<i>RT</i> (600 rpm, 10 min)	-	-
+ <i>N/A</i>	<i>ND2</i>	<i>RT</i> (600 rpm, 2 min)	<i>RT</i> (600 rpm, 10 min)	-	-
+ -	<i>FD1</i>	<i>RT</i> (600 rpm, 2 min)	<i>RT</i> (600 rpm, 10 min)	634.7	1.2
++	<i>FD2</i>	<i>RT</i> (600 rpm, 2 min)	<i>RT</i> (600 rpm, 10 min)	634.7	0.7
--	<i>FD3</i>	<i>IM</i> (1060 rpm, 2 min)	<i>IM</i> (400 rpm, 2min)	125.1	1.2
- +	<i>FD4</i>	<i>IM</i> (1060 rpm, 2 min)	<i>IM</i> (400 rpm, 2min)	125.1	0.7
0 0	<i>CR1</i>	<i>RT</i> (600 rpm, 2 min)	<i>RT</i> (485 rpm, 9 min)	594.9	0.9
0 0	<i>CR2</i>	<i>RT</i> (600 rpm, 2 min)	<i>RT</i> (485 rpm, 9 min)	594.9	0.9
0 0	<i>CA1</i>	<i>A310</i> (1250 rpm, 2 min)	<i>A310</i> (1000 rpm, 9 min)	207.7	0.9
0 0	<i>CA2</i>	<i>A310</i> (1250 rpm, 2 min)	<i>A310</i> (1000 rpm, 9 min)	207.7	0.9

*N/A* Not Applicable

*FD* runs had samples taken at 4 heights, other runs at 2 heights

#### 4.1.4 Sedimentation

After demulsifier dispersion, the impellers were stopped and the *CIST* fluid was allowed to settle. 1 ml samples were taken at either two heights ( $z_1$  and  $z_4$ ) or four heights for Karl-Fischer (*KF*) and microscopic analysis. Refer to Chapter 2 for the geometry and the sampling coordinates of side sampling *CIST*. The sampling point coordinates shown in Figure 2-1 are  $[(r/R, z): (0.9, z_1 = 52 \text{ mm}), (0.9, z_2 = 96 \text{ mm}), (0.9, z_3 = 140 \text{ mm}), (0.9, z_4 = 184 \text{ mm})]$ . The *CIST* liquid level is 225 mm.

#### 4.1.5 Sampling Schedule

One millilitre samples were obtained after the end of premixing, at the end of naphtha blending and 30 s before the end of demulsifier dispersion for *KF* and microscopic analysis. Once the impellers were stopped, the samples were taken during sedimentation at 3, 5, 7, 10, 30 and 60 min for either two heights or four heights. The detailed sampling schedule is given in Table B3-1. The froth sample was collected using a pipette tip attached to an auto-pipette. For naphtha diluted froth, samples were taken

using a pre-silanized 45° tapered tip 14 gauge needle (1.6 mm ID) attached to a pipette tip (1.5 mm) followed by an auto-pipette as shown in Figure 2-2. A wide opening pipette tip was used to minimize aggregate break up during sampling. A drop of sample was taken from sample vial using a pre-silanized Pasteur pipette, dropped onto a pre-silanized microscope slide and secured with a cover glass. Appendix D1 and D2 describe the procedures for Karl-Fischer analysis and microscope image acquisition respectively.

After 60 min of settling, three samples of 100 ml each were taken from the top ( $s/H = 0.1$ ), middle ( $z/H = 0.5$ ) and bottom ( $z/H = 0.9$ ) of the *CIST* for oil-water-solid (*OWS*) content using Dean Stark (*DS*) and computerized particle analysis (*CPA*) methods. Two additional samples of 15 ml each, one at  $z/H = 0.1$  and another at  $z/H = 0.9$  were taken for solid content using extraneous matter (*EXM*) method. Both top samples ( $z/H = 0.1$ ) were taken first, followed by middle and bottom samples to avoid disturbing the liquid before sampling.

#### 4.1.6 Experimental Design and Hypothesis

The campaign objective was to identify and distinguish between microscopic observations of clustering and coalescence at favorable vs. poor mixing conditions, different sampling heights and settling times. A total of 10 experimental runs were conducted in this campaign as given in Table 4-5 and Table A-4. The run numbers shown in Table A-4 represent the randomized order in which the experiments were conducted. The same mixing energy was used for all impellers in the naphtha blending step and the mixing variables ( $J$  and  $IC$ ) were varied in the demulsifier dispersion step as shown in Table 4-4. The demulsifier injection rates given in Table 4-5 were calculated using Equation 4-1. Two experiments were conducted with **no demulsifier** (*ND1* and *ND2*) to isolate its effect from naphtha dilution. Chong (2013) reported that there was more deviation between favorable (high  $J$ , low  $IC$ ) and poor (low  $J$ , high  $IC$ ) mixing conditions at a  $BC$  of 150 ppm than at 50 ppm, as shown in Figure 4-2. Based on this result, the bulk concentration was set at 150 ppm for the remaining 8 experiments. The rate of dissipation of turbulent kinetic energy per unit mass ( $\epsilon_{imp}$ ) and the mixing time ( $t_{mix}$ ), were combined into a single variable, the mixing energy ( $J$ ). The variable ranges for  $BC$ ,  $IC$  and  $J$  are

given in Table 4-6. Previous studies (Laplante, 2011; Chong, 2013; Leo, 2013) have demonstrated that high  $J$  and low  $IC$  set favorable hydrodynamic conditions which result in improved dewatering for diluted bitumen and bitumen froth using two different demulsifiers.

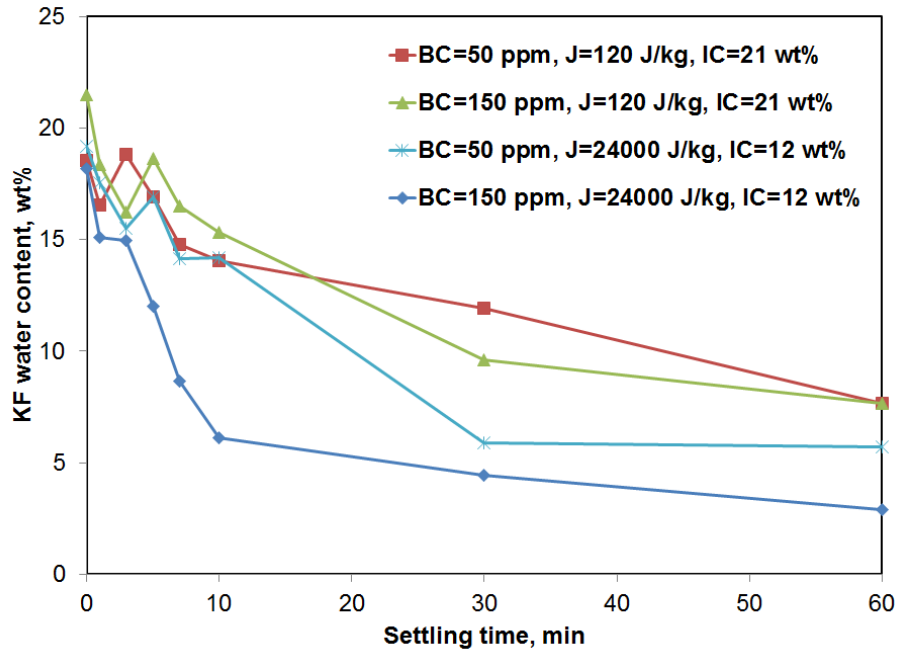


**Figure 4-2:** Effect of favorable vs. poor mixing conditions at 50 ppm and 150 ppm bulk concentration of demulsifier. Data produced with permission, Chong (2013)

**Table 4-6:** Variable range for demulsifier dispersion in bitumen froth experiments using Rushton ( $RT$ ),  $A310$  and Intermig ( $IM$ ) impellers

	Variable Code ( $X_i$ )			
	- ( $IM$ )	0 ( $A310$ )	0 ( $RT$ )	+ ( $RT$ )
$BC$ (ppm)		150		
$IC$ (wt%)	12	16.5	16.5	21
$J$ (J/kg)	425	12164	12120	22778
$N$ (rpm)	400	1000	485	600
$\epsilon_{imp}$ (W/kg)	3.5	22.5	22.4	38.0
$t_{mix}$ (min)	2	9	9	10

Four runs *FD1 - FD4* as shown in Table 4-5 were conducted by varying *IC* and *J* using a 2-level factorial design (Box et al., 1978), with sampling from four heights. These runs collectively are referred to as the **factorial design** runs. The variable *i* (*J* or *IC*) is varied at two levels [ $(i_{min}, -1)$  and  $(i_{max}, +1)$ ] using the following equation

$$X_i = 2 \times \frac{i - i_{min}}{i_{max} - i_{min}} - 1$$

(Equation 4-2)

The factorial design requires center point repeats ( $X_i = 0$ ) to verify the experimental repeatability which accounts for operator, equipment and feed material deviation. Two experiments with variables at mid-level ( $X_J = 0$  and  $X_{IC} = 0$ ) were conducted for each of the Rushton (*CR1* and *CR2*) and A310 (*CA1* and *CA2*) impellers, with sampling from two heights in all four experiments. These four experiments are also known as the **circulation pattern** runs (Table 4-5) since they are also used to test the hypothesis that mixing patterns (due to different impellers) do not alter the process outcome and that *J* can be used as a scaling variable. We expected similar dewatering and demineralization results in these experiments.

## 4.2 Results

The results section combines data analysis from Karl-Fischer (water concentration), *OWS* and *EXM* (solid concentration), *CPA* (solid size distribution) and microscope images (qualitative image analysis, clustering analysis and drop size distribution) to determine the dominant settling and dewatering mechanisms (coalescence or flocculation or sweep flocculation). The results are classified into four sections: no demulsifier runs, factorial design runs, circulation pattern runs and solids analysis. The no demulsifier runs provide a baseline and the factorial design runs capture the effects of mixing variables (*J* and *IC*). The circulation pattern section tests a hypothesis that different impellers running at the same *J* (product of  $\epsilon_{imp}$  and  $t_{mix}$ ) give similar water and solids removal results.

## 4.2.1 No Demulsifier Run Results

Figure 4-3 shows the Karl-Fisher water content at height  $z_1$  ( $z/H = 0.23$ ). The water from this height settles rapidly during the first 10 - 30 min of settling followed by a slow settling period till 60 min, even without demulsifier addition. Fast settling in first 10 min is owed to the big aggregates and free water that settle out fast leaving dispersed water and solids along with few small aggregates. At height  $z_4$  ( $z/H = 0.82$ ), the water content spikes up to 25 - 30 % before it levels down to 4 - 8 %. This indicates that the settled free water layer lies below height  $z_4$  (18 % of total liquid) at the end of the run. The final water content after 60 min of settling at height  $z_1$  is 2.55 % (*ND1*) and 1.45 % (*ND2*), which is above the 1 % operating limit. This limit is used as a reference for comparison between no demulsifier and demulsifier runs. The industry specification for pipelining diluted bitumen is more stringent [0.5 % total water and solids as per Angle, 2001]. For a 350 000 bbl/day diluted bitumen production plant, 2.5 % water would amount to 820 MT/day. Hence, it is essential to minimize water and solids.

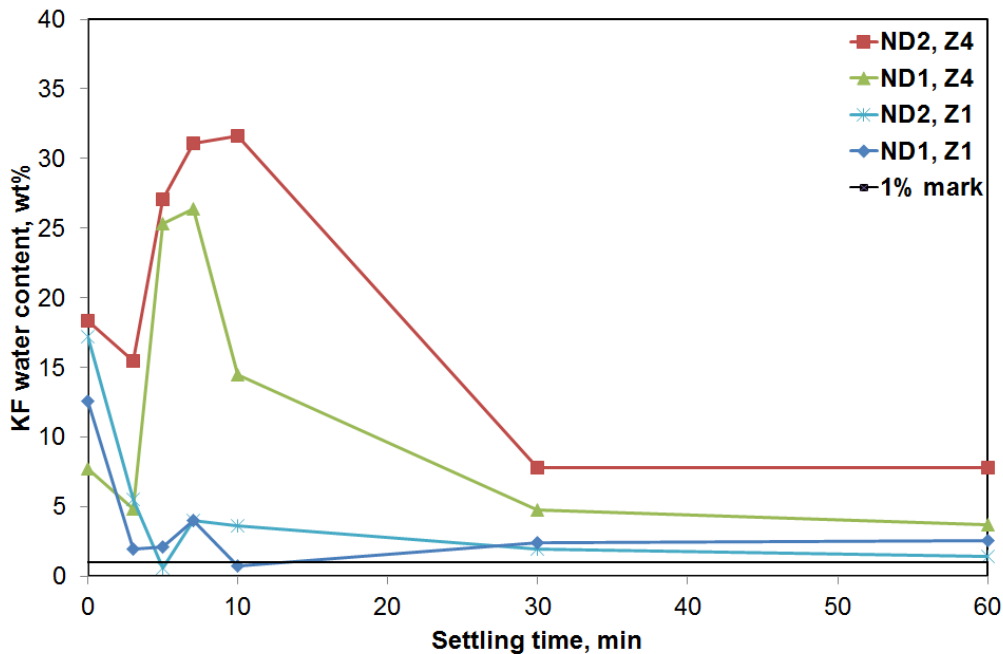


**Figure 4-3:** Water content (wt%) as a function of settling time at two sampling heights ( $z_1$  and  $z_4$ ) for runs: *ND1* and *ND2*, with no demulsifier addition

## 4.2.2 Factorial Design Run Results

Figure 4-4 shows the dewatering performance in the 4 factorial design runs with *FD1* and *FD4* being the best (high *J*, low *IC*) and the worst (low *J*, high *IC*) mixing conditions for two sampling heights  $z_1$  ( $z/H = 0.23$ ) and  $z_2$  ( $z/H = 0.43$ ). The other two runs *FD2* and *FD3* as shown in Table 4-5 have one favorable mixing variable (*J* or *IC*). In comparison to the no demulsifier runs, the final water content (60 min) is lower than 1 % except for the worst mixing condition (*FD4*) where it is 2.51 %, which is comparable to the no demulsifier *NDI* run. Thus, demulsifier addition with poor mixing conditions is equivalent to adding no demulsifier at all. Favorable mixing or hydrodynamic conditions enhance the dispersion of demulsifier and hence its effectiveness. The final water content for *FD1*, *FD2* and *FD3* is 0.89, 0.22 and 1.42 wt% respectively. The maximum initial dewatering rate (in first 10 min) or maximum slope corresponds to the best mixing conditions (*FD1*). Figure 4-5 shows the difference in water content at two heights. The maximum dewatering rate corresponds to the best mixing conditions (*FD1*). The *KF* data for all 10 experiments is shown in Table A-4.

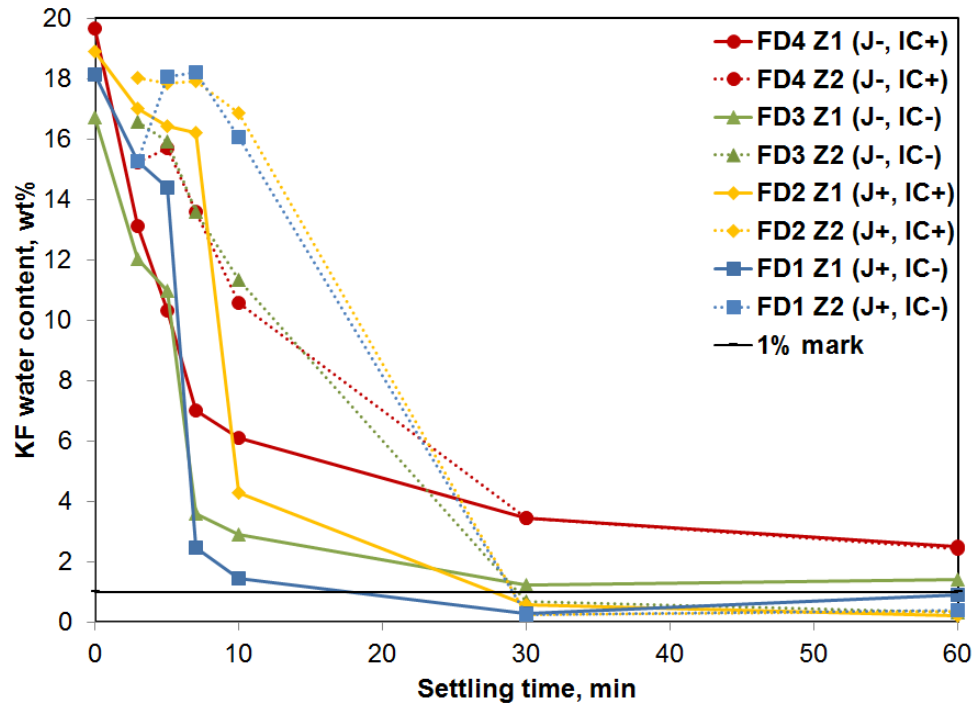


**Figure 4-4:** Water content (wt%) as a function of settling time at two sampling heights ( $z_1$  and  $z_2$ ) for factorial design runs ( $FD1 - FD4$ ). Runs are coded from the best ( $FD1$ : high J, low IC) to the worst ( $FD4$ : low J, high IC) mixing conditions.

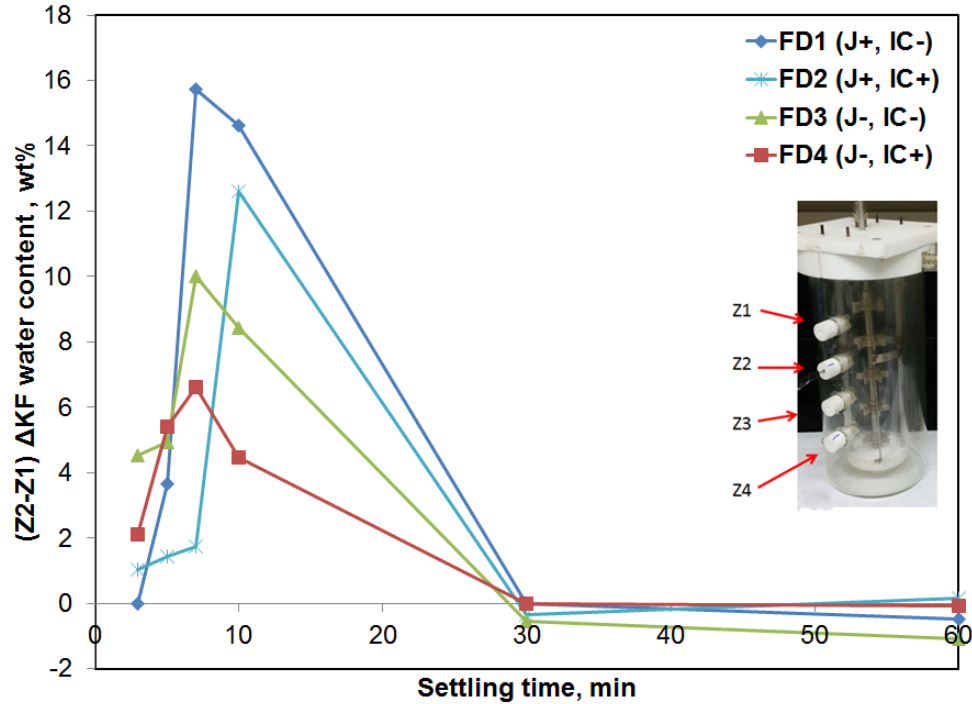


**Figure 4-5:** The difference in water content between first ( $z_1$ ) and second sampling ( $z_2$ ) height as a function of settling time for factorial design runs ( $FD1$ -  $FD4$ )

It is clear that the mixing variables ( $J$  and  $IC$ ) can have a significant effect on dewatering performance. The dominant variable is determined from the factorial analysis of water content  $[C(t)]$  at various settling times ( $t$ ) for the  $FD$  runs, The results can be used to estimate the coefficients in the model form

$$C(t) = \beta_0 + \beta_J X_J + \beta_{IC} X_{IC} + \beta_{J \times IC} X_{J \times IC}$$

(Equation 4-3)

Figure 4-6 shows that  $\beta_J$  is positive at 3 min, indicating that it increases the water content, probably due to residual turbulence in system as impellers are stopped at  $t = 0$  min. Later, the variable effect becomes negative, which implies that increased mixing power helps to reduce the final water content in the top layer (height  $z_1$ ) through formation of big and/ or dense flocs.  $\beta_{IC}$  is positive throughout the settling, indicating that high  $IC$  increases water content. A similar effect was observed by Chong (2013) in bitumen froth experiments.

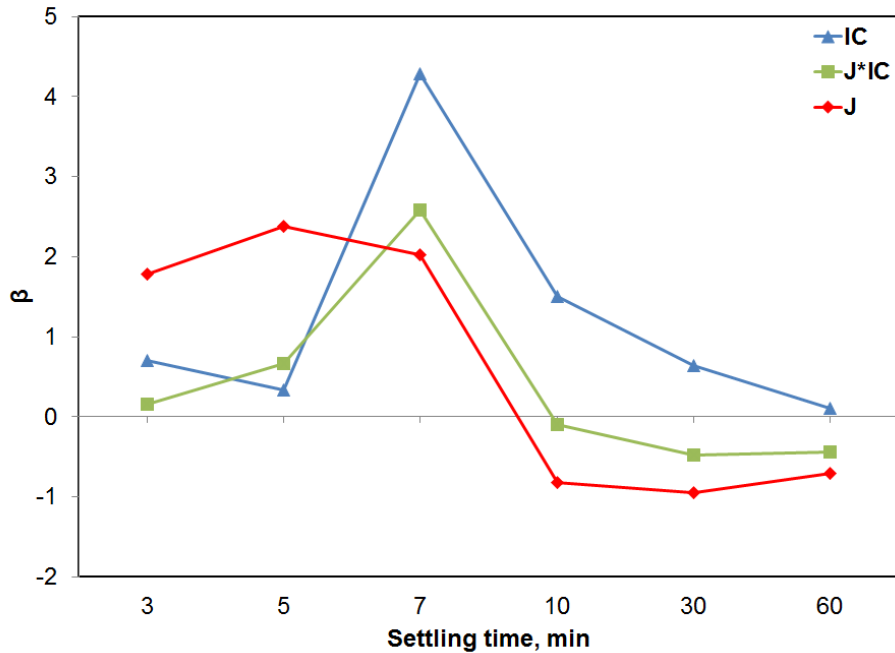


**Figure 4-6:** Regression coefficients ( $\beta$ ) for multi variable regression of water content at height  $z_1$  for factorial design runs

The results from previous studies are summarized here:

- Laplante, 2011: For diluted bitumen, bulk concentration was the dominant variable followed by  $IC$  and then  $J$ . The demulsifier performance can be enhanced by as much as 50 % through increasing mixing dissipation, increasing mixing time and pre-dilution of demulsifier (low  $IC$ ).
- Chong, 2013:  $IC$  was the dominant variable followed by  $BC$  and then  $J$  using a different demulsifier on diluted bitumen and a limited range of  $BC$ . Overdosing of demulsifier (excess  $BC$ ) can be detrimental to the process performance, but this effect can be mitigated by high mixing energy and pre-dilution of demulsifier. Chong set the experimental foundations for froth experiments.
- Leo, 2013 developed an algorithm to determine water drop size distribution in diluted bitumen images and worked alongside Chong in his experiments. The peak of the drop size distribution remained at 4  $\mu\text{m}$  throughout the 60 min settling period. Monitoring the number of drops per slide gave results

similar to Chong (2013). Overdosing of demulsifier increased the number of drops and reduced the peak of the drop size distribution to 2  $\mu\text{m}$ , which explains the observation of inefficient dewatering.

Leo (2013) highlighted the need to determine the dominant settling mechanism for which the side sampling (Chapter 2) and clustering algorithm (Chapter 3) were developed. A qualitative analysis of the microscope images is considered at all four sampling heights next.

#### 4.2.2.1 Qualitative Image Analysis

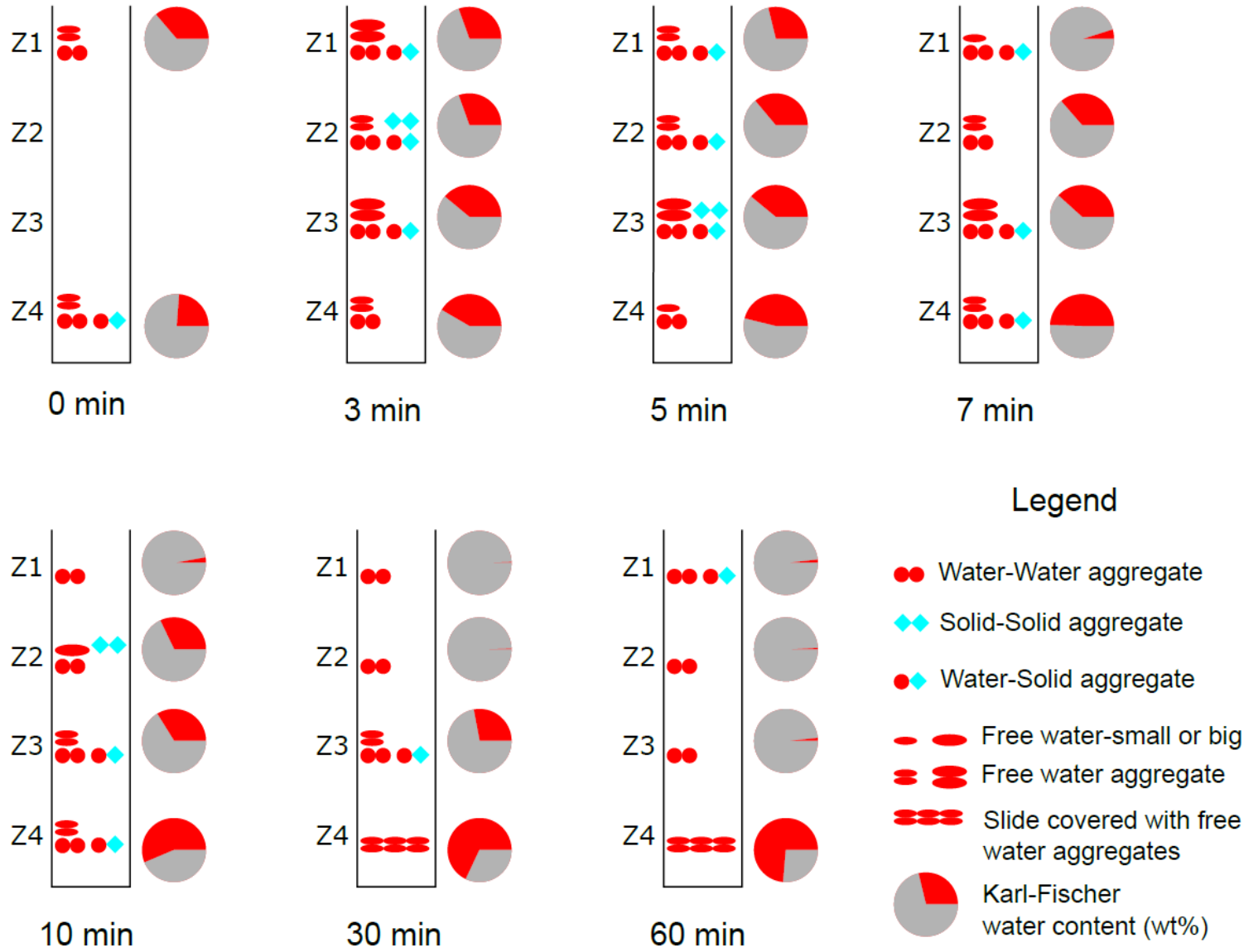
Qualitative image analysis is based on visual observation of different types of clusters seen on individual images over the entire experiment. This analysis was performed using both 10x or 40x magnification lenses. The representative images of different types of aggregates seen on froth images have already been shown in Section 3.1 of Chapter 3.

Figure 4-7 and Figure 4-8 show which type of aggregates [water-water ( $W-W$ ) or water-solid ( $W-S$ )] were observed on microscope images for good ( $FD1$ : high  $J$ , low  $IC$ ) and bad ( $FD4$ : low  $J$ , high  $IC$ ) mixing conditions.  $S-S$  aggregates are rarely seen in either case.  $W-W$  (flocculation) and  $W-S$  aggregates are common. This indicates that solids prefer to settle with water (sweep flocculation) rather than with other solids. It should be noted that clay particles are smaller than 2  $\mu\text{m}$ , which is close to the microscope resolution and hence any aggregation of clay may or may not be observable. Mineral and sand solids are bigger than clays and are readily observable under the microscope.

Water is present in the form of spherical water drops and non-spherical free water. Spherical drops are typically 1 - 10  $\mu\text{m}$  in size and can be readily detected with the 40x lens, whose image frame size is 160  $\mu\text{m} \times 120 \mu\text{m}$ .  $W-W$  aggregates can be present in the form of either spherical flocs or longitudinal chains comprised of spherical drops. Free water has a rigid skin-like interface, coated with biwettable asphaltenes and solids (Jiang et al., 2008), and its size can vary from 20  $\mu\text{m}$  to >1000  $\mu\text{m}$ . Refer to Section 3.1 of Chapter 3 for more details. An image taken with 10x lens is 641  $\mu\text{m} \times 480 \mu\text{m}$ . For the qualitative observations, free water was broadly classified into small or big free water as

shown in Figure 4-7 and Figure 4-8. Big free water can not be fully contained in one 10x image. This is a crude definition as some free water bodies could be smaller or greater than single 10x image. Moreover, some free water bodies can be elongated leading to the wrong categorization. If two or more big free water bodies are seen on microscope slide, it is put into the category of big free water.

As per Figure 4-7 and Figure 4-8, free water aggregates are present in the first 10 min of settling at all sampling heights and they start to disappear by 30 and 60 min of settling. This agrees with the corresponding *KF* observations showing a fast dewatering rate in the first 10 min followed by slow dewatering until 60 min. The scale of the *KF* pie chart shown in both figures is from 0 to 50 wt%. Free water aggregates are much bigger and heavier than individual spherical drops and hence settle faster. The fast dewatering rate in the first 10 min is owed to settling of free water aggregates that have much higher water content volumetrically than individual spherical drops. By 30 and 60 min at the top three sampling heights ( $z_1$ ,  $z_2$  and  $z_3$ ), the microscope slide is primarily covered with dispersed water drops, solids, some flocs and some dispersed free water bodies. The 30 and 60 min sample at top three sampling heights corresponds to low *KF* water content (< 2 wt%). By 30 and 60 min at height  $z_4$ , the microscope slide is fully covered with free water bodies. This observation agrees with the measured high *KF* water content (35 - 40 wt%).



**Figure 4-7:** Qualitative image analysis from beginning (0 min) till the end of settling (60 min) for best mixing conditions (FD1: J+, IC-), indicating the types of species and aggregates, along with Karl-Fischer pie chart for comparison

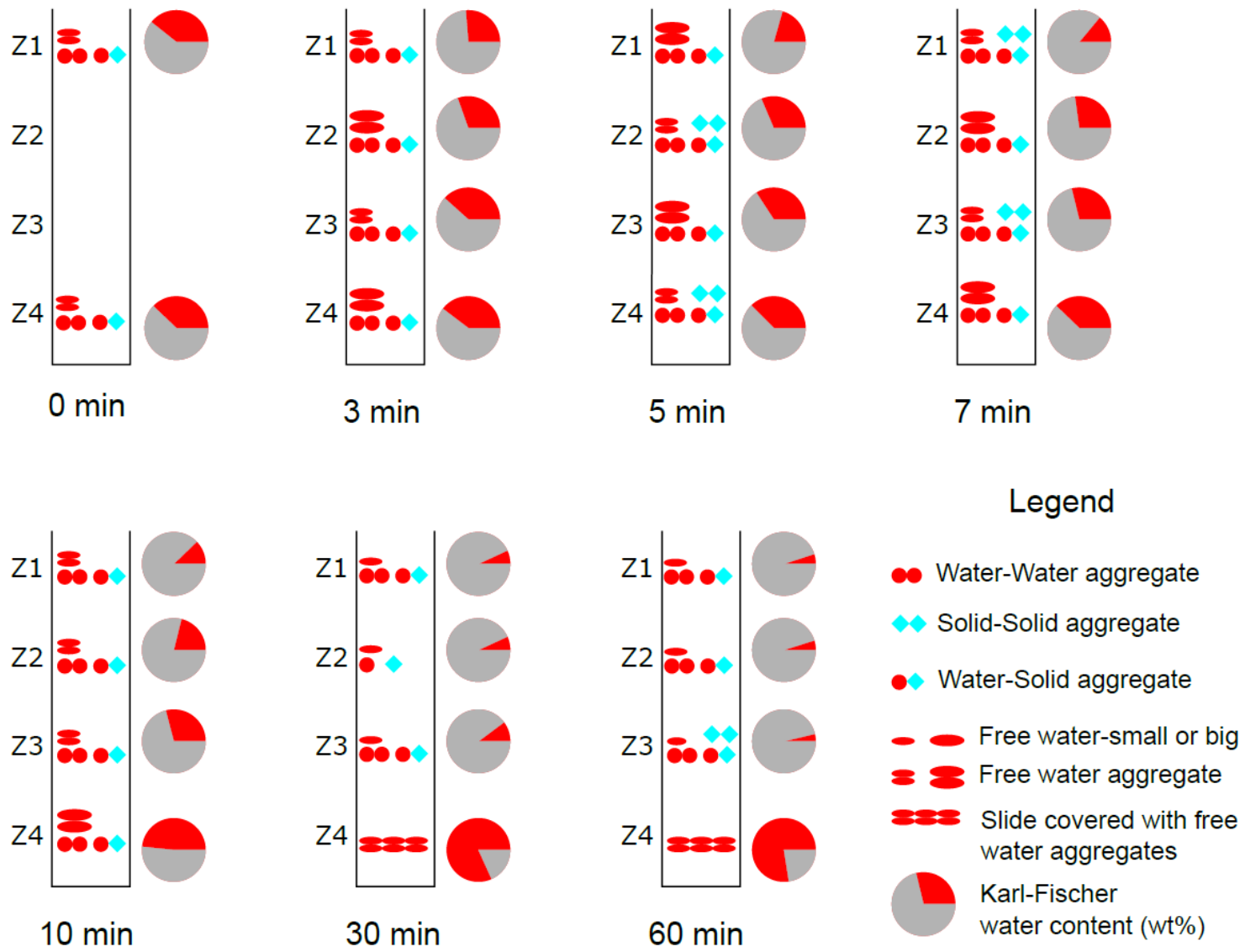


**Figure 4-8:** Qualitative image analysis from beginning (0 min) till the end of settling (60 min) for worst mixing conditions (FD4: J-, IC+), indicating the types of species and aggregates, along with Karl-Fischer pie chart for comparison

The only notable difference between favorable (*FDI*) and poor (*FD4*) mixing runs in Figure 4-7 and Figure 4-8 is that the microscope slide corresponding to the former is more clean and has no free water bodies at 30 and 60 min at the top three sampling heights. Hence, microscope and *KF* data are in qualitative agreement. The settling mechanism (water-water or water-solid) does not differ between the good or bad mixing conditions, but the aggregate formation and settling rates do. This is evident in Figure 4-4 from the slower dewatering rate in *FD4* than *FDI* at height  $z_1$  and  $z_2$ . The final water content at 60 min at *FDI* ( $z_1 = 0.89\%$ ,  $z_2 = 0.41\%$ ) was much lower than for *FD4* ( $z_1 = 2.51\%$ ,  $z_2 = 2.44\%$ ). Poor mixing stalls the efficiency of the demulsifier. The demulsifier needs to solubilize in the bitumen phase and reach the oil-water interface in order for it to be effective. Mixing induces convective transport of demulsifier along with turbulent eddies that are much faster and more efficient than a molecular diffusion process.

How do the images differ between the good (*FDI*) and bad (*FD4*) mixing conditions? Figure 4-9 shows representative images taken at 60 min and height  $z_1$ . Figure 4-9a, corresponding to good mixing conditions, shows a clean slide with few solids. Figure 4-9b, corresponding to bad mixing conditions, shows that water-water aggregates are still present after 60 min of settling. The *KF* water content for samples corresponding to Figure 4-9a and Figure 4-9b was 0.89 % and 2.51 % respectively. Figure 4-10a and Figure 4-10b show the difference between good and bad mixing conditions at height  $z_4$  ( $z/H = 0.82$ ) after 60 min of settling. The free water aggregates with free water bodies are bigger for good mixing than those resulting from bad mixing. At this height ( $z_4$ ) by 60 min, the whole microscope slide ( $22 \times 22$  mm) is typically covered with free water aggregates and solids for both mixing conditions. The *KF* water content of samples corresponding to Figure 4-10a and Figure 4-10b is 36.8 % and 38.8 % respectively. The water content is nearly the same as *KF* instrument has typically less than 10% reproducibility error (0.1 standard deviation/ mean).

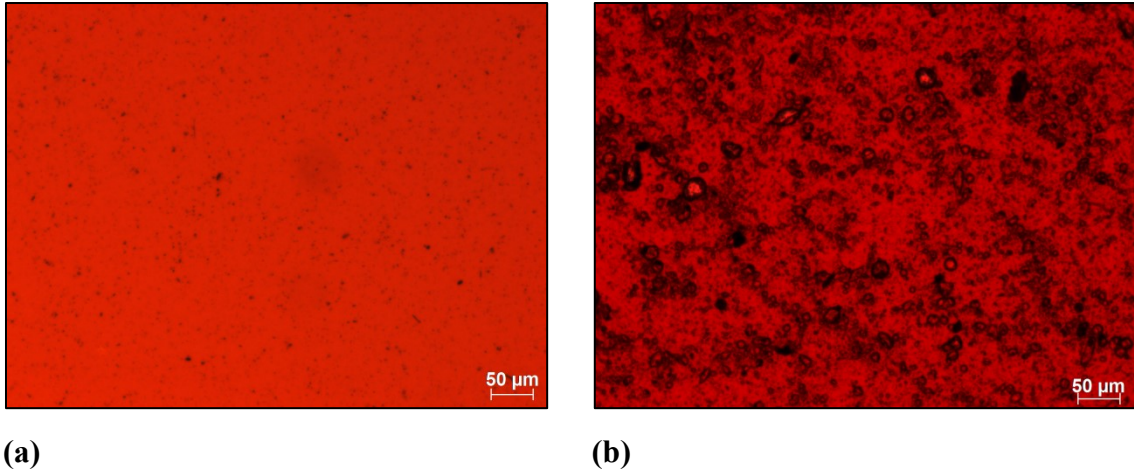


**Figure 4-9:** Representative microscope image at 60 min and height  $z_1$  ( $z/H = 0.23$ ) for (a): good (run *FD1*) and (b): bad (run *FD4*) mixing conditions

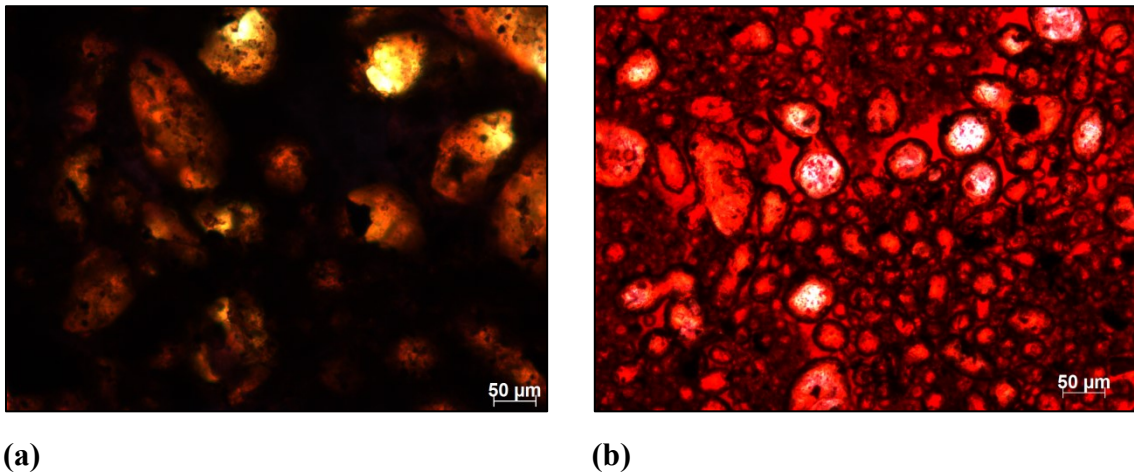


**Figure 4-10:** Representative microscope image at 60 min at height  $z_2$  ( $z/H = 0.82$ ), for (a): good (run *FD1*) and (b): bad (run *FD4*) mixing conditions

There are some challenges associated with drawing meaningful conclusions from microscope observations. First, a drop of sample taken from the same bottle may differ depending on if it is withdrawn from top or bottom liquid layer. This is believed to be due to micro-settling of water and solids within the 1 millilitre of liquid in the sample bottle. To avoid this, the bottle is shaken and a drop of sample is taken from the bottom layer. Second, there is some interaction between aggregates and the microscope slide. The aggregates may get broken or compressed in the limited space between slide and the cover slip. The average froth sample thickness was  $26 \mu\text{m}$  with a standard deviation of  $6.5 \mu\text{m}$  based on measurement of 8 slides, cover slips, and assembled slides. Third,  $W-W$

chains that stretch across the slide have been seen. These chains are believed to be an artifact caused by scratch on a slide (troughs in surface) or incomplete or uneven silanization of the slide.

#### 4.2.2.2 Clustering Image Analysis

Clustering image analysis provides a more quantitative measure of cluster size, number of clusters etc. The reader is referred to Chapter 3 for the input, output and coding details of the clustering algorithm. The analysis is discussed at four levels:

1. Single image (contains aggregates)
2. Single sample (e.g.: all images in a sample, 5 min at height  $z_l$ )
3. Single sampling height (3, 5, 7, 10, 30 and 60 min at height  $z_l$ )
4. Multiple sampling heights and times (e.g.: all samples for single run)

The extensive data analysis presented in this section took 105 working days (5 months) which includes experimental execution, program processing and data analysis for 10 experiments.

#### Relation between $W-W$ and $W-S$ Cluster Size

In the clustering algorithm, the cluster size is defined as the maximum centroid-centroid distance between any two connected objects (water drop or solid) in a cluster. For a single image, we have shown in Figure 3-19 that  $W-S$  and  $W-W$  cluster sizes are of similar order indicating that water and solids settle together. Figure 4-11 illustrates that either  $W-W$  or  $W-S$  cluster size can be higher depending upon whether a water drop is able to find a nearest water or solid. So, the cluster size depends on the spatial location of water and solids. Figure 4-12 shows the  $W-W$  and  $W-S$  cluster size averaged over each image in a sample (e.g.: 5 min at height  $z_l$ ), with a sample containing 18 images. Each data point represents the mean cluster size for that image. Figure 4-12 shows that the relationship between the two variables is close to linear with some deviations. For each image, the Sauter mean ( $D_{32}$ ) cluster size is obtained using the following equation:

$$D32 = \frac{\sum_i n_i d_i^3}{\sum_i n_i d_i^2}$$

(Equation 4-4)

where  $n_i$  is number of clusters of certain size in  $i^{\text{th}}$  bin,  $d_i$  is the cluster size (or max centroid-centroid distance) and  $i$  is number of bins + 1. The mean size can be obtained over an image (containing several clusters) or a sample (containing several images). For all  $D32$  values reported here, the bin size of  $0.1 \mu\text{m}$  (or 2000 bins) was used.

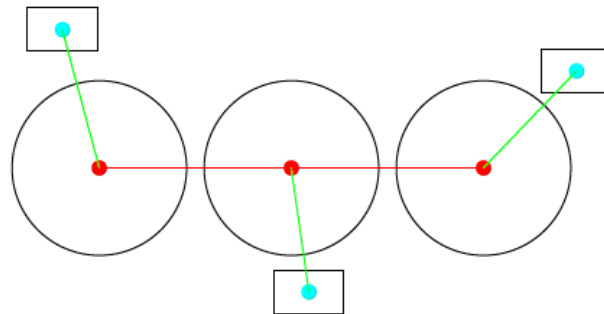


**Figure 4-11:** An illustration of cluster size depending on spatial orientation. Red and blue dots correspond to centroids of water and solid respectively

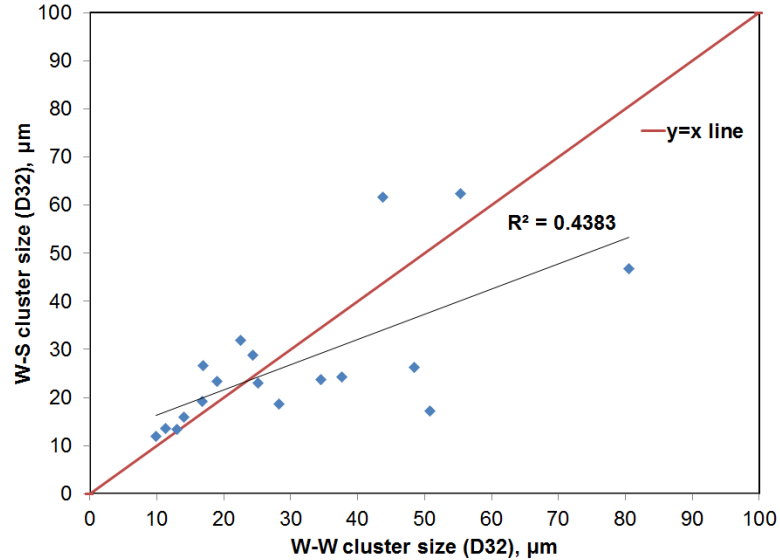


**Figure 4-12:** Comparison between *W-W* and *W-S* Sauter mean (*D32*) cluster size for all images in a single sample (e.g.: 3 min at height  $z_l$ ). Each data point corresponds to the mean cluster size for that image.

*D32* was chosen to characterize the cluster size distribution because it is a measure of volume per unit surface area which is important for settling. Several variables such as median, mean and max could be used to define this distribution. The median is influenced by a large number of small clusters (ASTM Standard E799-03, 2015) and the maximum is affected by outliers. The number mean diameter ( $D_{10} = \frac{\sum_i n_i d_i^1}{\sum_i n_i}$ ) gives equal weighting to small and big clusters whereas big clusters settle faster and have more volumetric water content. Therefore, the bigger cluster size needs to be given more weight. The physics of Stokes law at steady state was investigated (Equation 4-5). Form drag (due to pressure) is influenced by the particle projected area and hence the projected diameter ( $d_p$ ) is important (Leith, 1987). Friction drag (fluid friction) is dependent on fluid-particle contact/surface area ( $d_s^2$ ) (Leith, 1987). The gravity and buoyancy terms are dependent on particle volume ( $d_v^3$ ). Madhav and Chhabra (1995) stated that for non-spherical objects, both a volume based approach and a volume-surface area-projected area approach yield acceptable drag coefficient correlations. It should be noted that higher floc porosity would increase the fluid friction surface area and the floc density is also important for

determining the settling rate. For  $Re < 0.1$  (Stokes regime), the settling equation (Leith, 1987) for a single spherical particle in fluid can be written as

gravitational force  $\downarrow$  = buoyancy force  $\uparrow$  + friction drag  $\uparrow$  + form drag  $\uparrow$

$$\left(\frac{\pi}{6} d_v^3\right) \rho_d g = \left(\frac{\pi}{6} d_v^3\right) \rho_c g + 2\pi\mu_c V_t d_s + \pi\mu_c V_t d_p$$

(Equation 4-5)

where  $\rho_d$  and  $\rho_c$  are the densities of the settling particle/ drop and the fluid (or continuous phase) respectively,  $\mu_c$  is the fluid viscosity, and  $V_t$  is the particle terminal settling velocity. (Equation 4-5 can be obtained by substituting  $C_d$  = laminar drag coefficient =  $\frac{24}{Re} = \frac{24 \mu_c}{d V_t \rho_c}$  into the following general equation

$$\left(\frac{\pi}{6} d_v^3\right) \rho_d g = \left(\frac{\pi}{6} d_v^3\right) \rho_c g + C_d \left(\frac{1}{2} \rho V_t^2\right) \left(\frac{\pi}{4} d^2\right)$$

(Equation 4-6)

The relationship between the *W-W* and *W-S* cluster size is now considered at single height as shown in Figure 4-13. Again, the *W-S* and *W-W* cluster size trend with respect to settling time is similar. The *S-S* cluster size is smaller than the *W-W* cluster size and does not change significantly throughout the settling time.

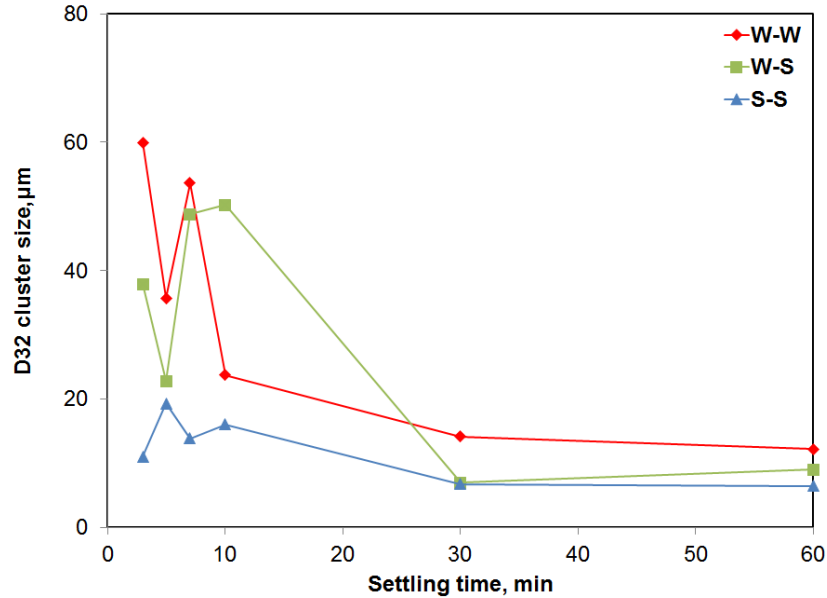


**Figure 4-13:** Mean cluster size as a function of settling time at a single sampling height

If the  $W-W$  and  $W-S$  cluster sizes shown in Figure 4-13 are plotted on horizontal and vertical axis respectively, the resulting linear  $R^2$  value would correspond to one sampling height ( $z_i$ ) in a run as shown by one data point in Figure 4-14. Figure 4-14 shows the strength of correlation ( $R^2$  value) between  $W-W$  and  $W-S$  cluster size when considered at multiple heights for all 10 experiments. Recall that samples were taken at 0, 3, 5, 7, 10, 30 and 60 min for 4 sampling heights ( $z_1 - z_4$ ) in the factorial design runs and at 2 sampling heights ( $z_1$  and  $z_4$ ) in other runs. Thus, there are less data points available for heights  $z_2$  and  $z_3$ . There is a weak correlation at height  $z_1$  but the correlation is moderate to strong at heights  $z_2$ ,  $z_3$  and  $z_4$ . 2 out of 28 data points have an  $R^2$  value less than 0.2 and most data points lie above an  $R^2$  value of 0.5 shown as grey line.  $R^2$  value is sensitive to outliers; hence, there is at least a moderate correlation between the two variables. A big  $W-W$  cluster size indicates that water drops tend to flocculate with each other. Because the  $W-S$  and  $W-W$  cluster sizes are similar, we conclude that water drops also sweep flocculate nearby solids while they settle. This phenomenon is also called differential settling as the faster moving big clusters will sweep small solids. Thus, dewatering by flocculation also promotes the removal of hydrophilic solids.

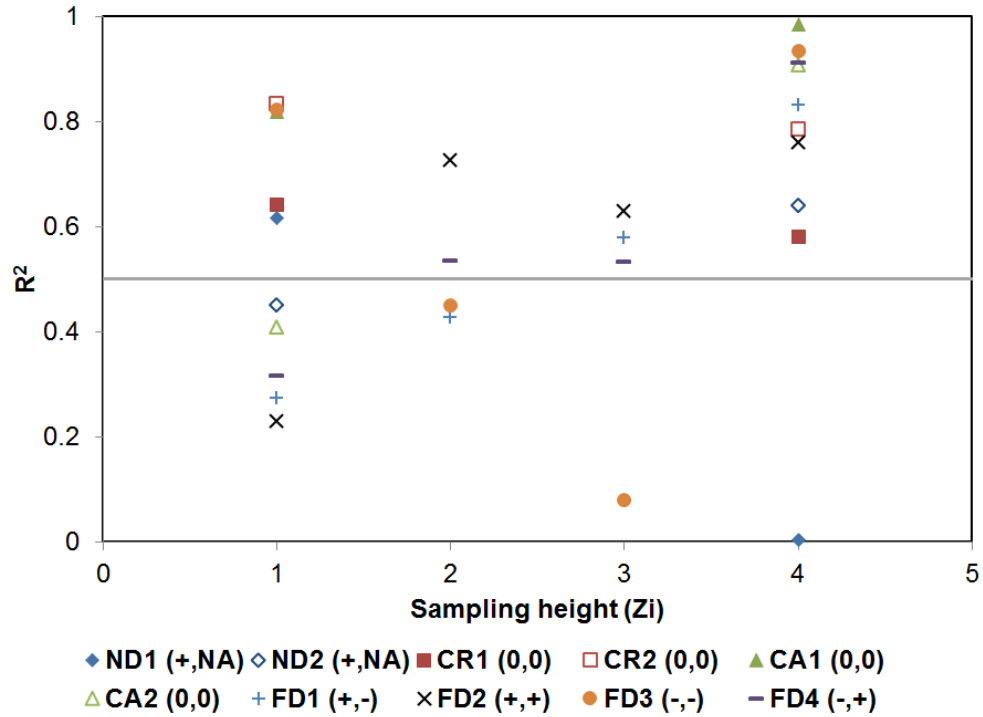


**Figure 4-14:** Correlation coefficient ( $R^2$ ) between  $W$ - $W$  and  $W$ - $S$  Sauter mean ( $D_{32}$ ) cluster size at multiple sampling heights and mixing conditions. Runs:  $FD1$  and  $FD4$  are at the best and worst mixing conditions respectively.

### Relation between $W$ - $W$ and $S$ - $S$ Cluster Size

$S$ - $S$  clusters are generally small in comparison to  $W$ - $W$  clusters. Small  $S$ - $S$  clusters are detected because the clustering minimum threshold distance for cluster detection is set at  $3 \mu\text{m}$  (Equation 3-8). The single image example for  $S$ - $S$  clusters has already been discussed in Chapter 3. Figure 4-15 compares  $S$ - $S$  and  $W$ - $W$  cluster sizes at single sample level. This sample is the same as one for which  $W$ - $W$  and  $W$ - $S$  data was shown in Figure 4-12. There seems to be no correlation between the two variables at this level. Figure 4-16 compares these two variables at multiple sampling heights. At all levels, it seems that there is no correlation between the two variables. Most of the data points have an  $R^2$  value less than 0.5, indicating a weak correlation.  $R^2$  is sensitive to outliers and hence there is a lot of scatter in its values.

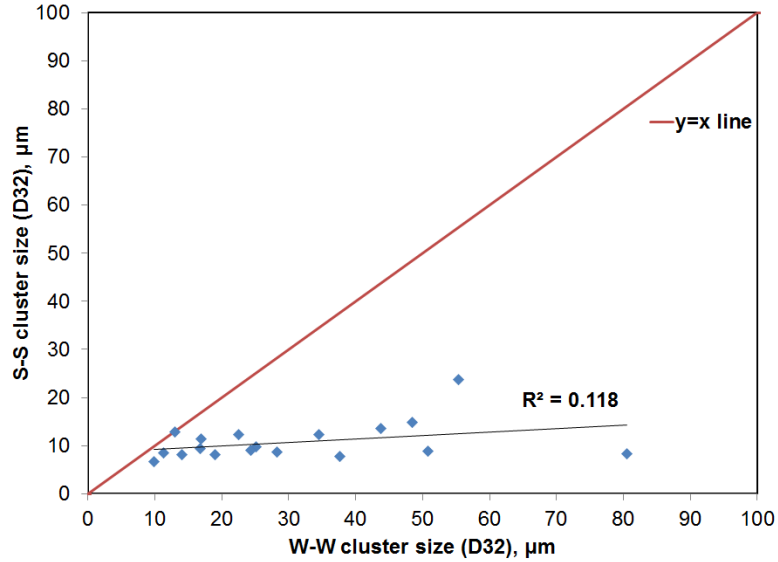


**Figure 4-15:** Comparison between *W-W* and *S-S* Sauter mean (*D32*) cluster size for all images in a single sample (e.g.: 3 min at height  $z_I$ ). Each data point corresponds to mean cluster size for that image.

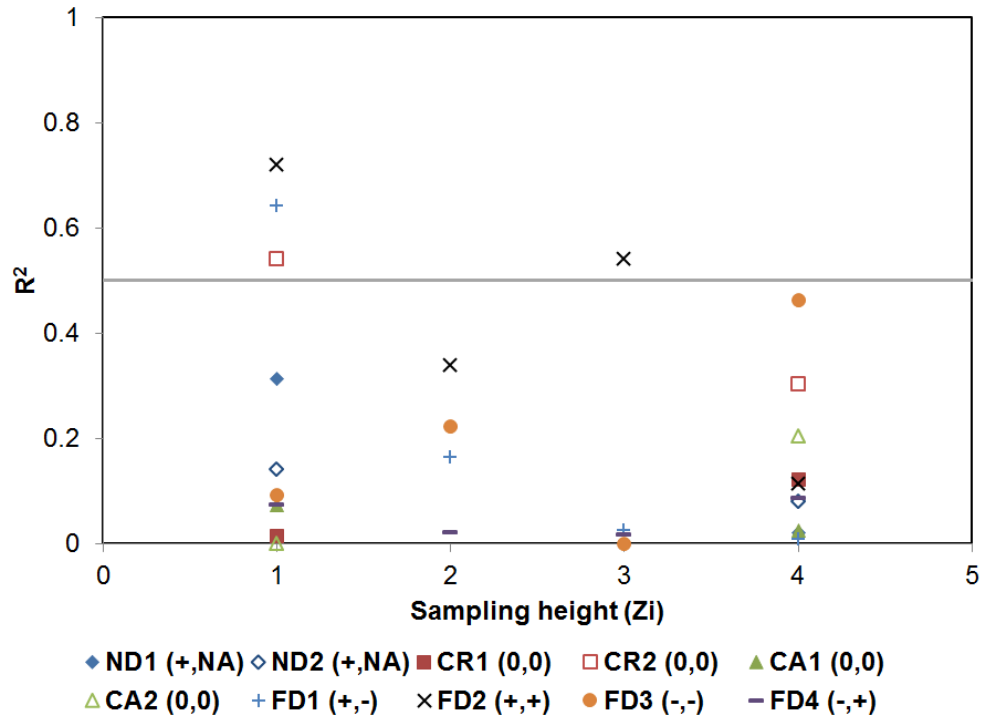


**Figure 4-16:** Correlation coefficient ( $R^2$ ) between *W-W* and *S-S* Sauter mean (*D32*) cluster size at multiple sampling heights and mixing conditions. Runs: *FD1* and *FD4* are best and worst mixing conditions respectively.

From careful observation of Figure 4-13, it can be seen that the *S-S* cluster size seems to track *W-W* cluster size for few data points. This was attributed to one of the two reasons. First, that the small water drops ( $\sim 2 \mu\text{m}$ ) are detected as solids as illustrated with example in Figure 4-17 and second, that over-segmented (due to their non-uniform shape) edges of free water get detected as solids. Both scenarios could create a false conclusion that there is *S-S* clustering. Thus, there is insufficient evidence for *S-S* clustering. It should be noted that objects below 20 pixels ( $2.3 \mu\text{m}$ ) are rejected before clustering analysis to reduce data noise. Clays are smaller than  $2 \mu\text{m}$  which is close to the microscope resolution. Kaolinite clay which is predominant clay type in oil sands is known to aggregate but these structures are in the sub-micron range (Gupta et al., 2011). Demulsifiers that enhance clustering of clays and minerals with each other (*S-S* clustering) and with other interfacial species such as asphaltenes and naphthenic acids should be synthesized. Once the interface is clean, *W-W* flocculation and coalescence will be enhanced because of removal of steric barrier between water drops.

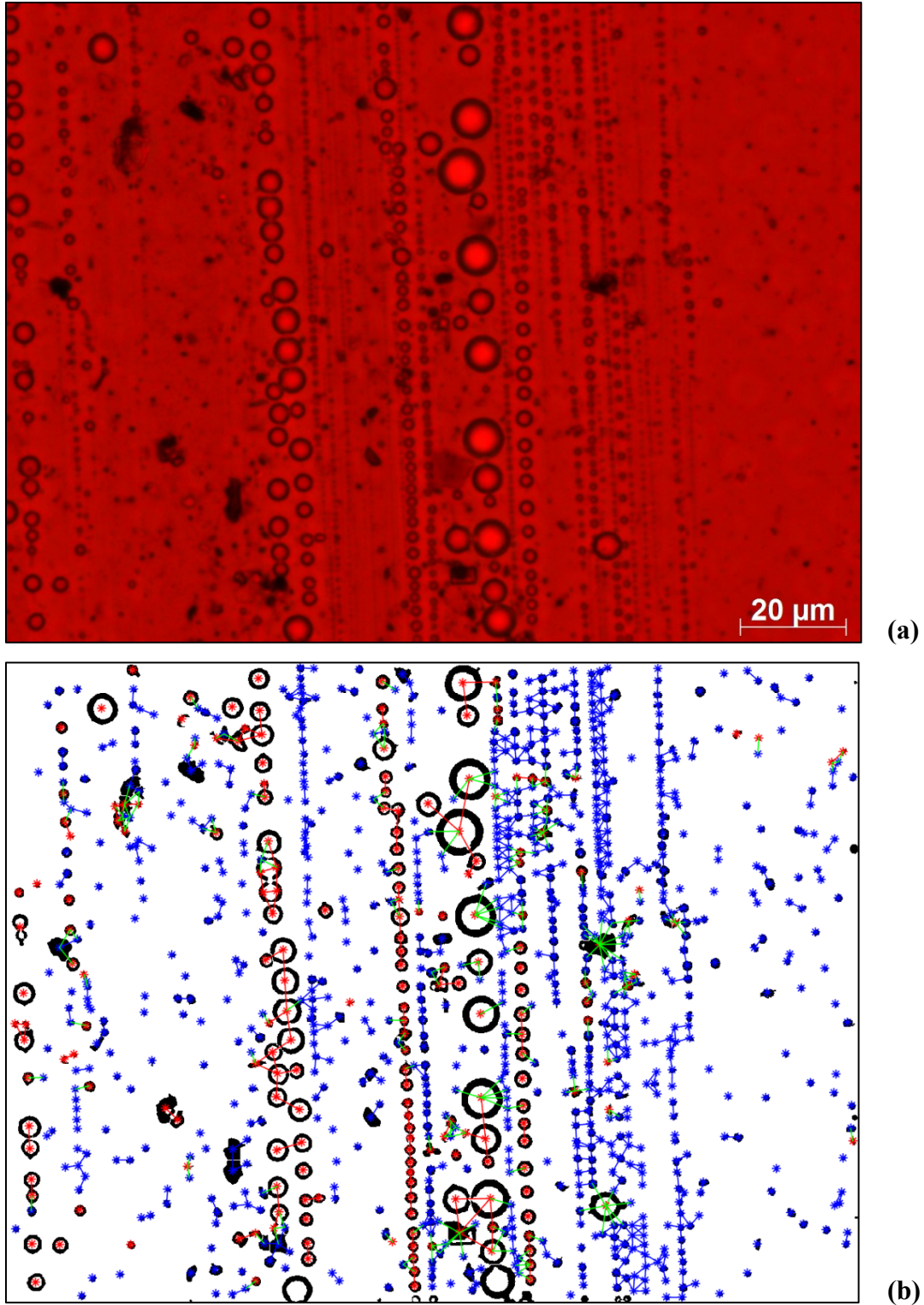


**Figure 4-17:** Microscope image showing small water drops ( $\sim 2 \mu\text{m}$ ) being detected as solids (blue centroids). (a): Original color image, (b): Same image after clustering algorithm

## Relationship between Karl-Fisher Data and Clustering Analysis

An effort was made to test whether there is a correlation between the *KF* water content and some variable in the clustering analysis. *W-S* cluster size follows *W-W* cluster size and *S-S* cluster size does not change with respect to settling time. Several variables such as mean *W-W* cluster size as shown in Figure 4-18 and mean number of drops/objects per *W-W* cluster were tested. There is a weak to no correlation between these variables. Small *W-W* cluster sizes at certain settling times and sampling heights could be due to two scenarios:

1. Good scenario: Clusters grew in size, settled and only small clusters were left.
2. Bad scenario: Clusters remained small, did not grow in size and did not settle

In order to account for this, a new variable, *W-W mean cluster size (D32) times total number of W-W clusters per number of images* in the sample, was introduced. Ideally, the *KF* water content should be equivalent to  $\sum \text{number of drops} \times \text{diameter of drops}^3$ . The cluster size was not cubed to prevent magnification of errors. This new variable considers both the number and size of clusters but still correlation was weak to moderate as shown in Figure 4-19. Following are some reasons that *KF* and clustering analysis could not be correlated:

1. Free water cannot be analyzed by clustering analysis because it either gets thrown to the background (during image thresholding) or it is over-segmented during watershed segmentation due to its uneven shape. Moreover, clustering analysis is performed on images obtained using the 40x lens and free water is generally much bigger than 40x or 10x image frame. In qualitative analysis, we found that free water contains a significant quantity of water in comparison to small drops.
2. Loner or two connected drops are not considered in the clustering algorithm. Three or more connected points are considered as clusters. This would introduce small errors as small drops do not have significant water volume.
3. Multiple centroids are detected for drops that are over-segmented which introduces errors in the number of objects per cluster and cluster size.

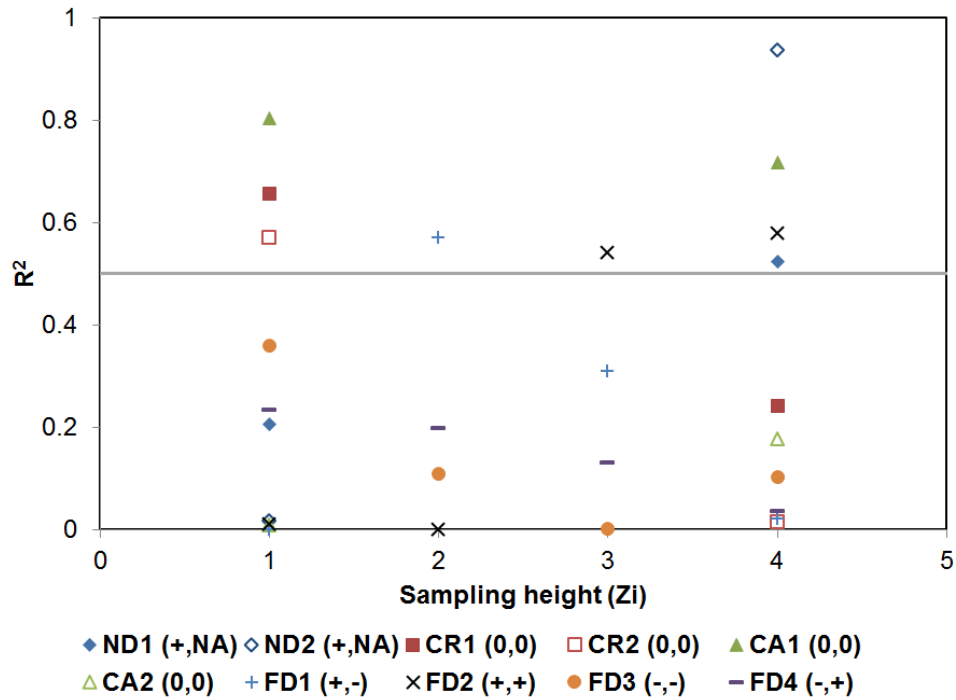


**Figure 4-18:** Correlation coefficient ( $R^2$ ) between  $KF$  water content (wt%) and  $W-W$  cluster size ( $D_{32}$ ) at multiple sampling heights and mixing conditions

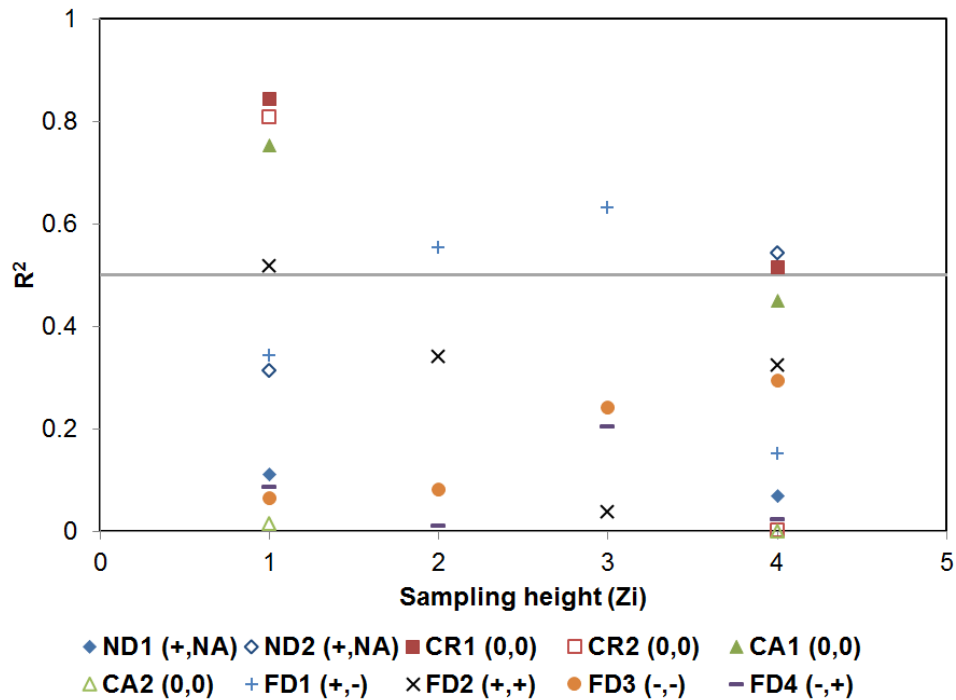


**Figure 4-19:** Correlation coefficient ( $R^2$ ) between  $KF$  water content (wt%) and [W-W cluster size ( $D_{32}$ ) times total number of  $W-W$  clusters per images in a sample] at multiple sampling heights and mixing conditions.

### 4.2.2.3 Drop Size Distribution and Coalescence

Up to this point, we have focussed on flocculation and sweep flocculation as the settling mechanism. This section aims to further probe the data for signs of coalescence. As the froth images were divided into two separate images: one containing water drops and the other containing solids, the water drop size distribution could also be easily obtained. Because the parent image was watershed segmented, flocs of water drops were broken up into individual drops. This turned out to be an advantage because the effect of flocculation was removed so that coalescence could be isolated and statistically determined.

Figure 4-20 shows the drop size distribution (*DSD*) at the first sampling height ( $z_1$ ) for favorable mixing conditions (*FDI*). A shift in the peak of the distribution towards the right (bigger drops) would have been an indication of strong coalescence. But there is no significant shift, except at 10 and 30 min of settling to 9  $\mu\text{m}$  before it returns to its original value (8  $\mu\text{m}$ ). This indicates that drops coalesce slowly from 10 to 30 min, and bigger drops settle out, resulting in a left shift of the distribution at 60 min. The drop in peak height is an indication of dewatering, validated by the *KF* trend corresponding to the samples in run *FDI* at height  $z_1$  in Figure 4-4. The drop count (number of drops) is factored towards bigger drops (more volume) and number of images. The number of images captured for a sample is typically 30-50 and depends on the amount of clusters (flocs, chains) on a slide and the operator. One operator captured all the images for samples shown in Figure 4-20. Normalizing the number of drops by the number of images ensured that the trends from different samples could be justifiably compared. The square factoring ( $d^2$ ) was chosen instead of cube factoring ( $d^3$ ) in Figure 4-20 and Figure 4-21 so that if there is an error in determining circumscribed radius of water drops, the error magnification would be less in case of square factoring.

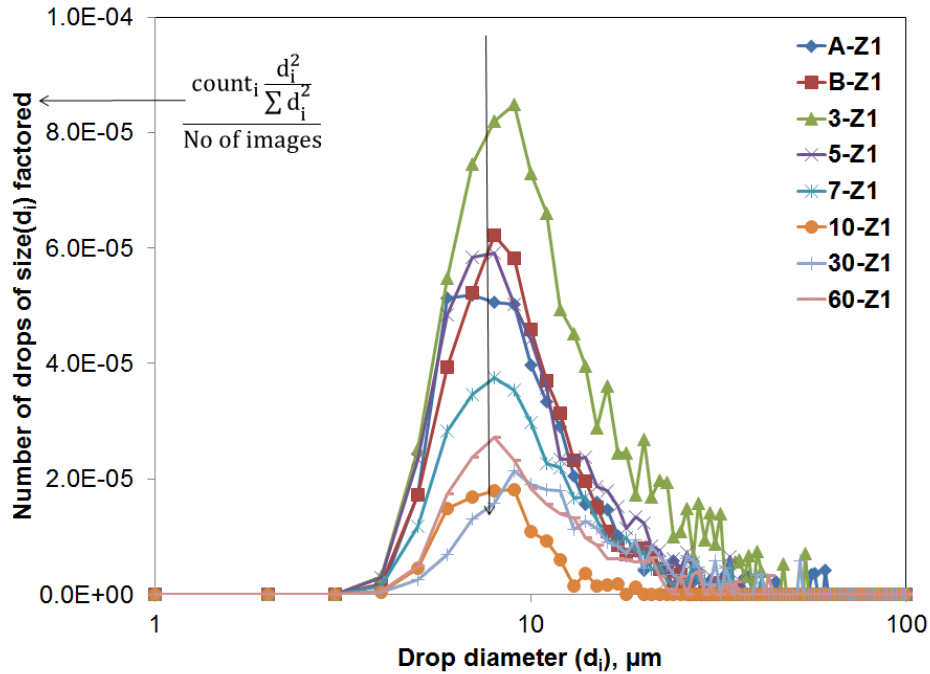


**Figure 4-20:** Water drop size distribution of all samples at height  $z_I$  for naphtha blending ( $A-ZI$ ), demulsifier dispersion ( $B-ZI$ ) and settling samples (3 min to 60 min) at favorable mixing conditions ( $FDI$ : high  $J$ , low  $IC$ )

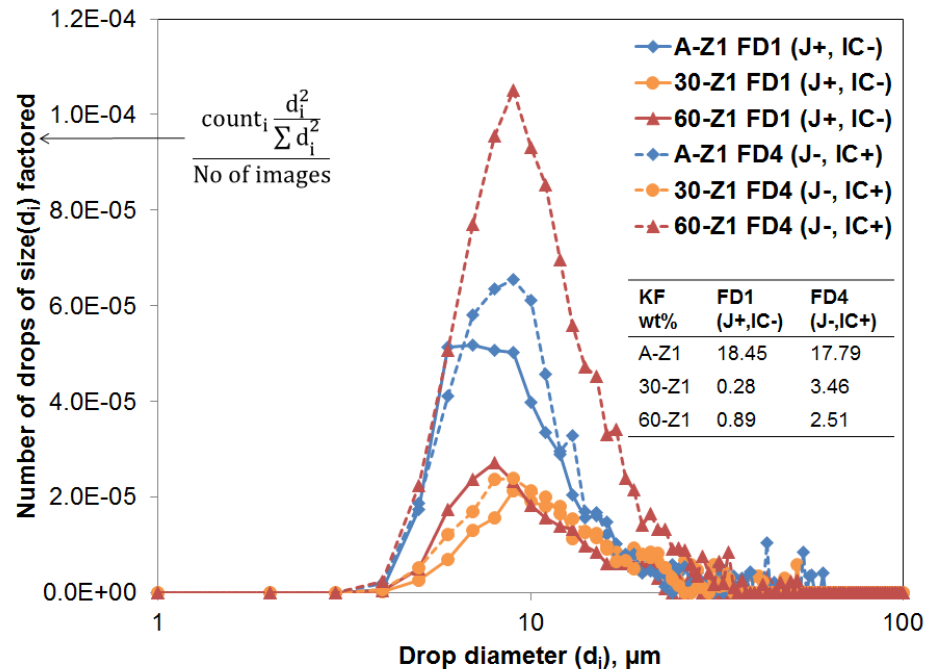


**Figure 4-21:** Comparison of water drop size distribution between  $FDI$  (high  $J$ , low  $IC$ ) and  $FD4$  (low  $J$ , high  $IC$ ) at height  $z_I$  for naphtha blending ( $A-ZI$ ) and end of settling (30 and 60 min) samples

We needed to find out whether the settling mechanism was dependent on mixing conditions ( $J$  and  $IC$ ). There is a subtle difference in  $DSD$  between favorable ( $FD1$ : high  $J$ , low  $IC$ ) and poor ( $FD3$ : low  $J$ , high  $IC$ ) mixing conditions as shown in Figure 4-21. The figure shows that at favorable mixing condition, the distribution does not change significantly between 30 and 60 min. However at the poor mixing conditions, settling is still in progress. One might argue that for poor mixing conditions, the distribution for 60 min is higher than 30 min although  $KF$  indicates lower water content for the former. This distribution captures water drops smaller than 200  $\mu\text{m}$  (diagonal length of image from 40x lens). However, free water has much bigger scale ( $>1000 \mu\text{m}$ ) that could not be imaged. Therefore, we are looking at part of the size distribution. Free water accounts for significant water volume and hence affects the final  $KF$  reading. For all experiments, there was no significant right peak shift. Hence, coalescence does happen but it is a slow phenomenon and it happens in concert with sedimentation.

Some coalescence activity has been noticed on the microscope images. Coalescence is a real-time phenomenon involving the merging of two drops into a single big drop. The Image acquisition of one sample (e.g.: 3 min at height  $z_1$ ) typically takes 45 - 60 min depending on the operator. No live coalescence was observed in any sample for all 10 runs during the image acquisition period. This suggests that coalescence did not occur at all. The slow rate of coalescence could be due to higher bitumen viscosity at room temperature (during imaging) in comparison to 80°C in CIST and industrial operations. To validate the existence of coalescence, the images were taken at the same location over several hours. Figure 4-22 and Figure 4-23 show that coalescence can occur over a period of hours or even days. Figure 4-22 corresponds to a silanized glass slide with an unsilanized cover slip which is our normal protocol. It was questioned that unsilanized cover slip might have aided in coalescence of free water. Figure 4-23 corresponds to another sample with both glass slide and cover slip silanized. Coalescence was again observed. It is interesting that some free water interfaces did not break while others did.

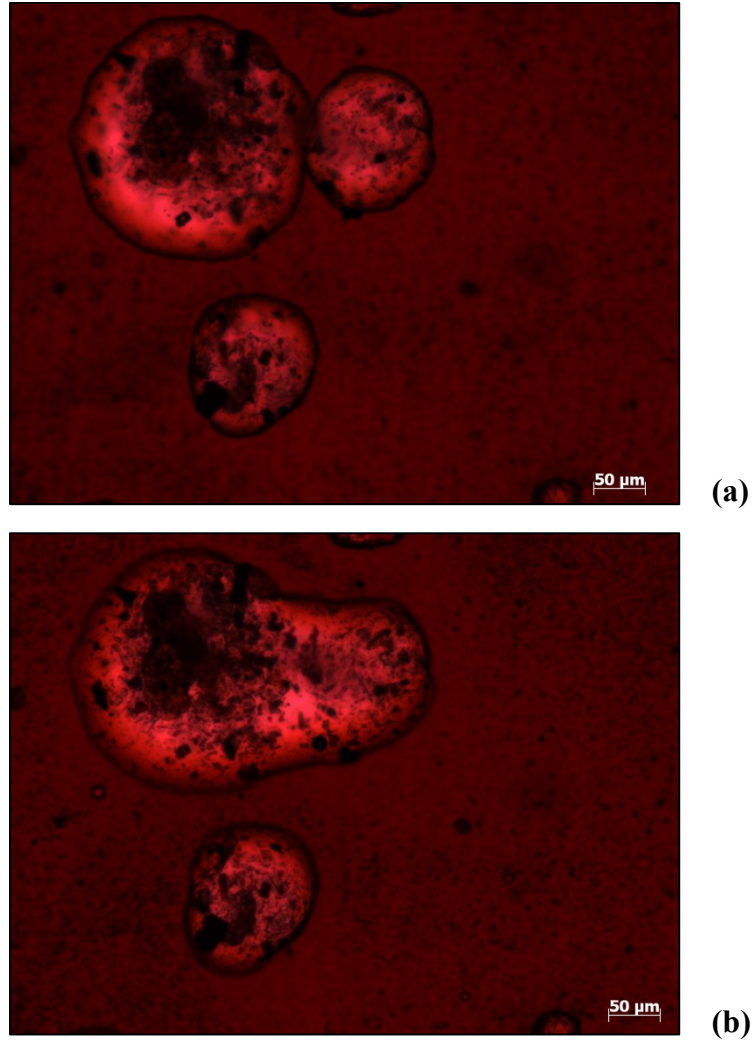


**Figure 4-22:** Coalescence of free water in bitumen froth is a slow process, (a): image taken at time = 0 hr, (b): image taken at same location at time = 16 hr.

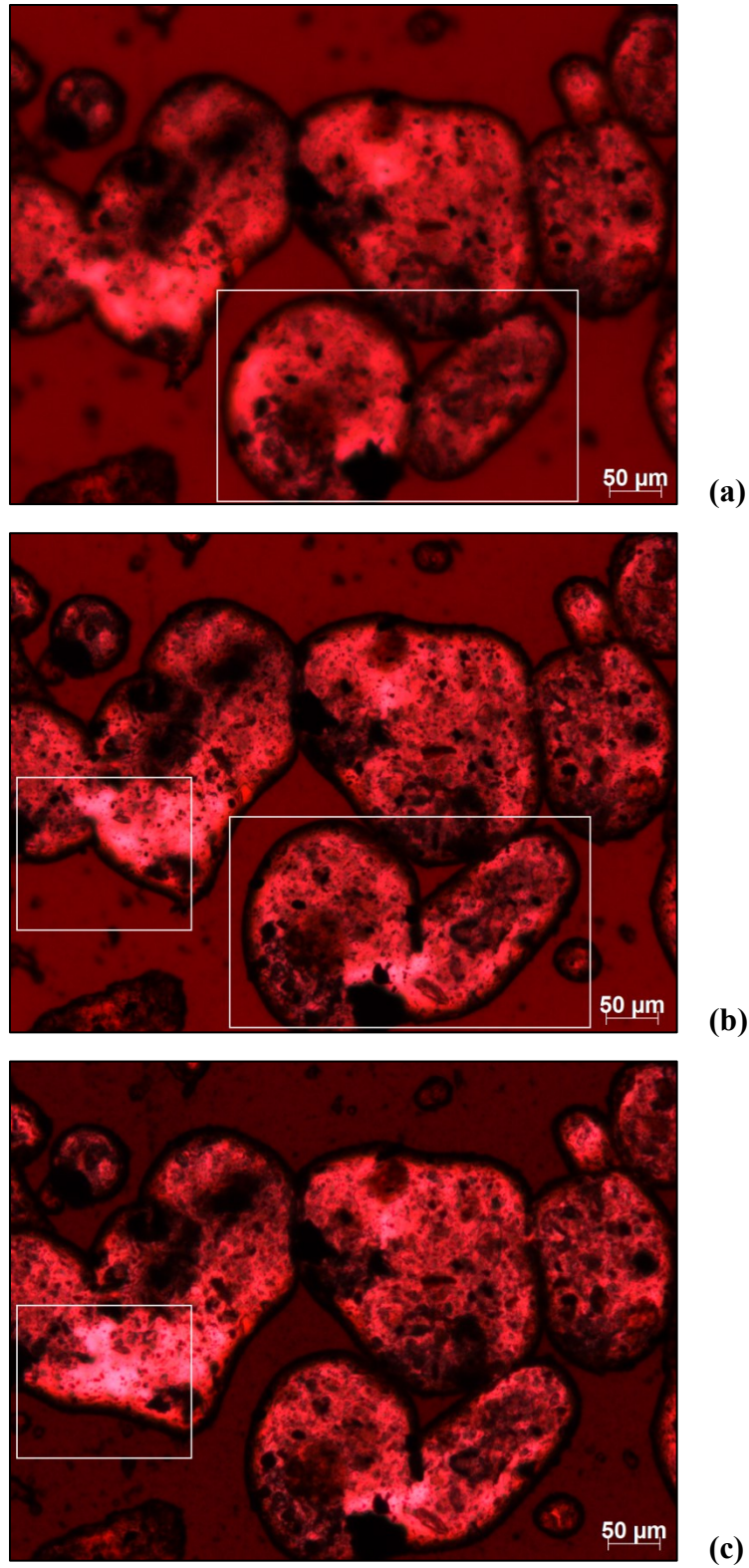


**Figure 4-23:** Coalescence of free water in bitumen froth is a slow process, image taken at same location at (a): time = 0 hr, (b): time = 1 hr, (c): time = 17 hr. Some interfaces did not break for coalescence to happen.

We did not spend much time on understanding the coalescence with respect to variables such as sampling height, settling times and mixing conditions. Time lapse imaging should be done to gather more evidence on this mechanism. Demulsifiers can promote flocculation (water drop bridging) or coalescence depending upon their properties (Czarnecki et al., 2007). Recent evidence indicates that coalescence is a slower phenomenon in comparison to flocculation for water-in-diluted bitumen using ethyl cellulose demulsifier (Chen et al., 2015). “Flocculation-assisted-coalescence” has also been suggested (Feng et al., 2009). Free water in bitumen froth has been known to coalesce and form a separate layer under static conditions without demulsifier and solvent addition (Neiman et al., 1999).

### 4.2.3 Circulation Pattern Run Results

Let us go back and check if the impeller circulation pattern (radial or axial) matters. The *KF* results for these experiments, done at  $X_I = 0$  and  $X_{IC} = 0$ , are shown in Figure 4-24. These runs also provide a measure of the repeatability of the experiment, feed material and operator. Runs: *CA1* and *CA2*, performed with A310 impellers and run: *CR2*, performed with Rushton impellers, have similar and fast settling rates. The settling rate for these three runs is similar to the best mixing condition run: *FDI* shown in Figure 4-4. However, run: *CRI*, conducted with Rushton impellers, has slower settling rate as shown in Figure 4-24. The different dewatering rate in this run could be due to froth can variability (different initial water/ solid content and nature of the solids). The final water content (60 min) at height  $z_I$  for the Rushton repeat runs (0.37 wt%, 0.27 wt%) was less than that of A310 repeat runs (0.84 wt%, 0.56 wt%). But, this difference is quite small in comparison to the difference between good (0.89 % in *FDI*) and bad mixing (2.51 % in *FD4*) runs. So, the effect of flow pattern was not significant.

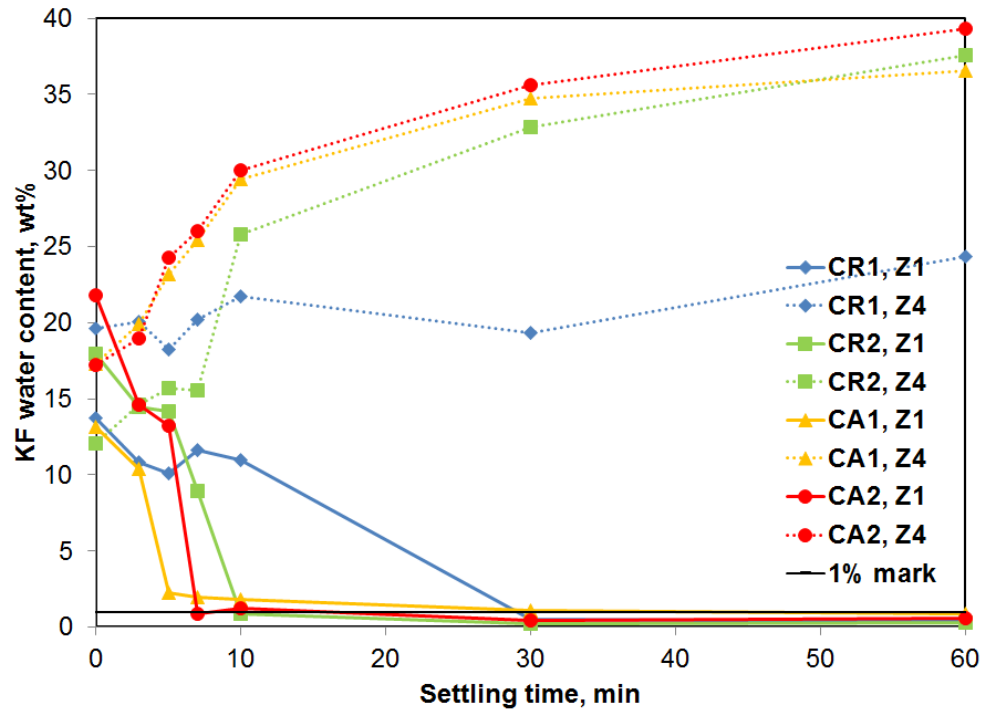


**Figure 4-24:** Water content (wt%) as a function of settling time at two sampling heights ( $z_1$  and  $z_4$ ) for circulation pattern runs: *CA1* and *CA2* with A310 impellers and runs: *CR1* and *CR2* with Rushton impellers (*RT*). For both impellers, same mid-level  $J$  and  $IC$  were used.

We will use three other methods: qualitative analysis, clustering analysis and drop size distribution as discussed in Section 4.2.2 to consider the effect of circulation pattern. Figure 4-25 presents qualitative image analysis for all four runs at 10 min and height  $z_1$ . Figure 4-25a (representative of sample in *CR1*), has lot more water and solids in comparison to Figure 4-25b (*CR2*), Figure 4-25c (*CA1*) and Figure 4-25d (*CA2*). The corresponding *KF* water content for these samples from *CR1*, *CR2*, *CA1* and *CA2* are 11 %, 0.85 %, 1.8 % and 1.2 % respectively. Note that these are images taken from 10x magnification lens, which presents a bird's eye view of the slide activity and is good for qualitative analysis. It seems that run: *CR1* is an outlier and clusters got trapped in this run which resulted in slow settling rate as shown in Figure 4-24.

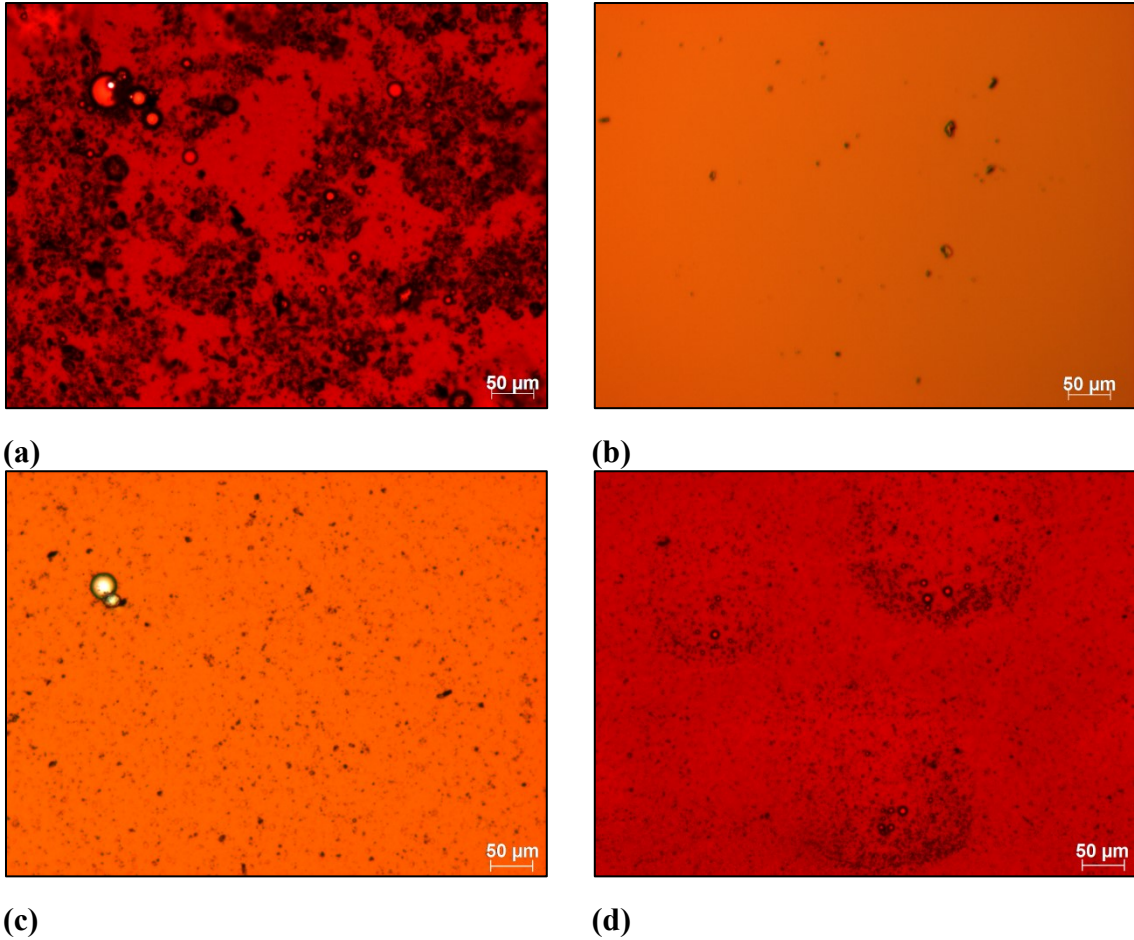


**Figure 4-25:** Representative microscope image at 10 min and height  $z_1$  for (a): *CR1* run, (b): *CR2* run, (c): *CA1* run and (d): *CA2* run. All runs were conducted at same mixing conditions.

Clustering image analysis is considered next at height  $z_1$  for four circulation pattern runs. Figure 4-26 shows that the clusters grow in first 10 minutes, which settle out and small clusters are left behind. Cluster size for *CR1* was smaller than other three runs which explain the slow settling rate in Figure 4-24 for this run in comparison to 3 other runs. Again, run: *CR1* seems to be an outlier because clusters did not grow in this run. Spicer et al. (1996) studied the effect of impeller flow pattern on flocculation of polystyrene beads in a stirred tank. He found that for same  $\varepsilon_{avg}$  (dissipation over tank volume), Rushton impellers gave bigger steady state flocs than hydrofoils (similar to A310) impellers but took longer to reach steady state. In our study, we kept  $\varepsilon_{imp}$  (dissipation over impeller volume) same as shown in Table 4-4. Using  $\frac{\varepsilon_{imp}}{\varepsilon_{avg}}$  ratios

(Machado and Kresta, 2015), Rushton impellers gave bigger flocs as the dissipation was higher ( $\epsilon_{imp RT} = 2 \times \epsilon_{imp A310}$ ) for Spicer's study. Hence, these results are not directly applicable in this study.

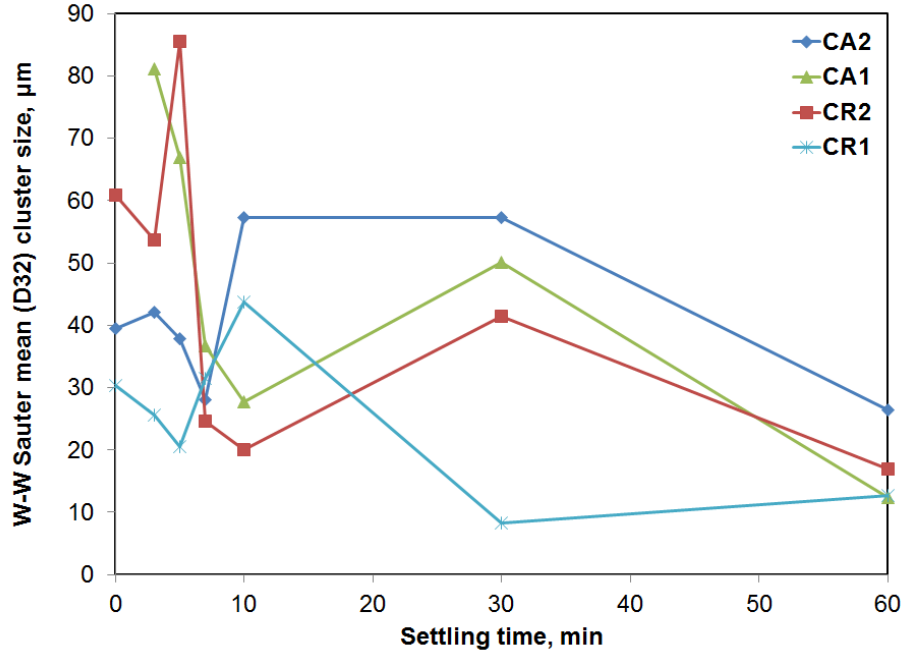


**Figure 4-26:** Mean cluster size as a function of settling time at height  $z_l$  for circulation pattern runs conducted at same mixing conditions ( $J$  and  $IC$ )

The water drop size distribution is considered next at height  $z_l$ . Figure 4-27 shows the drop size distribution for two Rushton runs. The distribution seems repeatable at the end of naphtha blending, 10 min and 30 min into settling unlike the  $KF$  data. Run CR1 had slow settling rate in comparison to run CR2 as per Figure 4-24. Figure 4-28 shows the drop size distribution for the two A310 runs which is not repeatable unlike  $KF$  data shown in Figure 4-24. This anomaly could be due to two reasons: one that we are looking at sub-distribution (free water is not considered which is generally bigger than 40x image frame used to develop this distribution) and second that watershed segmentation might have altered the distribution through over-segmentation. It is interesting that in Rushton runs, there is a significant right shift in comparison to A310 runs which could be an indication of coalescence enhanced by radial flow pattern.

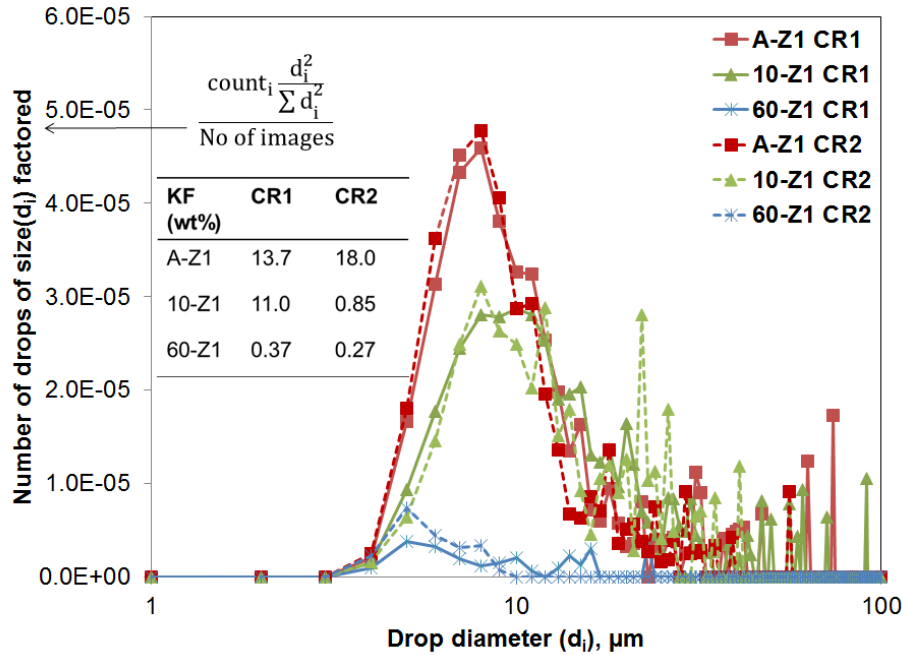


**Figure 4-27:** Comparison of drop size distribution between Rushton runs (*CR1* and *CR2*) at height  $z_1$  for naphtha blending (A-Z1), 10 min and 60 min of settling

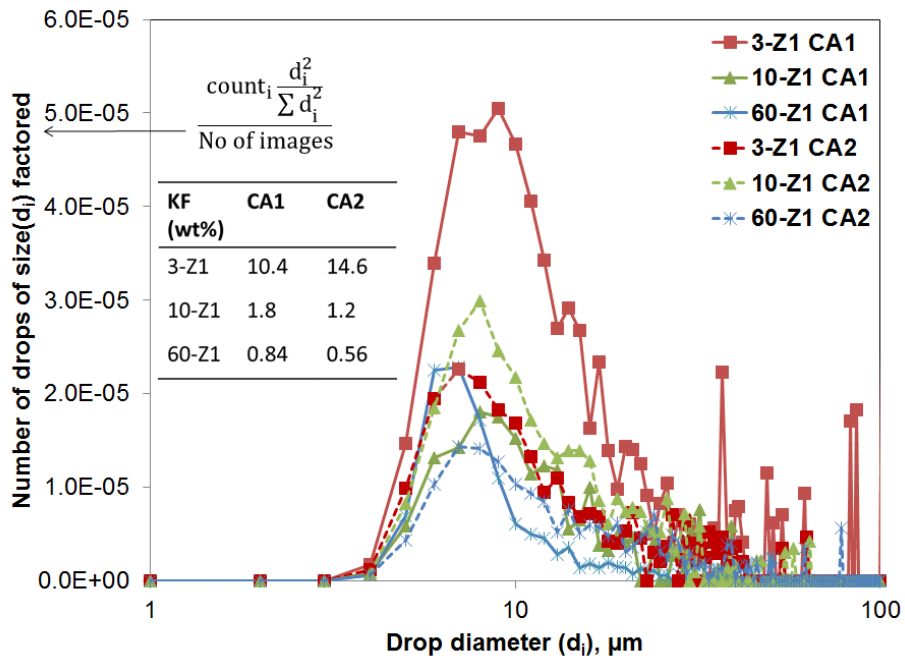


**Figure 4-28:** Comparison of drop size distribution between A310 runs (*CA1* and *CA2*) at height  $z_1$  for 3, 10 and 60 min of settling

*OWS* solid and water concentration results along with previous analysis is summarized in Table 4-7. Both *OWS* water and *OWS* solid concentration for Rushton runs is less than that of A310 runs. The *OWS* analysis overestimates the water content in comparison with *KF* analysis if water soluble organic compounds are present (Laplante, 2011; Smets et al., 2011). Considering all results shown in Table 4-7, Rushton impellers were slightly better than A310 impellers but the effect of flow pattern was not strikingly different in comparison to the effect of mixing variables ( $J$  and  $IC$ ). Hence,  $J$  could be used as a scaling variable.

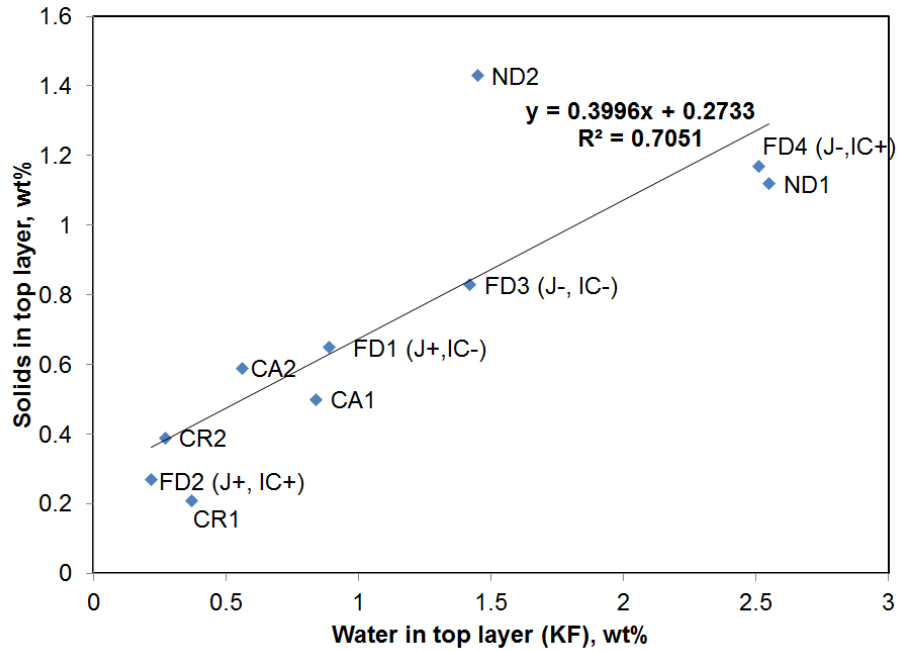
**Table 4-7:** Comparison of Rushton and A310 runs at same mixing conditions

<b>Circulation Pattern Runs</b> <b>(<math>X_J = 0, X_{IC} = 0</math>)</b>	<b>CR1</b>	<b>CR2</b>	<b>CA1</b>	<b>CA2</b>
<i>KF</i> settling rate (qualitative)	Slow	Fast	Fast	Fast
<i>KF</i> water [60 min and height $z_I$ (wt%)]	0.37	0.27	0.84	0.56
<i>OWS</i> water at 60 min in top/middle layer (wt%)	0.62/0.49	0.74/0.62	1.3/1.08	1.68/1.02
<i>OWS</i> solid at 60 min in top/middle layer (wt%)	0.21/0.16	0.39/0.41	0.5/ 0.52	0.59/0.58
Qualitative analysis (10 min at height $z_I$ )	Clusters got stuck	Clean	Few water and solids	Few water and solids
Clustering algorithm (height $z_I$ )	Small clusters	Big clusters	Big clusters	Big clusters
Water drop size distribution (height $z_I$ )	Repeatable distribution		Unrepeatable distribution	

#### 4.2.4 OWS and CPA Analysis

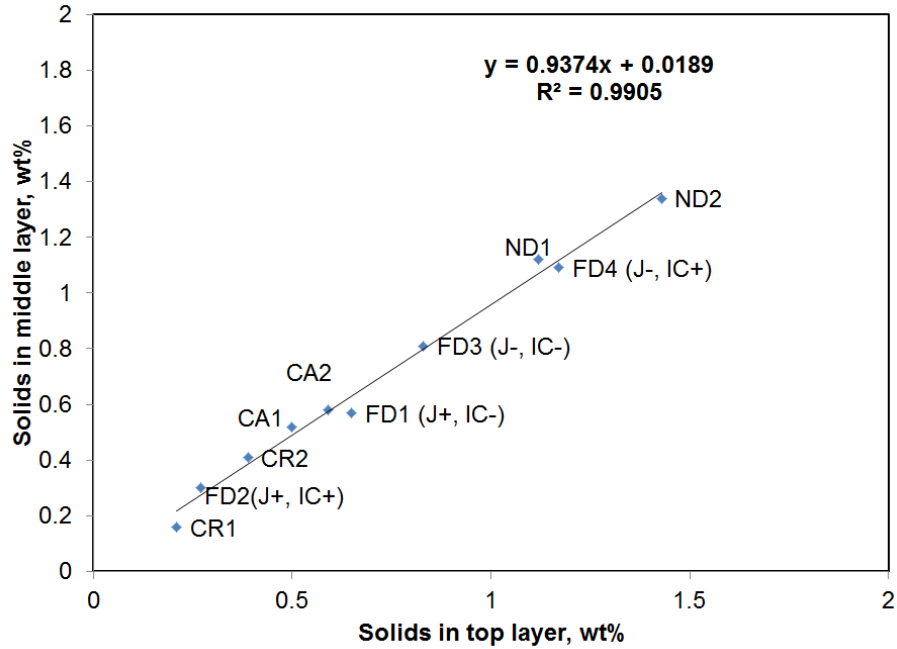
Now that the settling mechanisms and effect of circulation pattern are established let us compare all the experiments using *OWS* and *CPA* analysis. The *OWS* data is considered first. The data for all 10 experiments is presented here and is shown in Table A-5 for reference. Figure 4-29 compares water and solid content in top layer. The figure shows that in runs with no demulsifier, both solid and water content in top layer ( $z/H = 0.1$ ) are high. At poor mixing conditions (*FD4*: low  $J$ , high  $IC$ ), the water and solid content are 2.51 wt% and 1.17 wt% respectively, which is close to the no demulsifier run: *NDI* performance. At the best operating condition (*FD1*: high  $J$ , low  $IC$ ), both the water and solid content are much lower. It is surprising that the best dewatering and demineralization (removal of solids) is achieved at run *FD2* (low  $J$ , low  $IC$ ), moderate mixing conditions. The data suggests that demulsifier at right mixing conditions removes both water and solids through sweep flocculation. Clustering analysis (Section 4.2.2.2) also supports this observation.

The performance for circulation pattern runs ( $X_J = 0$ ,  $X_{IC} = 0$ ) with Rushton (*RT*) and A310 impellers is also shown in Figure 4-29. The Rushton runs (*CR1* and *CR2*) result in lower water and solid content in comparison to A310 runs (*CA1* and *CA2*), although the settling rate was slower in the case of *RT* runs as per Figure 4-24. It is surprising that *FD2* (high  $J$ , high  $IC$ ) and the circulation pattern runs performed better than the *FD1* run (high  $J$ , low  $IC$ ). This anomaly can be explained by the hypothesis that high  $J$  breaks up the aggregates whereas mid-level  $J$  ( $X_J = 0$ ) provides the right amount of mixing energy to form big and dense flocs. The better performance of *FD2* in comparison to *FD1* could be due to high  $J$  compensating for the detrimental effect of high  $IC$ . Recall that in Chapter 1, we discussed that both flocculation and coalescence are enhanced by gentle shear (optimum  $\epsilon$ ). The intercept of trendline on vertical axis in Figure 4-29 shows that even if water in product layer is 0 wt%, there would still be some solids present in the product (or top) layer. These solids are believed to be hydrophobic in nature and hence do not settle with water.

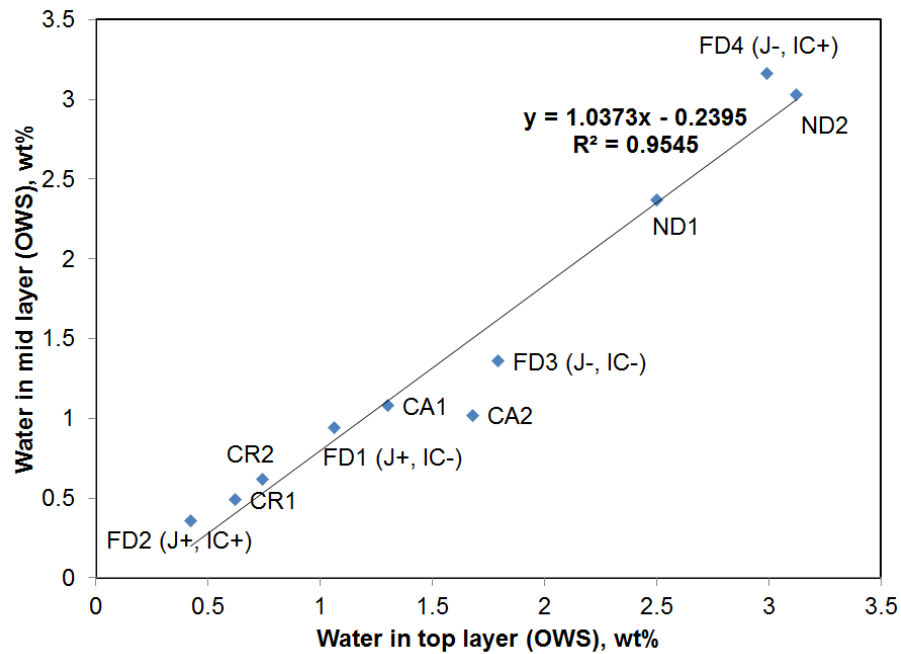


**Figure 4-29:** Relation between solids (*OWS*) and water (*KF*) content present in top layer ( $z/H = 0.1$ ) after 60 min of settling for 10 experiments

Figure 4-30 shows that the solids content in the top and middle ( $z/H = 0.5$ ) layers is identical. Figure 4-31 shows that the water content is also similar in the top and middle layers. This is further evidence that the water and solids settle together.

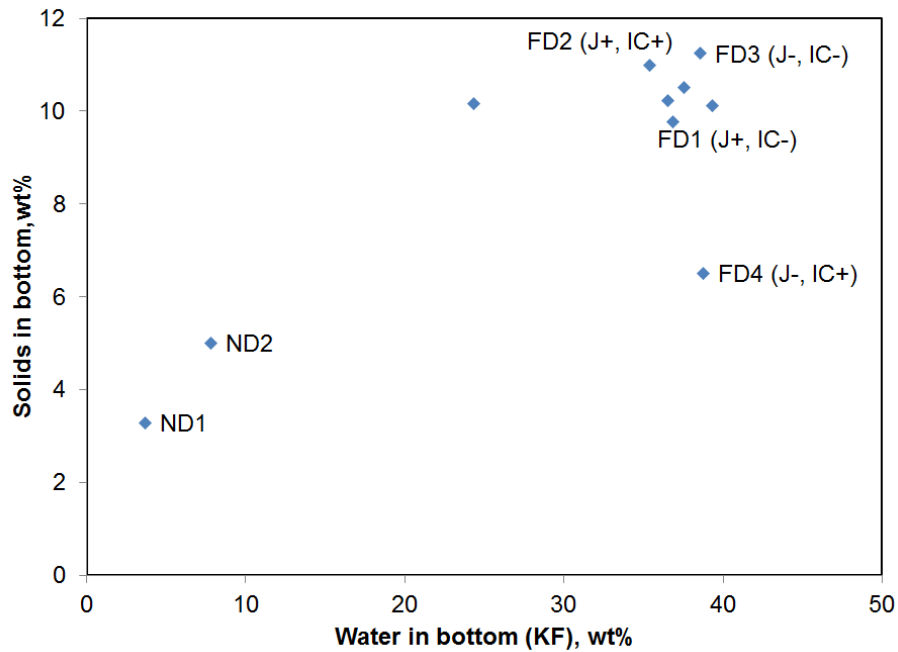


**Figure 4-30:** Relation between solids in top ( $z/H = 0.1$ ) and middle ( $z/H = 0.5$ ) layers after 60 min of settling for 10 experiments



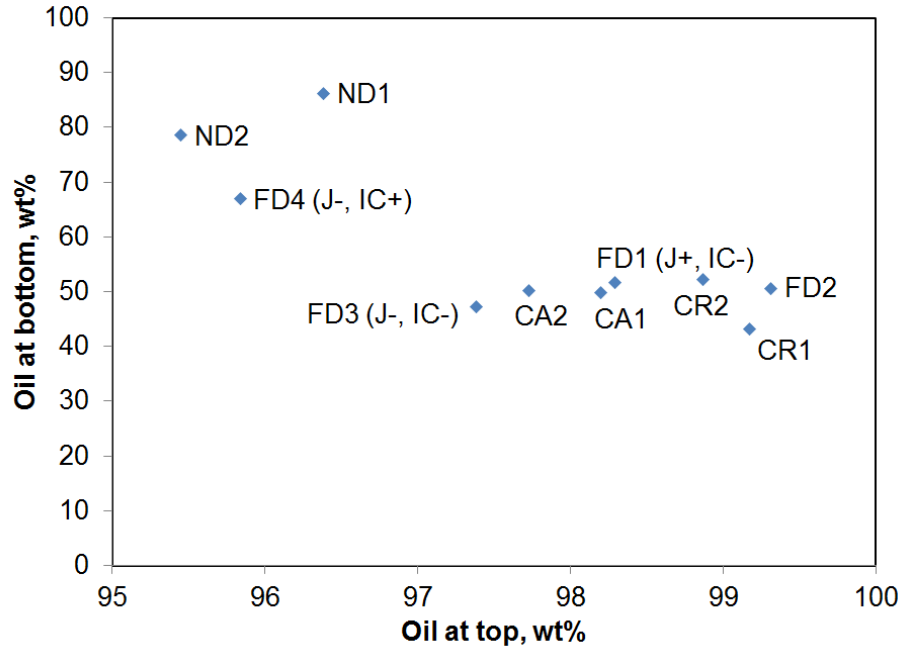
**Figure 4-31:** Relation between water (*OWS*) in top ( $z/H = 0.1$ ) and middle ( $z/H = 0.5$ ) layers after 60 min of settling for 10 experiments

The water and solids present in the bottom layer as shown in Figure 4-32 do not relate linearly like top and middle layers as shown previously in Figure 4-30 and Figure 4-31. There is no significant difference in water or solid content with respect to mixing conditions ( $J$  and  $IC$ ). However, for no demulsifier run, there is much less water and solid content indicating inadequate dewatering and demineralization. It is believed that the settled water behaves like a packed bed where water concentrates over time through coalescence and hence releasing bitumen trapped in void spaces.



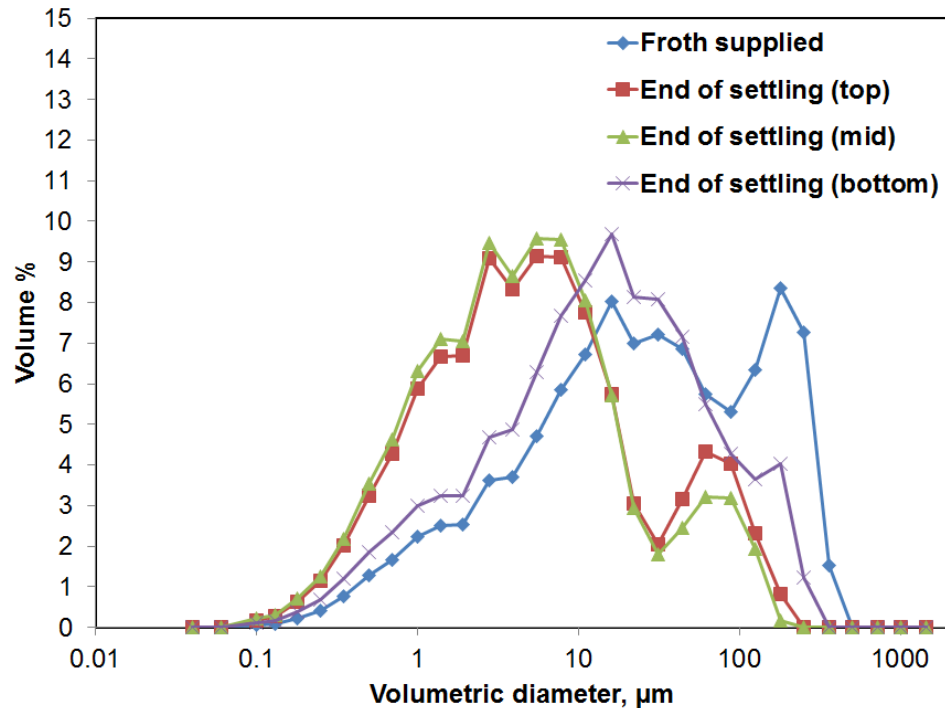
**Figure 4-32:** Relation between solids and water ( $KF$ ) in bottom layer ( $z/H = 0.9$ ) after 60 min of settling for 10 experiments

Figure 4-33 presents the same oil-water-solid data (add up to  $100 \pm 2$  wt%) from an oil recovery perspective. This oil would include both bitumen and naphtha. Low and high oil content in bottom and top layers respectively would indicate better performance. The figure clearly shows that for no demulsifier runs ( $ND1$  and  $ND2$ ) and poor mixing conditions ( $FD4: J-, IC+$ ), more oil reports to the bottom. Best performance is again observed for run  $FD2 (J+, IC+)$ .



**Figure 4-33:** *OWS* oil content (bitumen + naphtha) comparison between top and bottom layers for all 10 experiments

Computerized Particle Analysis (*CPA*) provides volumetric particle size distribution of dried solids (left after *OWS* analysis) using laser low angle forward scattering. The solid size distribution for no demulsifier run is shown in Figure 4-34. The supplied froth has a bimodal distribution (two peaks), with the first and second peaks located at 16 and 180  $\mu\text{m}$ . After 60 min of settling, the top and middle layers have a similar size distribution and less big particles. As expected, the bottom layer has more big particles than the top layer and is similar to the as supplied (undiluted) froth solids distribution. The *CPA* distribution for the top and middle layers for all 8 demulsifier experiments could not be obtained because they had insufficient fines quantity. The size distribution of solids in the bottom layers for 8 demulsifier experiments did not vary significantly with respect to mixing conditions (*J* and *IC*) and hence is not shown here.



**Figure 4-34:** Computerized Particle Analysis (*CPA*) of solids collected after *OWS* analysis, in supplied undiluted froth and end of settling diluted froth for no demulsifier run

*EXM* solid concentration data is not shown here because it gave similar results to the *OWS* method and did not help to understand the process. For reference, the data is shown in Table A-5. Both methods use toluene as a solvent. The *OWS* method uses a 10  $\mu\text{m}$  filter for collecting solids and the filtrate is run through a high speed centrifuge to collect even more solids. The *EXM* method just passes the sample through a 1.6  $\mu\text{m}$  filter for collecting solids.

### 4.3 Conclusion

Through Karl-Fisher water concentration, image analysis and oil-water-solid analysis, it was determined that adding demulsifier at poor mixing conditions (low mixing energy and high demulsifier injection concentration) gave similar dewatering results to adding no demulsifier. Therefore, adding demulsifier at sub-optimal mixing conditions could limit demulsifier performance. This agrees with the previous studies.

The contributions of this study including the ones discussed in previous chapters are listed below:

1. **Flocculation and sweep flocculation are the dominant aggregation and settling mechanisms.** Through qualitative and quantitative clustering image analysis, it was concluded that water forms water-water and water-solid aggregates. Solid-solid aggregates were rarely seen on microscope images and were smaller in comparison to other two aggregates types. Hence, water drops flocculate with each other and also sweep flocculate the nearby solids. The quantitative oil-water-solid analysis confirmed the observation that low water in product layer ensured low solids concentration as well. Coalescence of free water has been noticed on microscope images but it is a slow phenomenon which happens over hours or even days. Water drop size distribution also indicated statistical evidence of slow coalescence. The slow rate of coalescence could be due to higher bitumen viscosity at room temperature (during imaging) in comparison to 80°C in *CIST* and industrial operations.
2. The dominant settling mechanism does not change significantly with mixing variables (mixing energy and demulsifier injection concentration) but the aggregate growth does. The good mixing variables (high mixing energy and low demulsifier injection concentration) enhance aggregate growth resulting in faster settling rate and lower final water and solid content.
3. The dominant settling mechanism does not change with respect to sampling height. For the mixing variables and the average quality bitumen froth used in this study, all experiments indicated that the water and solid content after 60 min of settling is of similar order (< 2 wt%) at first three sampling heights ( $z_1$ ,  $z_2$  and  $z_3$ ). The consolidation layer where free water and aggregates would settle was at height  $z_4$  which indicated a water content of ~ 40 wt%.
4. Solids prefer to settle with water via sweep flocculation.

5. The significance of fast water settling in first 10 min during 60 min settling period is that the free water and big aggregates settle much faster because of their bigger size (and/or density) in comparison to micron sized loner drops.
6. For experiments performed at the same mixing conditions (mixing energy and demulsifier injection concentration) using two different impellers (Rushton and A310), the total water and solid content after 60 min of sedimentation in Rushton was less than that of A310. Both impellers gave good results and the difference in performance was not significant in comparison to the effect of mixing conditions. This indicates that flow pattern (radial for Ruston and axial for A310) does matter but its effects are not strikingly different. Hence, mixing energy could be used as a scale up variable.
7. Clustering image analysis algorithm (Chapter 3) helped to isolate two species (water and solids) in bitumen froth microscope images and was useful for measuring cluster size and other properties. The clustering algorithm based on object-object distance was able to identify the type of cluster (water-water or water-solid or solid-solid), the cluster size, the number of objects in a cluster and their distributions. The method helped to identify the dominant interaction (water-water and water-solid) on bitumen froth images.
8. Side sampling gave more physically meaningful results than top sampling (Chapter 2).

#### **4.4 Future Work**

More evidence needs to be gathered on the time scale of coalescence using time lapse imaging. The effect of mixing variables (mixing energy and demulsifier injection concentration), settling time and sampling height on coalescence time scale should be investigated. The factors that affect experimental repeatability for bitumen froth should be investigated to get more meaningful trends. Effect of circulation pattern at same mixing energy and demulsifier injection concentration should be extended to other impellers such as Intermig and *PBT*. The experimental validation of mixing energy as a scale up variable for other systems such as clean liquid-liquid and flocculating solids in

liquid should be executed. Physical and chemical characterization of solids that remain in product (or top) layer even after good mixing conditions should be done.

## References

- Angle, C., 2001. Chemical Demulsification of Stable Crude Oil and Bitumen Emulsions in Petroleum Recovery-a Review, in: Sjöblom, J. (Ed.), *Encyclopedic Handbook of Emulsion Technology*, CRC Press, 541–594, doi:10.1201/9781420029581.ch24.
- ASTM Standard E799-03, 2015. *Standard Practice for Determining Data Criteria and Processing for Liquid Drop Size Analysis*, ASTM International, West Conshohocken, PA, doi:10.1520/E0799-03R09.2.
- Box, G.E.P. et al., 1978. Chapter 10: Factorial Design at Two Levels, in: *Statistics for Experimenters*, John Wiley and Sons, Inc., New York, 306–351.
- Bulmer, J.T., Starr, J., 1979. *Syncrude Analytical Methods for Oil Sand and Bitumen Processing*, AOSTRA, Edmonton.
- Chen, Z. et al., 2015. Demulsifying Water-in-Oil Emulsions by Ethyl Cellulose Demulsifiers Studied Using Focused Beam Reflectance Measurement, *Chem. Eng. Sci.*, **130**, 254–263, doi:10.1016/j.ces.2015.03.014.
- Chong, J.Y., 2013. *Mixing Effects on Chemical Demulsifier Performance in Diluted Bitumen and Froth*, MSc Thesis, University of Alberta, Canada.
- Czarnecki, J. et al., 2007. On the “Rag Layer” and Diluted Bitumen Froth Dewatering, *Can. J. Chem. Eng.*, **85**, 748–755, doi:10.1002/cjce.5450850520.
- Feng, X. et al., 2009. Biodegradable Polymer for Demulsification of Water-in-Bitumen Emulsions, *Energy and Fuels*, **23**, 451–456, doi:10.1021/ef800825n.
- Gupta, V. et al., 2011. Particle Interactions in Kaolinite Suspensions and Corresponding Aggregate Structures, *J. Colloid Interface Sci.*, **359**, 95–103, doi:10.1016/j.jcis.2011.03.043.
- Hemrajani, R., Tatterson, G., 2004. Chapter 6: Mechanically Stirred Vessels, in: L. Paul, E. et al. (Eds.), *Handbook of Industrial Mixing: Science and Practice*, John Wiley and Sons, Inc., Hoboken, New Jersey, 345–390, doi:10.1002/0471451452.ch6.
- Jiang, T. et al., 2008. Using Silicate and pH Control for Removal of the Rag Layer Containing Clay Solids Formed During Demulsification, *Energy and Fuels*, **22**, 4158–4164, doi:10.1021/ef8001845.
- Laplante, G.P., 2011. *On Mixing and Demulsifier Performance in Oil Sands Froth*

- Treatment, MSc Thesis, University of Alberta, Canada.
- Laplante, P. et al., 2015. Demulsifier Performance in Froth Treatment: Untangling the Effects of Mixing, Bulk Concentration and Injection Concentration Using a Standardized Mixing Test Cell (CIST), *Fuel Process. Technol.*, **138**, 361–367, doi:<http://dx.doi.org/10.1016/j.fuproc.2015.05.028>.
- Leith, D., 1987. Drag on Nonspherical Objects, *Aerosol Sci. Technol.*, **6**, 153–161, doi:[10.1080/02786828708959128](http://dx.doi.org/10.1080/02786828708959128).
- Leo, S.S., 2013. Measurement and Analysis of Changes in Drop Size Distribution during Bitumen Clarification using Image Analysis, MSc Thesis, University of Alberta, Canada.
- Machado, M.B., Kresta, S.M., 2013. The Confined Impeller Stirred Tank (CIST): a Bench Scale Testing Device for Specification of Local Mixing Conditions Required in Large Scale Vessels, *Chem. Eng. Res. Des.*, **91**, 2209–2224, doi:[10.1016/j.cherd.2013.06.025](http://dx.doi.org/10.1016/j.cherd.2013.06.025).
- Machado, M.B., Kresta, S.M., 2015. Chapter 2b: Update to Turbulence in Mixing Applications, in: Kresta, S.M. et al. (Eds.), *Advances in Industrial Mixing: A Companion to the Handbook of Industrial Mixing*, John Wiley & Sons Inc., Hoboken, New Jersey, 47–84.
- Madhav, G.V., Chhabra, R.P., 1995. Drag on Non-Spherical Particles in Viscous Fluids, *Int. J. Miner. Process.*, **43**, 15–29, doi:[http://dx.doi.org/10.1016/0301-7516\(94\)00038-2](http://dx.doi.org/10.1016/0301-7516(94)00038-2).
- Masliyah, J.H. et al., 2011b. Chapter 7: Froth Treatment Fundamentals, in: *Handbook on Theory and Practice of Bitumen Recovery from Athabasca Oil Sands, Volume 1: Theoretical Basis*, Kingsley Knowledge Publishing, 349–386.
- Neiman, O. et al., 1999. US Patent 5988198a: Process for Pumping Bitumen Froth Through a Pipeline.
- Romanova, U.G. et al., 2004. The Effect of Bitumen Extraction Shear Conditions on Froth Treatment Performance, *Pet. Soc. Canada*, 1–3, doi:<http://dx.doi.org/10.2118/2004-028-EA>.
- Seyer, F., Gyte, C., 1989. Chapter 7: Viscosity, in: Hepler, L., Hsi, C. (Eds.), *AOSTRA Technical Handbook on Oil Sands, Bitumens and Heavy Oils*, Alberta Oil Sands Technology and Research Authority, Edmonton, 181.
- Smets, K. et al., 2011. Water Content of Pyrolysis Oil: Comparison between Karl Fischer Titration, GC/MS-Corrected Azeotropic Distillation and <sup>1</sup>H NMR Spectroscopy, *J.*

Anal. Appl. Pyrolysis, **90**, 100–105, doi:10.1016/j.jaap.2010.10.010.

Spicer, P. et al., 1996. The Effect of Impeller Type on Floc Size and Structure during Shear-Induced Flocculation, J. Colloid Interface Sci., **184**, 112–122, doi:<http://dx.doi.org/10.1006/jcis.1996.0601>.

## References (All)

- Alban, F.B. et al., 2004. Dynamic Tracking of Fast Liquid–Liquid Dispersion Processes with a Real-Time in-Situ Optical Technique, *Chem. Eng. Res. Des.*, **82**, 1054–1060, doi:<http://dx.doi.org/10.1205/0263876041580631>.
- Alberta Energy Regulator, 2015. Alberta’s Energy Reserves 2014 and Supply/Demand Outlook, 2015-2024.
- Angle, C., 2001. Chemical Demulsification of Stable Crude Oil and Bitumen Emulsions in Petroleum Recovery-a Review, in: Sjöblom, J. (Ed.), *Encyclopedic Handbook of Emulsion Technology*, CRC Press, 541–594, doi:10.1201/9781420029581.ch24.
- ASTM Standard E799-03, 2015. Standard Practice for Determining Data Criteria and Processing for Liquid Drop Size Analysis, ASTM International, West Conshohocken, PA, doi:10.1520/E0799-03R09.2.
- Bancroft, W.D., 1913. The Theory of Emulsification, *V. J. Phys. Chem.*, **17**, 501–519, doi:10.1021/j150141a002.
- Berger, P.D. et al., 1987. Designing and Selecting Demulsifiers for Optimum Field Performance Based on Production Fluid Characteristics, in: *SPE International Symposium on Oilfield Chemistry*.
- Bhardwaj, A., Hartland, S., 1994. Kinetics of Coalescence of Water Droplets in Water-in-Crude Oil Emulsions, *J. Dispers. Sci. Technol.*, **15**, 133–146, doi:10.1080/01932699408943549.
- Bhattacharya, S., Kresta, S.M., 2004. Surface Feed with Minimum by-Product Formation for Competitive Reactions, *Chem. Eng. Res. Des.*, **82**, 1153–1160, doi:<http://dx.doi.org/10.1205/cerd.82.9.1153.44173>.
- Bourne, J.R., 2003. Mixing and the Selectivity of Chemical Reactions, *Org. Process Res. Dev.*, **7**, 471–508, doi:10.1021/op020074q.
- Box, G.E.P. et al., 1978. Chapter 10: Factorial Design at Two Levels, in: *Statistics for Experimenters*, John Wiley and Sons, Inc., New York, 306–351.
- Bulmer, J.T., Starr, J., 1979. *Syn crude Analytical Methods for Oil Sand and Bitumen Processing*, AOSTRA, Edmonton.
- Chen, Z. et al., 2015. Demulsifying Water-in-Oil Emulsions by Ethyl Cellulose Demulsifiers Studied Using Focused Beam Reflectance Measurement, *Chem. Eng. Sci.*, **130**, 254–263, doi:10.1016/j.ces.2015.03.014.

- Chong, J.Y., 2013. Mixing Effects on Chemical Demulsifier Performance in Diluted Bitumen and Froth, MSc Thesis, University of Alberta, Canada.
- Chong, J.Y. et al., 2016. Reduce Overdosing Effects in Chemical Demulsifier Applications by Increasing Mixing Energy and Decreasing Injection Concentration, *Energy and Fuels*, **30**, 5183–5189, doi:10.1021/acs.energyfuels.6b00621.
- Clark, K.A., 1929. The Separation of the Bitumen from Alberta Bituminous Sands, *Can. Inst. Min. Met. Bull.*, **22**, 1385–1395.
- Coulaloglou, C.A., Tavlarides, L.L., 1977. Description of Interaction Processes in Agitated Liquid-Liquid Dispersions, *Chem. Eng. Sci.*, **32**, 1289–1297.
- Crittenden, J.C., Montgomery, W.H. (Firm), 2012. Chapter 10: Gravity Separation, in: *MWH's Water Treatment: Principles and Design*, John Wiley & Sons, 641–726.
- Czarnecki, J., Moran, K., 2005. On the Stabilization Mechanism of Water-in-Oil Emulsions in Petroleum Systems, *Energy and Fuels*, **19**, 2074–2079, doi:10.1021/ef0501400.
- Czarnecki, J. et al., 2007. On the “Rag Layer” and Diluted Bitumen Froth Dewatering. *Can. J. Chem. Eng.*, **85**, 748–755, doi:10.1002/cjce.5450850520.
- Das, P.K. et al., 1987. Coalescence of Drops in Stirred Dispersion. A White Noise Model for Coalescence, *Chem. Eng. Sci.*, **42**, 213–220.
- Davies, J.T., 1987. A Physical Interpretation of Drop Sizes in Homogenizers and Agitated Tanks, Including the Dispersion of Viscous Oils, *Chem. Eng. Sci.*, **42**, 1671–1676, doi:10.1016/0009-2509(87)80172-0.
- Demoz, A., 2015. Scaling Inline Static Mixers for Flocculation of Oil Sand Mature Fine Tailings, *AIChE J.*, **61**, 4402–4411.
- Dey, T., Naughton, D., 2016. Cleaning and Anti-Reflective (AR) Hydrophobic Coating of Glass Surface: a Review from Materials Science Perspective, *J. Sol-Gel Sci. Technol.*, **77**, 1–27, doi:10.1007/s10971-015-3879-x.
- Diggle, P.J., 2013a. Chapter 2: Preliminary Testing, in: *Statistical Analysis of Spatial and Spatio-Temporal Point Patterns*, Third Edition, C and H/CRC Monographs on Statistics and Applied Probability, Chapman and Hall/CRC, 17–37, doi:10.1201/b15326-3.
- Diggle, P.J., 2013b. Chapter 1: Introduction, in: *Statistical Analysis of Spatial and Spatio-Temporal Point Patterns*, Third Edition, C and H/CRC Monographs on Statistics and Applied Probability, Chapman and Hall/CRC, 1–16, doi:10.1201/b15326-2.

- Dyer, K.R., Manning, A.J., 1999. Observation of the Size, Settling Velocity and Effective Density of Floccs, and their Fractal Dimensions, *J. Sea Res.*, **41**, 87–95.
- Eisenhawer, A., Jantunen-Cross, K., 2013. Chapter 11: Speciality Chemicals in Oil Sands Extraction, in: Masliyah, J.H. et al. (Eds.), *Handbook on Theory and Practice of Bitumen Recovery from Athabasca Oil Sands, Volume II: Industrial Practice*, Kingsley Knowledge Publishing, 363–387.
- Emulsion Stability and Testing, 2011, Part. Sci., *Drug Dev. Serv. Br.* 2.
- Ese, M.H., Kilpatrick, P.K., 2004. Stabilization of Water in Oil Emulsions by Naphthenic Acids and their Salts: Model Compounds, Role of pH, and Soap: Acid Ratio, *J. Dispers. Sci. Technol.*, **25**, 253–261, doi:10.1081/DIS-120038634.
- Espinat, D. et al., 2004. Effects of Temperature and Pressure on Asphaltenes Agglomeration in Toluene. A Light, X-ray, and Neutron Scattering Investigation, *Energy and Fuels*, **18**, 1243–1249, doi:10.1021/ef030190.
- Everett, D.H., 1988. *Basic Principles of Colloid Science*, Royal Society of Chemistry: London.
- Feng, X. et al., 2009. Biodegradable Polymer for Demulsification of Water-in-Bitumen Emulsions, *Energy and Fuels*, **23**, 451–456, doi:10.1021/ef800825n.
- Feng, X. et al., 2010. Mechanistic Study on Demulsification of Water-in-Diluted Bitumen Emulsions by Ethylcellulose, *Langmuir*, **26**, 3050–3057, doi:10.1021/la9029563.
- Ferreira, T., Rasband, W., 2012. Watershed [WWW Document], Image J User Guid., URL <http://imagej.nih.gov/ij/docs/guide/146-29.html#toc-Subsection-29.8>.
- Gray, M. et al., 2009. Physics in the Oil sands of Alberta, *Phys. Today*, **62**, 31–35.
- Gregory, J., 2009. Monitoring Particle Aggregation Processes, *Adv. Colloid Interface Sci.*, **147**, 109–123.
- Grubbs, F.E., 1950. Sample Criteria for Testing Outlying Observations, *Ann. Math. Stat.*, **21**, 27–58.
- Gu, G. et al., 2002. Influence of Water-Soluble and Water-Insoluble Natural Surface Active Components on the Stability of Water-in-Toluene-Diluted Bitumen Emulsion, *Fuel*, **81**, 1859–1869, doi:10.1016/S0016-2361(02)00113-8.
- Gupta, V. et al., 2011. Particle Interactions in Kaolinite Suspensions and Corresponding Aggregate Structures, *J. Colloid Interface Sci.*, **359**, 95–103, doi:10.1016/j.jcis.2011.03.043.
- Haight, F.A., 1967. *Handbook of the Poisson Distribution*, Publications in Operations

- Research: no. 11, Wiley, New York.
- Hamarneh, G., Li, X., 2009. Watershed Segmentation Using Prior Shape and Appearance Knowledge, *Image Vis. Comput.*, **27**, 59–68, doi:10.1016/j.imavis.2006.10.009.
- Hemrajani, R., Tatterson, G., 2004. Chapter 6: Mechanically Stirred Vessels, in: Paul, E.L. et al. (Eds.), *Handbook of Industrial Mixing: Science and Practice*. John Wiley and Sons, Inc., Hoboken, New Jersey, 345–390, doi:10.1002/0471451452.ch6.
- Hinze, J.O., 1955. Fundamentals of the Hydrodynamic Mechanism of Splitting in Dispersion Processes, *AIChE J.*, **1**, 289–295, doi:10.1002/aic.690010303.
- Jiang, T. et al., 2008. Using Silicate and pH Control for Removal of the Rag Layer Containing Clay Solids Formed During Demulsification, *Energy and Fuels*, **22**, 4158–4164, doi:10.1021/ef8001845.
- Johannsen, G., Bille, J., 1982. A Threshold Selection Method Using Information Measures, in: *ICPR*, 140–143.
- Jung, C.R., Scharcanski, J., 2005. Robust Watershed Segmentation Using Wavelets, *Image Vis. Comput.*, **23**, 661–669, doi:10.1016/j.imavis.2005.03.001.
- Kailey, I., Behles, J., 2015. Evaluation of the Performance of Newly developed Demulsifiers on Dilbit Dehydration, Demineralization, and Hydrocarbon Losses to Tailings, *Ind. Eng. Chem. Res.*, **54**, 4839–4850, doi:10.1021/acs.iecr.5b00435.
- Khrstov, K. et al., 2000. Thin Liquid Film Technique - Application to Water-Oil-Water Bitumen Emulsion Films, *Colloids Surfaces A Physicochem. Eng. Asp.*, **174**, 183–196, doi:10.1016/S0927-7757(00)00510-0.
- Kokal, S.L., 2005. Crude Oil Emulsions: A State-of-the-Art Review, *SPE Prod. Facil.*, **20**, 5–13.
- Kotlyar, L.S. et al., 1999. Solids Associated With the Asphaltene Fraction of Oil Sands Bitumen, *Energy and Fuels*, **13**, 346–350, doi:10.1021/ef980204p.
- Kresta, S.M., Brodkey, R.S., 2004. Chapter 2: Turbulence in Mixing Applications, in: Paul, E.L. et al. (Eds.), *Handbook of Industrial Mixing: Science and Practice*. John Wiley and Sons, Inc., Hoboken, New Jersey, 19–87, doi:10.1002/0471451452.ch2.
- Kresta, S.M. et al. (Eds.), 2015. *Advances in Industrial Mixing: A Companion to the Handbook of Industrial Mixing*. John Wiley & Sons Inc., Hoboken, New Jersey.
- Kukukova, A. et al., 2009. A New Definition of Mixing and Segregation: Three Dimensions of a Key Process Variable, *Chem. Eng. Res. Des.*, **87**, 633–647, doi:10.1016/j.cherd.2009.01.001.

- Kukukova, A. et al., 2011. Measuring the Scale of Segregation in Mixing Data, *Can. J. Chem. Eng.*, **89**, 1122–1138, doi:10.1002/cjce.20532.
- Kukukova, A., 2011. Spatial Statistics as a Means of Characterizing Mixing and Segregation, PhD Thesis, University of Alberta, Canada.
- Kuzmanic, N., Rušic, D., 1999. Solids concentration measurements of floating particles suspended in a stirred vessel using sample withdrawal techniques, *Ind. Eng. Chem. Res.*, **38**, 2794–2802.
- Laplante, G.P., 2011. On Mixing and Demulsifier Performance in Oil Sands Froth Treatment, MSc Thesis, University of Alberta, Canada.
- Laplante, P. et al., 2015. Demulsifier Performance in Froth Treatment: Untangling the Effects of Mixing, Bulk Concentration and Injection Concentration Using a Standardized Mixing Test Cell (CIST), *Fuel Process. Technol.*, **138**, 361–367, doi:http://dx.doi.org/10.1016/j.fuproc.2015.05.028.
- Lee, C.Y., 1961. An Algorithm for Path Connections and its Applications, *Electron. Comput. IRE Trans.*, **EC-10**, 1389–1401, doi:10.1109/TEC.1961.5219222.
- Lefebvre, E.G., 1979. US Patent 4 165 385: Water-in-Oil Emulsion for Skin Moisturizing.
- Leith, D., 1987. Drag on Nonspherical Objects, *Aerosol Sci. Technol.*, **6**, 153–161, doi:10.1080/02786828708959128.
- Leng, D.E., Calabrese, R. V., 2004. Chapter 12: Immiscible Liquid – Liquid Systems, in: Paul, E.L. et al. (Eds.), *Handbook of Industrial Mixing: Science and Practice*. John Wiley and Sons, Inc., Hoboken, New Jersey, 639–753.
- Leo, S.S., 2013. Measurement and Analysis of Changes in Drop Size Distribution during Bitumen Clarification using Image Analysis, MSc Thesis, University of Alberta, Canada.
- Levich, V.G., 1962. *Physicochemical Hydrodynamics*, Prentice Hall, Englewood Cliffs, New Jersey.
- Li, W. et al., 2012. Au/SiO<sub>2</sub> as a Highly Active Catalyst for the Selective Oxidation of Silanes to Silanols, *Chem. Commun.*, **48**, 9183, doi:10.1039/c2cc33949h.
- Liu, J. et al., 2005. Processability of Oil Sand Ores in Alberta, *Energy and Fuels*, **19**, 2056–2063, doi:10.1021/ef050091r.
- Long, Y. et al., 2002. Stability and Settling Characteristics of Solvent-Diluted Bitumen Emulsions, *Fuel*, **81**, 1945–1952, doi:10.1016/S0016-2361(02)00132-1.

- Machado, M.B. et al., 2013. Transition from Turbulent to Transitional Flow in the Top Half of a Stirred Tank, *Chem. Eng. Sci.*, **98**, 218–230.
- Machado, M.B., Kresta, S.M., 2013. The Confined Impeller Stirred Tank (CIST): a Bench Scale Testing Device for Specification of Local Mixing Conditions Required in Large Scale Vessels, *Chem. Eng. Res. Des.*, **91**, 2209–2224, doi:10.1016/j.cherd.2013.06.025.
- Machado, M.B., Kresta, S.M., 2015. Chapter 2b: Update to Turbulence in Mixing Applications, in: Kresta, S.M. et al. (Eds.), *Advances in Industrial Mixing: A Companion to the Handbook of Industrial Mixing*, John Wiley & Sons Inc., Hoboken, New Jersey, 47–84.
- MacTaggart, R.S., 1993. Sample Withdrawal from a Slurry Mixing Tank, *Chem. Eng. Sci.*, **48**, 921–931.
- Madhav, G.V., Chhabra, R.P., 1995. Drag on Non-Spherical Particles in Viscous Fluids, *Int. J. Miner. Process.*, **43**, 15–29, doi:http://dx.doi.org/10.1016/0301-7516(94)00038-2.
- Madjlessikupai, M., 2012. Study of the Rag Layer: Characterization of Solids, MSc Thesis, University of Alberta, Canada.
- Masliyah, J.H. et al., 2011a. Chapter 1: Introduction to the Athabasca Oil Sands, in: *Handbook on Theory and Practice of Bitumen Recovery from Athabasca Oil Sands, Volume 1: Theoretical Basis*, Kingsley Knowledge Publishing, 1–39.
- Masliyah, J.H. et al., 2011b. Chapter 7: Froth Treatment Fundamentals, in: *Handbook on Theory and Practice of Bitumen Recovery from Athabasca Oil Sands, Volume 1: Theoretical Basis*, Kingsley Knowledge Publishing, 349–386.
- Masliyah, J.H. et al., 2011c. Chapter 3: Fluid Particle Dynamics as Applied to Oil Sands Operations, in: *Handbook on Theory and Practice of Bitumen Recovery from Athabasca Oil Sands, Volume 1: Theoretical Basis*, Kingsley Knowledge Publishing, 129–172.
- Masliyah, J.H. et al., 2011d. Chapter 4: Physical and Chemical Properties of Oil Sands, in: *Handbook on Theory and Practice of Bitumen Recovery from Athabasca Oil Sands*, Kingsley Knowledge Publishing, 173–256.
- Mason, S.L. et al., 1995. Drop Size and Concentration Profile Determination in Petroleum Emulsion Separation, *Colloids Surfaces A Physicochem. Eng. Asp.*, **96**, 85–92, doi:10.1016/0927-7757(94)03030-4.
- McClements, D.J., 2015. Chapter 7: Emulsion Stability, in: *Food Emulsions (Principles,*

- Practices, and Techniques), CRC Press, Boca Raton, Florida, 289–382, doi:10.1201/b18868-8.
- McLean, J.D., Kilpatrick, P.K., 1997. Effects of Asphaltene Solvency on Stability of Water-in-Crude-Oil Emulsions, *J. Colloid Interface Sci.*, **189**, 242–253, doi:10.1006/jcis.1997.4807.
- Melik, D.H., Fogler, H.S., 1984. Gravity-Induced Flocculation, *J. Colloid Interface Sci.*, **101**, 72–83, doi:10.1016/0021-9797(84)90009-2.
- Neal, B. et al., 1998. A Superresolution Approach to Perimeter Measurement, *J. Comput. Assist. Microsc.*, **10**, 11–21.
- Neiman, O. et al., 1999. US Patent 5988198a: Process for Pumping Bitumen Froth Through a Pipeline.
- Ng, Y.M.S. et al., 2015. CA Patent 2851192: Demulsifier Injection System for Froth Treatment Product Quality Enhancement.
- Oil Sands [WWW Document], 2016, Can. Assoc. Pet. Prod., URL <http://www.capp.ca/canadian-oil-and-natural-gas/oil-sands> (accessed 2.2.16).
- Pacek, A.W. et al., 1994. On the Structure of Turbulent Liquid-Liquid Dispersed Flows in an Agitated Vessel, *Chem. Eng. Sci.*, **49**, 3485–3498.
- Paul, E.L. et al. (Eds.), 2004. *Handbook of Industrial Mixing: Science and Practice*. John Wiley and Sons, Inc., Hoboken, New Jersey.
- Peña, A. a. et al., 2005. Chemically Induced Destabilization of Water-in-Crude Oil Emulsions, *Ind. Eng. Chem. Res.*, **44**, 1139–1149, doi:10.1021/ie049666i.
- Photoshop Help/Color modes [WWW Document], 2015, Adobe URL, <https://helpx.adobe.com/photoshop/using/color-modes.html> (accessed 4.13.15).
- Rahmani, N.H.G. et al., 2004. Evolution of Asphaltene Floc Size Distribution in Organic Solvents under Shear, *Chem. Eng. Sci.*, **59**, 685–697.
- Rao, F., Liu, Q., 2013. Froth Treatment in Athabasca Oil Sands Bitumen Recovery Process : A Review. *Energy and Fuels*, **27**, 7199–7207, doi:10.1021/ef4016697.
- Ribeiro, M., 2004. Non-Invasive System and Procedures for the Characterization of Liquid–Liquid dispersions, *Chem. Eng. J.*, **97**, 173–182, doi:10.1016/S1385-8947(03)00179-7.
- Romanova, U.G. et al., 2004. The Effect of Bitumen Extraction Shear Conditions on Froth Treatment Performance, *Pet. Soc. Canada*, 1–3, doi:http://dx.doi.org/10.2118/2004-028-EA.

- Rourke, A.M.O., Macloughlin, P.F., 2005. A Comparison of Measurement Techniques Used in the Analysis of Evolving Liquid – Liquid Dispersions, **44**, 885–894, doi:10.1016/j.cep.2004.10.001.
- Rushton, J.H. et al., 1950. Power Characteristics of Mixing Impellers, *Chem. Eng. Prog.*, **46**, 395–404.
- Russ, J.C., 2011. Chapter 7: Processing Binary Images, in: *The Image Processing Handbook, Sixth Edition*, CRC Press, doi:10.1201/b10720-9.
- Russ, J.C., 2002a. Chapter 10: Feature Recognition and Classification, in: *The Image Processing Handbook, Fourth Edition*, CRC Press, doi:10.1201/9781420040760.ch10.
- Russ, J.C., 2002b. Chapter 9: Feature-Specific Measurements, in: *The Image Processing Handbook, Fourth Edition*, CRC Press, doi:10.1201/9781420040760.ch9.
- Russ, J.C., 2002c. Chapter 8: Global Image Measurements, in: *The Image Processing Handbook, Fourth Edition*, CRC Press, doi:10.1201/9781420040760.ch8.
- Schramm, L.L., 1992. Chapter 1: Petroleum Emulsions: Basic Principles, in: Schramm, L.L. (Ed.), *Emulsions: Fundamentals and Applications in the Petroleum Industry*, American Chemical Society, Washington, DC, 1–49.
- Selomulya, C. et al., 2002. Aggregation Mechanisms of Latex of Different Particle Sizes in a Controlled Shear Environment, *Langmuir*, **18**, 1974–1984.
- Serra, T., Casamitjana, X., 1998. Effect of the Shear and Volume Fraction on the Aggregation and Breakup of Particles, *AIChE J.*, **44**, 1724–1730.
- Seyer, F., Gyte, C., 1989. Chapter 7: Viscosity, in: Hepler, L., Hsi, C. (Eds.), *AOSTRA Technical Handbook on Oil Sands, Bitumens and Heavy Oils*, Alberta Oil Sands Technology and Research Authority, Edmonton, 181.
- Shelfantook, W.E., 2004. A Perspective on the Selection of Froth Treatment Processes, *Can. J. Chem. Eng.*, **82**, 704–709.
- Sjöblom, J. et al., 2007. Chapter 21: The Role of Asphaltenes in Stabilizing Water-in-Crude Oil Emulsions, in: Mullins, O.C. et al. (Eds.), *Asphaltenes, Heavy Oils, and Petroleomics*, Springer Science and Business Media, 580.
- Skinner, F.K. et al., 1989. Contact Angle Measurements from the Contact Diameter of Sessile Drops by Means of a Modified Axisymmetric Drop Shape Analysis, *J. Colloid Interface Sci.*, **130**, 25–34, doi:http://dx.doi.org/10.1016/0021-9797(89)90074-X.

- Smets, K. et al., 2011. Water Content of Pyrolysis Oil: Comparison between Karl Fischer Titration, GC/MS-Corrected Azeotropic Distillation and <sup>1</sup>H NMR Spectroscopy, *J. Anal. Appl. Pyrolysis*, **90**, 100–105, doi:10.1016/j.jaap.2010.10.010.
- Solovyev, A. et al., 2006. Langmuir Films of Bitumen at Oil / Water Interfaces, *Energy and Fuels*, **20**, 1572–1578, doi:10.1021/ef050409f.
- Spicer, P. et al., 1996. The Effect of Impeller Type on Floc Size and Structure during Shear-Induced Flocculation, *J. Colloid Interface Sci.*, **184**, 112–122, doi:http://dx.doi.org/10.1006/jcis.1996.0601.
- Stasiuk, E.N., Schramm, L.L., 2001. The Influence of Solvent and Demulsifier Additions on Nascent Froth Formation during Flotation Recovery of Bitumen from Athabasca Oil Sands, *Fuel Process. Technol.*, **73**, 95–110, doi:http://dx.doi.org/10.1016/S0378-3820(01)00197-7.
- Sullivan, A.P., Kilpatrick, P.K., 2002. The Effects of Inorganic Solid Particles on Water and Crude Oil Emulsion Stability, *Ind. Eng. Chem. Res.*, **41**, 3389–3404, doi:10.1021/ie010927n.
- Tipman, R., 2013. Chapter 7: Froth Treatment, in: Masliyah, J.H. et al. (Eds.), *Handbook on Theory and Practice of Bitumen Recovery from Athabasca Oil Sands, Volume II: Industrial Practice*, Kingsley Knowledge Publishing, 211–253.
- Tobias, P., Croarkin, C. (Eds.), 2003. *NIST/SEMATECH Ebook of Statistical Methods*. National Institute of Standards and Technology, U.S. department of commerce.
- Torbacke, M., Rasmuson, Å.C., 2001. Influence of Different Scales of Mixing in Reaction Crystallization, *Chem. Eng. Sci.*, **56**, 2459–2473, doi:http://dx.doi.org/10.1016/S0009-2509(00)00452-8.
- Yang, X., Czarnecki, J., 2002. The Effect of Naphtha to Bitumen Ratio on Properties of Water in Diluted Bitumen Emulsions, *Colloids Surfaces A Physicochem. Eng. Asp.*, **211**, 213–222, doi:10.1016/S0927-7757(02)00279-0.
- Zawala, J. et al., 2012. Settling Properties of Aggregates in Paraffinic Froth Treatment, *Energy and Fuels*, **26**, 5775–5781, doi:10.1021/ef300885t
- Zhang, L.Y. et al., 2003. Langmuir and Langmuir-Blodgett Films of Mixed Asphaltene and a Demulsifier, *Langmuir*, **19**, 9730–9741, doi:10.1021/la034894n.
- Zhang, Z. et al., 2005. Demulsification by Amphiphilic Dendrimer Copolymers, *J. Colloid Interface Sci.*, **282**, 1–4, doi:http://dx.doi.org/10.1016/j.jcis.2004.08.144.
- Zhou, G., Kresta, S.M., 1996. Distribution of Energy between Convective and Turbulent-Flow for 3 Frequently used Impellers, *Chem. Eng. Res. Des.*, **74**, 379–389.

Zhou, G., Kresta, S.M., 1998. Correlation of Mean Drop Size and Minimum Drop Size with the Turbulence Energy Dissipation and the Flow in an Agitated Tank, Chem. Eng. Sci., doi:10.1016/S0009-2509(97)00438-7.

## Appendix A: Experimental Data

The appendix compiles the complete Karl-Fischer data for all the experiments discussed in the thesis. Table captions indicate where the results are discussed.

**Table A-1:** Water content in wt % determined by Karl-Fischer for diluted bitumen experiments discussed in Chapter 2 (*TS* = Top sampling *CIST*, *SS* = Side sampling *CIST*)

Run	Label	Sampling Height	Settling Time (min)							
			0	1	3	5	7	10	30	60
<i>A</i>	( + - + )	<i>z</i> <sub>1</sub>	0.98	0.97	1.09	0.67	0.55	0.44	0.43	0.29
		<i>z</i> <sub>2</sub>		0.91	0.93	0.83	0.62	0.46	0.39	0.21
	<i>TS</i>	<i>z</i> <sub>3</sub>		1.05	1.05	0.92	0.61	0.48	0.42	0.38
		<i>z</i> <sub>4</sub>		1.02	0.87	0.93	0.74	0.57	0.58	0.38
<i>RA</i>	( + - + )	<i>z</i> <sub>1</sub>	0.88	0.99	0.73	0.64	0.85	0.43	0.30	0.31
		<i>z</i> <sub>2</sub>		1.01	0.89	0.27	0.62	0.39	0.05	0.06
	<i>TS</i>	<i>z</i> <sub>3</sub>		0.93	0.93	0.76	0.58	0.51	0.42	0.25
		<i>z</i> <sub>4</sub>		0.99	0.97	1.03	0.71	0.82	0.38	0.23
<i>B</i>	( + - + )	<i>z</i> <sub>1</sub>	0.53	-	0.43	0.08	0.23	0.34	0.26	0.09
		<i>z</i> <sub>2</sub>		-	0.17	0.21	0.20	0.11	0.34	0.37
	<i>SS</i>	<i>z</i> <sub>3</sub>		-	0.32	0.35	0.07	0.02	0.23	0.05
		<i>z</i> <sub>4</sub>		0.56	-	0.54	0.50	0.54	0.53	0.44
<i>RB</i>	( + - + )	<i>z</i> <sub>1</sub>	0.97	0.87	0.90	0.56	0.21	0.29	0.18	0.31
		<i>z</i> <sub>2</sub>		0.94	0.67	0.85	0.27	0.31	0.41	0.46

	<i>SS</i>	$z_3$		0.91	1.07	1.10	0.64	0.47	0.41	0.26
		$z_4$	0.94	0.93	1.00	1.23	1.85	1.66	0.45	0.26
<b>C</b>	(- + -)	$z_1$	0.63	0.68	0.66	0.69	0.73	0.71	0.71	0.62
		$z_2$		0.63	0.61	0.65	0.62	0.63	0.61	0.62
	<i>TS</i>	$z_3$		0.69	0.68	0.66	0.70	0.67	0.59	0.66
		$z_4$		0.71	0.64	0.72	0.69	0.73	0.68	0.65
<b>RC</b>	(- + -)	$z_1$	0.85	0.82	0.90	0.78	1.00	0.82	0.94	0.53
		$z_2$		0.58	0.91	0.94	0.89	0.90	0.74	0.87
	<i>TS</i>	$z_3$		0.85	1.03	0.98	0.86	0.89	0.81	0.68
		$z_4$		0.61	1.01	0.92	0.74	0.86	0.89	0.83
<b>D</b>	(- + -)	$z_1$	0.34	0.07	0.34	0.39	0.35	0.32	0.06	0.08
		$z_2$		0.11	0.35	0.38	0.42	0.37	0.07	0.19
	<i>SS</i>	$z_3$		0.09	0.36	0.38	0.37	0.37	0.07	0.13
		$z_4$		0.45	0.08	0.38	0.37	0.35	0.37	0.18
<b>RD</b>	(- + -)	$z_1$	0.87	0.81	0.83	0.82	0.85	0.37	0.79	0.87
		$z_2$		0.67	0.86	0.75	0.86	0.50	0.36	0.78
	<i>SS</i>	$z_3$		0.71	0.77	0.86	0.82	0.75	0.83	0.61
		$z_4$		0.88	0.86	0.74	0.62	0.64	0.75	0.63

**Table A-2:** Water content in wt% for repeatability experiments (Table 2-1) discussed in Chapter 2. Top and side samples were taken from the same tank using a needle attached to an auto-pipette. Outliers are highlighted in bold and were identified using Grubbs test.

System	Sampling Orientation	Sampling Height/Time (min)	Sample Number					
			1	2	3	4	5	6
<b>Diluted bitumen-Poor Mixing</b>	Top	$z_2/10$	0.81	0.86	0.73	0.76	0.52	0.89
	Side	$z_2/10$	0.84	0.76	0.79	0.65	0.84	0.81
	Top	$z_3/15$	0.87	0.91	0.78	0.85	0.90	0.88
	Side	$z_3/15$	0.86	0.80	0.81	0.89	0.84	0.88
	Top	$z_4/30$	-	1.97	2.33	2.12	2.06	2.43
	Side	$z_4/30$	0.39	0.80	0.71	0.40	0.82	0.77
<b>Diluted Bitumen-Favorable mixing</b>	Top	$z_2/10$	0.45	0.44	0.35	0.40	<b>0.80</b>	0.38
	Side	$z_2/10$	0.49	0.50	0.46	0.49	0.53	<b>0.30</b>
	Top	$z_3/20$	0.34	0.38	0.38	0.42	0.42	0.44
	Side	$z_3/20$	0.45	0.34	0.35	0.43	0.30	0.42
	Top	$z_4/30$	0.37	0.38	0.19	0.30	0.42	0.47
	Side	$z_4/30$	0.47	0.36	0.47	0.47	0.44	0.50
<b>Water-Mineral Oil</b>	Top	$z_2/10$	0.99	1.02	0.78	0.80	0.58	1.04
	Side	$z_2/10$	1.64	1.30	1.23	1.05	1.01	0.91
	Top	$z_3/20$	1.61	1.52	1.99	1.75	1.01	1.03
	Side	$z_3/20$	1.41	1.35	1.13	1.57	1.73	1.67
	Top	$z_4/30$	0.69	0.59	0.71	0.58	0.68	<b>1.24</b>
	Side	$z_4/30$	0.87	0.51	0.49	0.80	0.52	0.57

**Table A-3:** Water content in wt% for full profile comparison (Figure 2-5) of top vs. side sampling in water-mineral oil system. Top and side samples were taken from the same tank using a needle attached to an auto-pipette.

Sampling Orientation	Sampling Height	Settling Time (min)						
		1	3	5	7	10	30	60
Side	$z_2$	3.32	3.92	3.93	2.59	2.51	0.70	0.42
Side	$z_4$	1.28	1.27	1.40	1.43	0.61	0.57	0.49
Top	$z_2$	2.78	2.60	2.03	1.54	1.06	0.50	0.43
Top	$z_4$	1.02	1.08	1.12	0.87	1.17	0.71	0.93

**Table A-4:** Water content in wt% determined by Karl-Fischer for bitumen froth experiments at  $BC = 150$  ppm, discussed in Chapter 4

Run	Label ( $X_J, X_{IC}$ )	Sampling Height	Settling Time (min)						
			0	3	5	7	10	30	60
<b>1 (NDI)</b>	(+ N/A*)	$z_1$	12.55	1.97	2.11	3.97	0.71	2.39	2.55
		$z_4$	7.69	4.85	25.29	26.38	14.44	4.79	3.70
<b>2 (CRI)</b>	(0 0 Rushton)	$z_1$	13.71	10.84	10.11	11.60	10.97	0.49	0.37
		$z_4$	19.64	20.06	18.25	20.17	21.75	19.30	24.31
<b>3 (CAI)</b>	(0 0 A310)	$z_1$	13.15	10.41	2.24	1.98	1.79	1.07	0.84
		$z_4$	17.26	19.90	23.22	25.41	29.42	34.75	36.55
<b>4 (CA2)</b>	(0 0 A310)	$z_1$	21.82	14.64	13.20	0.88	1.23	0.45	0.56
		$z_4$	17.23	18.95	24.29	26.02	30.02	35.60	39.34

<b>5 (ND2)</b>	(+ N/A*)	$z_1$	17.21	5.49	0.62	4.05	3.64	1.96	1.45
		$z_4$	18.37	15.44	27.04	31.11	31.62	7.81	7.83
<b>6 (FD3)</b>	(- -)	$z_1$	16.71	12.02	10.97	3.59	2.91	1.23	1.42
		$z_2$		16.55	15.91	13.58	11.33	0.69	0.34
		$z_3$		17.52	15.97	13.31	16.10	0.53	0.62
		$z_4$	20.19	18.71	19.02	22.83	29.37	38.40	38.56
<b>7 (FD1)</b>	(+-)	$z_1$	18.13	15.27	14.40	2.46	1.46	0.28	0.89
		$z_2$		15.25	18.06	18.19	16.08	0.26	0.41
		$z_3$		19.49	19.52	19.16	16.93	14.00	0.85
		$z_4$	11.93	20.82	23.09	24.73	28.18	33.99	36.83
<b>8 (CR2)</b>	(0 0 Rushton)	$z_1$	17.95	14.48	14.19	8.93	0.85	0.22	0.27
		$z_4$	12.05	14.62	15.66	15.55	25.80	32.88	37.55
<b>9 (FD4)</b>	(- +)	$z_1$	19.66	13.13	10.31	6.99	6.12	3.46	2.51
		$z_2$		15.23	15.70	13.60	10.59	3.45	2.44
		$z_3$		19.18	17.10	14.45	14.55	5.10	1.87
		$z_4$	18.94	19.83	18.74	18.90	24.20	40.90	38.75
<b>10 (FD2)</b>	(++)	$z_1$	18.91	16.99	16.41	16.19	4.27	0.60	0.22
		$z_2$		18.02	17.83	17.92	16.87	0.26	0.36
		$z_3$		12.91	21.53	18.01	17.39	24.47	4.40
		$z_4$	15.78	19.02	19.96	20.58	23.02	36.65	35.36

\*N/A Not applicable

**Table A-5:** Solid concentration (*OWS* and *EXM*) and water concentration (*OWS*) in wt% for bitumen froth experiments at BC = 150 ppm, discussed in Chapter 4

<b>Run</b>	<b>Label (<math>X_J, X_{IC}</math>)</b>	<b><i>OWS</i> Water</b>			<b><i>OWS</i> Solid</b>			<b><i>EXM</i> Solid</b>	
		<b>Top</b>	<b>Mid</b>	<b>Btm</b>	<b>Top</b>	<b>Mid</b>	<b>Btm</b>	<b>Top</b>	<b>Btm</b>
<b>1(ND1)</b>	(+ N/A*)	2.50	2.37	10.58	1.12	1.12	3.29	0.93	5.52
<b>2(CR1)</b>	(0 0 RT)	0.62	0.49	46.63	0.21	0.16	10.16	0.07	10.63
<b>3(CA1)</b>	(0 0 A310)	1.30	1.08	39.95	0.50	0.52	10.22	0.35	7.09
<b>4(CA2)</b>	(0 0 A310)	1.68	1.02	39.6	0.59	0.58	10.12	0.29	9.57
<b>5(ND2)</b>	(+ N/A*)	3.12	3.03	16.44	1.43	1.34	5.01	1.00	13.00
<b>6(FD3)</b>	(- -)	1.79	1.36	41.51	0.83	0.81	11.24	0.51	11.06
<b>7(FD1)</b>	(+ -)	1.06	0.94	38.57	0.65	0.57	9.76	0.31	7.81
<b>8(CR2)</b>	(0 0 RT)	0.74	0.62	37.3	0.39	0.41	10.51	0.14	10.72
<b>9(FD4)</b>	(- +)	2.99	3.16	26.59	1.17	1.09	6.51	0.92	6.04
<b>10(FD2)</b>	(+ +)	0.42	0.36	38.46	0.27	0.30	10.98	0.19	8.25

\*N/A Not applicable

## Appendix B1: Repeatability Experiments (Side vs. Top Sampling) for Diluted Bitumen

This experimental procedure was followed for comparing the side and top sampling *CIST* for diluted bitumen at favorable mixing conditions (Rushton impellers with  $N = 600$  rpm,  $t_{mix} = 10$  min,  $J = 24000$  J/kg,  $BC = 50$  ppm,  $IC = 3$  wt %). Water was added to one can of sample that had a water content less than 0.5 wt%. This appendix is referred to in Chapter 2.

### Before the Experiment

- Keep the diluted bitumen cans in the fridge at 5°C
- Needles
  - Silanize
  - Mark needles for insertion depth
    - Side sampling needles (45 mm for sample  $z_1$ , 60 mm for samples  $z_2$ ,  $z_3$  and  $z_4$ )
    - Top sampling needles (115 mm for  $z_1$ , 160 mm for  $z_2$ , 205 mm for  $z_3$  and 250 mm for  $z_4$ )
  - Attach needles to pipette tips using duck tape
- Microscope slides
  - Silanize and label
- Pasteur pipettes for dropping sample on slide
  - Silanize
- Label *OWS* bottles for analysis (refer to Appendix C1)
  - Cut plastic tubing for three sampling depths (from sampling port above tank lid): 115 mm, 205 mm and 295 mm for  $z/H = 0.1$ ,  $z/H = 0.5$  and  $z/H = 0.9$
  - Attach tubing to 100 ml glass syringes with duck tape
- Label 20 ml glass vials and weigh them for Karl-Fischer analysis
- *CIST* preparation

- Install septum inside sampling ports making sure septa are not buckled. Screw in teflon blocks over sampling ports (Side sampling *CIST*)
- Put baffles and teflon bearing at the bottom of *CIST*
- The *CISTs* are supported inside the fume hood and secured against the back support plate using Velcro
- Rushton impellers are mounted on the shaft. The motor is set at 600 rpm for 10 min. Do not run impellers yet.
- Load demulsifier in syringe and prepare syringe pump. The demulsifier injection pipe is marked for insertion depth (86 mm from injection port installed above tank lid).
- Hook up ethylene glycol lines

### **Morning of the Experiment**

- Take diluted bitumen can out of the fridge, agitate by hand back and forth 5 times (to re-suspend water and solids) and store in the fume hood until the bath is heated up
- Heat shaker table bath to 85°C
- Start ethylene glycol circulation to and from *CIST* at 76.5°C but limit the flow until the diluted bitumen is transferred
- Adding water to Premix can: Prepare one syringe for water injection in premix can (if needed) and another syringe with 3 wt % demulsifier for injection in the *CIST*
- Label both connecting tubes for injection just above the impeller tip.

### **Premixing (Normal)**

- Heat diluted bitumen can to 60°C in 30 min without mixing
- Once diluted bitumen reaches 60°C, install 45° *PBTD* impeller with  $D = T/2 = 0.08$  m and four  $T/10$  baffles. Mix at 1000 rpm for 15 min while it heats up to 76.5°C

- Once premix is complete, fully open the inlet and outlet ethylene glycol circulation valves to the *CIST*
- Start masterflex pump to transfer diluted bitumen to *CIST*

### **Premixing (with Water Injection into Can, if Needed)**

- Heat diluted bitumen can to 60°C in 30 min without mixing
- After 10 min of premixing, stop the impellers and take a sample from top and bottom of can. If the water content drops below 0.5 wt%, bring it back to 1.0 wt% by adding ultrapure deionized water.
- Once diluted bitumen reaches 60°C, add ultrapure deionized water at following conditions
  - 45° *PBTD* impeller with  $D = T/2 = 0.08$  m and four  $T/10$  baffles
  - x ml water injection (Target 1 wt% water in diluted bitumen) at 634.7 ml/hr
  - Impeller speed = 1000 rpm
  - Impeller mixing time = 15 (Normal) + Injection time + 5 min
  - Target temperature = 76.5°C (Record temperature)
  - Take additional samples from the top and bottom of the can after adding water and suspending for 5 min. If the water does not reach target 1 wt%, then inject more water and suspend for another 5 min and take another reading to verify the water content.
- Once premix is complete, fully open the inlet and outlet ethylene glycol circulation valves to the *CIST*
- Start masterflex pump to transfer diluted bitumen to the *CIST*

### **Demulsifier Dispersion**

- Install teflon lid on the side sampling *CIST*
- Start Rushton impellers at 600 rpm
- After 5 s, inject demulsifier at  $BC = 50$  ppm and  $IC = 12$  wt% using syringe pump at the plane of top impeller

- Mix for 10 min and motor will stop

## Sampling

- Start stop watch when the impeller stops (settling time = 0 min)
- Take samples as per sampling schedule below

**Table B1-1:** Sampling schedule followed for diluted bitumen repeatability (*italics*) experiments. Sample volume = 1 ml

		Sampling Location	Time
<b>Premix</b>		Premixing can-top and bottom check sample	10 minutes after premixing. Add 5 min of mixing and additional sample if more water is added.
		Premixing can-top and bottom	After water addition at the end of premixing
		1 <i>OWS</i> sample from can	End of premixing
<b>Demulsifier Dispersion</b>			60 s after demulsifier addition
		<i>CIST</i> heights $z_1, z_4$	30 s before end of mixing
<b>Settling (Side Sampling Profile)</b>			1 min of settling
			3 min of settling
			5 min of settling
		<i>CIST</i> heights $z_1, z_2, z_3, z_4$	7 min of settling
			10 min of settling
			30 min of settling
			60 min of settling
<b>Repeatability Samples</b>		<i>6 samples-Side at height <math>z_2</math></i>	<i>10 min of settling*</i>
		<i>6 samples-Top at height <math>z_2</math></i>	<i>10 min of settling</i>
		<i>6 samples-Side at height <math>z_3</math></i>	<i>15 min of settling*</i>
		<i>6 samples-Top at height <math>z_3</math></i>	<i>15 min of settling</i>
		<i>6 samples-Side at height <math>z_4</math></i>	<i>30 min of settling*</i>
		<i>6 samples-Top at height <math>z_4</math></i>	<i>30 min of settling</i>
<b>OWS</b>		100 ml samples at $z/H=0.1,0.5,0.9$	End of settling

\*after regular settling samples are taken

## Appendix B2: Repeatability Experiments (Side vs. Top sampling) for Water in Mineral Oil

This experimental procedure was followed while comparing side vs. top sampling in a single side sampling *CIST* using repeatability tests and full profile comparison. The repeatability test involved withdrawing multiple samples from one sampling location using both techniques. For full profile comparison, sampling techniques were compared by taking samples at two heights over the settling time. This appendix is discussed in Chapter 2.

### Before the Experiment

- Needles
  - Silanize
  - Mark needles for insertion depth
    - Side sampling needles (45 mm for sample  $z_1$ , 60 mm for samples  $z_2$ ,  $z_3$  and  $z_4$ )
    - Top sampling needles (115 mm for  $z_1$ , 160 mm for  $z_2$ , 205 mm for  $z_3$  and 250 mm for  $z_4$ )
  - Attach needles to pipette tips using duck tape
- Microscope slides
  - Silanize and label
- Pasteur pipettes for dropping sample on slide
  - Silanize
- Label 20 ml glass vials and weigh them for Karl-Fischer analysis
- Side sampling *CIST* preparation
  - Install septum inside sampling ports making sure septa are not buckled.  
Screw in teflon blocks over sampling ports
  - Put baffles and teflon bearing at the bottom of *CIST*
  - *CIST* is supported inside the fume hood and secured against back support plate using Velcro

- Rushton impellers are mounted on the shaft. The motor is set at 600 rpm for 15 min. Do not run impellers yet.
- The injection pipe is marked for insertion depth (86 mm from injection port installed above tank lid)
- Hook up ethylene glycol lines
- Prepare a test emulsion, take a sample and inspect under microscope for
  - Water in oil emulsion
  - Note: Oil in water emulsion was not considered because of Karl-Fischer limitation

### **Emulsion Preparation and Surfactant Dispersion**

- No need to circulate ethylene glycol through *CIST* as the experiment is conducted at room temperature
- Add 950 ml of Crystal Plus 70FG mineral Oil into *CIST*
- Install Rushton impellers, baffles and run at 600 rpm
- Add Tergitol NP-4 surfactant at  $5 \times 10^{-4}$  mol/L to *CIST* because surfactant is oil soluble. (To prepare oil in water emulsion, use Tergitol NP-7 surfactant pre-dissolved in water before injecting oil into *CIST*)
- Add 50 ml of ultrapure deionized water at 634.7 ml/hr (target = 5.7 wt % water) using syringe pump above the upper impeller
- After water addition, run impellers for 10 min
- Total mixing time = 5 min (water addition) + 10 min (dispersion) = 15 min

### **Sampling**

- Start stop watch when the impeller stops (settling time = 0 min)
- Take samples as per sampling schedule below

**Table B2-1:** Sampling schedule followed for water in mineral oil for repeatability (italics) and full profile experiments. Sample volume = 1 ml

	<b>Sampling Location</b>	<b>Time</b>
<b>Mixing</b>	Water Dispersion-heights $z_1, z_4$	60 s after completion of water addition
		30 s before end of mixing
<b>Settling (Side Sampling Profile)</b>	2 samples-Side at heights $z_2$ and $z_4$	1 min of settling
		3 min of settling
		5 min of settling
		7 min of settling
		10 min of settling
		30 min of settling
		60 min of settling
<b>Repeatability Samples</b>	<i>6 samples-Side at height <math>z_2</math></i>	<i>10 min of settling*</i>
	<i>6 samples-Top at height <math>z_2</math></i>	<i>10 min of settling</i>
	<i>6 samples-Side at height <math>z_3</math></i>	<i>20 min of settling*</i>
	<i>6 samples-Top at height <math>z_3</math></i>	<i>20 min of settling</i>
	<i>6 samples-Side at height <math>z_4</math></i>	<i>30 min of settling*</i>
	<i>6 samples-Top at height <math>z_4</math></i>	<i>30 min of settling</i>
<b>Settling (Top Sampling Profile)</b>	2 samples-Top at heights $z_2$ and $z_4$	1 min of settling
		3 min of settling
		5 min of settling
		7 min of settling
		10 min of settling
		30 min of settling
		60 min of settling

\*after regular settling samples are taken

## Appendix B3: Bitumen Froth Experimental Procedure

The bitumen froth experiments discussed in Chapter 4 were conducted using the following procedure. The addition order was [(Froth + Naphtha) + Demulsifier].

### Before the Experiment

- Store the froth cans in fridge, turned upside down at 5°C to bring water and solids close to lid surface and hence easier to suspend to create worst case emulsification scenario. Ensure that the lids are tight to prevent leakage.
- Needles
  - Silanize
  - Chop pipette tips using plate with standard hole (1.5 mm diameter).
  - Mark needles for insertion depth (45 mm for  $r/R = 0.9$ , all sampling heights)
  - Attach needles to pipette tips using duck tape
- Microscope slides
  - Silanize and label (Table B3-1)
- Pasteur pipettes for dropping sample on slide
  - Silanize
- Label *OWS/CPA/EXM* bottles for analysis (refer to Appendix C1)
  - Cut plastic tubing for three sampling depths (from sampling tube from *CIST* top without lid installed)
    - 58 mm for  $z/H = 0.1$
    - 150 mm for  $z/H = 0.5$
    - 242 mm for  $z/H = 0.9$
  - Attach tubing to 100 ml glass syringe with duck tape.
- Label 20 ml glass vials and weigh them for Karl-Fischer analysis
- Froth can variance
  - Different cans had widely varying amounts of froth

- For controlling liquid level in *CIST* at 1L mark, one froth can was heated and premixed to disperse water and solids uniformly and then transferred to several cans until each can weight was ~780 g (including lid)

## Morning of the Experiment

- Take the **upside down** can out of fridge and keep in fume hood in the same orientation
- Turn the ethylene glycol bath on
- Side sampling *CIST* preparation
  - Install septum inside sampling ports making sure septa are not buckled. Screw in teflon blocks over sampling ports
  - Put baffles and teflon bearing at the bottom of *CIST*
  - Install impellers (Rushton, Intermig or A310) on shaft in *CIST*
  - Set *CIST* in fume hood and secured against the back support plate using Velcro
- Prepare demulsifier at 12 % ( $X_{IC} = -1$ ), 16.5 % ( $X_{IC} = 0$ ) or 21 % ( $X_{IC} = +1$ ) by weight according to the experiment performed as per Table B3-2 and Table B3-3
- Load demulsifier in syringe and prepare syringe pump. Enter injection rate and volume as per Table B3-3. The demulsifier injection pipe is marked for insertion depth (86 mm from injection port installed above tank lid)

## Premixing

- Heat shaker table bath to 82°C for at least 1 hour
- Measure the weight of froth can and based on  $N/B = 0.7$  (by weight), fill naphtha in another can and cover with aluminium foil
- Heat froth can to 70°C for 1.5 hours without mixing
- Install *CIST* in fume hood and start ethylene glycol circulation and heating to 80°C
- Heat naphtha can for 30 min

- Once froth reaches 70°C, install 45° *PBTD* impeller with  $D = T/2 = 0.06$  m and two T/10 baffles. Mix at 1000 rpm for 15 min while it heats up to 80°C
- Both froth premixing and naphtha should be ready for transferring to the *CIST* at the same time

## Naphtha Blending

- Transfer heated naphtha to *CIST* first, followed by froth using thermal glove
- Install teflon lid on side sampling *CIST*
- Set impeller speed (rpm) and time (min) as per Table B3-3

## Demulsifier Dispersion

- After naphtha blending, set impeller speed (rpm), time (min) and demulsifier dosage as per Table B3-3
- After 5 s of starting impellers, inject demulsifier at  $BC = 150$  ppm using syringe pump at the plane of top impeller

## Sampling

- Start stop watch when the impeller stops (settling time = 0 min)
- Take samples as per sampling schedule below
- For end of run samples (*OWS/ CPA/ EXM* analysis), start sampling from top and then move down such that the disturbance of fluid is minimized
  - Collect approximately 120 ml for top sample and distribute 100 ml in *DS\_1* and rest in *EXM\_11* bottles
  - Collect 100 ml for middle sample and discharge in *DS\_2* bottle
  - Collect approximately 120 ml for bottom sample and distribute 100 ml in *DS\_3* and rest in *EXM\_12* bottles
  - Take two samples for *FBRM*: 200 ml sample from top and bottom each

**Table B3-1:** Sampling schedule and labelling criteria for bitumen froth experiments

<b>Label</b>	<b>Time</b>	<b>Location</b>	<b>Analysis</b>	<b>No of samples</b>
<i>P</i>	End of premixing	Just below the liquid surface	<i>KF</i>	1
<i>A</i>	End of naphtha blending	$z_1$ mm below the liquid surface	<i>KF</i> , Microscope	1
<i>B</i>	During demulsifier dispersion (30 s before mixing ends)	$z_1$ and $z_4$	<i>KF</i> , Microscope	2
<i>3, 5, 7, 10, 30, 60</i>	During settling	( $z_1, z_4$ ) or ( $z_1, z_2, z_3, z_4$ )	<i>KF</i> , Microscope	12 or 24
<i>DS_1, DS_2, DS_3</i>	End of settling	At $z/H = 0.1, 0.5, 0.9$	<i>OWS (DS, CPA):</i> 100 ml each	3
<i>EXM_11, EXM_12</i>	End of settling	At $z/H = 0.1$ and $0.9$	<i>EXM:</i> 15ml each	2
<i>FBRM_B, FBRM_T</i>	After <i>DS</i> and <i>EXM</i> samples	B – bottom section	<i>FBRM:</i> 200 ml each	2

**Table B3-2:** Variable range for demulsifier dispersion in bitumen froth experiments using Rushton (*RT*), *A310* and Intermig (*IM*) impellers

	Variable Code ( $X_i$ )			
	- ( <i>IM</i> )	0 ( <i>A310</i> )	0 ( <i>RT</i> )	+ ( <i>RT</i> )
<i>BC</i> (ppm)			150	
<i>IC</i> (wt%)	<b>12</b>	<b>16.5</b>	<b>16.5</b>	<b>21</b>
<i>J</i> (J/kg)	<b>425</b>	<b>12164</b>	<b>12120</b>	<b>22778</b>
<i>N</i> (rpm)	400	1000	485	600
$\epsilon_{imp}$ (W/kg)	3.5	22.5	22.4	38.0
$t_{mix}$ (min)	2	9	9	10

**Table B3-3:** Operating conditions and run summary for bitumen froth experiments using Rushton (*RT*), *A310* and Intermig (*IM*) impellers

$X_J$ , $X_{IC}$	Run	Naphtha Blending	Demulsifier Dispersion	Demulsifier Injection	
				Rate (ml/hr)	Volume (ml)
+ <i>N/A</i>	<i>ND1</i>	<i>RT</i> (600 rpm, 2 min)	<i>RT</i> (600 rpm, 10 min)	-	-
+ <i>N/A</i>	<i>ND2</i>	<i>RT</i> (600 rpm, 2 min)	<i>RT</i> (600 rpm, 10 min)	-	-
+ -	<i>FD1</i>	<i>RT</i> (600 rpm, 2 min)	<i>RT</i> (600 rpm, 10 min)	634.7	1.2
++	<i>FD2</i>	<i>RT</i> (600 rpm, 2 min)	<i>RT</i> (600 rpm, 10 min)	634.7	0.7
--	<i>FD3</i>	<i>IM</i> (1060 rpm, 2 min)	<i>IM</i> (400 rpm, 2min)	125.1	1.2
- +	<i>FD4</i>	<i>IM</i> (1060 rpm, 2 min)	<i>IM</i> (400 rpm, 2min)	125.1	0.7
0 0	<i>CR1</i>	<i>RT</i> (600 rpm, 2 min)	<i>RT</i> (485 rpm, 9 min)	594.9	0.9
0 0	<i>CR2</i>	<i>RT</i> (600 rpm, 2 min)	<i>RT</i> (485 rpm, 9 min)	594.9	0.9
0 0	<i>CA1</i>	<i>A310</i> (1250 rpm, 2 min)	<i>A310</i> (1000 rpm, 9 min)	207.7	0.9
0 0	<i>CA2</i>	<i>A310</i> (1250 rpm, 2 min)	<i>A310</i> (1000 rpm, 9 min)	207.7	0.9

*N/A* Not Applicable

*FD* runs had samples taken at 4 heights, other runs at 2 heights

## Appendix C1: Standard Operating Procedure for Sending *OWS/CPA/EXM* Samples to Syncrude

This Procedure applies to diluted bitumen samples that are sent to Syncrude for *OWS* (oil, water and solids), *CPA* (Computerized Particle Analyzer) and *EXM* (Extraneous matter) analysis. This analysis is a part of bitumen froth experiments (Chapter 4).

### Sample Information

The following samples are taken during experiment at the end of 60 min settling period using tubing connected to a 100 mL glass syringe.

**Table C3-1:** The labelling criteria for end of run samples

Tag	<i>CIST</i> Sampling location	Sample Quantity (ml)	Analysis	Sample Tag Checkbox
Run#- <i>DS</i> _1	Top ( $z/H=0.1$ )	100	<i>OWS, CPA</i>	<i>UFX, CPA</i>
Run#- <i>DS</i> _2	Middle ( $z/H=0.5$ )	100	<i>OWS, CPA</i>	<i>UFX, CPA</i>
Run#- <i>DS</i> _3	Bottom ( $z/H=0.9$ )	100	<i>OWS, CPA</i>	<i>UFX, CPA</i>
Run#- <i>EXM</i> _11	Top ( $z/H=0.1$ )	15	<i>EXM</i>	<i>EXM</i>
Run#- <i>EXM</i> _12	Bottom ( $z/H=0.9$ )	15	<i>EXM</i>	<i>EXM</i>

*UFX* refers to *OWS* analysis

### Procedure

1. Ensure samples are bottled correctly in 100 mL sample bottles with alternative cap (Qorpak Catalogue: CAP-00268).
2. **Fill out a sample tag for each sample ensuring separate series for *CPA/OWS* and *EXM* analysis.** These are provided by Syncrude in the form of a booklet. Fill them out as follows:
  - a. Date and time of the sample taken
  - b. Submitter: U of A
  - c. Stream: Your identifier. Put a tag such as Run #-Sample A.
  - d. Work order: Leave it empty. Syncrude will fill this part.
  - e. Wet/dry/pan: Leave it empty.

- f. Check the desired tests: *CPA*, *EXM*, and *OWS* (*EXM* must be written in).
3. Keep the left side of the sample tag for matching up with the data received later and for tracking. Affix the right sample tag to the sample with a rubber band and ensure it is secure. Copy the serial numbers and stream names into lab records.
  4. Put the samples into a box in numerical order, with consecutive tag numbers if possible, and write “start here” at the first sample.
  5. Tighten all the sample bottle lids to make sure that none of them leak.
  6. Put a “This Side Up” sticker on the box and indicate the top very clearly with the arrow. Leakage can occur as a result of placing the box upside-down.
  7. **Store the sample box in the refrigerator until pick-up.**
  8. Shipping Guidelines:
    - a. Inform Allan ([yeung.allan@syncrude.com](mailto:yeung.allan@syncrude.com)) in advance that he will be receiving samples.
    - b. Pack/repack the samples according to Transportation of Dangerous Goods (*TDG*) requirements (must be trained in *TDG* or get help from Andrée ([akoenig@ualberta.ca](mailto:akoenig@ualberta.ca)) or other *TDG* certified person). Print and attach “Instructions for courier” on the last page of this Appendix.
    - c. Fill out the [shipping form](#) located on the department website and get it signed by Marcio or Dr. Kresta. The signed shipping form, the *TDG* ground form, your *TDG* training record, and the applicable *MSDS* should be sent to *SMS* (780-492-4121; [shipping@ualberta.ca](mailto:shipping@ualberta.ca)) for review 2-3 days prior to shipping day. Wait for *SMS* approval before sending the samples.
    - d. **It is extremely important that the samples be delivered on the same day as shipping day.** Matt Express ([780-944-1582](tel:780-944-1582)) provides same day shipping. Matt Express can pick up the samples from you directly (**not through *SMS***) if you are certified in *TDG* (Transportation of Dangerous Goods) and you have complete paper work (*MSDS*, shipping form, *TDG* ground form).
    - e. Syncrude delivery address

**Allan Yeung**

Syncrude Canada Ltd

Research and Development Centre

9421-17 Avenue NW

Edmonton, AB T6N 1H4

E: [yeung.allan@syncrude.com](mailto:yeung.allan@syncrude.com) T: 780-970-6942

## **INSTRUCTION FOR COURIER:**

- **PERISHABLE ITEMS, DELIVER WITHIN SAME DAY**
- **HANDLE WITH CARE (GLASS BOTTLES)**
- **TDG CHEMICALS**
- **LOOK FOR “THIS SIDE UP”**

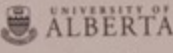
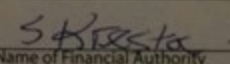
 <b>UNIVERSITY OF ALBERTA</b> Supply Management Services Distribution Operations Edmonton, AB T6G 2R3	<b>SHIPPING FORM</b>	<b>Information and Assistance</b> Shipping: 492-4121 / 2739      Customs: 492-4121 Mailroom: 492-4732 / 3231      Pick up/Dispatch: 492-4122 Dangerous Goods Info: 492-4121	
		Customer Reference Number <b>KJJK0941</b>	
<b>CONSIGNEE (SHIP TO)</b>			
Individual Name <b>Allan Yeung</b>		Company Name <b>Syncrude Canada Ltd</b>	
Address <b>Research and Development Centre</b>		Phone <b>780-970-6942</b>	
Address <b>9421-17 Avenue NW</b>		City <b>Edmonton</b>	
Prov./State <b>Alberta</b>	Country <b>Canada</b>	Postal (ZIP) Code <b>T6N 1H4</b>	
<b>PAYMENT</b>			
<input checked="" type="radio"/> Prepaid <b>ZD017502115</b> <small>charge to U of A speed code /account</small>		<input type="radio"/> Collect <input type="radio"/> Third Party <small>charge to carrier account</small>	
<b>CONSIGNOR (SHIP FROM)</b>		via (carrier) _____	
Individual Name <b>Colin Saraka/Nitin Arora</b>		email <b>saraka@ualberta.ca</b>	
University Department <b>Chemical and Materials Engineering</b>		Phone <b>306-280-0357/780-932-0</b>	
<b>SHIPPING INSTRUCTIONS</b>			
<input type="checkbox"/> Speed Essential <small>deliver by: (date)</small>		Number of Pieces <b>1</b>	Weight <b>1.9</b> <input type="radio"/> lbs <input checked="" type="radio"/> kgs
Special Instructions: (e.g. specific carrier, traceability)		<b>deliver within same day (Perishable Items)</b>	
<b>REASON FOR SHIPPING:</b>			
<input type="radio"/> Sold <input checked="" type="radio"/> Research <input type="radio"/> Repair <input type="radio"/> Return to Supplier: (return authorization number): _____			
<input type="radio"/> On Loan <input type="radio"/> Other (specify): _____			
<b>DANGEROUS GOODS</b>			
<input type="radio"/> Shipment contains dangerous goods. Shippers declaration not required.		SPECIFY CONTENTS: <b>Petroleum naphtha distillates</b>	
<input type="radio"/> Shipment contains no dangerous goods.			
<input checked="" type="radio"/> Dangerous goods as per attached shipper's declaration.			
<b>PLEASE COMPLETE APPLICABLE SECTIONS BELOW FOR ALL ITEMS LEAVING CANADA</b>			
Value _____	Consignee Federal ID Number _____		
Country of Manufacture _____			
Model / Serial Number _____	U of A Tag Number _____		
Description of Goods _____			
<b>SHIPPED VIA:</b>			
CARRIER _____			
DATE _____			
BILL OF LADING NUMBER _____			
COST _____			
<b>SHIPPING OFFICE USE ONLY</b>			
<b>SIGNATURE</b>			
 Name of Financial Authority		 Signature of Financial Authority	
			Date: <b>Sep 9, 2015</b>

Figure C1-1: Sample shipping form



## Appendix C2: Standard Operating Procedure for Receiving Feed Material from Syncrude

This procedure is for receiving material such as bitumen froth cans, demulsifier and naphtha from Syncrude.

### Lab (University) Procedure

1. Send an email to Samson ([ng.samson@syncrude.com](mailto:ng.samson@syncrude.com)) or Sujit ([bhattacharya.sujit@syncrude.com](mailto:bhattacharya.sujit@syncrude.com)) requesting material.
2. Once Samson or Sujit approve the request, Allan (contact information below) will send the items.
3. Tell Kevin ([Kevin.Heidebrecht@ualberta.ca](mailto:Kevin.Heidebrecht@ualberta.ca)) that he will be receiving a package soon and ask him to inform you as soon as he does.
4. Unpack the material and store the froth cans in the fridge upside-down, ensuring the lids are on tightly enough to allow this. Naphtha and demulsifier should be stored in flammable storage.
5. Add the received to the chemical receiving form.

### Syncrude Procedure

**Note: Same-day shipment is critical as aging effects have been observed. Minimizing the time outside of refrigerated storage is important.**

1. Store froth at 5°C until courier pickup.
2. Package and prepare for shipment according to *TDG* requirements. The requirement does not apply to shipment of froth only.
3. Ensure someone is available (Nitin 780 932 0507 or Colin 306 280 0357) to receive shipment.
4. Order courier with same-day (not one-day) shipment. Give courier directions to coordinate with receiver at University, and to bypass Supply Management at University. Indicating direct chemical engineering department or lab address would not ensure that supply management at university has been bypassed.

## Shipping Information

Matt Express ([780-944-1582](tel:780-944-1582)) provides same day shipping. Please provide documentation (*MSDS*, shipping form, *TDG* certification etc) to the courier company.

## Delivery address

**Kevin Heidebrecht** (for Nitin Arora/Colin Saraka CME 6-120)

Purchasing and facilities administrator

CME 256

9107, 116 street

Edmonton, AB, Canada

T6G2V4

780-492-0416/780-932-0507/306-280-0357

[Kevin.Heidebrecht@ualberta.ca](mailto:Kevin.Heidebrecht@ualberta.ca)

Please print the instructions on next page and paste on the package for courier company. Before they come for pick up, inform them about same day delivery requirement.

# PRINT OUT FOR COURIER COMPANY

- **PERISHABLE ITEMS, DELIVER WITHIN SAME DAY**
- **DELIVER TO ADDRESSEE DIRECTLY**
- **LOOK FOR “THIS SIDE UP”**
- **TDG CHEMICALS**

## Appendix C3: Lab floor Cleaning and General Housekeeping

Lab floor cleaning and general housekeeping procedures associated with bitumen experiments are discussed here.

### Lab Floor Cleaning

1. Avoid bitumen stains on lab floor. Clean up with toluene immediately.
2. Download 'work requisitions form' from the following link  
[http://www.facilities.ualberta.ca/FO\\_Forms.aspx](http://www.facilities.ualberta.ca/FO_Forms.aspx)
3. Do not request for an estimate cost of cleaning. The cost is 200-300 CAD approximately.
4. Get the speed code and account number from Dr. Kresta.
5. Fill out the form and write the following message
  - a. LAB FLOOR HAS SPILLS OF BITUMEN AND MINERAL OIL THAT NEED TO BE CLEANED. PLEASE DO NOT TOUCH OR MOVE ANY EQUIPMENT FOR CLEANING PURPOSE.
6. Get an authorization signature from Márcio or Dr. Kresta.
7. Once the form is signed, it can be send to Facilities department via following modes
  - a. In person at 4<sup>th</sup> floor General Services building
  - b. Email to [iwc@ualberta.ca](mailto:iwc@ualberta.ca) or [mdesk@ualberta.ca](mailto:mdesk@ualberta.ca)
  - c. Fax to 2-7582

### Housekeeping

1. Complete *WHMIS*, lab and chemical safety training.
2. Store bitumen froth cans in fridge at 5°C.
3. Chemicals to be stored in flammable cabinet
  - a. Toluene
    - i. Lab grade: cleaning bitumen contaminated material
    - ii. Reagent grade: making Unisol for Karl Fischer analysis
  - b. Ethylene glycol (heating media in bath)

- c. Xylene ( diluent for demulsifier, cleaning *KF* cell)
- d. Acetone (used in silanization)
- e. Iso-propanol
  - i. Lab grade: cleaning mineral oil contaminated material
  - ii. Reagent grade: making Unisol for Karl Fischer analysis
- f. Methanol (dissolving precipitates from contaminated KF cell)
- g. Silanization solution (silanization of needles, slides, glass pipettes)
- h. Karl Fischer reagents, naphtha can and demulsifier

Note: Incompatible chemicals should be stored away from each other. This information can be found in *MSDS*.

4. Chemical ordering information in “Lab supplies” sheet placed in mixing folder.
5. Cabinets have been assigned for each tool. After using the tool, please put it back in its original place.
6. Wear appropriate personal protective equipment as per “Hazard assessment form” placed in mixing folder.
7. After performing experiments, clean the bitumen contaminated material as soon as possible. Bitumen along with saline water corrodes steel needles and impellers.
8. Dispose of experimental waste in designated container and label the contents in categories: contaminated glass, chemical pail (for mixture of chemicals) and miscellaneous contaminated material. Friday afternoons are reserved for cleaning.

Note: Stainless steel needles are cleaned and recycled after each experiment. If they wear out, dispose them separately from the above mentioned categories.

9. On the Friday of each week or depending on the experimental frequency, set up waste pick up through Chematix. You will need to create an account first.  
<http://www.ehs.ualberta.ca/EHSDivisions/EnvironmentalServices.aspx>
10. In case of questions, contact Shaofeng Yang ([Shaofeng@ualberta.ca](mailto:Shaofeng@ualberta.ca)), Nitin Arora ([Nitin@ualberta.ca](mailto:Nitin@ualberta.ca)) or Dr. Suzanne Kresta ([Kresta@ualberta.ca](mailto:Kresta@ualberta.ca)).

## Appendix D1: Karl Fischer Procedure

Karl Fischer is standard equipment used to determine the water content in crude oil and organic liquids (“GR Scientific FAQs,” 2015). This procedure was used for the Karl Fischer data discussed in Chapter 2 and Chapter 4. It should be used in addition to the moisture analyzer user manual and ASTM D4928 standard. For any questions, please contact [info@parkesscientific.com](mailto:info@parkesscientific.com)

### Karl Fischer Calibration

The purpose of *KF* calibration is to generate a curve between actual water content (as per water standard) and *KF* measured reading.

1. Use Aqualine water standard AL2710-40 which contains 1000  $\mu\text{g}$  water/ml solution.
2. Break 4 ml ampoule and perform following 5 titrations as soon as possible. Exposure to air will lead to water ingress.
3. Use 25 and 50  $\mu\text{L}$  injection volume using *1705 Hamilton Gastight syringe*, 100, 250 and 500  $\mu\text{L}$  injection volume using *1750 Hamilton Gastight syringe*.
4. Draw sample using syringe **three** times and discharge the sample into waste container. This ensures that sample collected is not contaminated with previous liquid in syringe, and that air bubbles are minimized.
5. Wipe the needle with tissue to remove any excess liquid.
6. Measure syringe weight before and after injection to get the weight of injected liquid. Sometimes, tiny air bubbles are hard to expel and measuring the weight nullifies this effect provided water content is measured in wt% and not vol%.
7. Ensure *KF* reagents are in good condition and do not need to be changed. Press the reset button on moisture analyzer and inject the sample (by dipping the needle into the reagent) through the sample injection port. Record the measured water content in  $\mu\text{g}$ . Calculate the water content in wt% based on the following equation

$$\text{KF measured water, wt\%} = \frac{\text{Karl Fischer water reading, } \mu\text{g}}{(\text{Syr wt before inj, g} - \text{Syr wt after inj, g}) \times 10000}$$

(Equation D1-1)

- Plot measured water content vs. expected water content. The expected water content is typically 969-1029  $\mu\text{g}$  water/g sample injected. Sample calibration curve is given below.

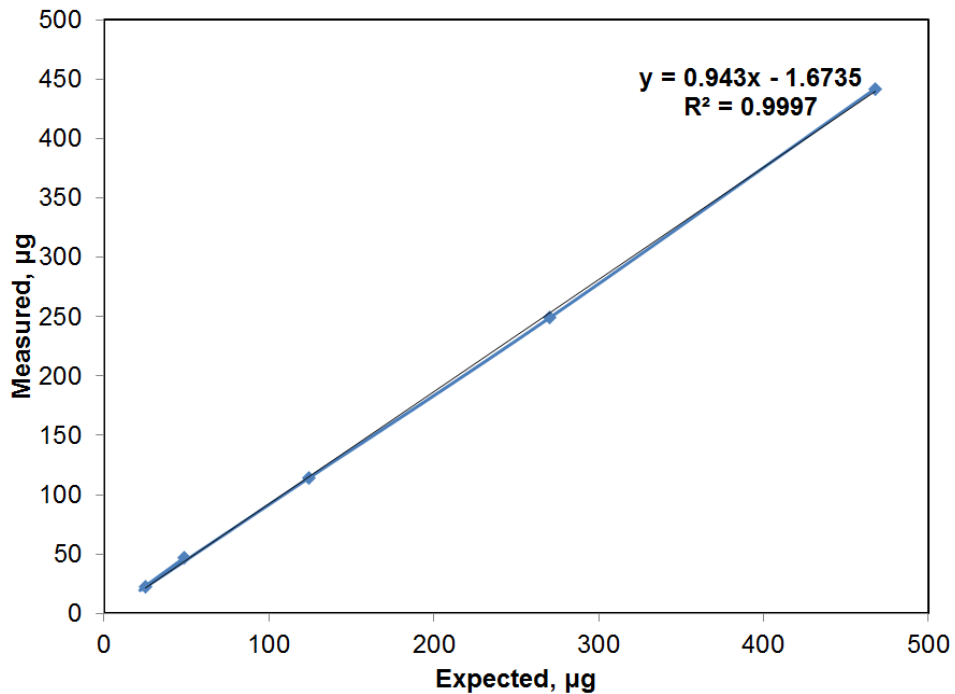


**Figure D1-1:** Karl Fischer calibration curve

## Unisol Preparation

The samples may contain very high water content (~25 wt% in bitumen froth) which may take long time to get an end point and may also be outside the *KF* calibration range. So the samples need to be diluted using Unisol which also increases the life of *KF* reagents. Dilution also decreases the sample viscosity, resulting in easier water droplet dispersion and homogenization required for accurate results.

- Fill 200 mL bottle approximately 75 % full with silica beads.

2. Mix 1 part high-grade 2-propanol with 3 parts high-grade toluene to create Unisol. Approximately 90 mL will fill a 200 mL bottle containing silica beads.
3. Pour into bottle and leave for 1-2 days.
4. Determine water content of Unisol before using it for diluted bitumen samples.
  - a. With chosen syringe, fill and empty 3-5 times to clear syringe of previous samples
  - b. Fill syringe, wipe needle tip, and weigh
  - c. Insert syringe into titration cell (below liquid level) and depress plunger
  - d. Wipe needle tip and weigh again
  - e. Take reading from titration unit and calculate water content

### **Analyzing Bitumen Samples**

1. Weigh empty sample vials prior to experiment.
2. After sample is collected and microscope slide is prepared from sample, clean vials of excess bitumen (outside the vials) and weigh again.
3. Calculate weight of sample and dilute with Unisol according to desired dilution ratio. Dilution ratio varies by sample for bitumen froth and is anywhere from 6 g Unisol / 1 g sample for low-water samples to 20 g Unisol / 1 g sample for high-water samples. Dilution ratios should be chosen by experience and practicality. Filling more than half the sample vial is not recommended as it will lead to spillage. Aiming for readings less than 700 on the titration equipment is recommended for speed. Getting an exact dilution ratio is not essential.
4. The storage vial is agitated on the vortex mixer at 3000 rpm for 20 s. The homogenization time can be increased if the three readings are not consistent.
5. Take sample with syringe, wipe needle tip, and weigh. If it is the first titration with sample, fill and empty 3-5 times to clear syringe of previous samples.
6. Insert syringe into titration cell (below liquid level) and depress plunger.
7. Wipe needle tip and weigh empty.
8. Record water content in  $\mu\text{g}$  water from titration equipment.
9. Correct water content using equation determined by calibration curve.

10. Calculate the bitumen sample water content from measured water content (wt%) by the following equation

Wt% water in Bit sample

$$= \frac{\text{wt\% KF measured water} - \text{wt\% water in Unisol} \times \text{Unisol wt. fraction}}{1 - \text{Unisol wt. fraction}}$$

(Equation D1-2)

11. Check the repeatability of *KF* results. If the sample is homogenized properly, the samples standard deviation/mean should be less than 0.1. From previous experience, very low water content may not be repeatable.

### General Maintenance and Troubleshooting

1. Karl Fischer calibration by the vendor needs to be done once a year. The calibration can be done by Joel or Lance at **Parkes Scientific** (17360-108 Ave, Edmonton, AB T5S 1E8; Tel: 780-484-1849).
2. Silica gel is used in a drying tube to dry the Generator Solution Cell. If silica gel changes color from blue to pink, it is a sign that the silica gel is saturated with water and needs to be replaced.
3. Special “Apiezon M grease” is used at glass to glass contact points to prevent glass freezing and hence facilitates easy removal of *detector electrode* and *cathode solution cell* for cleaning. A thin layer of grease is sufficient. No grease is required for *sample injection port* and *drying tube* as there is no glass-glass contact.
4. The septum in the sample injection port needs to be changed if it stops sealing or gets a view through hole.
5. Electrodes should be cleaned if the generator solution cell seems dirty and precipitates are observed. The procedure given in moisture analyzer user manual involving use of nitric acid and acetone should be avoided. Use the electrode cleaning procedure mentioned below.
6. **Electrode cleaning procedure:** Clean with xylene followed by methanol. Soak in methanol for 30 min for effective precipitate removal.

7. Problem: *KF* chemicals have changed color from transparent green (normal) to deep red color (abnormal) and do not detect the water upon injection. It means that the solution is over titrated. In this case, inject 5  $\mu\text{L}$  of pure water using CR-700 Hamilton syringe.
8. Problem: *KF* cell does not detect water but color of reagent seems normal. This may happen if two anode electrodes are touching. Use a thin card to gently separate the touching electrodes. If you are not confident, contact Parkes Scientific.
9. When to change the reagents (“GR Scientific FAQs,” 2015)?
  1. 50-60 ml of sample injected
  2. 1 g of water injected ( $10^6$   $\mu\text{g}$  water)
  3. Lasts for 2-3 weeks (depends on 1 and 2)
  4. Other indications:
    - a. Slow titration
    - b. Darkening of cathode reagent
    - c. Precipitate formation in cathode cell
    - d. Phase separation in anode cell
    - e. Unstable titration current and lack of reproducible results

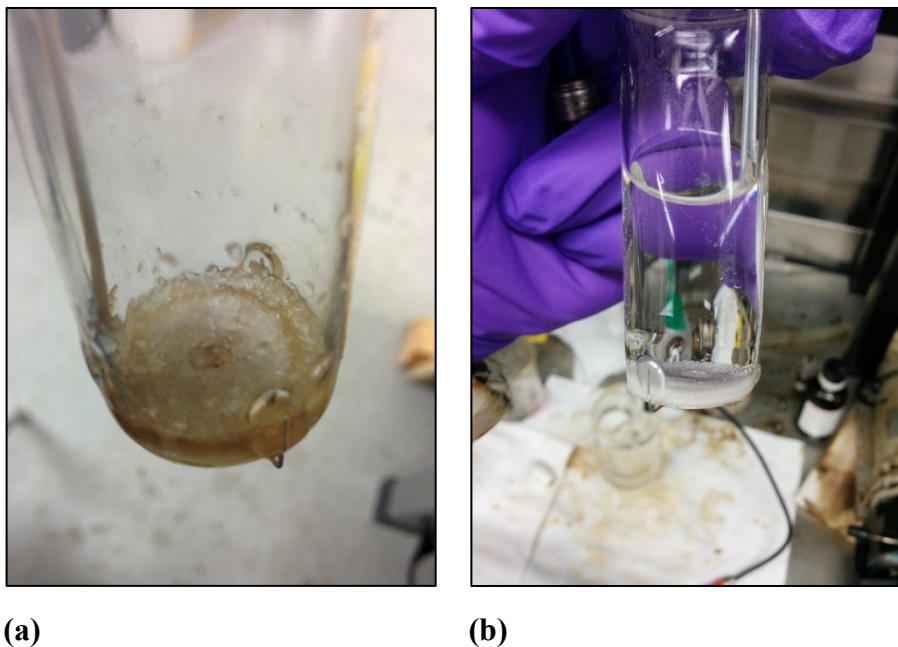


**Figure D1-2:** The difference between (a): dirty cathode electrode with precipitates and (b): cleaned electrode of Karl-Fischer cell

### General References

- Basics of Karl Fischer Titration [WWW Document], 2015. URL <http://www.sigmaaldrich.com/analytical-chromatography/titration/hydranal/learning-center/theory.html> (accessed 12.21.15).
- GR Scientific FAQs [WWW Document], 2015. URL <http://www.grscientific.com/faqs/> (accessed 12.21.15).

## Appendix D2: Microscope Image Acquisition Procedure

This document describes the procedure used to obtain the microscope images shown in Chapter 2 and Chapter 4. The multiple images stitching procedure is also discussed here.

### Microscope Calibration

The calibration according to KÖHLER illumination principle is essential to get a good contrast image and avoid uneven illumination across the image. The steps are listed here but for details, refer the Section 4.1.1 in the Axioscope operating manual.

1. Turn on the microscope.
2. Calibration for 10x lens
  - a. Set microscope lens to 10x.
  - b. Put a glass slide.
  - c. Close the field diaphragm to the smallest diameter. You should see a hexagon.
  - d. Raise the condenser to the maximum height without bumping the glass slide. This can be done using a limit stop.
  - e. Center the hexagon using centering screws for condenser.
  - f. Focus the hexagon by turning the focus knob.
  - g. Open the field diaphragm just enough to cover the field of view as seen from eyepiece.
3. Remove eyepiece from tube barrel and adjust aperture diaphragm to cover 70 % of the area (differs with different magnifications). Numerical aperture markings are present on the lens for easy calibration.
4. Repeat Steps 2 and 3 for 40x lens.
5. Scaling calibration is required for Axiovision software to convert pixel values into a meaningful dimension such as  $\mu\text{m}$ . These can be found in the group folder and need to be done only once per computer.
6. Perform white balance with a white piece of paper on the sampling platform.
7. Perform shading correction with an empty microscope slide.

## Microscope Care

1. Optimal size for microscope slide covers: 1.5 mm thickness.
2. Check refractive index for immersion oil when purchasing new immersion oil for 100x lens.
3. Clean microscope lenses with 70 % ethanol in water.

## Image Acquisition

1. Open Axiovision LE software and turn the microscope power on.
2. Click 'Live' to open live camera view.
3. Place a microscope slide on stage and secure it.
4. For each slide (one slide per sample), store 10x and 40x images in separate folders. Cluster image analysis (Chapter 3) is performed on 40x images only.
5. Start with 10x images. The 10x lens gives high level view and within minutes, the whole slide can be seen.
6. Capturing 10x images
  - a. Make sure 10x lens is placed above the microscope slide.
  - b. Set condensor slider to 0.25 aperture. This helps to maximize resolution for 10x lens.
  - c. Set scaling on axiovision software to 10x and hit 'activate selection'.
  - d. Set images storage location by '*Tools > Options > Storage > folder*' for '*auto save*'. Hit '*apply*' and '*ok*'.
  - e. Move from left to right (+x direction), then down (-y direction) and from right to left (-x direction) till entire slide is covered.
  - f. The image seen by the camera would appear on live view. Make sure that EVERY image is focused. **Unfocussed images are useless for subsequent image analysis.**
  - g. Keep '*A min/max setting*' on live view page. Hit '*exposure*' to get an appropriate exposure. '*Exposure*' sometimes yields very dark images and hence increase the exposure manually by '*properties > adjust > exposure*'.

Increase exposure till most of the background is clear but not to the extent that you start losing objects (over-exposure).

- h. Avoid cutting objects across the edges of image.
  - i. See '*what to capture*' section below.
7. Capture 40x images
- a. Repeat step 6 for 40x lens using 0.65 aperture and 40x scaling.
  - b. Ensure that 40x images are stored in a separate folder than 10x.

## **What to Capture in Bitumen Froth Images?**

Diluted bitumen contains water, free water and solids dispersed in bitumen (red to yellow background).

1. Water drops (hollow spherical objects with black edges)
2. Free water (hollow non-spherical objects covered with solids and other interfacial materials and look like crumpled paper). These can range from 20 to >1000  $\mu\text{m}$  in size.
3. Solids (Black specks): Solids consist of clays and heavy minerals. Clays are below microscope resolution and hence cannot be observed.

We want to study clustering or aggregation between different components and analyze which one is dominating. Capture image containing following:

1. Water-Water interaction: Water drops have been seen to form chains and flocs.
2. Solid-solid interaction: Solids have been seen to form chains and flocs although rare.
3. Solid- Liquid interaction: Solids are generally seen to be dispersed in W-W floc.
4. Free water: These objects are covered with dark specs and other material. They are best captured by stitching multiple 10x images because of their huge size. See 'image stitching procedure' below.

Avoid capturing artefacts such as

1. Air bubbles: white objects when seen directly from eyepiece.
2. Fibres: These could be left out due to wiping clean slide with tissue.

3. Halos: Sometimes, they appear and can be removed by increasing exposure, raising condenser (reducing depth of field) and/or changing the focus point (z location).

## Image stitching Procedure

This procedure can be used for stitching multiple 10x or 40x images if objects are much bigger than one image can capture.

1. While capturing images, ensure that the images that need to be stitched have '*same exposure*' and '*z location*'. Ensure that there is minimum 15 % overlap area between consecutive images so that Photoshop can stitch them.
2. Open Photoshop CC and hit '*File > Automate > Photomerge*'.
3. In the '*photomerge*' window, hit browse to select the images to be stitched.
4. Ensure that '*blend images together*' is checked and layout as '*Auto*'. Hit '*ok*'.
5. Once the images are merged, select '*Layers > Flatten image*'.
6. You will notice that there are some empty areas. These areas can be filled by selecting that area (including some existing background) using '*rectangular marquee tool*' and '*Edit > Fill > Content aware fill*'.
7. Scale bar can be added in Axiovision LE by selecting '*pixel*' scaling and manually converting '*pixel value*' to ' $\mu\text{m}$ ' using 10x image calibration (0.4619  $\mu\text{m}/\text{pixel}$ ) or 40x image calibration (0.1152  $\mu\text{m}/\text{pixel}$ ).
8. For details, refer to the following links
  - a. <https://helpx.adobe.com/photoshop/using/create-panoramic-images-photomerge.html>
  - b. [https://helpx.adobe.com/photoshop/using/filling-stroking-selections-layers-paths.html#content\\_aware\\_pattern\\_or\\_history\\_fills](https://helpx.adobe.com/photoshop/using/filling-stroking-selections-layers-paths.html#content_aware_pattern_or_history_fills)